Residual Stress Measurement and Structural Integrity Evaluation of SLM Ti-6Al-4V

Craig Russell Knowles

Dissertation presented in partial fulfillment of the requirements for the degree of Master of Science in the Department of Mechanical Engineering, University of Cape Town

July 2012

Declaration

I hereby,

1. grant the University free license to reproduce the above thesis in whole or in part, for the purpose of research;

2. declare that:
   (a) the above thesis is my own unaided work, both in conception and execution, and that apart from the normal guidance of my supervisor, I have received no assistance apart from that stated below;
   (b) except as stated below, neither the substance nor any part of the thesis has been submitted in the past, is being, or will be submitted for a degree at this or any other University.
   (c) I am now presenting the thesis for examination for the Degree of MSc.

Word Count: 46459

_____

Craig Russell Knowles

_____

Date

ABSTRACT

The constant drive toward cleaner, more powerful and more efficient jet turbines in the aerospace industry has narrowed the gap between the aircraft performance envelope requirements and the material limits. The most advanced turbine engines are incredibly complex in design and the weight-saving requirements have placed significant pressure on material capabilities and the manufacturing systems. The next generation of manufacturing methodologies are being developed in the Additive Manufacturing (AM) arena from which Selective Laser Melting (SLM) has emerged as a promising candidate for producing highly complex components. Selective Laser Melting is a laser-based AM technique which builds 3-dimensionsal parts from CAD models in a layerwise fashion. This technique is capable of exceptional accuracy and build complexity while producing very little material waste. SLM has been highly successful in the biomedical industry in creating intricate implants and could prove highly effective in producing the sophisticated turbine components in modern jet engines.

A potential area of concern in laser-based manufacturing is the generation of thermal residual stresses. The heat generated from the laser to melt the powder causes very high localised temperature gradients which, on cooling are capable of producing high residual stresses. The presence of residual stress is a concern for an environment in which fatigue loading is present. Residual stresses reduce the threshold flaw size required for a fatigue crack to initiate and propagate. This is highly undesirable in the aerospace industry in which fatigue loading is commonplace and high material integrity is required. Historically, laser-based AM machines have produced materials which are plagued by material voids and micro-flaws, however recent developments in the laser power and powder laying capabilities have improved the density and reduced the porosity significantly. Indeed, the EOSINT M270 DMLS machine employed in this study is reported to be capable of densities greater than 99.7%.

In a pilot study conducted in this investigation, the residual stresses in Selective Laser Melted Ti-6Al-4V were measured in components with observable deformation using the hole-drilling strain gauge method (ASTM E837-08). The residual stress levels were found to be exceedingly high and approached the yield strength of 1090 MPa in some regions. Following these results, the acquisition of cylindrical SLM Ti-6Al-4V specimens permitted an evaluation of heat treatment

as a stress-alleviation technique. The heat treatments tested included a simple stress-relief treatment, a recrystallization anneal, a duplex anneal and a beta anneal. The general response to heat treatment was excellent with drastic reductions in residual stress levels post treatment. The simple stress-relief treatment reduced stress levels by between 76-81% and retained the martensitic microstructure. The recrystallization anneal reduced residual stresses by between 94-97% and produced a microstructure consisting of primary α in a matrix of transformed β containing acicular α. The duplex anneal reduced residual stresses by between 91-95% and transformed the microstructure into one with small amounts of equiaxed α in a matrix of acicular α (transformed β). The beta anneal reduced residual stress levels by 90-91% and transformed the microstructure into an acicular α (transformed β) with prior β grain boundaries.

The porosity levels were generally observed to be low however a single layer of highly porous material was identified in one specimen and severe circumferential cracking was observed in two cylindrical specimens. The cracking appeared to have been generated from a single highly porous layer which was most likely due to inconsistencies in the powder layer. The presence of high residual stresses and regions of high porosity necessitated an investigation into possible micro-flaw interaction under a tensile load. A miniature tensile rig was designed for use under the microscope to expose hidden defects and monitor any flaw interaction. This rig was designed using a proof ring concept which introduced force to the specimen in increasing intervals until the specimen fractured. The rig was successful in identifying micro-flaw interaction in one specimen and the opening of micro-cracks from sharp-edged voids. An attempt using Digital Image Correlation to make a quantitative assessment of any micro-flaw interaction was not successful due primarily to poor image quality produced by the microscope camera.

The specimens produced for this study contained high residual stresses in the as-built form with localised regions of high porosity. This is an area of concern in fatigue environments due to the increased propensity for fatigue crack initiation and propagation. Heat treatment proved highly effective in alleviating the residual stresses and shows great potential in developing a system for reducing residual stresses at their conception through a powder bed heating scheme. Further work is required in directly assessing the fatigue behaviour of SLM Ti-6Al-4V before and after heat treatment to quantitatively assess the effects of residual stress on the fatigue crack threshold flaw size.

ACKNOWLEDGEMENTS

The author is indebted to many individuals who aided this MSc dissertation and to whom he would like to express his sincere appreciation. In particular, the author would like to thank his supervisors, Prof Robert Tait and Dr Thorsten Becker at the University of Cape Town for their exceptional support and guidance. Special mention needs to be made for the following people without whom this project would not have been possible:

- To Professor Robert Tait for his support, interest and direction in all aspects of this study;
- To Dr Thorsten Becker for his time and effort in the completion of this study;
- To the author's family: Joan, Russell and Ashleigh Knowles to whom he is indebted for their unwavering support throughout his academic career;
- To the author's friends, in particular his MSc office-mate Mathew Molteno for the camaraderie and humour found in countless adventures and for the support whenever the roof came crashing down;
- To Maryann Bennett for her wonderful companionship, curiosity and humour;
- The author would like to thank Dr Glen Sneddon and the CSIR for their interest and financial assistance with this project.

The author would also like to thank the many people involved in facilitating this project at the University of Cape Town. In particular, Professor Rob Knutson for the use of the Materials Science Laboratory and Glen Newins for his tireless efforts in manufacturing the tools employed in this project.

TABLE OF CONTENTS

LIST OF FIGURES

LIST OF TABLES

CHAPTER 1 - INTRODUCTION

This thesis concerns an investigation into the material performance and integrity of components built using a new form of manufacturing known as Selective Laser Melting (SLM). This chapter will introduce the industries which would benefit from this new technique and discuss the motivation behind this project. The first section discusses the current state of the aerospace industry and the potential arena in which SLM could make an impact.

1.1 AEROSPACE MANUFACTURING

The increasing demand on the performance capabilities of modern aircraft have led to greater complexities in proposed designs, especially in the jet engine arena. Jet engines are exposed to temperature and stress extremes during operation and are subjected to intense cyclic loading [1]. The increasing fuel efficiency requirements have led to drastic weight saving in component designs, meaning the conditions experienced during operation are significantly closer to the material limits [2]. This industry drive for efficiency has placed additional pressure on the manufacturing systems to produce components which are near-flawless to reduce the risk in air travel [3]. The current standards of manufacture are fast becoming obsolete in terms of producing components with the intricate geometry required in the latest designs [4]. The next generation of manufacturing methodologies could stem from the Additive Manufacturing (AM) arena in which Selective Laser Melting (SLM) is a promising candidate.

SLM is a laser-based manufacturing system which uses CAD models to create 3-dimensional parts in a layerwise fashion. These systems are capable of producing highly complex designs with exceptional accuracy and minimal material waste [5]. It is also highly versatile in that no system changes are required for different components to be manufactured on the same machine. This has particular appeal in industries where cost-saving is of paramount importance.

SLM has shown its versatility in the biomedical industry in which it has proved to be highly versatile in producing implants and prosthetic devices intended for rehabilitation [6]. The requirements of the biotechnology industry are equally, if not more demanding in terms of build

complexity, particularly in the construction of implants [7]. Complex shapes are required which match human anatomy and in some cases requiring a specific porous layer such that the tissue will bond with the implant [8]. It follows that this type of manufacture is highly specific to the patient's requirements and every implant is a different shape and size [9]. The versatility of SLM through its CAD interface allows seamless transitions between implants without any changes to the machine setup.

The advantages of SLM in the aerospace industry are numerous, particularly in the construction of components for aircraft turbine engines. The increasing complexity in jet turbine design is limited by the capability of the manufacturing systems. The fan and turbine blades have been constructed using investment casting methods with a wide variety of additional processing to improve the material behaviour. These techniques are complex and require a great deal of energy and material which leads to excessive manufacturing costs. There is significant potential for the SLM process, as it is a net-shape manufacturing technique thus eliminating machining and final finishing costs.

These benefits of SLM have justified an investigation into the applicability of this technique for producing components in the aerospace industry. The versatility of this technique would allow SLM machines to construct a wide variety of components from each machine without requiring modifications to the machine. The level of build complexity could allow significantly more advanced components to be designed which would ultimately increase the efficiency of aircraft systems and reduce the costs associated with their construction. The major barrier preventing any new manufacturing methodology from being implemented is the quality and integrity of the material after manufacture. This is especially true for the aerospace industry in which material integrity is of utmost importance. These material integrity requirements are discussed next.

1.2 MATERIAL INTEGRITY REQUIREMENTS

The most important assessment of Selective Laser Melting is in the level of build quality and material integrity. Stringent safety requirements in the aerospace industry, particularly in the construction of airliners, place great emphasis on ensuring their manufacturing systems produce components of the highest quality. As such, airline manufacturers follow strict quality control methods to ensure that their machines produce suitable parts for this industry [10].

With the material integrity in mind, a significant concern has been linked with laser-based manufacturing systems in terms of thermal residual stresses. These concerns have been discussed in terms of direct laser sintering systems by various authors, including Pohl [11] and Casavola et al [12], [13]. Tensile residual stresses can be highly detrimental to the structural integrity of a component, particularly when high cycle/fatigue loading is present of which several authors have reported unfavourable effects [14–16]. Material fatigue is among the most serious mechanisms to affect the ability of a structure to carry a load [17] and is thus a concern in the aerospace industry in which many failures have been attributed to this phenomenon such as the turbine disk failure examined by Tao [18]. Due to the aforementioned complexity and efficiency requirements, aircraft grade materials often have smaller safety margins in comparison to their standard counterparts which increase the risk of failure [19]. In order for a new manufacturing technology such as SLM to be used in constructing structural components in the aircraft industry, a thorough understanding of the material performance is essential.

This thesis aims to contribute to the understanding of the SLM material performance by investigating the residual stress levels in SLM Ti-6Al-4V components built by an EOSINT M270 machine. In addition, the levels of porosity and micro-flaws inherent from the manufacturing process are investigated in order to make an assessment on the effect of these stresses on the overall structural integrity.

Various authors including Kang [20] and Beiler [21] have suggested that heat treatment can prove effective in reducing residual stresses in conventionally-machined components. Heat treatment is particularly relevant for the SLM methodology since it is the least invasive in terms of process changes. If one of these techniques could be applied successfully to SLM produced material, the generation of thermal residual stresses may not be a substantial impediment to the successful implementation of this technique.

1.3 THESIS OBJECTIVES

The objectives of this study are concerned primarily with the possible implications of high residual stresses on SLM Ti-6Al-4V. This is split into several studies which evaluate the merits and limitations of this new manufacturing technique. These objectives are listed below.

- To measure the residual stress levels within Ti-6Al-4V components built with Selective Laser Melting (SLM).
- To evaluate the effectiveness of heat treatment in alleviating residual stresses in SLM Ti-6Al-4V.
- To evaluate the degree of porosity and micro-flaws within components built by SLM.
- To perform a microstructural analysis on SLM Ti-6Al-4V.
- To assess the structural integrity of components manufactured with SLM Ti-6Al-4V.

The implicit objective of this study is to further the overall understanding of SLM in terms of the mechanical and physical behaviour of the material produced by these systems.

1.4 THESIS LAYOUT

In order to fully understand the position of Selective Laser Melting in industry, the history and capabilities of SLM along with its competitors in the Additive Manufacturing arena are introduced in Chapter 2. This includes a detailed history of the AM methodology from its conception in the plastics industries. Chapter 2 also explains the limitations of such systems and describes the problems which can arise if processing parameters are not optimised. Residual stresses and their potential impact on a material in terms of fatigue cracking is discussed which elaborates on the concern mentioned above.

The Ti-6Al-4V material used in this study is introduced in Chapter 3 in its various industry forms. The physical, mechanical and microstructural properties are discussed and the effect of manufacture on the behavioural attributes of this alloy. The effect of heat treatment on Ti-6Al-4V from literature is deliberated in Chapter 3 such that suitable techniques may be identified for residual stress removal. The available literature on SLM Ti-6Al-4V in terms of its fatigue properties from recent studies has been included in Chapter 3 to highlight the need for further assessment in this topic.

Chapter 4 is an experimental review chapter which details all the experiments performed in this study (with the exception of the micro-flaw exposure study). This includes the residual stress analysis, the microscopy work, physical property testing and the mechanical testing. This chapter also specifies the heat treatments used in this study and the required equipment.

The investigation into micro-flaw interaction is described in Chapter 5 with the design of a miniaturised tensile rig for use under an optical microscope. This is extended with the use of software for a relatively new technique known as Digital Image Correlation to quantitatively assess micro-flaw behaviour invisible to the naked eye.

The results from all the investigations in this study are produced in Chapter 6 which includes the qualitative observations made during micro-flaw exposure attempts. The results are then discussed in Chapter 7 from which an assessment of the material quality and structural integrity of SLM Ti-6Al-4V is made. These topics are then concluded in Chapter 8 along with suggestions of future work in this field.

CHAPTER 2 - BACKGROUND

This chapter aims to provide some general information on the history and industry direction of Additive Manufacturing (AM) such that the early successes of SLM and its predecessors are clear. It was from these early developments that the potential for SLM in the aerospace industry was initially identified. The historical perspective on the Additive Manufacturing arena is a brief outline of the work done by the authors Bourell and Beaman Jr. [22], [23], [24] and Agarwala et al [25]. The overview of the predecessors to laser-sintering in Section 2.2.1 is a brief summary of the historical development study done by Shellabear and Nyrhilä [26].

2.1 ADDITIVE MANUFACTURING

Additive Manufacturing is a relatively new ideology in which materials are bonded or joined to create a three-dimensional part from Computer Aided Design (CAD) data. This is typically completed in a layer-wise fashion in which successive cross-sections are built to create a model from the base upwards [27]. Traditional machining processes are termed 'Subtractive Manufacturing' since material is removed from the bulk material to create the component. AM is largely synonymous with Solid Freeform Fabrication (SFF) which is the term given to a new group of technologies also known as rapid prototyping or rapid manufacturing. This form of manufacturing was created for prototype design purposes in which prototypes could be built quickly and then changed easily without requiring new machines.

The AM industry has grown substantially and in 2008, the products and services of AM had an estimated value of $1.2 billion [22]. This industry continues to grow by more than 10% each year and is fast becoming an established manufacturing methodology. Historically, these freeform fabrication techniques were used for short-run components as well as casting inserts and initial prototypes. These technologies were limited by material capabilities and a poor surface finish in completed components. The last decade has seen drastic improvements into the capabilities of these freeform machines with particular emphasis in the mechanical properties and density of AM produced metallic components [28]. The biomedical industry has found particular interest in

this type of technology with much research being invested into titanium alloy implants created via AM. This chapter gives a brief history of the Additive Manufacturing revolution and an insight into the Direct Metal Laser Sintering (DMLS) process which is employed in this project.

2.2 HISTORY

The Additive Manufacturing (AM) roots can be traced back around 60 years during which several theoretical layerwise methods were proposed. The first successful Additive Manufacturing process however was only completed in 1972 by Ciraud [29] and in modern terms, would be considered a powder deposition technique [22]. It was in 1951 however, when Munz proposed a system resembling the current Stereolithography technique [30]. This system exposes layers of a transparent photo liquid to a radiation source. A piston collects appropriate amounts of the photo emulsion and a fixing agent to complete the next layer. The process is shown in Figure 2.1 below. The cylinder which is completed at the end of the process contains an image of the object. A three-dimensional object would then be created from this solid cylinder by a carving process or through photochemical etching [22].

A process known as Photochemical Machining was developed in 1968 by Swainson [31] in which a plastic pattern was created by three-dimensional selective polymerization of a photosensitive polymer [22]. This technique employed the intersection of two laser beams to create the polymer. This process was further developed by Battelle Laboratories which included the construction of the system hardware but ultimately no commercial process was successfully produced. A schematic of this system is shown below in Figure 2.2.

As mentioned earlier in this chapter, the first successful AM technique was proposed by Ciraud in 1971. This system was able to use a variety of materials, some of which were partially melted. Small particles of a material were applied to the matrix using a nozzle, gravity, electrostatics or magnetostatics [22]. The particles were then heated locally using a radiation source such as a laser, electron or plasma beam. The layer was then completed as the heat source bonded the particles together. If so desired, a second laser could be employed to increase the strength of the bond formed between the particles. This system is shown in the schematic in Figure 2.3 (note the use of two lasers in this case).

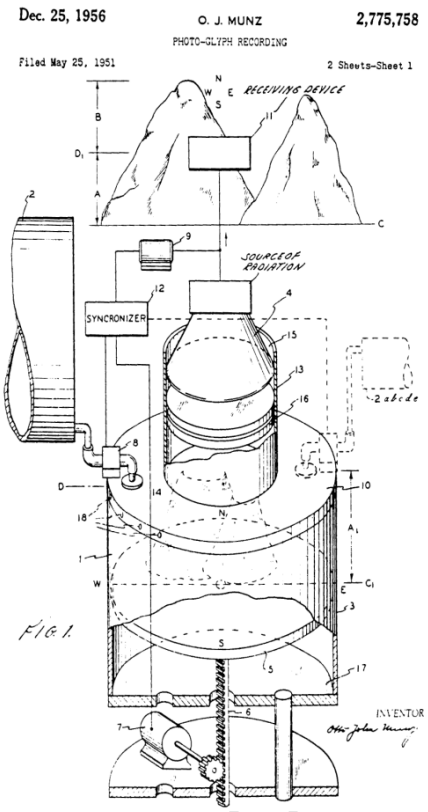

Figure 2.1: Munz's photo-glyph recording system developed in 1951. [22], [30]

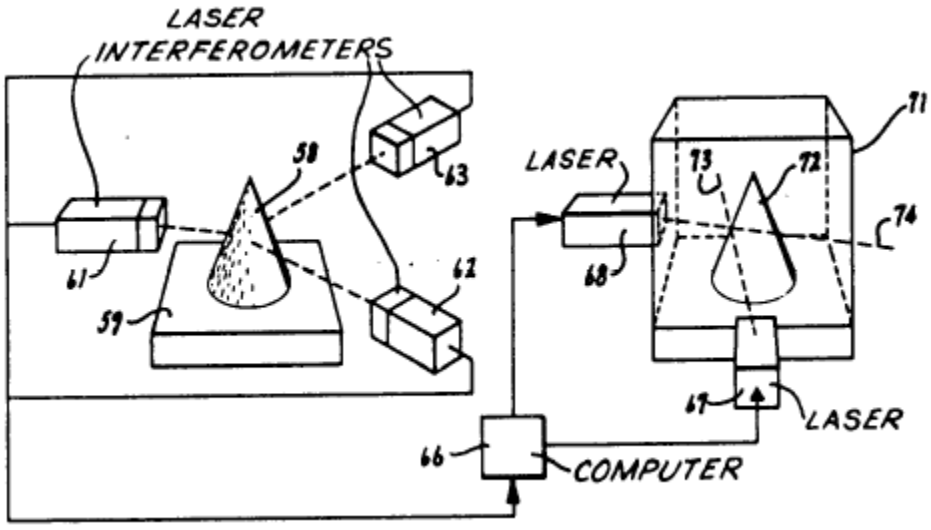

Figure 2.2: The Photochemical Machining technique developed by Swainson in 1968. [22], [31]

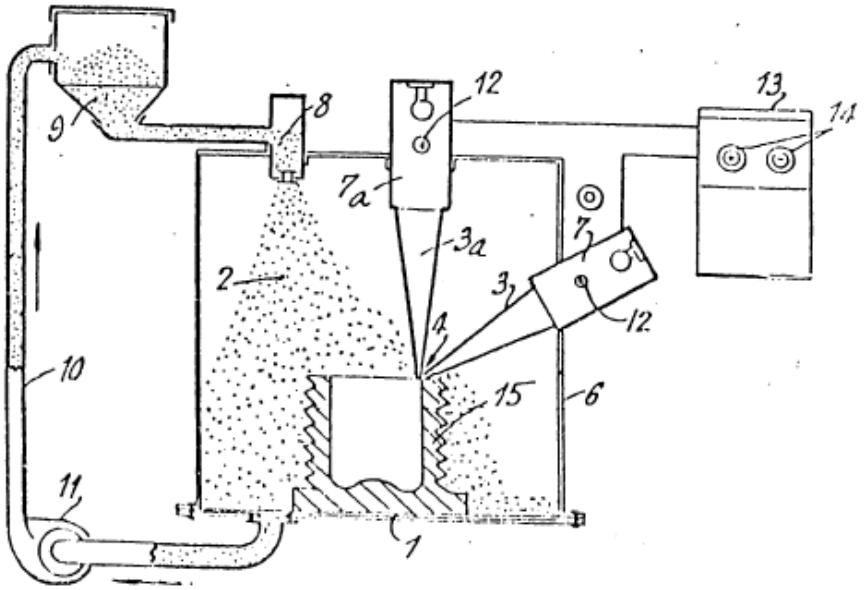

Figure 2.3: Powder based AM technique developed by Ciraud in 1971. [22], [29]

A powder laser sintering method was first presented in 1979 by Housholder [32]. In this patent, a planar layer of powder is solidified selectively using a controlled heat scanning source [26]. This could also be completed using a hand-held heat source. This process is shown below in Figure 2.4

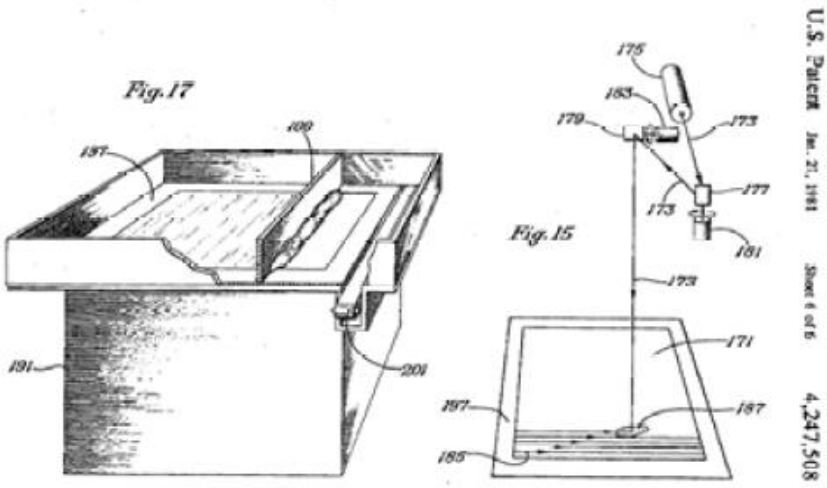

Figure 2.4: Housholder's powder laser sintering process developed in 1979. [22], [32]

Hideo Kodama published the first account of a functional rapid prototyping system using the photopolymer technique [33]. In this technique, exposed layers of the photo emulsion corresponded to cross section layers of a three-dimensional model [23]. His work focused on three separate designs as shown below in Figure 2.5. The first of which involved using a mask to control the UV source exposure and creating new layers by immersing the model downward into the vat of photopolymer liquid (Figure 2.5a). The second technique (Figure 2.5b) utilized the same mask with the exception that the model is drawn upwards for each new layer and the exposure equipment is positioned beneath the vat. The third system (Figure 2.5c) immersed the model in the same fashion as the first system, excepting that an x-y plotter and optical fibre was used to expose the layer in a very controlled manner [22].

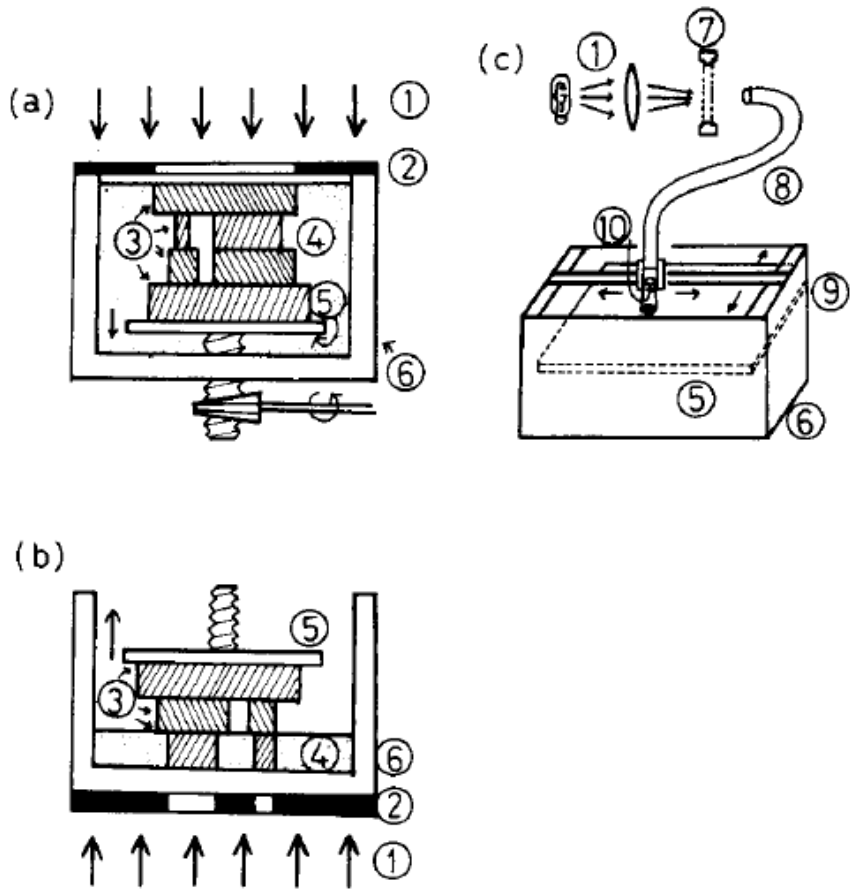

Figure 2.5: Stereolithography techniques employed by Hideo Kodama (Nagoya Municipal Industrial Research Institute). [22], [33]

Herbert developed a system in 1979 using a UV laser with a directional mirror system on an x-y plotter which directed the beam into a vessel of photopolymer liquid [34]. A computer system was used to control the movement of each layer and the vessel was lowered upon which more photopolymer liquid was added after the completion of each cross-section [23]. This system is shown in Figure 2.6 below. The components produced by these early systems were very rough and somewhat different from the intricate designs of which AM machines are capable today. Some of the early parts developed by Herbert, Kodama and Housholder are shown in Figure 2.7.

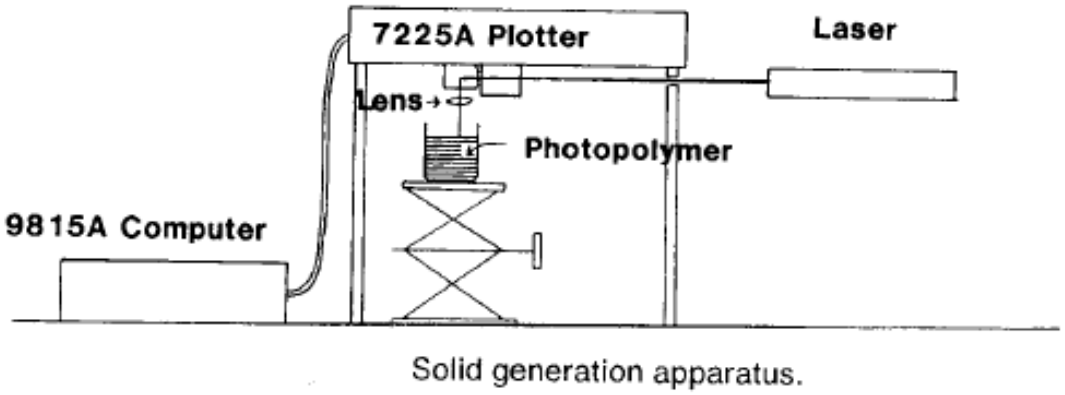

Figure 2.6: Herbert's Stereolithography system developed in 1979. [22]

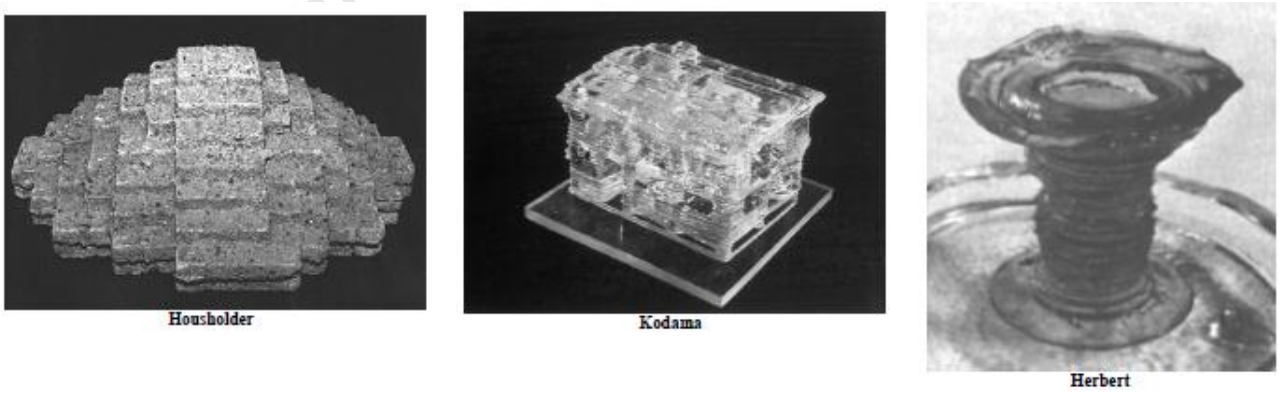

Figure 2.7: Early components developed by the Stereolithography machines from Housholder, Kodama and Herbert. [22]

2.2.1 DEVELOPMENT OF DIRECT METAL LASER SINTERING

These early machines gave rise to a sudden interest in AM processes during the 1980s and 1990s. The commercialisation of rapid prototyping was initiated by Charles Hull in the 1980's who founded the company known as 3D Systems [35]. Hull began with a patent describing a working method for producing 3-dimensional components layer by layer from a vat of resin similar to that of Kodama and named it "Stereolithography" [26]. 3D Systems dominated the stereolithography market for much of the 1980's and 1990's and in 1997 made the statement, "One specific stereolithography technology is known simply as stereolithography and uses a liquid medium, another stereolithography technology is known as Selective Laser Sintering (SLS). SLS is based on the selective solidification of a powdered medium" [26]. Many of the important developments in AM machines were produced by Hull and 3D Systems during the late 1990's, including the STL file type through triangulated models of data can be prepared. They also developed the laser hatching schemes now in use in modern SLS and DMLS machines. The rights to the complete patent portfolio for laser-sintering created by 3D Systems was acquired by EOS in 1997.

In 1986. Carl Deckard produced a method similar to Hull's original patent with the exception that powdered materials were used [36]. This was originally termed Part Generation by Layerwise Selective Sintering (PGLSS) but was later changed to Selective Laser Sintering (SLS) [26]. Deckard used a 100 Watt Nd:YAG laser with an ABS polymer powder in initial experiments yet the process was not restricted to plastics. The commercialisation of Deckard's machine was initially through a company called DTM (Desk Top Manufacturing). The first successful system to be developed by DTM and Carl Deckard was the Sinterstation 2000 in December 1992. This was closely followed by EOS in 1994 with the EOSINT (P) 350. The first successful sintering of single-phase metals was performed by Fraunhofer IPT and the Katholieke Universiteit Leuven (KUL) in 1994 using 316L stainless steel powder and Fe-Cu powder mixtures [26].

Direct Metal Laser Sintering (DMLS) was officially commercialised using EOS plastic sintering technology in combination with a development in metallic powder metallurgy by Electrolux Rapid Development (ERD). The first system to implement the new technology was the EOSINT M250 in 1995. This system used a 100 Watt CO_2 laser with high accuracy. This system was

further developed by Fockele & Schwarze to produce near fully dense components through complete powder melting [26].

The introduction of the EOSINT M250 produced a significant amount of interest in the AM field of metallic laser sintering. Several developments in powders allowed the system to utilise a more varied selection of powders to produce components for different applications. DirectSteel H20 was a tool steel powder which could attain a density of near 100% using the EOSINT M250. In 2004, the EOSINT M270 was produced which uses a solid-state fibre laser to produce near fully dense components with complete and partial melting scheme capabilities.

The timeline illustrating the developments of the AM machines mentioned in this section is shown in Table 2.1 below.

Table 2.1: Additive manufacturing timeline demonstrating the modern technology developments.

Year	Title	Inventor	Commercial Entity	Technology Arena
1986	Apparatus for production of 3D plastic objects	Charles W. Hull	3D Systems Inc.	Stereolithography (SLA)
1988	Apparatus and method for forming and integral object from laminations	Michael Feygin	Cubic Technologies	Laminated Object Manufacturing (LOM)
1989	Method for production of parts by laser sintering	Carl Deckard	DTM Inc.	Selective Laser Sintering (SLS)
1990	3D modelling apparatus	Itzchak Pomerantz; Joseph Cohen-Sabban; Avigdor Bieber; Josef Kamir; Mathew Katz; Michael Nagler	Scitex Corporation Ltd.	Solid Ground Curing (SGC)
1992	Apparatus and method for creating 3D solid parts	Scott Crump	Stratasys Inc.	Fused Deposition Modeling (FDM)
1993	Three-dimensional printing apparatus	Emanuel M. Sachs John S. Haggerty Michael J. Cima Paul A. Williams	M.I.T	Three-Dimensional Printing (3DP)

1994	Introduction of the EOSINT M250 laser sintering machine	EOS	EOS	Selective Laser Sintering (SLS)
1998	Method for producing 3D solid entities	Ralf Larson	Arcam Ltd.	Electron Beam Melting (EBM)
2003	Advancement in sintering systems for complete melting	Ralf Larson	Speed Part RP	Selective Laser Melting (SLS)
2004	Introduction of the EOSINT M270 DMLS machine	EOS	EOS	Direct Metal Laser Sintering (DMLS)

As is evident from Table 2.1, the plastics industry has benefitted for some time from the use of modern stereolithography and 3D printing equipment, but it is only in more recent times that the metallic capabilities of AM have been explored. The next section explores the types of AM equipment which is currently in use for both the plastics and the metallic industry.

2.3 MATERIALS, PROCESSES AND MACHINES

The development of the AM industry discussed in the previous sections has been split into several arenas which are separated primarily by the material capabilities. This section will briefly introduce the primary manufacturing processes in the AM industry at their current capacity. The rapid prototyping processes in the plastics industry is dominated by Stereolithography (SLA), Laminated Oject Manufacturing (LOM) and Fused Deposition Modelling (FDM). The recent improvements in technology mentioned in the preceeding sections has led to the material capabilities being extended to metals from which Electron Beam Melting (EBM) and the Selective Laser Sintering (SLS) technologies have emerged as major methodologies.

2.3.1 STEREOLITHOGRAPHY (SLA)

Stereolithography (SLA) is the most common rapid prototyping/manufacturing technology and has been extensively used in the plastics industry. This method uses a UV laser to selectively cure liquid photopolymer in successive layers or cross-sections. The photopolymer solidifies

immediately upon contact with the laser beam and after a layer has been completed, the model is lowered slightly into the vat of liquid to allow more photopolymer to cover the previously built layer. A resin sweeper is used to ensure adequate resin covers the previously built layer. The self-adhesive property of the photopolymer allows the layers to bond and create a complete three-dimensional object. Stereolithography provides a very good surface finish and is highly accurate, although post-curing is required for some materials. Excess resin is removed using a chemical bath. The versatility of the liquid/vat system allows larger sized objects to be created than other AM techniques. A schematic of the typical SLA process is shown below in Figure 2.8 [37].

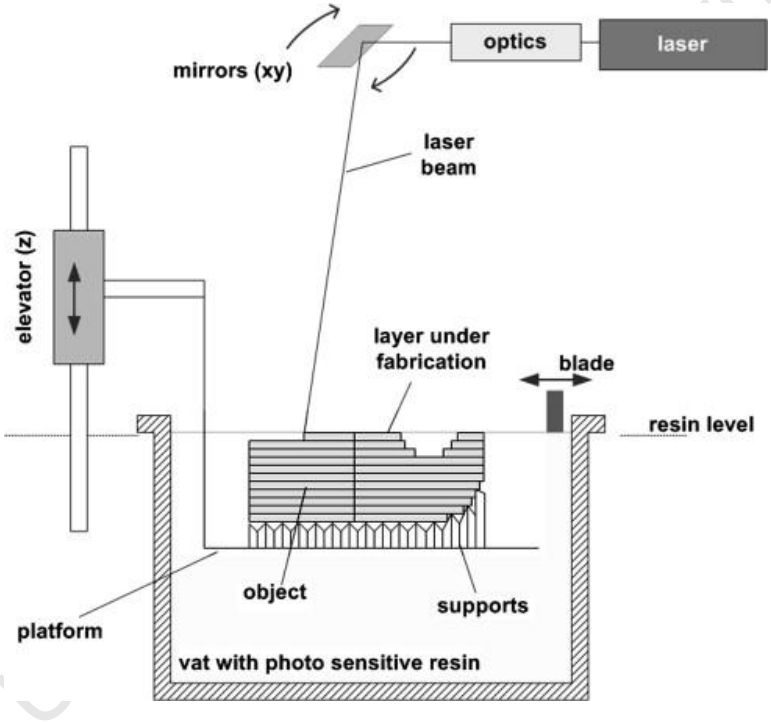

Figure 2.8: Stereolithography machine used to create 3D objects from photo-sensitive resin. [37]

2.3.2 LAMINATED OBJECT MANUFACTURING (LOM)

Laminated Object Manufacturing (LOM) is slightly different to the other additive manufacturing techniques in that a laser is used to cut successive cross-sections from sheet material. This process is shown below in Figure 2.9. Each sheet is adhered to the previous layer using the heated laminating roller. Following the completion of each layer, the waste material is rolled up

in the Take-up Roll. The complexity of the object design impacts on the time taken to remove the waste material as laser cross-hatching is used to facilitate the removal. The accuracy and finish of LOM produced objects are not as good as those of the other primary AM techniques. The advantages however are primarily the low material cost which makes it useful for applications such as pattern building for sand casting [38].

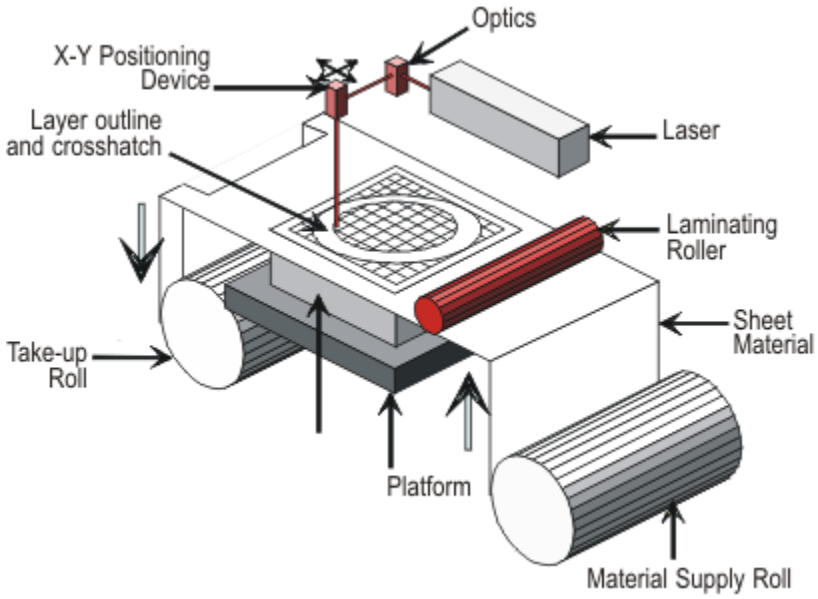

Figure 2.9: Laminated Object Manufacturing process. [39]

2.3.3 FUSED DEPOSITION MODELLING (FDM)

Fused Deposition Modelling (FDM) is second only to stereolithography in terms of its usage in the rapid prototyping industry. In this process, a plastic filament is drawn through a liquefier and deposited on the workspace via an extrusion nozzle as shown in Figure 2.10 below [40]. The plastic hardens immediately upon extrusion onto the object. The layer thickness is controlled using the feed rate of the plastic filament as an indicator. An important factor in FDM is the temperature of the previously built layer, which needs to be maintained at a temperature marginally below the melting point of the material. This is necessary for good adhesion between the layers since delamination can occur if this temperature drops too far below the material

melting point. FDM is relatively quick for smaller parts but objects requiring large cross-sections will take significantly longer since the process of moving the melting chamber and FDM head is timeous. The material finish is relatively good but does not have the dimensional accuracy of stereolithography [41]. FDM is used largely with thermoplastics which harden quickly following exposure to the environment. FDM is quiet and can be compacted into a standalone office unit which is particularly useful if small designs/prototypes are being built [42].

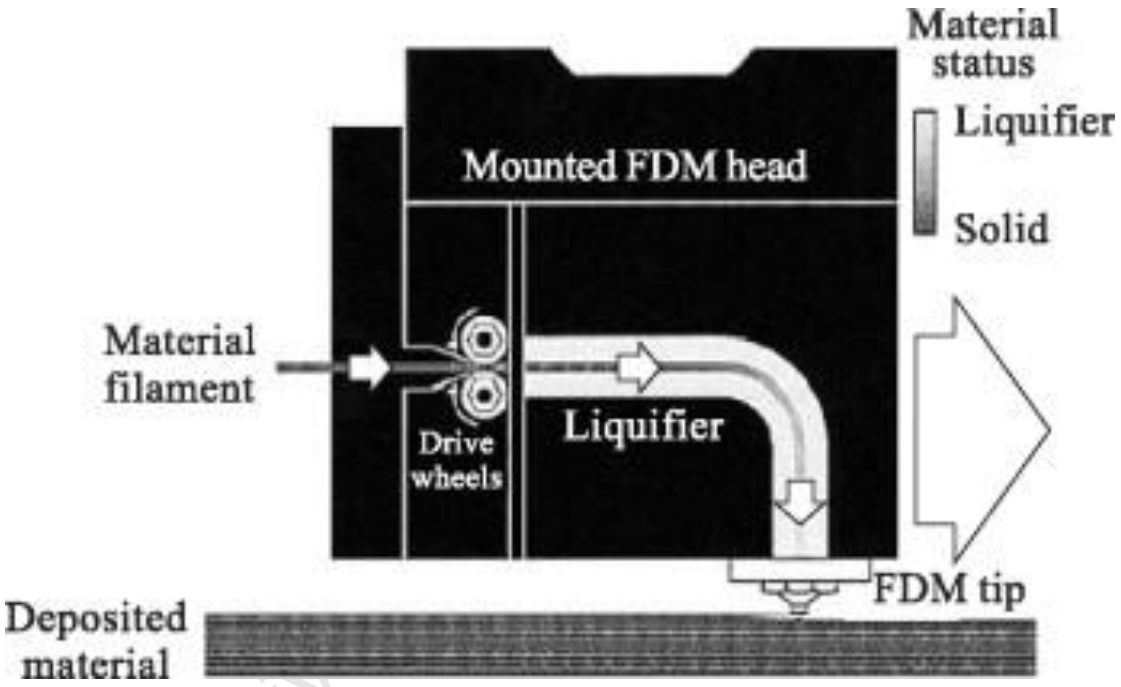

Figure 2.10: Schematic illustrating the Fused Deposition Modelling (FDM) process. [40]

2.3.4 ELECTRON BEAM MELTING (EBM)

Electron Beam Melting (EBM) is a highly competitive AM technique for use with metallic powders. In this technology, electrons are emitted from a filament which is heated to 2500°C and accelerated to approximately half the speed of light. The beam of electrons are pulled into focus using a magnetic field lens (focus coil) and then directed onto the build table using another magnetic field lens (directional coil). This system is shown in the schematic in Figure 2.11. The kinetic energy of the electrons is transformed into heat energy upon impact with the powder

which subsequently melts the powder locally around the beam spot. A computer package controls the movement of the directional coil to create cross-sections according to CAD data. A powder rake sweeps a fresh powder layer over the previously built layer and the process continues in a layerwise fashion. EBM operates in a vacuum to prevent harmful oxidation of the material during the process [43].

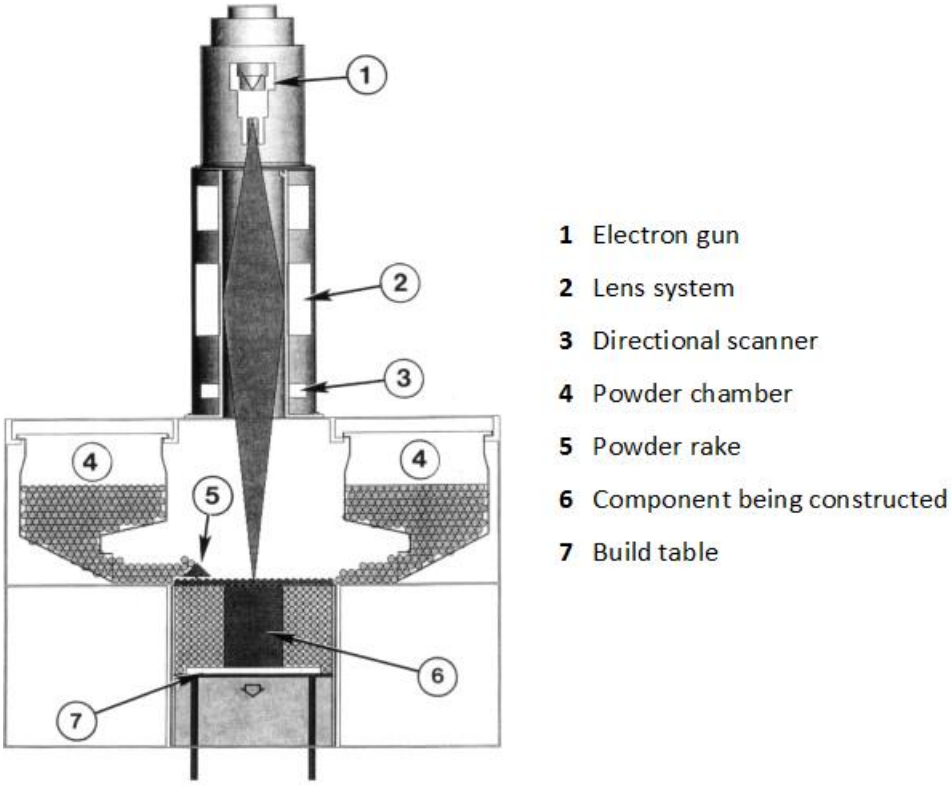

Figure 2.11: Electron Beam Melting (EBM) process schematic. [44]

2.3.5 SELECTIVE LASER SINTERING (SLS) TECHNOLOGIES

Selective Laser Sintering (SLS) is the term given to several techniques which can be differentiated by the degree of melting which occurs at the laser spot. SLS uses a high energy laser to bind small particles of plastic, metal or glass in successive cross-sections. The basic schematic for the SLS process is shown in Figure 2.12. The substrate in SLS is in a powder form similar to that of the EBM process. As each layer is traced out using the high energy laser, the

build platform lowers and a fresh layer of powder is spread across the part using the powder roller. The build chamber is maintained at a vacuum or filled with an inert gas such as argon for applications in which oxidation can occur. In some modern designs, the powder bed is heated to reduce the laser power necessary to bind the particles. The binding mechanism is divided into three primary categories: solid state sintering, partial melting/liquid phase sintering and complete melting. These processes are discussed briefly in the sections which follow.

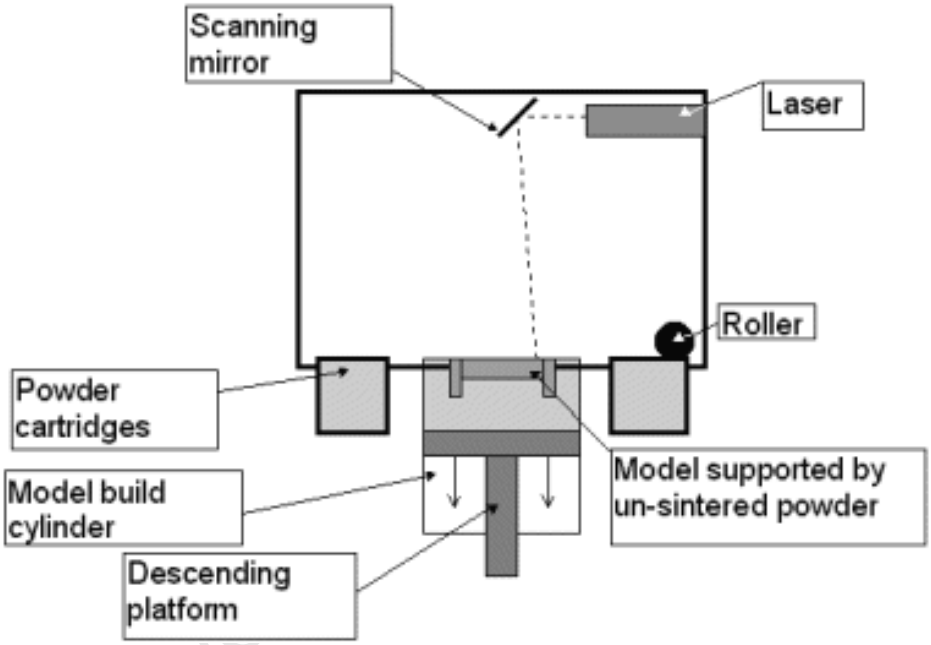

Figure 2.12: Selective Laser Sintering (SLS) process schematic.

2.3.5.1 Solid State Sintering

Fusion between particles in solid state sintering is achieved through the creation of a neck between two particles. The amount of heat required to bind the particles varies with different materials although it gives this technique great versatility with regard to the types of material which can be sintered. The major factors contributing to the required temperature or laser energy include the powder particle's distribution, shape and size [45]. The necking process can be described best using the two-sphere model as shown below in Figure 2.13. This sintering process is time dependent and the laser scan speed needs to be slower to allow the grain boundaries to

migrate and merge the spheres into one complete particle. This diffusion process occurs marginally below the melting temperature of the material [46]. Solid state sintering can be used as a post processing technique when partial laser sintering is used to bind metallic powders.

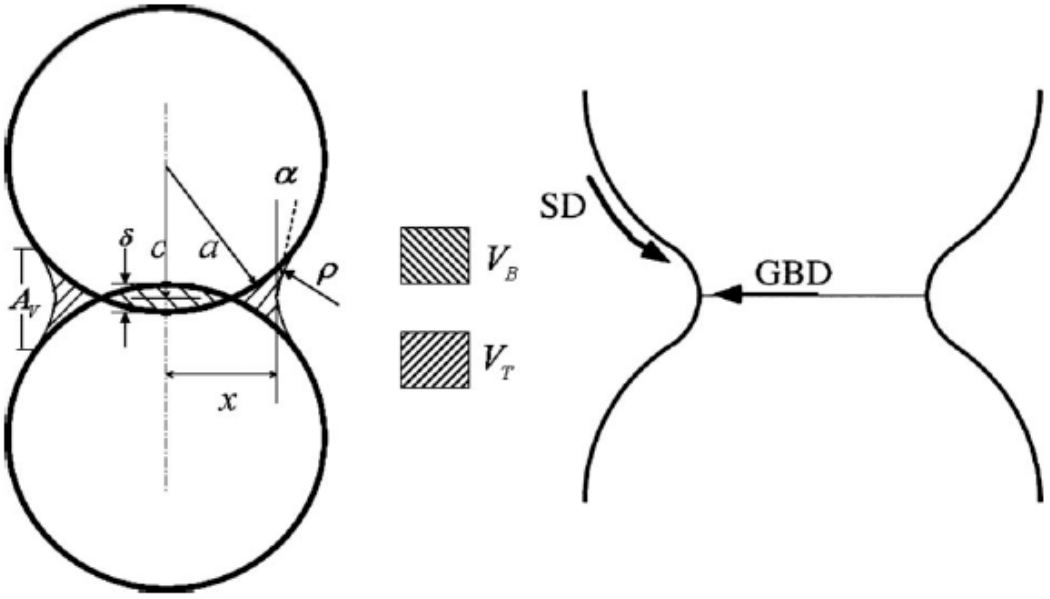

Figure 2.13: The development of a neck between two spheres through the solid state sintering process. [45]

Solid state sintering is relatively costly due to the low productivity (slow scan speed) and high cost and is generally only used with ceramics.

2.3.5.2 Partial melting/Liquid Phase Sintering

Liquid phase sintering is faster than solid state sintering since the laser scan speed is considerably faster. This is most common with powders consisting of more than one component. In this process, the laser completely melts one of the powder components and thus 'wets' the solid substrate and binds the particles together. The binding component powder particles are typically smaller than the substrate/structural particles [47]. The wetting characteristics of the powders must be well known before this process can be applied to a particular material. Single component powders can also be used with this process yet the powder characteristics need to be well researched such that sufficient surface melting occurs without any core particles melting. This can lead to a phenomenon known as 'balling' in which incomplete binding occurs due to

melt splashes or restricted liquid formation. Balling reduces the strength of the component and can lead to severe porosity if not carefully monitored [47]. The process through which balling occurs is shown in Figure 2.14. The major stages in liquid phase sintering are as follows [5]:

1. Particle re-arrangement after liquid formation and subsequent wetting.
2. Grain shape adjustment and solution re-precipitation.
3. Microstructural coarsening.

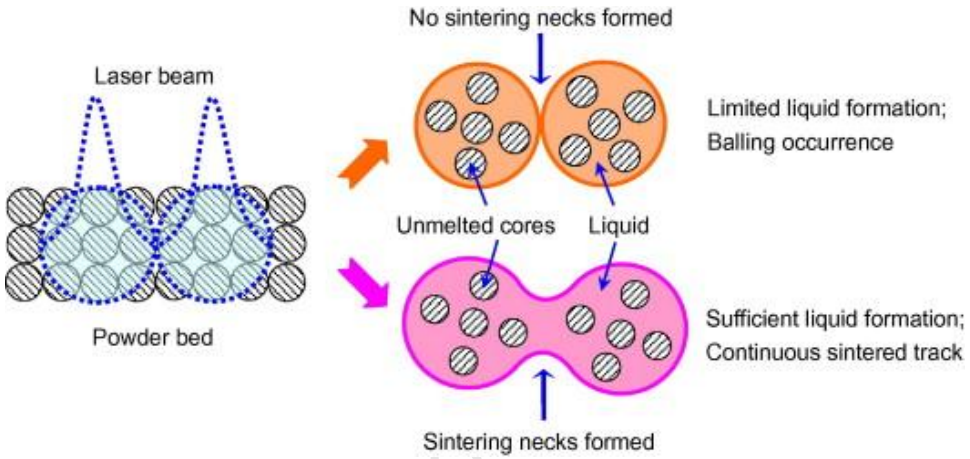

Figure 2.14: Balling phenomenon due to coarse balling with inadequate liquid formation. [47]

2.3.5.3 Complete Melting

A significant improvement in laser density and energy have led to the production of shorter wavelength lasers, Nd:YAG (1.06µm) which are capable of complete melting of substrate powders. In addition, the shorter wavelength lasers have a smaller laser spot size and are thus capable of higher accuracy than their CO_2 counterparts [5]. Metallic powders such as Cp Titanium and Ti-6Al-4V have been used very successfully with Selective Laser Melting (SLM) to produce near fully dense components (99.75%) [48]. The high temperatures are however problematic in that they cause severe thermal stresses which can induce high residual stresses. This ultimately leads to part distortion and fracture in some cases [49]. A very careful process parameter optimisation is required before this method be applied successfully. The binding classification chart illustrating the general characteristics of the sintering systems discussed

earlier in this chapter is shown below in Figure 2.15. Note the capabilities of SLM in Figure 2.15 which include single and alloyed material binding in addition to the fusion of powder mixtures.

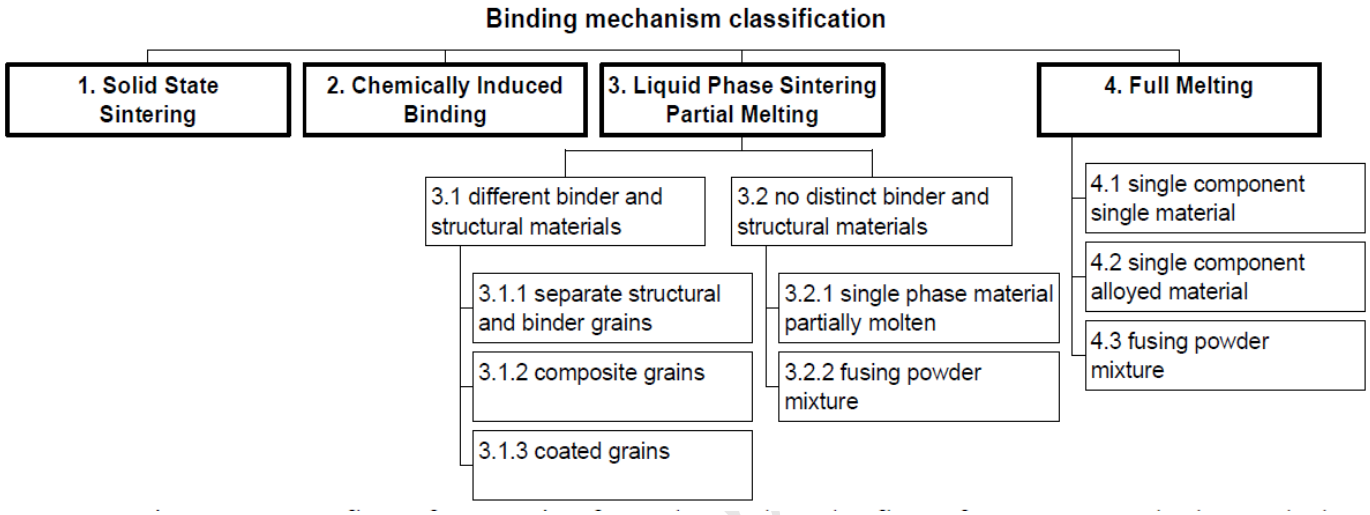

Figure 2.15: Binding classification chart for selective laser sintering processes. [46]

2.4 DIRECT METAL LASER FABRICATION (DMLF)

As discussed in the previous section, sintering technology has diversified into several techniques based on the method of bonding between the powder particles. The classification of Direct Metal Laser Fabrication (DMLF) systems is more accurately defined into three separate divisions [5]:

1. Selective Laser Sintering (SLS) and Laser Micro Sintering (LSM)
    - Partial melting contained within powder bed.
2. Selective Laser Melting (SLM)
    - Complete melting contained within powder bed.
3. 3D Cladding
    - Full melting using powder injection nozzles.

The similarities between the primary systems mentioned above are shown in Figure 2.16.

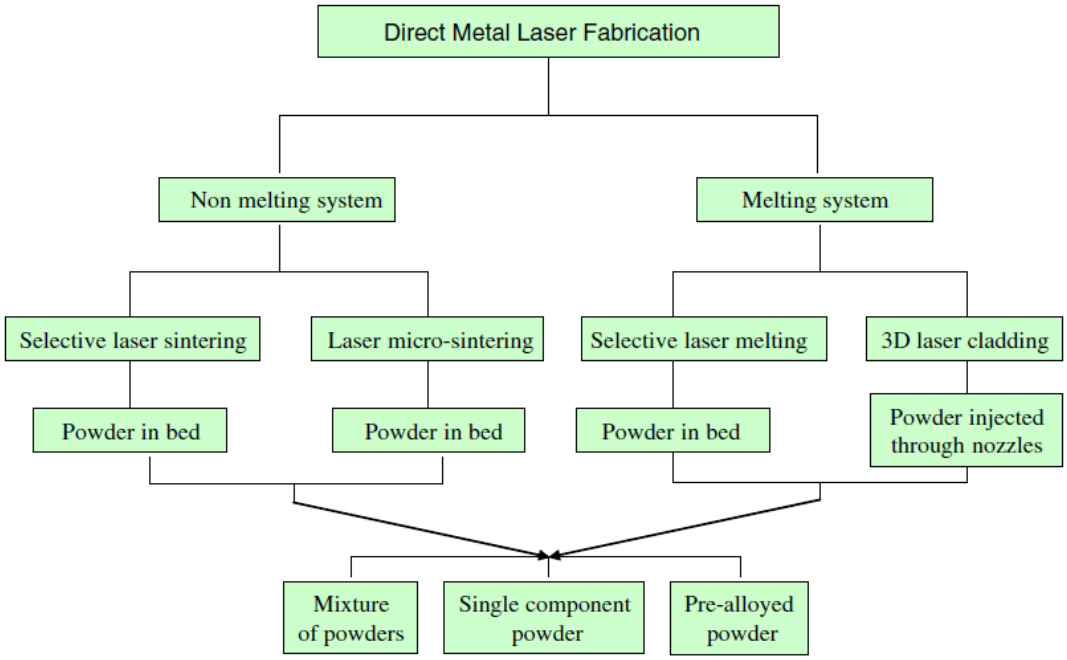

Figure 2.16: Direct Metal Laser Fabrication methods. [50]

The processes shown in Figure 2.16 are capable of producing components from a wide range of powders which include single component, pre-alloyed and mixed powders.

The process known as Direct Metal Laser Sintering (DMLS) used in this research project is a full melting technique which is based on the SLM methodology [50].

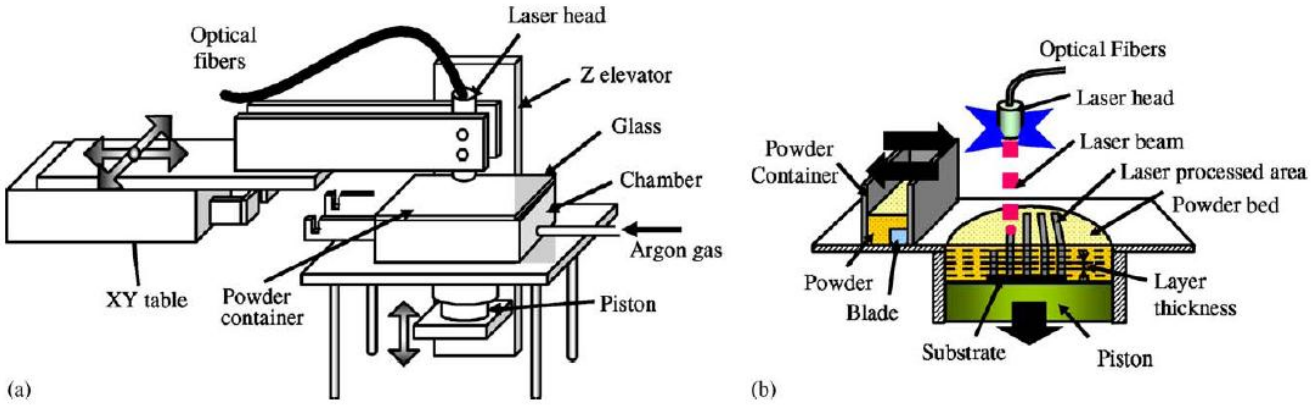

Figure 2.17: Direct Metal Laser Sintering (DMLS) technique using complete powder melting systems with, a) the machine schematic and, b) the working process schematic. [50]

The parameters which influence the material-laser interaction are critical in ensuring the DMLS process produces dimensionally accurate components with mechanical properties similar to that of the bulk material. The major factors are briefly discussed below:

1. Laser power
    - The energy density of the laser influences the temperature gradient in the material around the laser spot. Higher laser density is required for fully melting the powder yet will induce greater thermal gradients which can initiated higher residual stresses.

2. Scan speed
    - The laser scan speed is another important factor influencing the effective energy density applied to the powder layer. The laser-material interaction time is influenced by the scan speed with higher scan speeds reducing the amount of time which the laser has to melt the powder. Low scan speeds will drastically increase the build speed and may cause melt pool instabilities.

3. Scan pattern/spacing
    - The scan pattern influences the build time and the build quality. The scan pattern is the path in which the laser moves around the component layers. Economical use of scan patterns will result in quicker build times for larger components. The scan spacing is the distance between successive laser tracks. If this distance is too small, regions in the component may be over-exposed to the laser or vice-versa, for distances which are too large, unsintered powder will remain.

4. Layer thickness
    - The layer thickness refers to the thickness of successive layers of powder for each cross section. If the layers are too thick, the energy from the laser may not be sufficient for quality sintering to occur and vice versa with smaller thickness values, the powder deposition may not produce uniform powder layers which leads to porosity and poor part quality.

The section which follows describes the EOSINT M270 machine employed in this research project and the technical specification for the manufactured components.

2.4.1 EOSINT M270 DMLS MACHINE

The EOSINT M270 is produced by Electrical Optical Systems (EOS) for direct metal fabrication from CAD data. This machine builds components in a layerwise fashion through the action of a 200W Yb-fibre laser on a powder bed. The fibre-type laser completely melts the powder particles with the use of an f-theta lens system which focuses and directs the beam. The powders utilised with this system are an average of 0.02mm in diameter and the laser spot size can be varied between 0.1 and 0.5mm. The smaller spot dimension will increase the accuracy of the finished component however it will also sacrifice build time. The variable laser parameters can produce a build speed of between 2 - 20mm^3/s, with the build time being a function of the component complexity, layer thickness and material type. The scan strategies available in the software package include the *Skin & Core* strategies. The *Skin* strategy refers to the outer region of the component which is sintered with a higher laser energy concentration while the *Core* strategy is associated with the inner region which is sintered with a lower laser energy concentration.

The EOSINT M270 can incorporate both the partial melting and full melting regimes depending on the material type and powder form. The powder deposition technique utilises a single chamber with a blade type re-coater. This re-coater will deposit layers of between 0.02mm and 0.1mm thick which can be set according to the component requirements. The build platform is 250mm×250mm×215mm in dimension which is can be filled with argon or nitrogen to prevent oxidation of the sintered material. The complete technical data is given below in Figure 2.19. Since Selective Laser Melting is a more globally recognised term for the complete melting of metallic powder, the remainder of this report will refer to the processing of Ti-6Al-4V powder with the EOSINT M270 as Selective Laser Melting (SLM).

Figure 2.18: The EOSINT M270 machine. [51]

Technical Data

Effective building volume (including building platform)	*250 mm x 250 mm x 215 mm (9.85 x 9.85 x 8.5 in.)*
Building speed (material-dependent)	*2 - 20 mm³/s (0.0001 - 0.001 in³/sec.)*
Layer thickness (material-dependent)	*20 - 100 µm (0.001 - 0.004 in.)*
Laser type	*Yb-fibre laser, 200 W*
Precision optics	*F-theta-lens, high-speed scanner*
Scan speed	*up to 7.0 m/s (23 ft/sec.)*
Variable focus diameter	*100 - 500 µm (0.004 - 0.02 in.)*
Power supply	*32 A*
Power consumption	*maximum 5.5 kW*
Nitrogen generator	*standard*
Compressed air supply	*7,000 hPa; 20 m³/h (102 psi; 26.2 yd³/h.)*
Dimensions (B x D x H)	
System	*2,000 mm x 1,050 mm x 1,940 mm (78.8 x 41.4 x 76.4 in.)*
Recommended installation space	*approx. 3.5 m x 3.6 m x 2.5 m (137.9 x 141.8 x 100 in.)*
Weight	*approx. 1,130 kg (2,491 lb.)*
Data preparation	
PC	*current Windows operating system*
Software	*EOS RP Tools; Magics RP (Materialise)*
CAD interface	*STL. Optional: converter for all standard formats*
Network	*Ethernet*
Certification	*CE, NFPA*

Status 12/05. Technical data subject to change without notice. EOS®, EOSINT®, DMLS®, DirectTool®, DirectPart® and e-Manufacturing™ are registered trademarks of EOS GmbH. Windows is a registered trademark of Microsoft Corporation. EOS is certified according to ISO 9001.

Figure 2.19: Technical data for the EOS Gmbh M270 Direct Metal Laser Sintering machine. [52]

2.4.2 A SHORT DISCUSSION ON LASER FABRICATION SYSTEMS

The highly focused laser beam in both Selective Laser Sintering (SLS) and Selective Laser Melting (SLM) induces high temperature changes in the material with the full melting systems causing more severe gradients due to the increased laser power. This temperature gradient is required to produce very dense components but can also affect the melt pool stability which is detrimental to the structural integrity of the completed component. The common problems associated with laser based RM processes are briefly discussed in this section.

In the modern SLM systems, porosity has been minimised to produce the 99.8% density which several systems claim. The porosity can prove problematic in terms of stress concentrations which act as fatigue crack initiation locations when the component is subjected to a cyclic loading. This has been well researched in other materials, i.e. Lu et al found fatigue cracks initiating from the edges of pores during high cycle fatigue loading of Magnesium alloys [53]. This effect is magnified considerably when residual stress exists in the structure, with the net effect of a lower cyclic loading initiating fatigue cracking. Porosity can be caused by an incomplete melting of the powder layer, non-uniform powder deposition and shrinkage of the matrix when one phase diffuses into another (when sintering multi-phase materials).

The surface roughness remains a problem for laser-based AM techniques in the metallic arena. The plastics industry has overcome this problem in the new stereolithography machines yet the metal-based systems still require polishing to remove the surface roughness from manufacturing. This problematic feature of sintering technologies is discussed in the chapters which follow, particularly with regards to crack initiation from micro-flaws along the part surface.

Oxidation can occur if the atmosphere within the build chamber does not have an adequate inert gas concentration. The oxide contamination will affect the wetting characteristics of the molten metallic substrate. This is known as incomplete homologous wetting which will cause micro-flaws and micro-cracking in the component.

SLM is known to produce higher residual stresses than SLS due to the increased laser power applied to the powder. Casavola et al (2008) found that the major factors which may influence the residual stress levels are the material properties, laser scan strategy and speed, and layer thickness [12]. The residual stresses are known to cause deformation and fracture in components

and remain a major problem with laser based additive manufacturing [49]. This is unfortunately a significant problem in terms of producing components which may be used in failure-critical areas such as aircraft turbine engines.

The research completed on AM produced materials such as SLM Ti-6Al-4V is relatively limited due to the on-going changes in material and machine parameters. Several studies concerning the material properties of SLM materials have been completed by Kruth et al ([28], [46] and [48]) yet much of the behavioural attributes are still unknown. This thesis aims to further understand the material properties of components built through this new technique. A research area still requiring much work is in the effects of residual stress on the materials produced by laser-based systems such as SLM. With this in mind, the next two sections introduce residual stress and its effect on a material in terms of fatigue crack initiation.

2.5 RESIDUAL STRESS

Residual stress is defined as the stress in an object which remains in the absence of any external force or load [54]. Residual stresses will remain in a part as a result of plastic deformation, excessive temperature gradients, casting effects or mechanical treatment [55]. Residual stresses are sometimes beneficial (such as the compressive residual stress in toughened glass shown in Figure 2.20) but are more often detrimental to the stability of a structure [56]. Tensile residual stresses assist crack growth and can contribute to the premature failure of a structure [49]. Residual stresses are especially critical in components which are designed to operate near material limits. This is an area of concern for aerospace components which are designed to be as lightweight and efficient as possible [57]. Thus, as mentioned earlier, the presence of residual stresses could greatly affect the ability of SLM to produce complex components for the aerospace market.

Turbine and compressor blades in a jet engine are often manufactured from titanium-based alloys and are among the most critically affected components if detrimental residual stresses are present [58]. In many current gas turbine engines, compressive residual stresses are introduced into the surface of the turbine blades to improve the fatigue life [56]. Crack growth is hampered by

compressive residual stresses since a greater tensile crack-driving force is required to overcome this compressive stress [59]. This is particularly useful in the compressor stages which may suffer from FOD (Foreign Object Debris) damage since the surface compressive strength may be great enough to arrest crack growth at an impact site (common crack-initiation sites) [58]. The mechanisms through which these residual stresses can be generated in laser-based manufacturing systems, including SLM, are introduced in the next section.

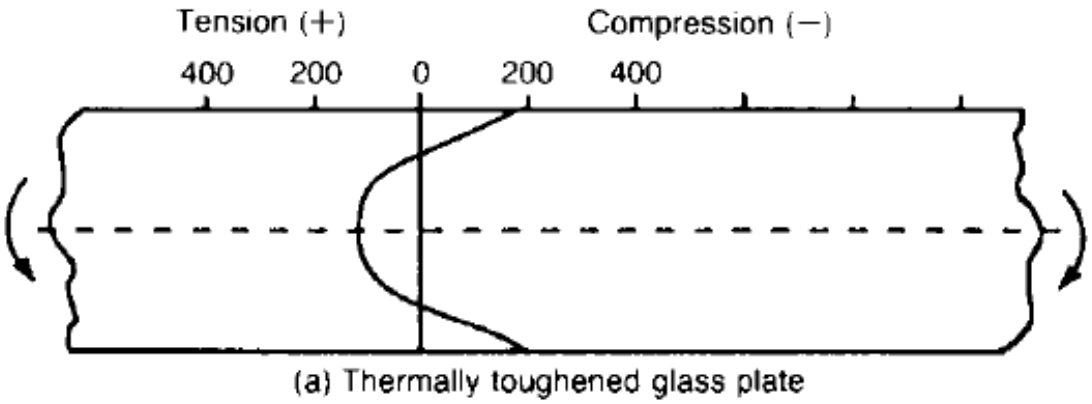

Figure 2.20: Compressive residual stress in the outer layers of toughened glass resists crack initiation and growth from the outside surfaces. [60]

2.5.1 RESIDUAL STRESS IN LASER-BASED MANUFACTURING

The high energy laser beam introduces very high temperature gradients in SLM produced material and consequently, thermal residual stresses can become a major factor in finished components. The thermal stresses produced by the expansion and contraction of the previously solidified layers can exceed the yield strength of the material. These residual stresses can cause distortion of the component (particularly in the regions near the base plate) and severely reduce the load bearing capacity of the finished product. In some cases, the residual stress can initiate fracture of the component [28]. Previous studies into the residual stress profiles in SLM produced materials indicate that the stress gradient before the part is removed from the base consists of a major region of tensile stress in the upper portion of the part (with a maximum stress attained at the surface) while the region between the upper and lower surfaces is

dominated by an intermediate compressive stress (see Figure 2.21 below). The major influences on residual stress were found to be the laser scan strategy, material properties, specimen height, and external heating. [49]

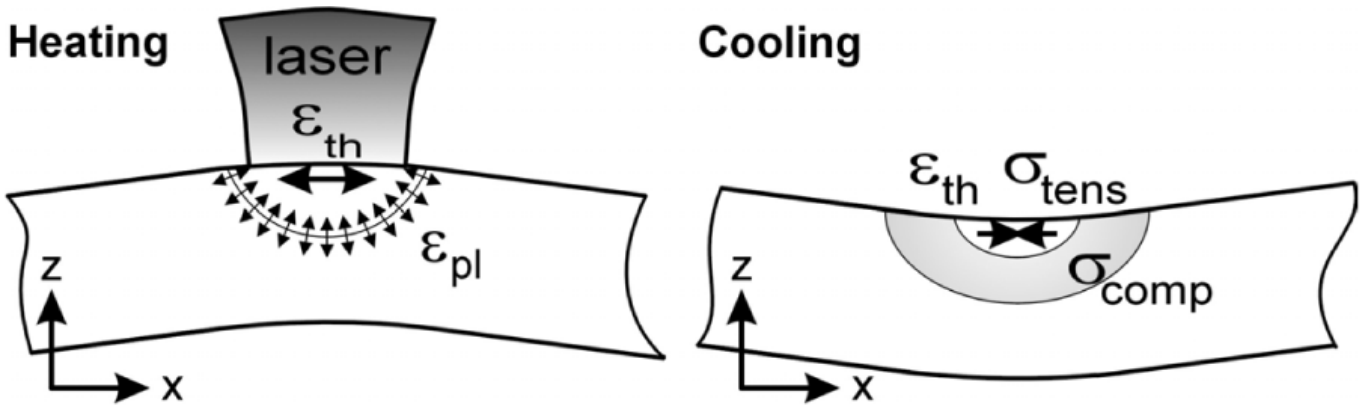

Figure 2.21: Temperature Gradient Mechanism (TGM) in SLM produced components. [49]

The mechanisms of residual stress in SLM produced components are primarily the Temperature Gradient Mechanism (TGM) and the cooling rate of the upper molten layers. TGM is caused by the high temperature induced by the laser spot and occurs due to the underlying layers hindering the expansion of the upper layers (material does not have to be molten for this to occur). In this case the restriction of the expansion of the heated layer induces elastic compressive strain in the material. The cooling mechanism occurs when the upper molten layers shrink via thermal contraction and are also hindered by the lower solidified layers. These two mechanisms are shown in the schematic in Figure 2.21. The cooling mechanism results in a tensile stress in the upper layer and a compressive stress in the layer below. [49]

Mercelis and Kruth (2006) used the Crack Compliance Method (which is introduced in the next section) to measure the residual stresses in SLM produced components [49]. Several conclusions were made based on their residual stress testing, particularly in the region nearest the base plate [49]. Components which remained attached to the base plate contained stress levels very near to that of the material yield strength. The components removed from the base plate had lower stress levels yet deformation was present. The residual stress distribution in the test specimens

consisted of tensile stress just below the upper surface, compressive stress in the central region and tensile stress on the lower surface. [49]

2.5.2 METHODS OF DETECTION

Residual stress detection methods are classified according to four distinct groups [54]:

1. Stress relaxation techniques
    - ASTM E837-08 Hole drilling technique
    - Ring-splitting method
    - Crack compliance method
    - Successive milling technique
2. Diffraction techniques
    - X-ray diffraction
    - Neutron-ray diffraction
    - Synchrotron
3. Cracking techniques
    - Hydrogen induced cracking
    - Stress corrosion cracking
4. Stress sensitive techniques
    - Magnetic techniques
    - Ultrasonic techniques
    - Hardness techniques

The stress relaxation techniques are among the most versatile for determining residual stresses 'on site' since the apparatus is typically very portable and small for difficult applications [61]. These techniques are based on the release of elastic strain energy following the removal of material. This methodology gives good indications of the residual stress levels without prior knowledge of the loading history. The hole-drilling technique as used in this project is based on the ASTM E837-08 standard and is classed as semi-destructive due to the introduction of a small hole into the structure.

The diffraction methods are also well-known techniques for determining residual stresses [62]. X-ray diffraction is particularly useful since it is non-destructive and has a relatively high accuracy. This method is not able to penetrate very deeply however since the X-rays weaken considerably through the surface layers. The equipment cost is also expensive and its usage is limited to materials which respond well to x-rays. The neutron diffraction is similar to that of the x-ray version with the exception that higher energy is attainable and deeper penetration is possible (40mm) [62]. This method does have the disadvantage of being limited to materials which respond to neutron diffraction and is not portable since a reactor is required.

The cracking techniques are used in laboratory environments and are classed as destructive methods which give qualitative assessments of the residual stresses [63]. The hydrogen induced technique involves immersing the specimen in an appropriate electrolyte and driving DC current through the specimen (which forms the cathode when connected to a lead anode). This process charges the specimen with hydrogen to produce a variety of crack patterns as an indication of residual stresses in the structure. The stress corrosion cracking technique is similar in that the specimen is immersed in a corrosive environment which induces cracking patterns. These cracking patterns will give an "indication" of the residual stress levels but not a fully quantitative assessment [64].

The stress sensitive techniques are based on the principle that the mechanical properties of a material change in the presence of a stress state. The magnetic technique is a non-destructive method which uses the Barkhausen noise phenomenon to measure the residual stresses [65]. It does however only work for magnetic materials and is subjected to a maximum depth limit of 0.2mm. The ultrasound techniques are common in fatigue crack testing and have been extended to residual stress analysis [66]. This technique uses the velocity and changes in the speed of sound with stress in a material to measure the average stress.

The influence of residual stress on the integrity of SLM components under a cyclic load has not yet been fully established in literature and the next section introduces fatigue cracking and the concerns behind a material afflicted by tensile residual stresses.

2.6 FATIGUE & ITS IMPLICATIONS

2.6.1 INTRODUCTION

Under the action of cyclic or repeated loading, materials can fail due to fatigue at stress levels far below the material strength [67]. Fatigue cracking is a particular area of concern in the aerospace industry in which fatigue cracks such as those in Figure 2.22a and b can result in catastrophic failure. Material crack analysis can be split into two regimes - Fracture Mechanics and Fatigue. Fracture Mechanics (FM) is considered to be an extension of conventional mechanics for use with structures containing flaws. Fatigue is a time dependant analysis which examines crack growth rates and life prediction. These concepts will be introduced here in order to clarify the concerns behind residual stresses in SLM material.

2.6.2 LINEAR ELASTIC FRACTURE MECHANICS (LEFM)

As aforementioned, FM is considered to be the extension of conventional mechanics for materials containing flaws. If the material may be considered elastic and homogeneous, a 'living with defects' approach known as Linear Elastic Fracture Mechanics (LEFM) can be used to evaluate the current load carrying capability of a structure containing a flaw. The basis of LEFM is the triangle of integrity as shown diagrammatically in Figure 2.23. This methodology is based on the fracture toughness criterion which is described by the stress intensity factor K given in (2-1) below.

$$K = \sigma Y \sqrt{\pi a} \qquad \textbf{(2-1)}$$

In which σ is the stress [MPa], Y is a dimensionless shape factor and 'a' is the flaw size. The flaw size 'a' is shown in Figure 2.24 for surface and embedded defects.

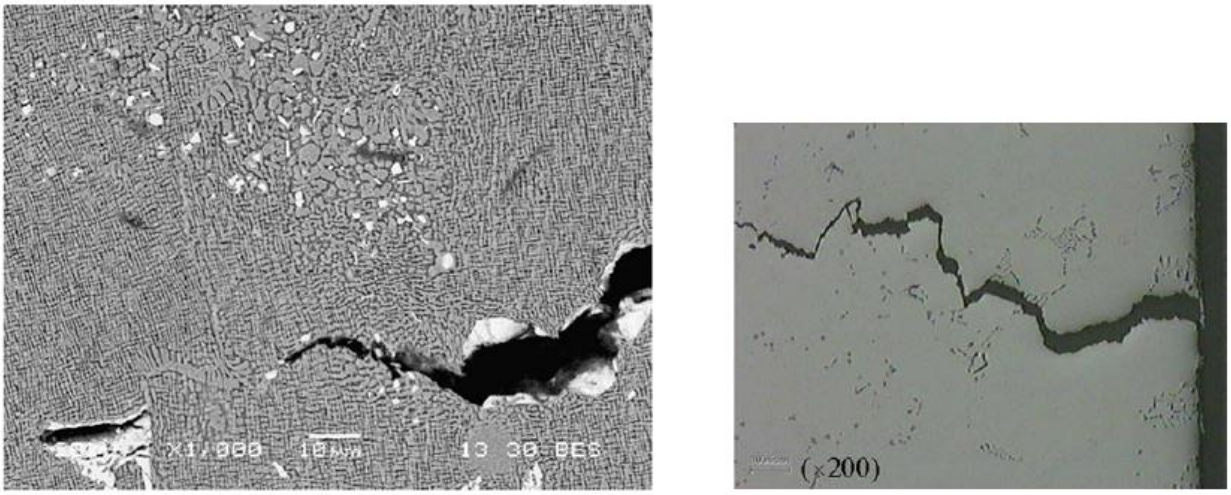

Figure 2.22: a) Crack propagating through a turbine blade originating from Foreign Object Debris damage [68] and, b) crack propagation from a micro-flaw at the trailing edge of a turbine blade [57].

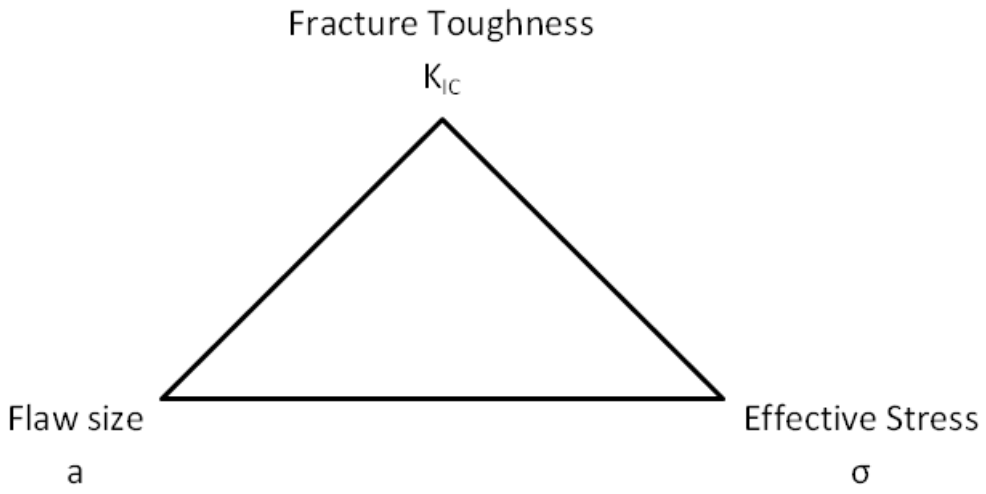

Figure 2.23: The 'Triangle of Integrity' methodology employed in Linear Elastic Fracture Mechanics (LEFM).

LEFM uses the fracture toughness criterion to determine the critical crack size (a_{crit}) at operational loads and hence the size of flaw which is permitted in a structure. Fracture will occur when the stress intensity of a driving crack reaches the fracture toughness for that particular material, i.e.

$$K = \sigma Y \sqrt{\pi a} =\geq K_{1C} \quad \textbf{(2-2)}$$

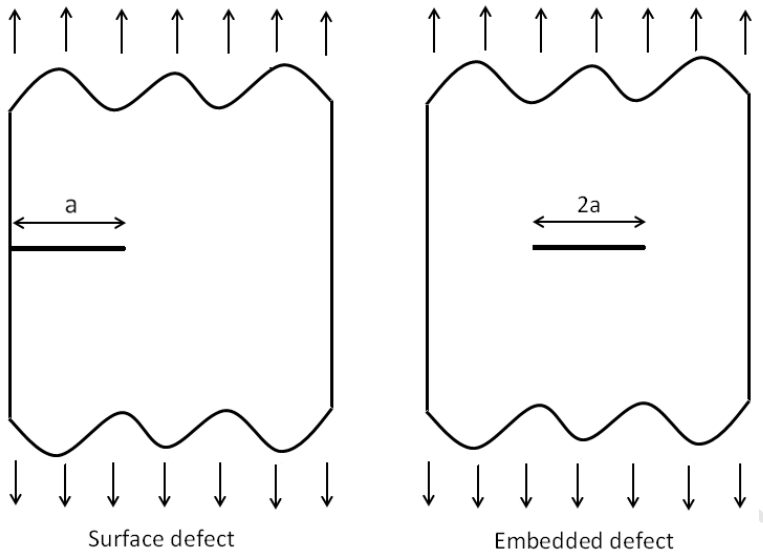

Figure 2.24: Crack dimensions for surface and embedded defects.

This is particularly useful in terms of the 'living with defects' philosophy since replacement costs of many components in the aerospace industry are often very high. The next section introduces Fatigue and the time-based estimation of a material through which a crack is propagating.

2.6.3 FATIGUE

Fatigue can be defined as the progressive damage to a structure under the action of a cyclic load. Fatigue is a time-based phenomenon in which a fatigue crack initiates, propagates and ultimately results in catastrophic failure. The fatigue crack growth rate graph in Figure 2.25 is a particularly useful tool in evaluating the remaining life in a structure containing a fatigue crack. This graph is divided into three regions, the crack initiation stage (Region 1), the propagation phase (Region 2) and fracture (Region 3). Region 1 contains the threshold stress intensity ($\Delta K_{threshold}$), below which fatigue cracks will not propagate. This property is used to describe the initiation of a fatigue crack from a defect or flaw. The threshold stress intensity is of particular importance in this study in terms of the effect of residual stress and is discussed in the next section. Region 2 is considered the stable crack growth regime in which the Paris law applies. The Paris law given in equation (2-3) relates the fatigue crack growth rate to the change in crack tip stress intensity at minimum and maximum load (cyclic stress).

$$\frac{da}{dN} = C\Delta K^m \quad (2\text{-}3)$$

$\frac{da}{dN}$ is the crack growth rate, *C* and *m* are material constants, and ΔK is the difference in the stress intensity factors at minimum and maximum loading as given by equation (2-4).

$$\Delta K = K_{max} - K_{min} \quad (2\text{-}4)$$

As the crack lengthens, so the stress intensity factor ΔK increases for a constant cyclic stress. The gradient of this region is dependant on the material properties in which different Ti-6Al-4V microstructures exhibit different stable crack behaviour.

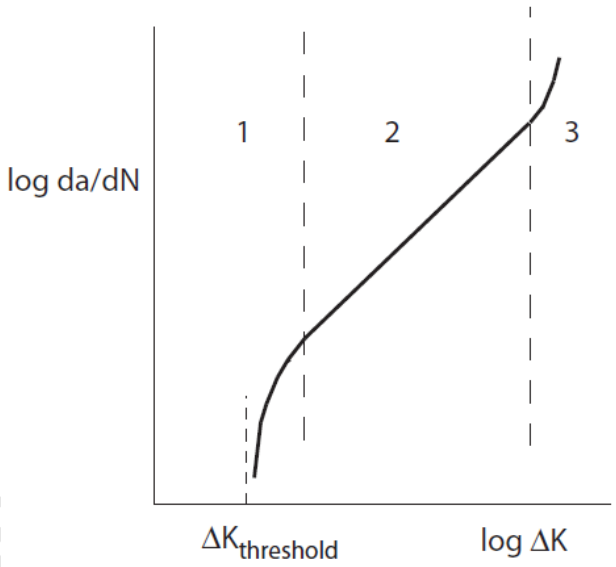

Figure 2.25: Schematic of fatigue crack growth rate under constant amplitude cyclic loading [67].

In terms of estimating the remaining life in a structure, the stress intensity factor (given in equation 2-1) can be substituted into the Paris equation to achieve the following:

$$\frac{da}{dN} = C\left(\Delta\sigma Y\sqrt{\pi a}\right)^m \quad (2\text{-}5)$$

Which may be separated as shown below in (2-6).

$$dN = \frac{da}{C\left(\Delta\sigma Y\sqrt{\pi a}\right)^m} \quad \textbf{(2-6)}$$

Equation (2-6) can be integrated between the initial flaw size a_i and the critical flaw size a_{crit} (at which failure will occur) to estimate the remaining life in the structure N_f as shown below in (2-7).

$$N_f = \int_0^{N_f} dN = \int_{a_i}^{a_{crit}} \frac{da}{C\left(\Delta\sigma Y\sqrt{\pi a}\right)^m} \quad \textbf{(2-7)}$$

This life prediction tool is thus very useful in interpreting when a component should be replaced. Residual stress will have an effect on the crack initiation threshold, *C* and *m* as will be made clear in the next section. The fatigue crack threshold shown in Region 1 of Figure 2.25 by the hashed line can be interpreted using the stress intensity equation (2-1) to give the minimum flaw size from which a fatigue crack will initiate for a given stress. Or vice-versa, given a flaw size, the threshold stress intensity can be used to determine the minimum stress under which a fatigue crack would initiate from that flaw. The importance of this value is thus obvious in terms of the levels of porosity and micro-flaws which have plagued laser-based manufacturing systems in the past. As stated earlier, residual stress is known to affect the stress intensity threshold and thus poses a concern for SLM components which may contain flaws. The next section reviews this effect of residual stress on fatigue crack initiation in a material.

2.6.4 EFFECT OF RESIDUAL STRESS

Residual stress has the effect of increasing the mean stress in a structure, which in turn increases the *R* ratio in cyclic loading. The *R* ratio is the ratio of the minimum to maximum stresses in a structure under a cyclic load as shown below in equation (2-8). The effect on the fatigue crack growth is shown in Figure 2.26 as the higher R ratio shifts the graph left which in turn decreases the crack initiation threshold ΔK_{th} [69]. This has the effect of reducing the required flaw size for which a fatigue crack will initiate and hence fatigue cracks can initiate and propagate from

smaller micro-flaws and pores. The increase in *R* ratio from residual stress was found to escalate the fatigue crack growth rate in wrought Ti-6Al-4V in addition to a reduction in ΔK_{th} as reported by Tsay et al [70].

$$R = \frac{\sigma_{min}}{\sigma_{max}} \quad \textbf{(2-8)}$$

It is clear then that residual stress can be highly detrimental to the structural integrity of a material. Given the massive potential for SLM in the aerospace, biomedical and automotive industries, it would be of interest to ascertain the levels of residual stress in the components built through this process. Residual stresses can also be relieved using a variety of techniques which could be tailor-made for SLM in order to preserve the net-shape benefits of this highly promising technique.

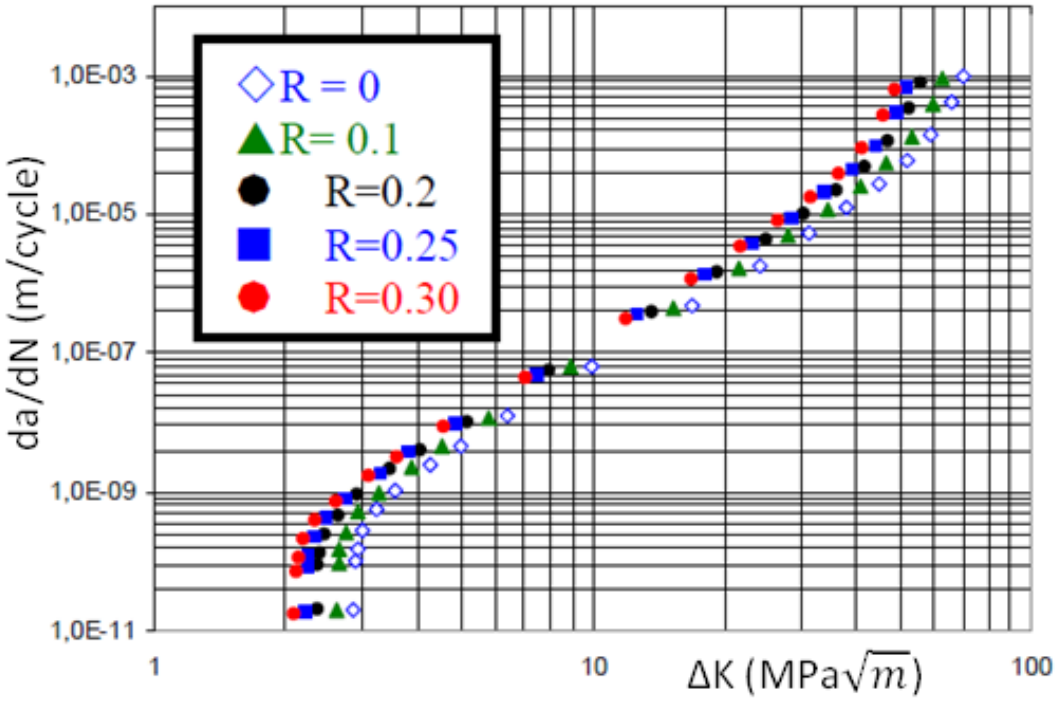

Figure 2.26: R ratio effect on fatigue crack growth rate. [69]

2.7 SUMMARY

This chapter has served as an introduction to the Additive Manufacturing arena with particular emphasis on the laser-based metallic rapid manufacture techniques. The capabilities of these systems are under constant development to improve their properties and versatility. The EOSINT M270 Direct Metal Laser Sintering (DMLS) machine is used in the following chapters to produce the components required for this research project. The economic incentive for SLM research is significant in that it has the potential to replace costly machining equipment from traditional manufacturing techniques and requires no modification for different components. The biomedical industry has driven a large portion of the initial research into these techniques due to its interest in complex implant building which would not be possible through traditional manufacture. The aerospace market has also recognised the benefits of the rapid manufacture techniques with regard to constructing highly complex engine parts.

The limitations associated with laser-based manufacturing systems have been described with particular emphasis on the generation of thermal residual stresses and porosity. The potential consequences of a residual stress in a material subjected to a fatigue loading has been described as well as introducing the Fracture Mechanics perspective. The generation of significant residual stresses in SLM components could hamper the ability of this technique to produce materials for the aerospace market and thus there is a definite need to quantify the residual stresses in SLM material and if necessary, explore possible methods for residual stress removal. In order to clarify the elements of this study further, the next chapter will discuss the material Ti-6Al-4V and some of the heat treatments used in industry.

CHAPTER 3 – LITERATURE REVIEW

3.1 INTRODUCTION

The previous chapter introduced the Additive Manufacturing (AM) system known as Selective Laser Melting (SLM) and revealed the anticipated direction of this novel technique. Chapter 2 also introduced residual stress and its effects in terms of fatigue crack initiation. This chapter describes Ti-6Al-4V in its industry forms and the available literature on SLM Ti-6Al-4V. The first section describes the current methods of manufacture in industry. The metallurgy and microstructure of Ti-6Al-4V is also discussed with the aim of comparing SLM Ti-6Al-4V to that produced by other manufacturing techniques. The heat treatment of this particular alloy is introduced along with the expected changes in material properties from each treatment. The final section in this chapter introduces the recent work undertaken on the residual stress and fatigue implications in SLM Ti-6Al-4V.

3.2 CONVENTIONALLY MANUFACTURED TI-6AL-4V

Ti-6Al-4V is the most common titanium alloy and accounts for more than 50% of the global titanium tonnage. This particular alloy is considered to be the workhorse of the titanium industry due to its versatility in applications ranging between aerospace, biotechnology, automotive, marine and chemical industries. Ti-6Al-4V is classed as an α+β alloy and is available in wrought, cast and Powder Metallurgy (P/M) forms. This section reviews the conventionally produced Ti-6Al-4V in terms of the metallurgy and mechanical properties with particular emphasis on the phase changes and microstructures produced during various forms of manufacturing. The general phase structure present in Ti-6Al-4V is introduced first.

3.2.1 METALLURGY OF TITANIUM ALLOYS

Titanium is subjected to an allotropic transformation at a temperature of 882.5 °C. The microstructure of titanium shifts from alpha (α) phase (hexagonal close-packed - HCP) to beta (β) phase (body-centred cubic - BCC). Alloying of titanium results in stabilising the alpha and beta phases such that they can coexist at room temperature. The alloys are divided into 3

categories – α alloys, α + β alloys and β alloys. Since Ti-6Al-4V is an α+β alloy, it consists of a combination of α stabilisers and β stabilisers which form a large two-phase mixture between the α and β regions in the phase diagram (see Figure 3.1).

Primary phases α and β

The dominant two-phase region in the centre of Figure 3.1 consists of various combinations of α and β phase in different crystallographic relationships. The α+β alloys will form significant amounts of β phase when heated and will contain untransformed β when solution treated and cooled. The amount of α and β phase in a Ti-6Al-4V specimen is dependant on the processing parameters during production. These alloys have a particularly good response to heat treatment due to this two-phase region which allows the amount of α and β phase to be 'tailor-made' using a variety of thermo-mechanical treatments.

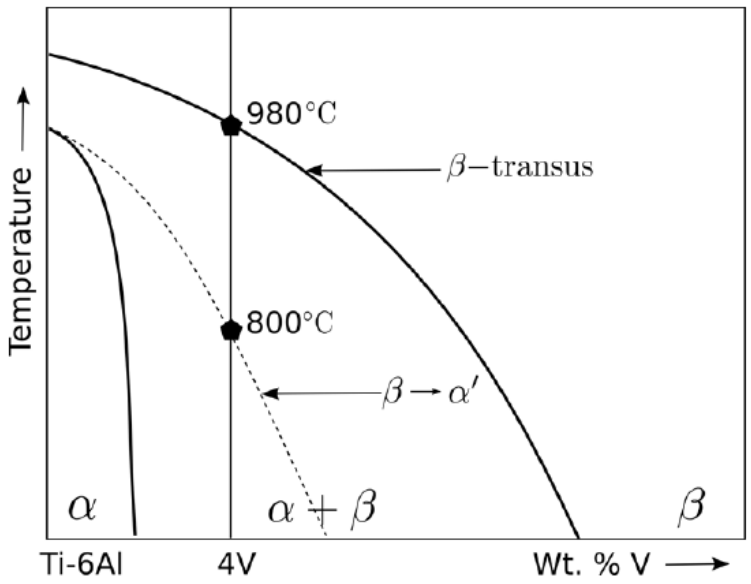

Figure 3.1: Section of a ternary phase diagram for Ti-6Al-4V illustrating the temperatures for phase transformations between α, β and α'. The MS (Martensite Start) temperature is given by the dotted line. [71]

Metastable Phases α' and α''

In addition to the primary phases of α and β, there are two metastable phases, α' and α'' which also have a significant influence in the physical and mechanical properties of Ti-6Al-4V [71].

The α’ phase has an HCP structure with a smaller grain size than α phase which results in a harder structure capable of more strain hardening. The α’ is formed from above the martensite start temperature (800°C) of Ti-6Al-4V and is shown in Figure 3.1. The α’’ phase is another metastable phase in Ti-6Al-4V with a rhombic structure. This phase produces mechanical properties similar to that of α phase and is considered to be intermediate between the HCP and BCC structures [71].

The next section introduces the microstructural forms of Ti-6Al-4V which contain different amounts and forms of the phases described above.

3.2.2 MICROSTRUCTURE EVOLUTION

In the previous section, it was mentioned that the microstructure of Ti-6Al-4V is heavily dependent on the processing parameters during its production. The cooling rate from the β region or the α+β region (depending on the method of processing) is a very important factor when considering the microstructure form which may result (clearly evident in Figure 3.2 below). The phase diagram in Figure 3.1 shows the transition temperatures between α and β phases however it does not describe all the possible microstructures in between. This section will briefly describe the common microstructural forms of Ti-6Al-4V such that the microstructures of SLM Ti-6Al-4V can be identified correctly.

Lamellar Microstructure

A lamellar microstructure (also known as basket-weave) is very coarse with more α phase and significantly smaller amounts of β phase in the boundaries as shown below in Figure 3.3a. Lamellar microstructures are controlled efficiently by slow cooling from above the β-transus (980°C). As the alloy cools from above this β-transus, α plates begin to appear and in doing so form a crystallographic relationship with the remaining β phase. If the cooling rate is intermediate, these plates continue to grow in size as the temperature drops and the formation of Widmanstätten structures will occur [72].

Equiaxed Microstructure

The equiaxed structure (α/β) contains similar amounts of α and β phase as shown below in Figure 3.3b. This type of microstructure is common with significant mechanical working in the

α+β region. The recrystallization annealing process discussed later in this chapter can also be adapted to produce equiaxed microstructures.

Bi-modal Microstructure

The bi-modal microstructure is considered to be a combination of both lamellar and equiaxed microstructures. This microstructure consists of isolated primary α-grains in a transformed β matrix [73]. Bi-modal microstructure is obtained by an anneal high in the α+β region followed by an air cool. A micrograph of a bi-modal microstructure is shown below in Figure 3.3d.

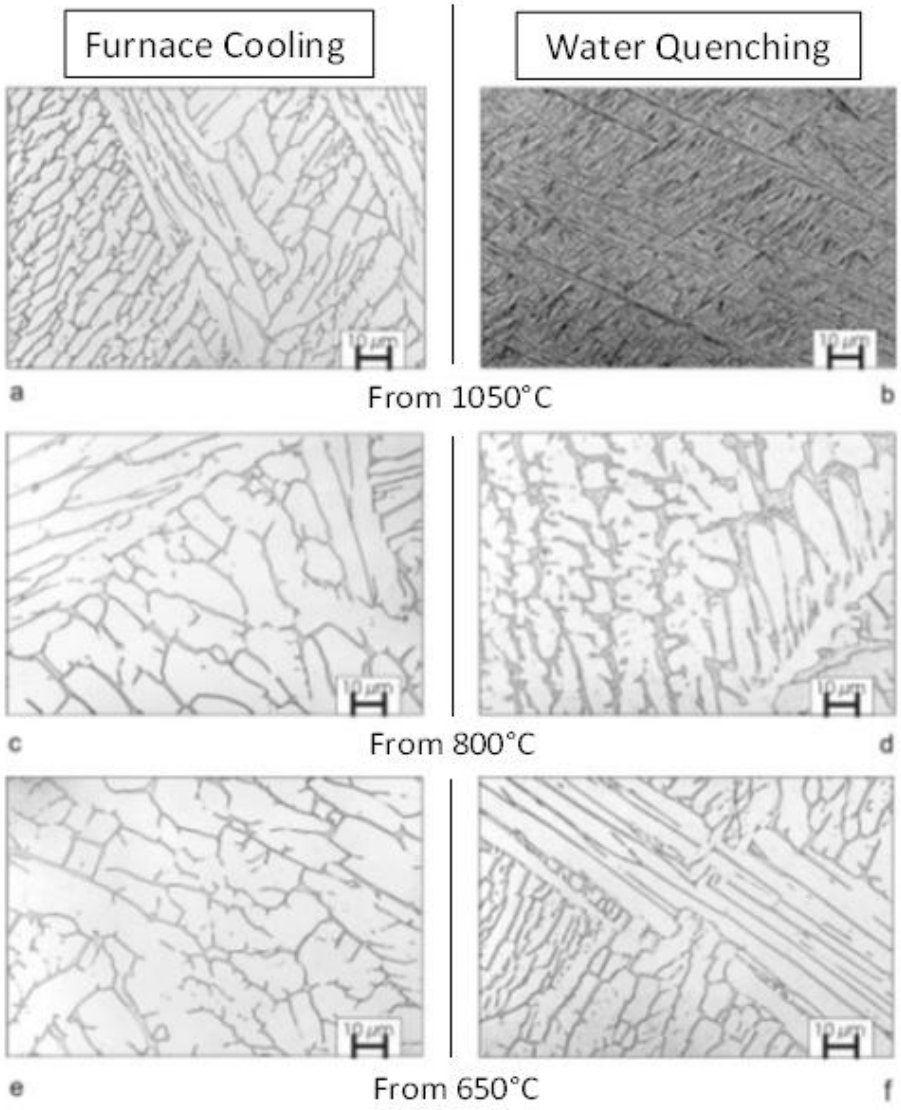

Figure 3.2: Micrographs of Ti-6Al-4V cooled from 1050°C, 800°C and 650°C using furnace/slow cooling (in a,c and e respectively) and water quenching (in b,d and e respectively). [74]

Martensite Microstructure

A martensite microstructure will form if the alloy is very rapidly cooled from above the MS temperature [72]. The martensitic microstructure is present in the material water quenched from 1050°C shown in Figure 3.2b and in the micrograph in Figure 3.3c which consists of α' needles. These micrographs are indicative of rapid quenching from above both the MS temperature and the β transus.

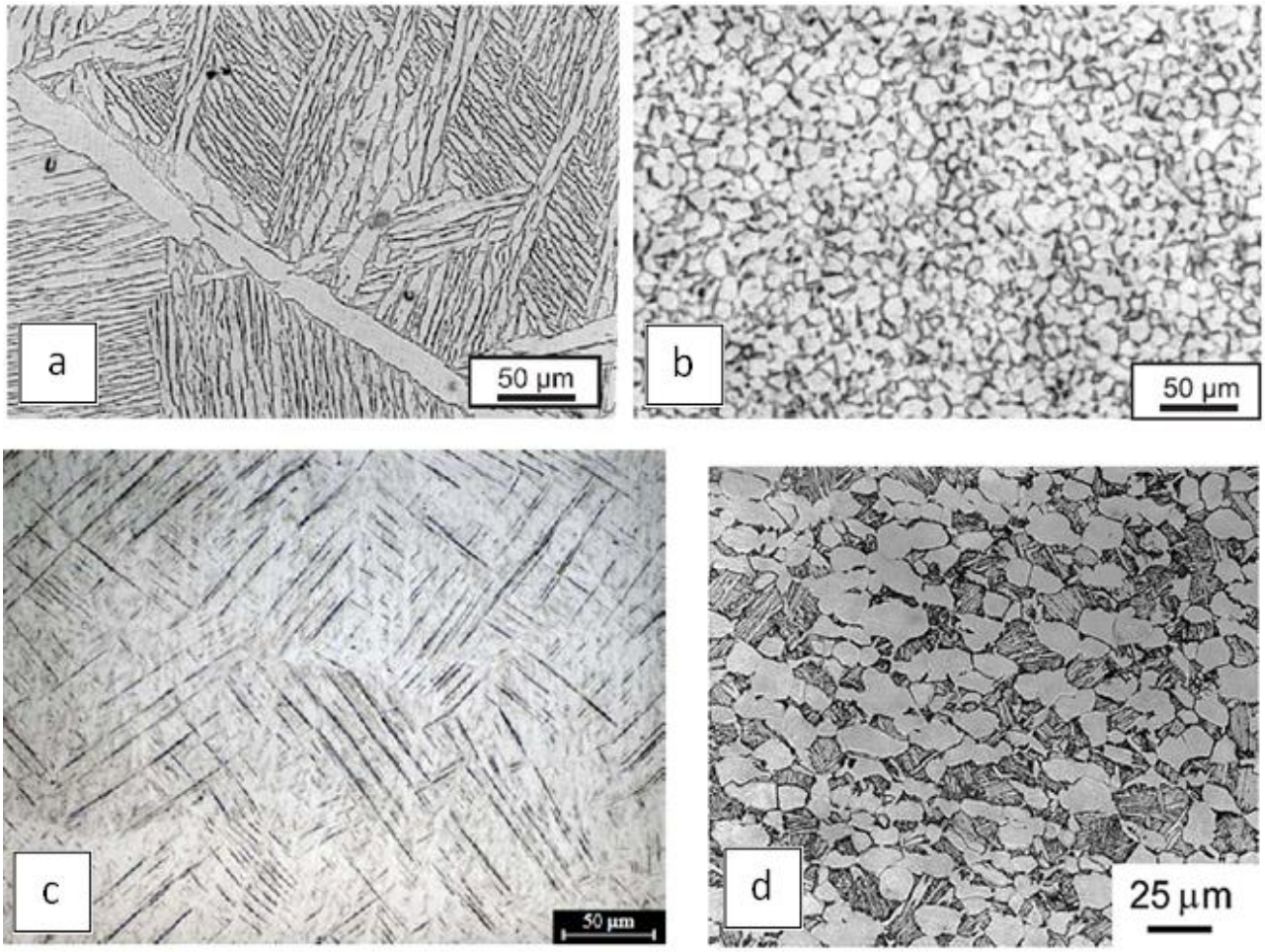

Figure 3.3: Optical metallographic views of Ti 6Al-4V alloys with, a) Coarse lamellar (basket-weave) structure [74], b) Coarse equiaxed α/β mixture [74], c) Ti-6Al-4V martensite microstructure [75] and, d) Ti-6Al-4V Bi-modal microstructure [76].

The common variants of Ti-6Al-4V produced in industry are presented next, from which the microstructures given in Figure 3.3 are formed.

3.2.3 INDUSTRY PRODUCTION

This section introduces the conventionally manufactured forms of Ti-6Al-4V which are found in industry. The methods of production have a significant impact on the microstructure and properties of this particular alloy (due to its affinity for heat treatment). Simple structures are most commonly associated with wrought/forged Ti-6Al-4V (depending on desired properties) whereas complex parts would typically be cast. Investment casting is the process through which aircraft engine components are typically constructed since the moulding system allows for the production of very complex components and hence is a major competitor with Selective Laser Melting.

3.2.3.1 Wrought Ti-6Al-4V

Wrought Ti 6Al-4V is typically bounded by two types of microstructure, lamellar and equiaxed. This form of Ti-6Al-4V is typically produced by the mill after which further processing can be applied to increase strength, hardness etc. Wrought Ti-6Al-4V is normally produced in a plate or sheet form for aerospace applications.

3.2.3.2 Cast Ti-6Al-4V

Casting is considered to be the classic near-net manufacturing technique. Unfortunately, casting is difficult with titanium alloys since titanium is highly reactive with the atmosphere and casting mold at elevated temperatures. The two casting techniques used with Ti-6Al-4V are investment casting and rammed graphite mold casting. The investment casting process is of particular interest here since it is used to manufacture gas turbine engine components. Investment casting provides closer tolerances and better surface finishing than the rammed graphite technique and is capable of much thinner components [74]. The primary advantages of investment cast Ti-6Al-4V over wrought forms of the alloy are lower cost for near-net shape components and shorter lead times [77]. The typical microstructure from cast Ti-6Al-4V is shown in Figure 3.4. Note here the coarse grain structure in cast Ti-6Al-4V. Cast Ti-6Al-4V has slightly reduced mechanical properties in comparison to the wrought forms of the alloy. Figure 3.5 below illustrates the variation in ultimate tensile strength, yield strength and elongation of wrought (both acicular α and equiaxed α/β forms) Ti 6Al-4V, HIP'ed (Hot Isostatic Pressed) cast Ti 6Al-4V and TCP (Thermochemically processed) cast Ti 6Al-4V [78]. The ductility of cast components is lower yet the fracture toughness and fatigue crack growth rates are very similar. The fatigue

characteristics of cast Ti-6Al-4V are worse than that of the wrought form yet the HIP process can be used to reduce internal porosity and hence improve the fatigue and crack initiation behaviour. The fatigue strength of both cast and wrought Ti-6Al-4V is shown in Figure 3.6. Note here the effect of the HIP process on the fatigue strength as a result of the removal of internal porosity.

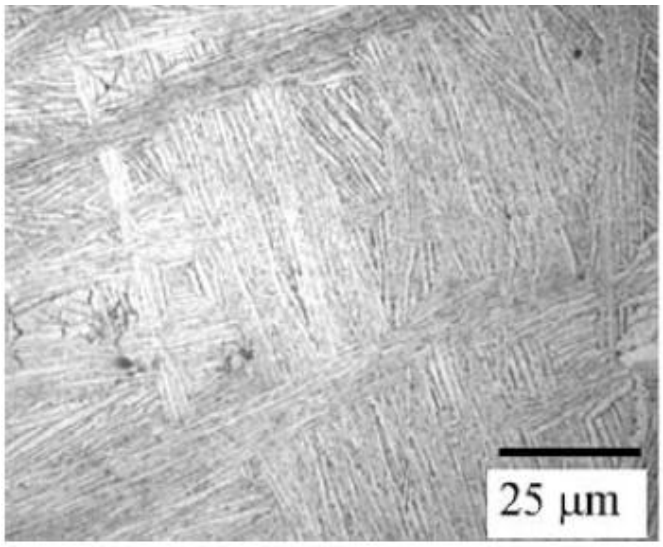

Figure 3.4: Micrograph of a plate specimen as-cast Ti-6Al-4V. [79]

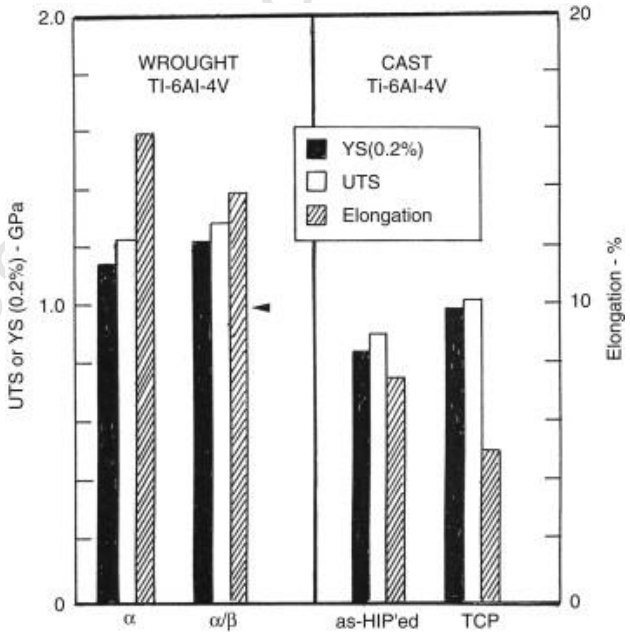

Figure 3.5: Ultimate Tensile Strength (UTS), Yield Strength (YS) and Elongation properties of wrought and cast Ti 6Al-4V specimens with various processing techniques [78]

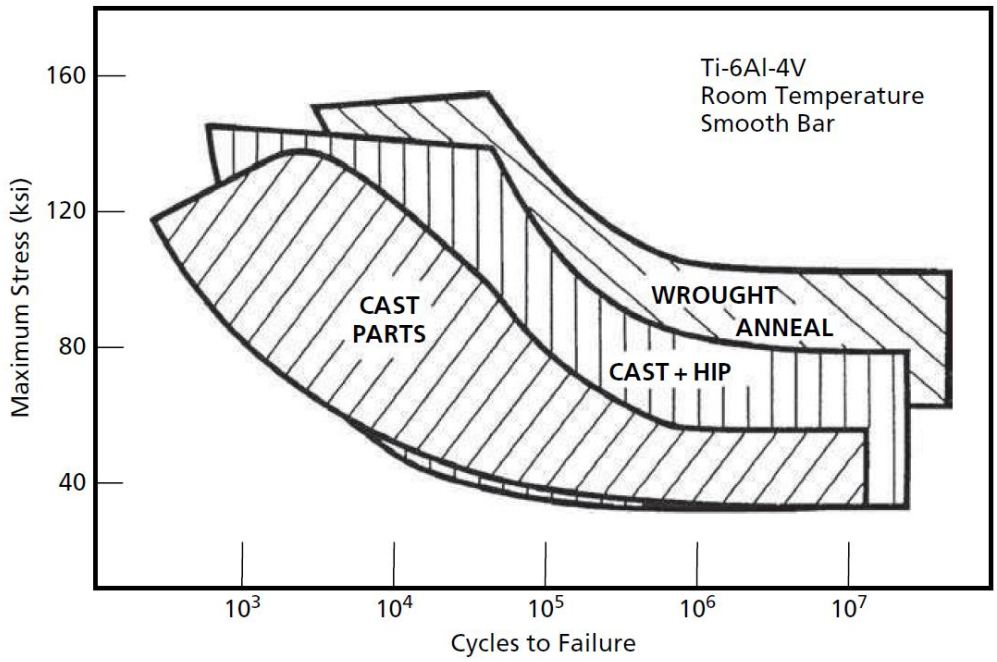

Figure 3.6: Cast and wrought Ti-6Al-4V fatigue strength. [77]

3.2.4 MICROSTRUCTURAL INFLUENCE ON FATIGUE CHARACTERISTICS

The different microstructures present in Ti-6Al-4V variants have been described in the preceding sections. This section describes the effect of microstructure on the fatigue properties in Ti-6Al-4V. The size and morphology of the α and β phases present within α+β alloys play a significant role in the material fatigue characteristics [70]. The flexibility of Ti-6Al-4V processing in achieving different microstructures results in variations in fatigue behaviour for different forms of the alloy. The important microstructural attributes to consider when analysing fatigue behaviour include the following:

- Colony size of α and β lamellae
- Prior β grain size
- Width of the α lamellae
- Volume fraction of α phase

Fatigue cracks tend to initiate in different regions for different microstructures. In lamellar Ti-6Al-4V, the fatigue cracks initiate along prior β grain boundaries or at slip bands within the α

phase as shown in Figure 3.7a. Equiaxed microstructures tend to evolve fatigue cracks only in the α lamellae as shown in Figure 3.7b. Bimodal/duplex structures initiate fatigue cracking within either α lamellae or the lamellar matrix. Fatigue cracking has also been observed at the interface of the lamellar matrix and the α phase as shown in Figure 3.7c.

The fatigue crack propagation behaviour for micro and macro-cracking of coarse lamellar and equiaxed microstructures is shown in Figure 3.8. Notice the poor resilience of the coarse lamellar structure with respect to micro/small cracks. As the graph shifts to the left, the fatigue threshold is reduced and an increased propensity for fatigue crack initiation will be observed as described in Chapter 2. The difference between micro and macro-cracking characteristics is due to additional crack propagation resistance through mechanisms such as crack closure effects and the geometry of the crack opening in large/macro-crack regimes.

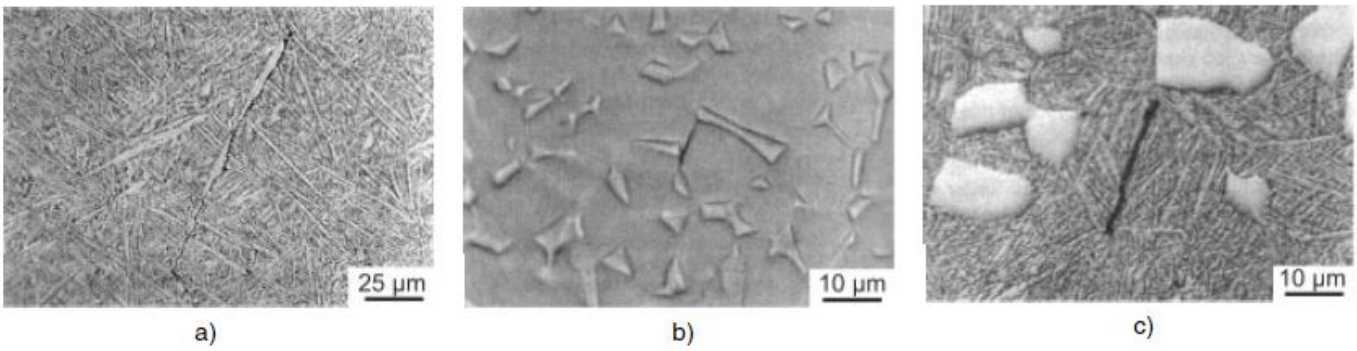

Figure 3.7: Fatigue crack initiation in Ti-6Al-4V specimens with a) lamellar, b) equiaxed and c) duplex/bimodal microstructures subjected to High Cycle Fatigue (R= -1, σ = 775MPa). [74]

It can be seen from Figure 3.8a that the microstructure morphology has a significant influence on the small and large crack behaviour in Ti-6Al-4V. Coarse lamellar (CL) structures are more resilient to long cracks than fine equiaxed (EQ) structures yet the equiaxed microstructure demonstrates far superior fatigue crack resistance to small/short cracking. The effect of heat treatment on the fatigue crack growth rate of Ti-6Al-4V is shown in Figure 3.8b.

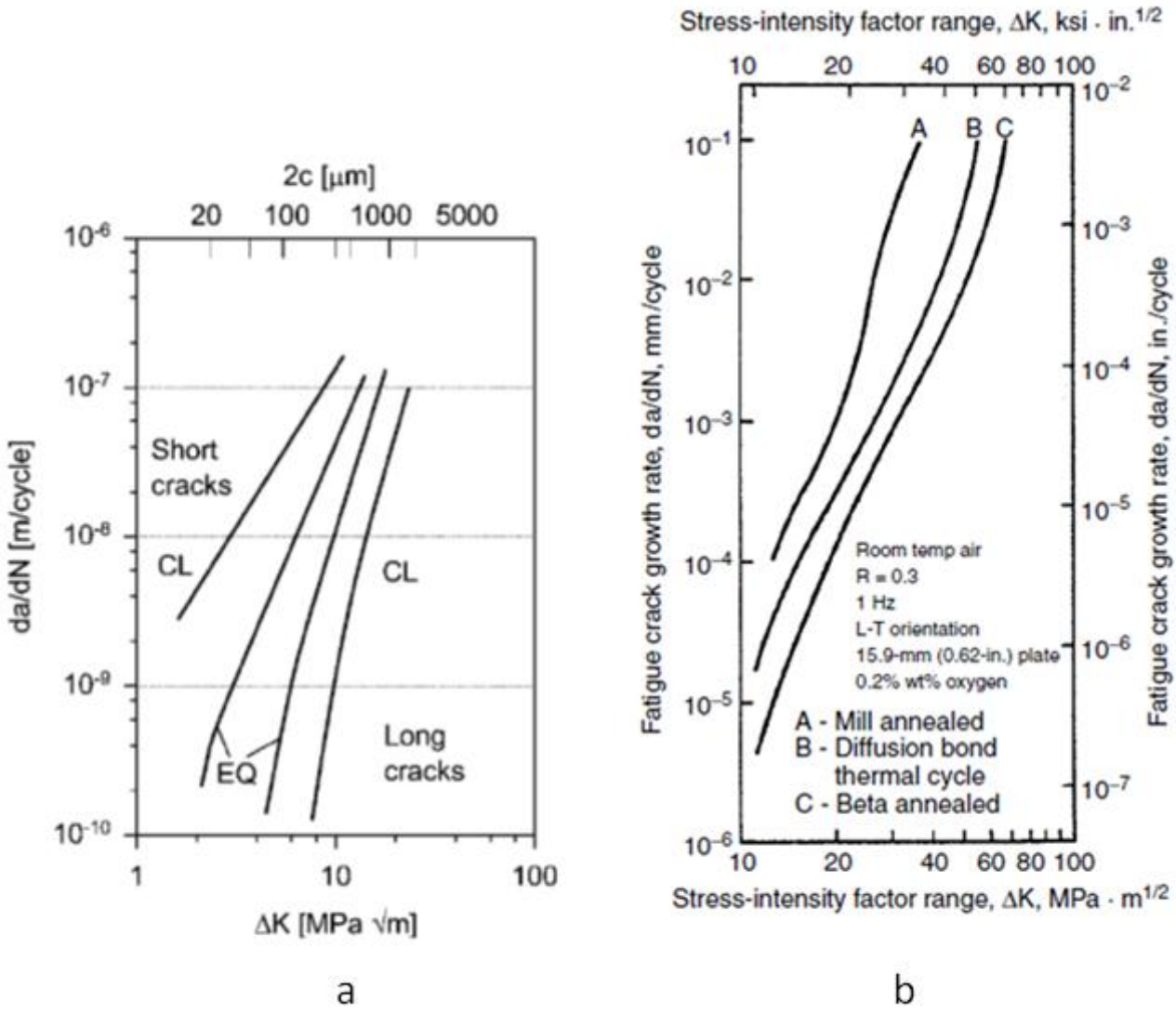

Figure 3.8: a) Micro-crack and macro-crack behaviour in Coarse Lamellar (CL) and fine Equiaxed (EQ) microstructures [74] and, b) Fatigue crack growth rate graph illustrating the effect of microstructure on the fatigue crack growth rate of Ti-6Al-4V alloys [80].

The heat treatment of Ti-6Al-4V has been extensively tested to examine the fatigue properties post-treatment since the change in microstructure has a significant impact on the resulting fatigue crack propagation as is evident from Figure 3.8b. The effect of heat treatments on the fracture toughness for various industry forms of Ti-6Al-4V is shown below in Table 3.1.

Table 3.1: Fracture toughness characteristics of common industry forms of Ti-6Al-4V. [72]

	Yield strength [MPa]	Ultimate Tensile Strength [MPa]	Elongation [%]	K_{IC} [MPa$\sqrt{m}$]
As cast	758	930	13	40
Cast + Annealing	855	930	12	55
Cast + Hot Isostatic Press	869	958	10	70
Typical wrought annealed	860	955	9	65
Standard (α+β) forging + Mill anneal	862	931	10	60
Standard (α+β) forging + Recrystallization anneal	841	925	10	92
Standard (α+β) forging + Beta anneal	827	862	8	99

Since the microstructure of Ti-6Al-4V has a significant role in the fatigue properties of a component, it can be deduced that the manufacturing methodology will have a significant effect. The effect of heat treatment on the fracture toughness and strength of Ti-6Al-4V indicate the alloy's affinity for heat treatment. The next section reviews some of the heat treatments used in industry and their intended purpose.

3.2.5 HEAT TREATMENTS

Titanium alloys are heat treated for a variety of reasons. Heat treatments can relieve residual stresses developed in a component during manufacture, increase strength and produce an optimum combination of properties for a specific application. The common properties which can be improved through heat treating include; tensile strength, creep strength and fracture toughness. Heat treatment techniques for use with Ti-6Al-4V include stress relieving, annealing, and solution treatment and aging (STA) [77].

This section describes in detail the heat treatments which are used with Ti-6Al-4V and in particular, their effects on the microstructure and properties of the end-product. Heat treatments have particular importance in this project since they can be used quite effectively to remove residual stresses. In addition, it may be possible to heat treat a component during the manufacture process such that when the component is removed from the machine, it is free from residual stress. It is important to consider the reactivity of titanium with oxygen and hydrogen at high temperatures and it is essential that all heat treatments above 427 °C are performed in an inert or vacuum environment.

3.2.5.1 Stress-Relief Heat Treatment

The stress-relief heat treatments are the most common form of thermal treatment in titanium and its alloys. Stress relief treatment is used to remove the residual stresses within a material which may have been caused by high temperature gradients, non-uniform hot forging, asymmetric machining, mechanical working, welding and other manufacturing or processing techniques. This treatment is used to ensure the mechanical properties of the material are not hindered by the residual stresses. Stress-relief treatment is common in titanium alloy producers in order to reduce the Bauschinger effect in which the residual stresses hamper the compressive yield strength of the material [72]. This type of treatment is highly beneficial for Ti-6Al-4V since it can be applied without affecting the strength or ductility of the material [77].

Stress-relief can be applied using various combinations of temperature and time. Specimens exposed to higher temperatures for less time will respond similarly to those exposed to lower temperatures for an extended exposure period. The cooling rate is not critical for this treatment however it is very important to ensure the component is both heated and cooled in a uniform manner since severe thermal gradients may re-introduce residual stresses. The cooling phase is typically accomplished through furnace cooling to prevent oxidation. The temperatures, treatment time and corresponding stress relief are listed below [60].

Table 3.2: Stress relief treatments for Ti-6Al-4V [60].

Temperature [°C]	Treatment Time [hrs]	Stress relief [%]
540	8	55
590	8	75
650	8	100

3.2.5.2 Annealing

The annealing process is very similar to the stress-relief treatment with the exception that it is performed at higher temperatures. The annealing processes are defined according to the temperature and exposure times. The high temperature stability of Ti-6Al-4V is improved by an annealing process since the β phase is stabilised. The common annealing processes are mill annealing, duplex annealing, beta annealing, recrystallization annealing and solution treatment. Mill annealing is the most common and simplest anneal, which produces components with good fracture toughness. Duplex annealing is commonly used for increases in creep resistance. Beta annealing will maximise fracture toughness and minimise fatigue crack growth rates. Recrystallization annealing produces results similar to beta annealing and is used to produce damage tolerant components. These annealing processes are described below.

Mill annealing

This process is termed mill annealing since it is typically performed at the mill. It is a partial anneal and is used to remove the effects of cold or hot working. Mill annealing is performed for Ti-6Al-4V at 700-780°C while holding for a minimum of 1hr as shown in Figure 3.9.

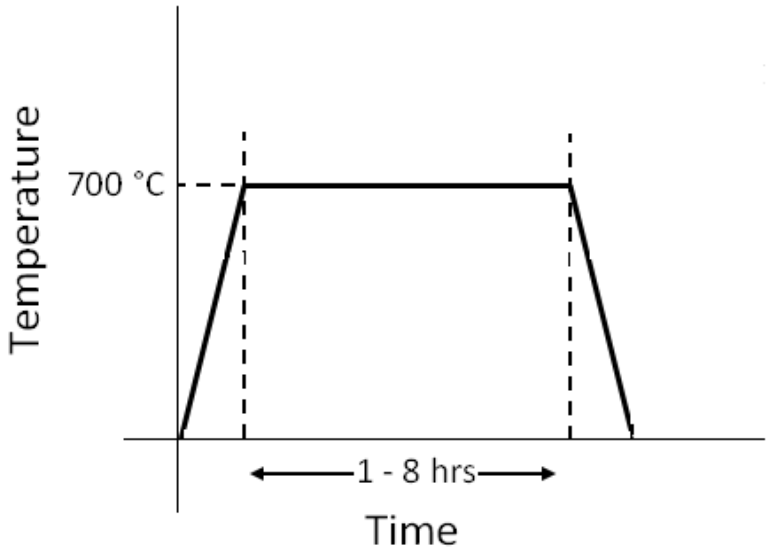

Figure 3.9: Mill annealing process schematic

Duplex annealing

Duplex annealing is a useful process for increasing the creep resistance of Ti-6Al-4V. The duplex term implies a two-part annealing process which begins with the first anneal in the high α+β region and followed by an air cool as shown in Figure 3.10. The second anneal is used to introduce thermal stability and is performed at a lower temperature and again completed with an air cool. This process is conducted for Ti-6Al-4V at a temperature of between 955-980 °C (first anneal) followed by a mill anneal (see above).

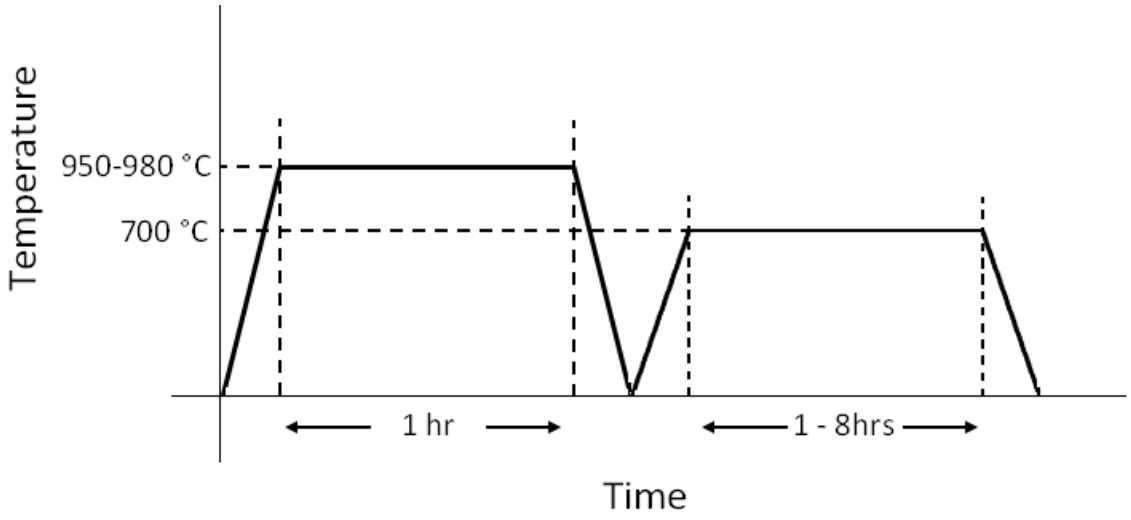

Figure 3.10: Duplex annealing process diagram

Beta annealing

This annealing is performed above the β transus and followed by water quenching or air cooling. The faster cooling rate is necessary to reduce the rapid grain growth at these temperatures. The formation of grain boundary α can result in an undesirable microstructure if the process time and cooling rate are not monitored carefully. The fracture toughness is greatly improved by this process. Beta annealing is performed at temperatures ranging between 1010-1050 °C for Ti-6Al-4V.

Recrystallization annealing

The recrystallization annealing process is also used to improve the fracture toughness of Ti-6Al-4V. This anneal is performed high in the α+β region for an extended period. The alloy is then cooled slowly using furnace cooling to complete the anneal. This process is used in preference to

beta annealing for fracture critical structural airframe components. It is performed at temperatures similar to the first anneal in duplex annealing (955-980 °C) yet is followed by a slow cool.

Solution Treating and Aging (STA)

The solution treatment is used to transform some of the α phase into β such that some β will be retained at room temperature. The cooling rate needs to be rapid in order for the β to be retained without transforming back into α phase. The aging process is then used to precipitate α phase from the retained β phase. This treatment begins with the solution treatment process in which the component is heated into the upper zone of the α+β region (955-970 °C) for approximately 1hr and then rapidly quenched as shown in Figure 1.11. The temperature is marginally below the β-transus temperature for maximum strength levels without detrimental effects on the ductility.

This section has presented the literature on the heat treatment types most commonly used with Ti-6Al-4V. The final section in this review of conventionally produced Ti-6Al-4V is a comparison in the mechanical properties of wrought Ti-6Al-4V and the known properties of SLM produced Ti-6Al-4V.

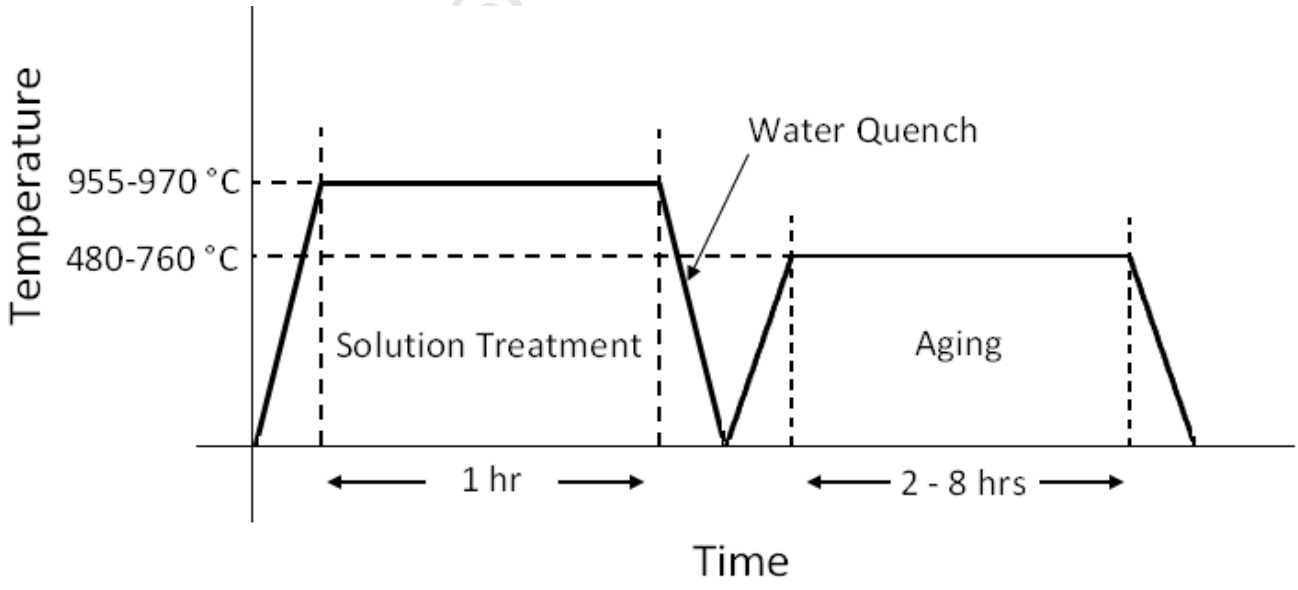

Figure 1.11: Solution treatment and aging process diagram

3.2.5.3 Effect of Phase Change on Residual Stress Levels

As stated earlier, the substantial affinity of Ti-6Al-4V for heat treatment is due to the large two-phase (α+β) region in the phase diagram as shown in Figure 3.1. The broad range of microstructures which have been explored in the earlier sections of this Chapter demonstrate a dynamic response to heat treatment. The generation of different phases can have an impact on the internal stress states within a material as is evident from literature on steel [81]. The effect of transformation and internal stresses due to phase change is beyond the scope of this study however more information may be found from published work in [82], [83].

3.3 SELECTIVE LASER MELTED TI-6AL-4V

The previous section reviewed conventionally produced Ti-6Al-4V and the methods of its production. A thorough review of the microstructures and their effect on the fatigue properties of Ti-6Al-4V has also been completed in anticipation of comparing SLM Ti-6Al-4V to its industry counterparts. Having reviewed the common forms of Ti-6Al-4V and their methods of processing, this section presents the available literature on SLM produced Ti-6Al-4V with specific emphasis on the recent studies into the fatigue behaviour.

3.3.1 MECHANICAL PROPERTIES

The recent introduction of the SLM systems into the manufacturing arena has meant that many of the properties well-known in traditional forms of Ti-6Al-4V are still unknown in literature for the SLM systems. The material properties which are as yet uncharacterised are predominantly in the fracture and creep sections. This section outlines the general material properties in the most common form of the Ti-6Al-4V alloy from which initial general assessments of the SLM material can be made. The initial work into the fracture and fatigue properties of this material done by Hooreweder et al [84] is presented later in this chapter. The material properties for wrought Ti-6Al-4V are compared with the known properties of SLM produced Ti-6Al-4V in Table 3.3 below.

Table 3.3: Material properties of common industry produced forms of Ti-6Al-4V and SLM produced Ti-6Al-4V.

	Wrought Ti-6Al-4V	Ref	SLM Ti-6Al-4V	Ref
Hardness (Vickers)	349 HV	[72]	400 – 430 HV	[85]
Ultimate Tensile Strength	900 - 1200 MPa	[72]	1180 ± 100 MPa	[85]
Tensile Yield Strength	800 - 1100 MPa	[72]	1090 ± 100 MPa	[85]
Elongation at break	14%	[72]	5% ± 3%	[85]
Reduction of Area	36%	[72]		
Modulus of Elasticity	113.8 GPa	[72]	120 ± 20 GPa	[85]
Compressive Yield Strength	970 MPa	[72]		
Poisson's Ratio	0.342	[72]	0.3246	[85]
Charpy Impact	17 J	[72]		
Fatigue strength (unnotched)	500 – 700 MPa	[72]		
Fatigue strength (notched)	160 – 240 MPa	[72]		
Fracture Toughness	33 – 110 MPa$\sqrt{m}$	[72]		
Shear Modulus	44 GPa	[72]	43 GPa	[85]
Shear Strength	550 MPa	[72]		
Density	4.43 g/cm^3	[72]	4.43 g/cm^3	[85]

3.3.2 FRACTURE TOUGHNESS AND CRACK PROPAGATION

The tensile/yield strengths, hardness and impact toughness of SLM Ti-6Al-4V are relatively well-known in literature (see ref [84]), yet the fatigue characteristics are still largely unknown. The versatility of the SLM machine parameters allow for a significant variety in material properties and the work by Hooreweder et al [84] has made a first attempt in understanding the fracture toughness and fatigue properties of this material. It has been noted in literature that the microstructural differences between the SLM and wrought Ti-6Al-4V can lead to substantial differences in the static and dynamic characteristics of this alloy. The standard wrought Ti-6Al-4V has a globular microstructure whereas the optimal SLM variant is produced with a thin acicular martensite (α' phase). The microstructures as used by Hooreweder et al are shown below in Figure 3.12 [84].

The results for the fracture toughness tests performed by Hooreweder et al [84] in Table 3.4 and Figure 3.13 show inferior fracture toughness values in comparison with the wrought material.

This was attributed to the martensitic microstructure produced by SLM and its brittle behaviour under loading. The martensitic microstructure however is beneficial for retarding crack growth since the acicular needles do not provide an easy route through which a crack may propagate. The density of the SLM part becomes significant with respect to crack initiation sites at micro-flaws/pores within the material (see Figure 3.12b and d).

Table 3.4: Fracture toughness properties of SLM Ti-6Al-4V as determined by Hooreweder et al [84]

	Wrought/Annealed Ti-6Al-4V	SLM Ti-6Al-4V
Density [%]	99.68 ± 0.046	99.73 ± 0.036
K_{IC} [MPa$\sqrt{m}$]	69.98 ± 3.53	52.4 ± 3.48
C [m/cycle]	4 x 10^{-14}	5 x 10^{-12}
m	4.757	3.376

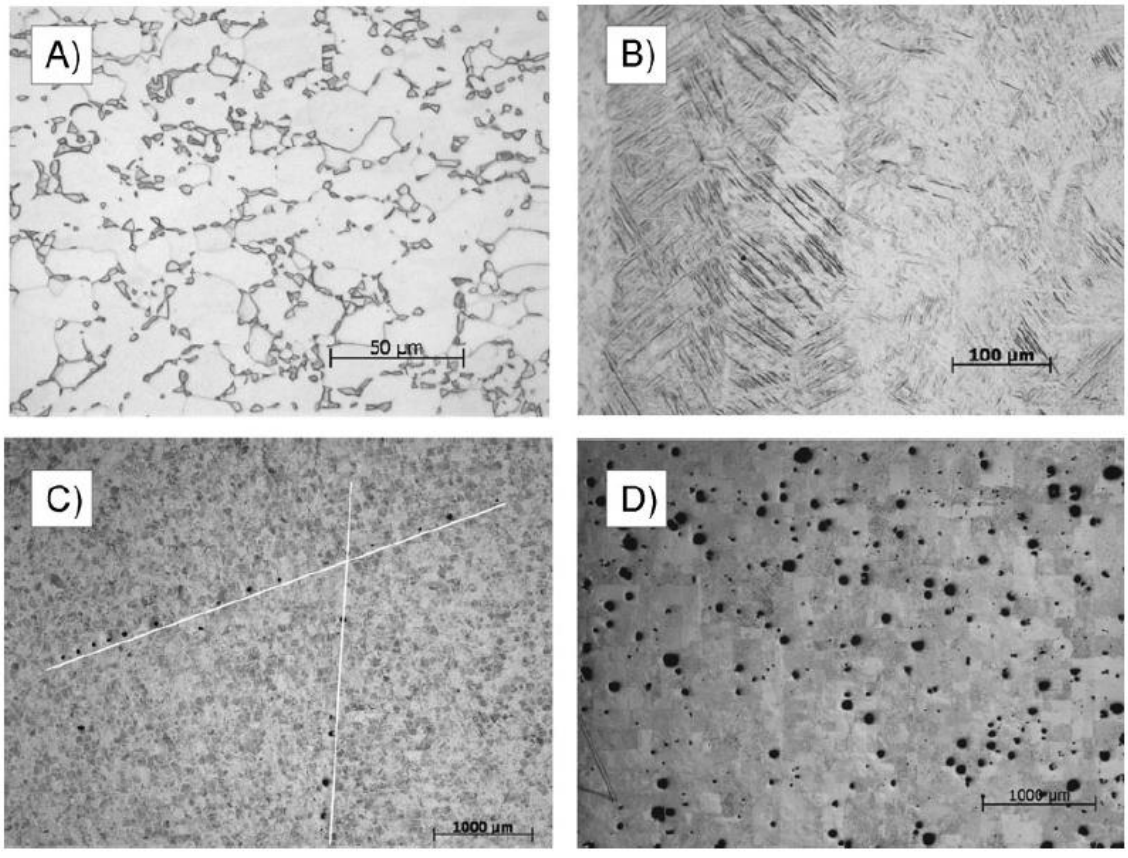

Figure 3.12: Microstructure of the Ti-6Al-4V used by Hooreweder et al in determining the fracture toughness properties, a) wrought/annealed, b) SLM with optimal parameters, c) SLM with island scanning, d) SLM with sub-optimal parameters. [84]

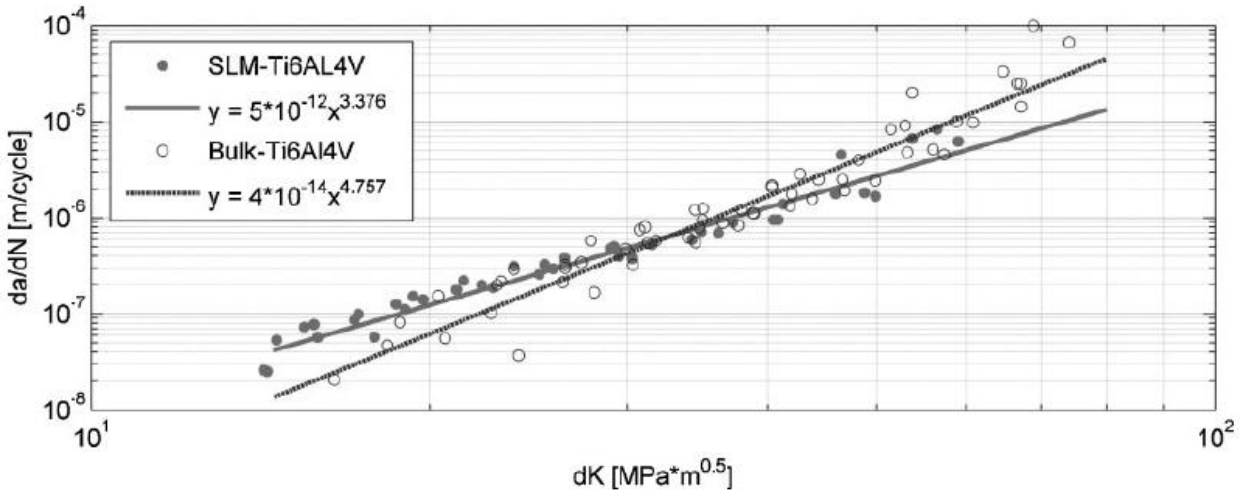

Figure 3.13: Crack growth rate vs. stress intensity for wrought and SLM Ti-6Al-4V (Paris equation format). [84]

3.4 SUMMARY

The sections in this chapter have introduced literature which describes the titanium alloy Ti-6Al-4V in great detail. The common microstructures and industry forms of this material have been discussed including the effects of numerous heat treatments. The variation in mechanical properties between industry variants of Ti-6Al-4V has been revealed, particularly the differences between cast and wrought forms of the alloy. It is apparent that processing and manufacturing techniques have a significant impact on the behaviour of this alloy, particularly through heat treatment. The review on the effect of microstructure on the fatigue properties of Ti-6Al-4V re-enforces this behavioural variation and further augments the uncertainty in the structural integrity of Selective Laser Melted Ti-6Al-4V. The initial investigations by Hooreweder [84] into the SLM Ti-6Al-4V fracture toughness suggest inferior performance yet the literature available in this area of material performance is extremely limited. The effect of residual stresses and their associated mechanisms on the structural integrity of SLM Ti-6Al-4V has not yet been identified. This is particularly important in the presence of porosity and micro-flaws as explained in Chapter 2. In order for Selective Laser Melting to be implemented in complex aerospace designs, the residual stress levels need to be quantified, understood and eliminated if necessary. The next chapter reviews the experimental methods used in the course of this study.

CHAPTER 4 – EXPERIMENTAL METHODS

4.1 INTRODUCTION

The previous chapters have introduced the background to the project and a review of the conventional and Selective Laser Melted (SLM) Ti-6Al-4V. This chapter outlines the experimental methods used in the residual stress testing phase of the project in addition to the post processing methodology used to assess the results. This study began with a pilot investigation into the root cause behind distortion observed in tensile specimens built from the DMLS machine. This analysis led to further research into the residual stress levels and the effect of heat treatment on specimens provided by the CFRM[1]. This analysis was complemented by microscopy and density work in an effort to further the understanding of this new manufacturing technique.

The hole-drilling residual stress analysis was performed in accordance with ASTM E837-08 and is described in Section 4.3. The heat treatments performed on the Ti-6Al-4V specimens are described in detail in Section 4.4. The density testing procedures in Section 4.5 include both the Archimedes principle test as standardised in ASTM B311-08, and an optical microscopy method. These density testing parameters are followed by the hardness testing in Section 4.6. The first section which follows describes the specimens received for this study and their methods of preparation.

4.2 SPECIMEN DETAILS

The Ti-6Al-4V specimens provided by the CFRM were produced by the EOSINT M270 DMLS machine. Twenty-two samples were received consisting of 2 pilot specimens, 8 residual stress cylinders and 12 tensile specimens.

[1] Centre for Rapid Manufacturing (CFRM) based at the Central University of Technology (CUT)

4.2.1 PILOT STUDY SPECIMENS

The pilot study specimens in Figure 4.1a were provided by the CFRM for a preliminary analysis into the residual stress profiles. The components were initially intended for tensile tests but upon their removal from the EOSINT M270 baseplate, the specimens distorted as shown in Figure 4.1b and c. The tensile specimen contained within the outer support shell had remained centrally aligned until the specimens were cut from the baseplate and an offset of 0.4mm was measured. It was then proposed to analyse the residual stresses contained within the components in an effort to determine whether they had caused the distortion observed following the removal of the lower constraint (baseplate). Detailed drawings of the pilot specimens are given in Appendix D.

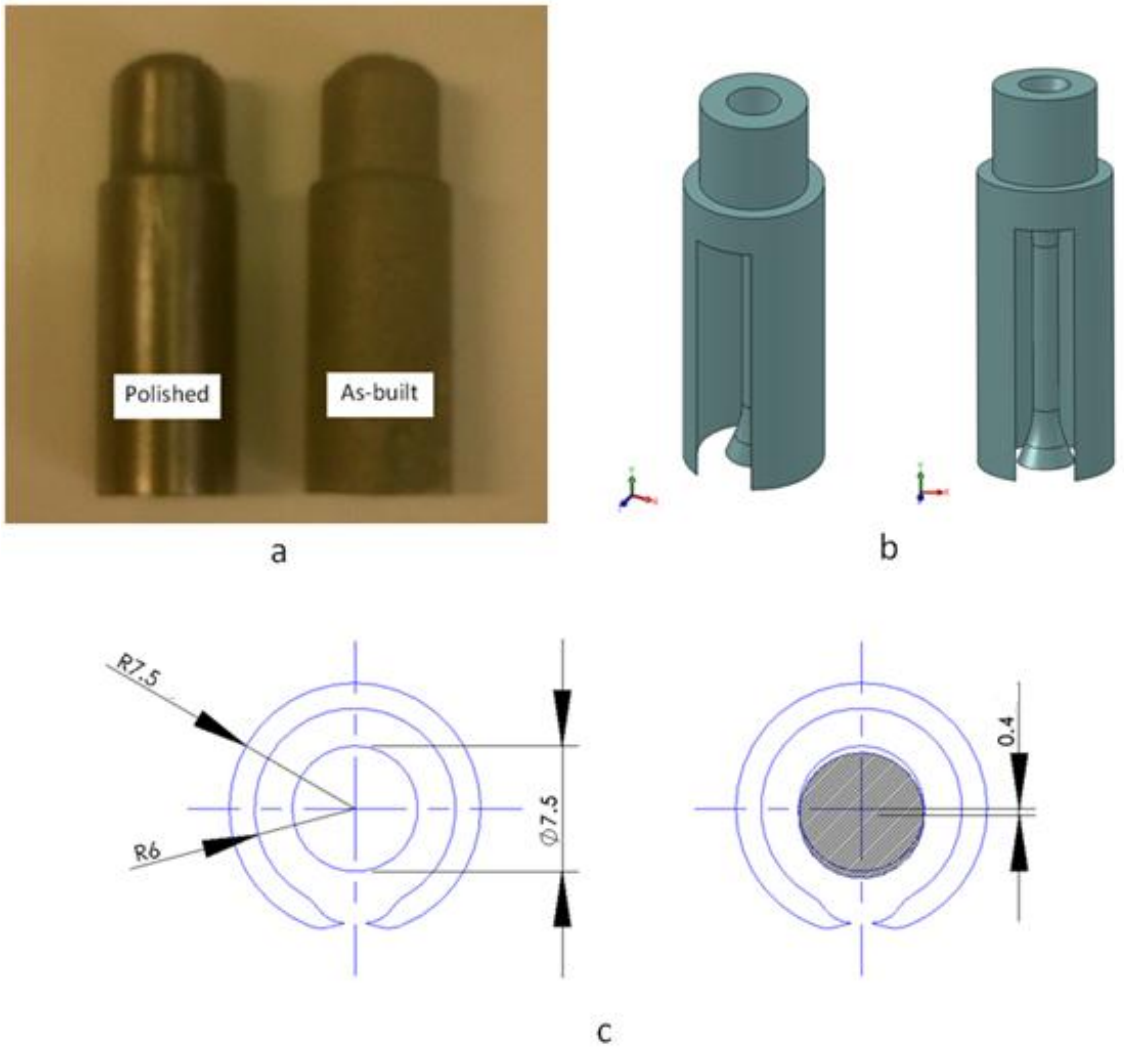

Figure 4.1: a) SLM Ti-6Al-4V specimens received for the study, b) CAD images of the tensile specimen contained within the outer sheath, c) plan view of the distortion observed post baseplate removal. A detailed drawing of the pilot study specimens may be found in Appendix D.

4.2.2 RESIDUAL STRESS SPECIMENS

The residual stress specimens provided by the CFRM consisted of eight 40mm cylinders with a diameter of 12mm. These specimens were grown both in the horizontal and vertical orientations such that any directional effects could be observed. The dimensions of the cylinders are given in Figure 4.3 below. A CAD image of the EOSINT M270 build platform with the Ti-6Al-4V components and their designation is shown in Figure 4.2. The specimens are labelled according to their position and build orientation in Table 4.1.

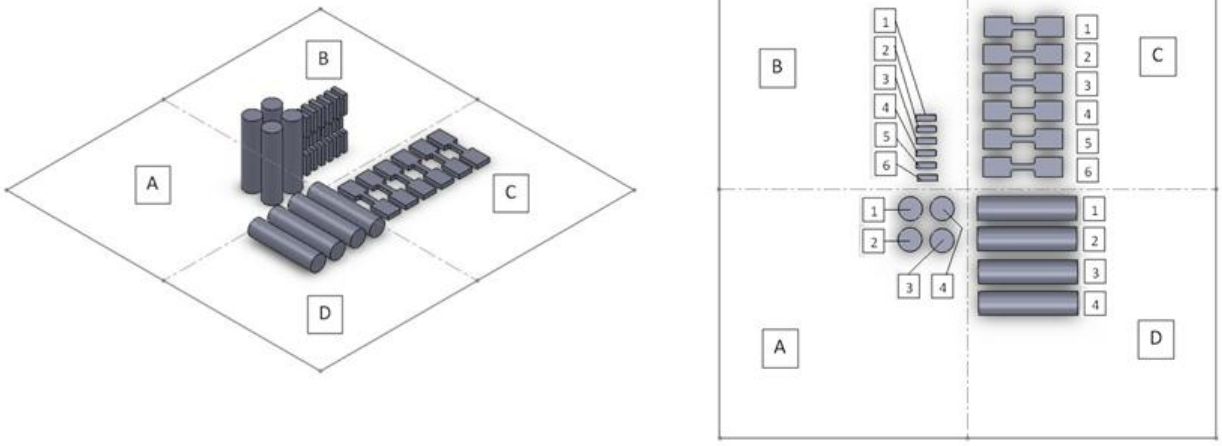

Figure 4.2: Isometric and plan view of the build platform and the sector divisions A, B, C, D and the specimen labels.

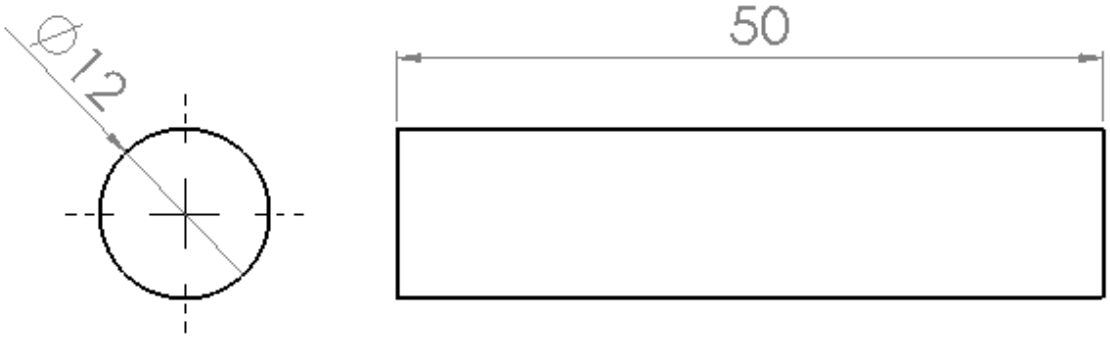

Figure 4.3: Residual stress specimen dimensions (all dimensions in mm).

Table 4.1: Residual stress specimen designation and orientation.

Specimen Designation	Specimen Type	Orientation
A1	Cylindrical Residual Stress Specimen	Vertical
A2	Cylindrical Residual Stress Specimen	Vertical
A3	Cylindrical Residual Stress Specimen	Vertical
A4	Cylindrical Residual Stress Specimen	Vertical
D1	Cylindrical Residual Stress Specimen	Horizontal
D2	Cylindrical Residual Stress Specimen	Horizontal
D3	Cylindrical Residual Stress Specimen	Horizontal
D4	Cylindrical Residual Stress Specimen	Horizontal

4.2.3 TENSILE SPECIMENS

The tensile specimens provided by the CFRM consisted of 6 horizontally grown specimens and 6 vertically grown specimens as shown in Figure 4.2 (and listed in Table 4.2). The specimens were drilled for the connection points after the specimens were built to ensure a smooth surface finish at the holes. The dimensions for the tensile specimens are shown below in Figure 4.4.

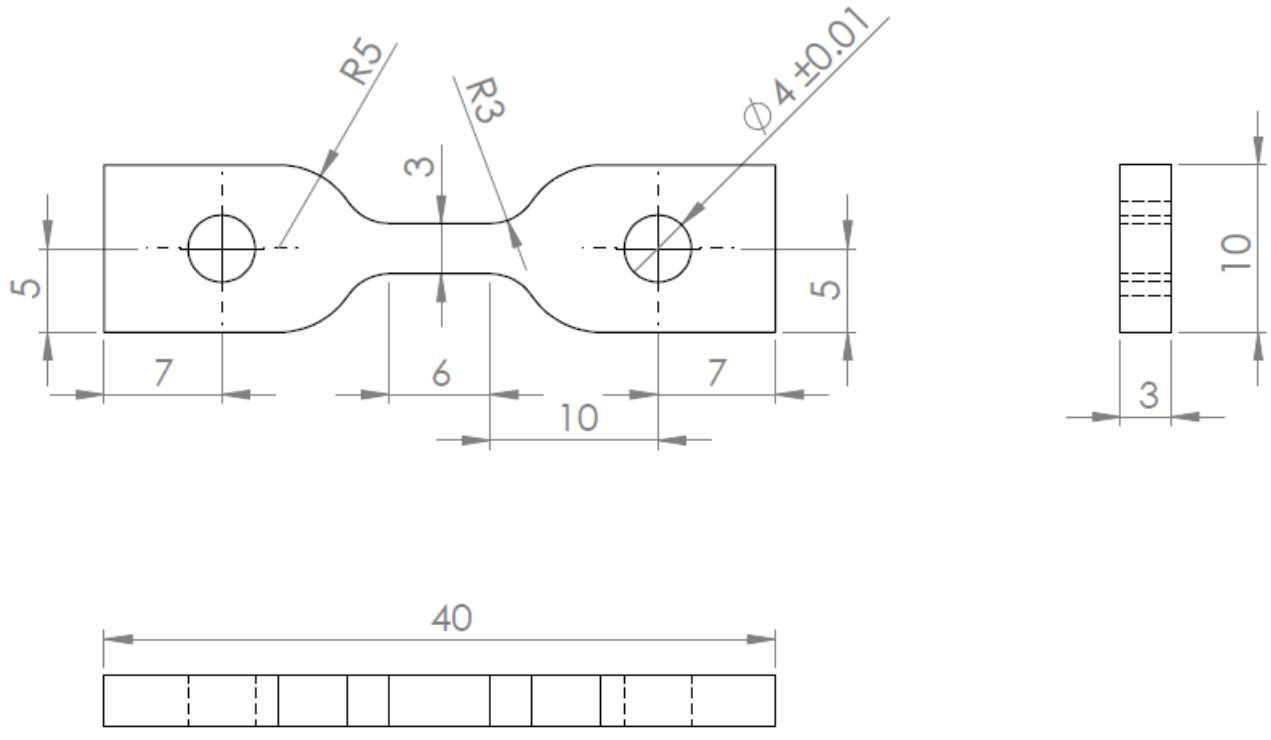

Figure 4.4: Tensile specimen dimensions (all dimensions in mm).

Table 4.2: Tensile specimen designation and orientation.

Specimen Designation	Specimen Type	Orientation
B1	Tensile Test Specimen	Vertical
B2	Tensile Test Specimen	Vertical
B3	Tensile Test Specimen	Vertical
B4	Tensile Test Specimen	Vertical
B5	Tensile Test Specimen	Vertical
B6	Tensile Test Specimen	Vertical
C1	Tensile Test Specimen	Horizontal
C2	Tensile Test Specimen	Horizontal
C3	Tensile Test Specimen	Horizontal
C4	Tensile Test Specimen	Horizontal
C5	Tensile Test Specimen	Horizontal
C6	Tensile Test Specimen	Horizontal

4.2.4 SPECIMEN PREPARATION

This section briefly reviews the preparation process applied to the specimens for the residual stress testing and the microstructural evaluation. The application of the strain gauges is crucial for accurate results from ASTM E837-08 since any slippage between the gauge and the material surface will invalidate the results. The microstructural preparation describes the specimen sample removal, polishing and etching procedures.

4.2.4.1 Strain Gauge Installation

The position of the strain gauge is particularly important to ensure a valid result is obtained. The general purpose gauges should not be positioned within 1.5 x (hole diameter) of the nearest edge or junction with another material. The application of the gauges is a delicate task in which the operator must exercise care in ensuring that the gauge is not damaged during the application. The instruments and adhesives required for the application of the strain gauges are listed in Table 4.3 below.

Table 4.3: Strain gauge installation materials.

Strain Gauges	CEA-06-062UM-120 (Type B) CEA-06-062UL-120 (Type A)

Adhesive	Kyowa CC-33A adhesive
Surface Preparation	Ethanol
	Scribe
	100 & 220 grit sandpaper
	Forceps

The procedure for adhering the strain gauges to the surface of the material are described in steps 1-7 which follow.

Step 1: Use the 100 grit sandpaper to remove the majority of the surface roughness as shown in Figure 4.6 below.

Step 2: A scribe is used to *lightly* mark the position of the gauge on the surface with a vertical and horizontal line as shown in Figure 4.5. (NB scribing the workpiece heavily may affect the residual stress result)

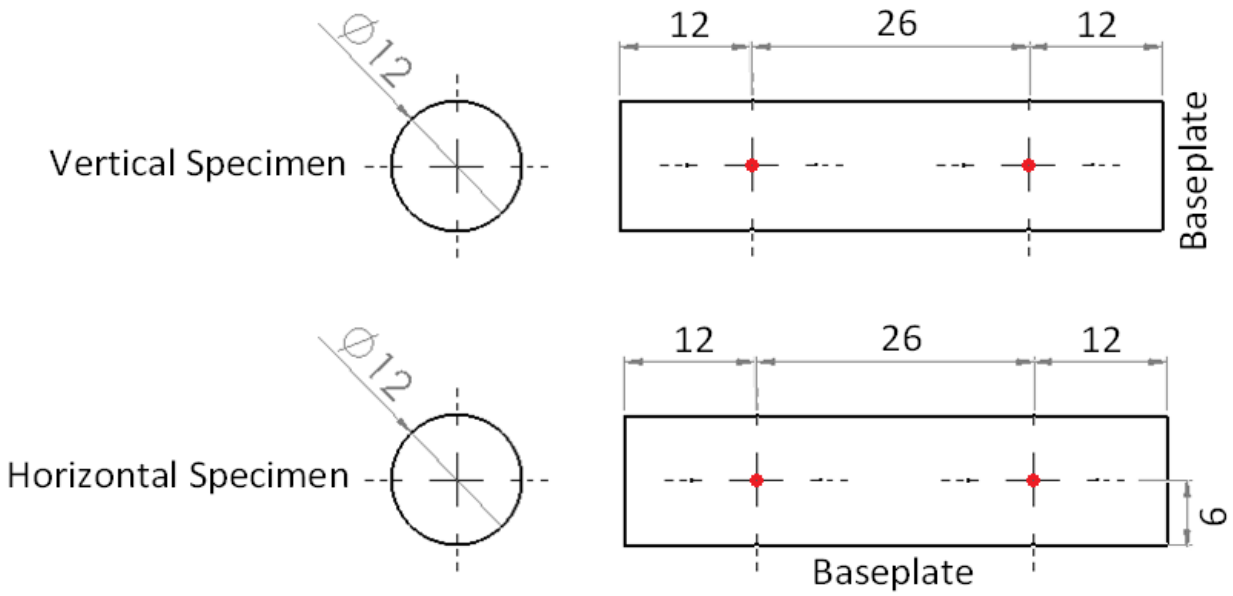

Figure 4.5: Strain gauge rosette locations for the horizontal and vertically grown cylinders.

Step 3: Use the 220 grit sandpaper to lightly abrade the surface for a successful gauge application.

Step 4: Clean the surface with ethanol and use a hairdryer to evaporate the solvent from the surface.

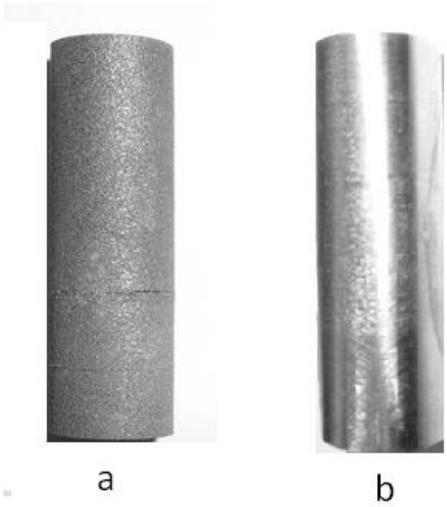

Figure 4.6: Specimen surface roughness a) prior to polishing, b) after polishing.

Step 5: Remove the strain gauge from the packaging using the forceps and ensure the gauge can be positioned correctly.

Step 6: Apply the adhesive to the back of the gauge and use the forceps to position the gauge accurately on the surface. Immediately apply pressure to the gauge using a poly-urethane sheet to prevent moisture being transferred to the gauge surface. Apply the pressure for approximately 2 minutes. The heat from the finger will help to cure the adhesive.

Step 7: Allow to cure fully for at least 6 hours before the lead wires are soldered.

Step 8: Solder the lead wires to the solder pads on the gauge surface and secure the wires such that no force is exerted on the solder pads as shown in Figure 4.7b.

Step 9: Connect the strain gauge lead wires to the instrumentation as described in Section 4.3.4 and place the specimen in a vice grip. Apply light pressure to the vice grip and ensure strain readings are recorded on the strain indicator. Ensure readings return to zero when pressure is removed.

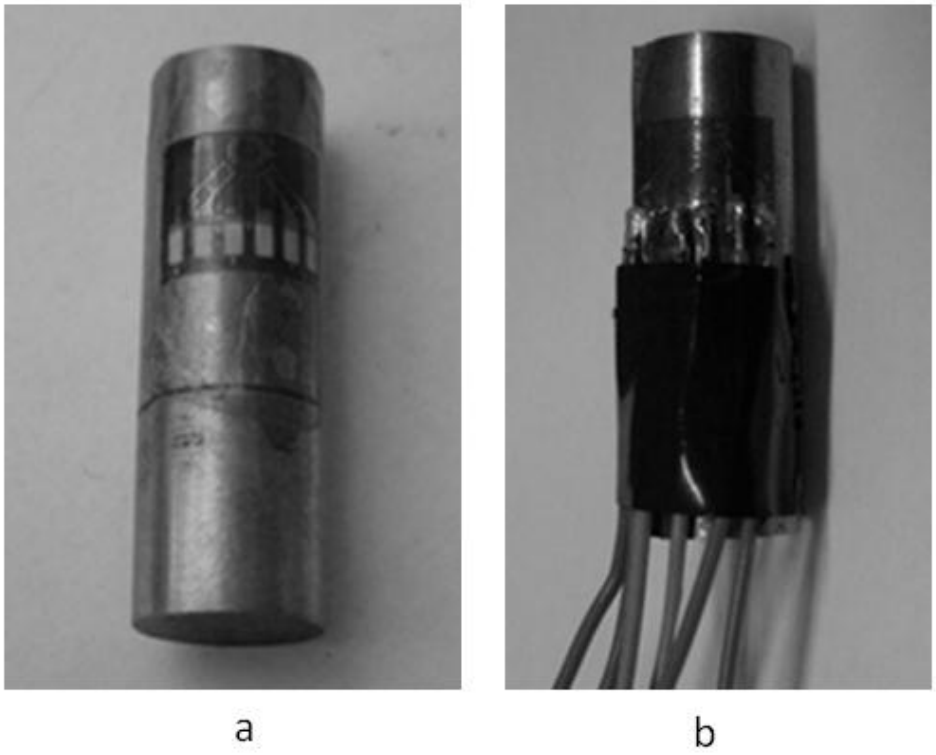

Figure 4.7: a) Strain gauge applied to specimen surface and, b) strain gauge soldered and lead wires secured.

4.2.4.2 Microscopy Preparation

The residual stress assessment for this project utilised cylindrical components which were examined on either end of each specimen by removing 2mm thick disk pieces using a micro-slicer with a diamond-tipped blade. The disk specimens were mounted for the microscopy analysis using the *Struers LaboPress-3* hot mounting system (see Figure 4.8a). Specimen polishing was accomplished using the Ti-6Al-4V attack polishing scheme with a *Struers TegraPol-11* automatic polisher (see Figure 4.8b). This is necessary to remove the surface roughness and ensure a 'mirror finish' before the etchant is applied.

4.2.4.3 Etching Procedure

The etchant used in this analysis is the Kroll's reagent for use with Ti-6Al-4V sections. This etchant is among the most common and effective for viewing the microstructure and grain boundaries in Ti-6Al-4V [86]. The reagent details are given below in Table 4.4. The etchant was

applied for durations of between 12-15 seconds for complete surface etching. The procedures specified in this section for the preparation of specimens for microscopy work were used on the material in its as-built form and after heat treatment. The next section details the experimental work done in determining the residual stress levels in the SLM Ti-6Al-4V.

Figure 4.8: a) Struers LaboPress-3 mounting system and, b) Struers TegraPol-11 automatic polisher.

Table 4.4: Kroll's reagent used for Ti-6Al-4V sample etching. [86]

Composition	Concentration (per 100ml)	Etching Duration
Distilled Water	92 ml	12-15 seconds
HNO_3	6 ml	
HF	2 ml	

4.3 RESIDUAL STRESS TESTING

This segment describes the test method used to evaluate the residual stresses in the sintered specimens. Measurements of the residual stress in an opaque material (such as a metal) require the locked-in stress to be relieved such that the sensor mechanism is able to register the strain change. This is accomplished by the removal of material through a drilled hole. The hole is unable to carry any stress and thus the strains around the hole must change to accommodate this change in the stress state. This strain change is related to the stress state through a series of data

reduction equations. The hole drilling method of determining residual stresses is standardised in the ASTM Standard Test Method E 837-08.

A brief overview of this method is given below.

1. A strain gauge (3 or 6 elements) rosette is positioned on the specimen undergoing the residual stress test.
2. The strain gauge is connected to the multi-channel static strain measuring indicator.
3. A precision drilling platform (RS-200 milling guide) is positioned around the specimen such that the drill piece is centred within ±0.038mm of the strain gauge rosette centre.
4. The strain gauges are zeroed and a small, shallow hole is drilled through the strain rosette centre.
5. The strain is registered at incremental depths of the hole such that the residual stress change with depth can be determined.
6. Data reduction relationships are used to determine the orientation and magnitude of the principal stresses.

4.3.1 REVIEW OF ASTM E837-08

The hole drilling strain-gauge method is a ‘semi-destructive’ technique with which the residual stresses near the surface of an isotropic linear-elastic material can be determined. This hole-drilling residual stress test is standardised in ASTM E837 and was revised in 2008 to include a technique for analysing non-uniform residual stresses. This standard is reviewed in the sections which follow.

This method is specified for the evaluation of residual stress profiles near the surface of an isotropic, linear-elastic material. The stresses may be uniform with depth (‘uniform’ stress) or they may vary significantly with depth (‘non-uniform’ stress). Specimens which have a thickness less than the diameter of the drilled hole may be considered ‘thin’ whereas those which have a thickness significantly greater than the hole diameter are considered ‘thick’. This method will provide valid results for residual stresses with a magnitude less than 60% of the material yield strength. The plasticity effects which occur after this threshold has been surpassed are not accounted for in ASTM E837-08.

4.3.2 MEASUREMENT THEORY

A small hole is drilled into the surface of the specimen through the centre of a strain gauge rosette to a maximum depth of approximately 0.4D (see Figure 4.9 below). The residual stresses are partially relieved as the hole increases in depth and the associated strain changes are detected via the surface strain of the strain gauge grid area. The sensitivity of the gauges is highest for those strains measured nearest to the surface and hence as the experiment proceeds, the strain gauge sensitivity will decrease.

The residual stresses which were present at the hole location are determined from the relieved strains using mathematical relationships derived from linear-elasticity theory. If the material contained uniform residual stresses, the surface strain relief is associated with the residual stresses in the following relationship:

$$\varepsilon = \frac{1+v}{E}\bar{a}\left(\frac{\sigma_x+\sigma_y}{2}\right) + \frac{1}{E}\bar{b}\left(\frac{\sigma_x-\sigma_y}{2}\right)cos2\theta + \frac{1}{E}\bar{b}\tau_{xy}sin2\theta \qquad \textbf{(4-1)}$$

In which the symbols are identified in Figure 4.9a.

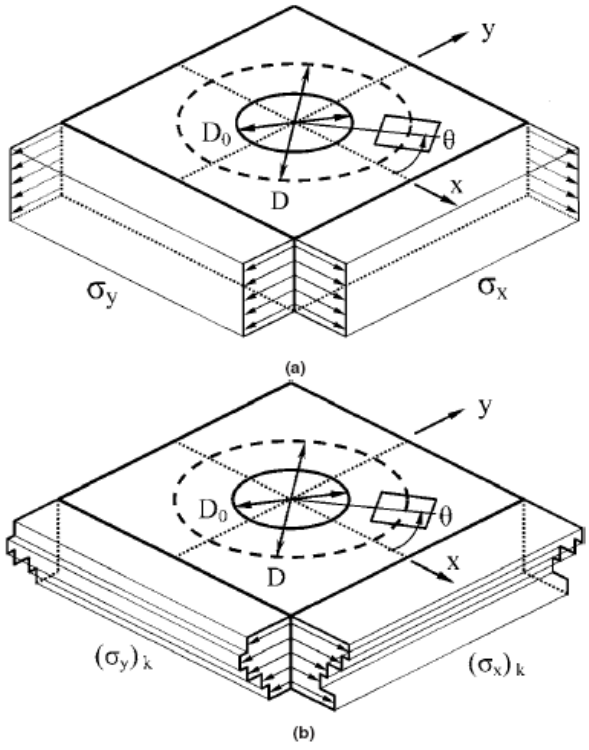

Figure 4.9: Hole terminology for a) uniform residual stress field and, b) non-uniform residual stress fields. [87]

If the material was subjected to non-uniform residual stresses as shown in Figure 4.9b, the relationship between the relieved strain and residual stresses is given below:

$$\varepsilon = \frac{1+v}{E}\sum_{k=1}^{j}\bar{a}_{jk}\left(\frac{\sigma_x+\sigma_y}{2}\right)_k + \frac{1}{E}\sum_{k=1}^{j}\bar{b}_{jk}\left(\frac{\sigma_x-\sigma_y}{2}\right)_k cos2\theta + \frac{1}{E}\sum_{k=1}^{j}\bar{b}_{jk}\left(\tau_{xy}\right)_k sin2\theta \quad \textbf{(4-2)}$$

In which the calibration constants $\bar{a}_{jk}$ and $\bar{b}_{jk}$ indicate the relieved strains in a hole with *j* incremental depths to a total hole depth of *k*.

A physical interpretation of the coefficients $\bar{a}_{jk}$ is given from the example drilling sequence illustrated in Figure 4.10 below. This sequence illustrates the formation of a hole with four incremental depth steps. The calibration constants here represent intermediate stages for the contribution of each layer's strain to the residual stresses recorded by the strain measuring equipment.

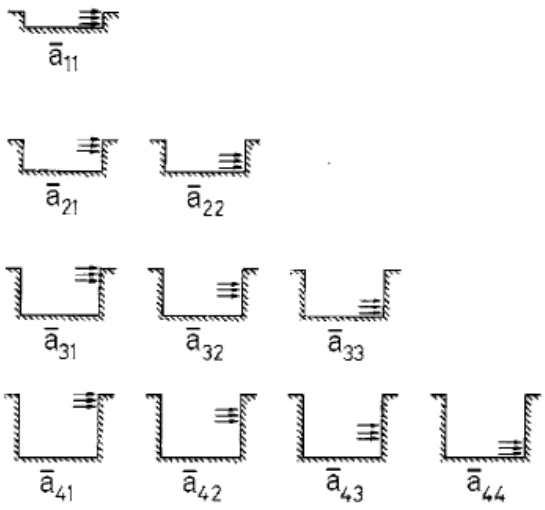

Figure 4.10: Physical interpretation of the calibration coefficients $\bar{a}_{jk}$. [88]

The relieved strains at each step provide sufficient information along with the calibration matrices to evaluate the Cartesian stresses: σ_x, σ_y and τ_{xy} for each step. These may be transformed into the maximum and minimum principal stresses σ_{max} and σ_{min} respectively. The orientation β of the principal stresses may also be determined from this data.

4.3.3 STRAIN GAUGE GEOMETRY

ASTM E837-08 is designed for strain gauge rosettes containing either three or six strain gauges arranged in a grid format surrounding the geometrical centre. The geometry of a typical three-element strain gauge rosette is shown below in Figure 4.11. The numbering convention of the strain gauges is significant when analysing the respective strains and is measured clockwise by convention. The common forms of strain rosette and their numbering convention are shown in Figure 4.12.

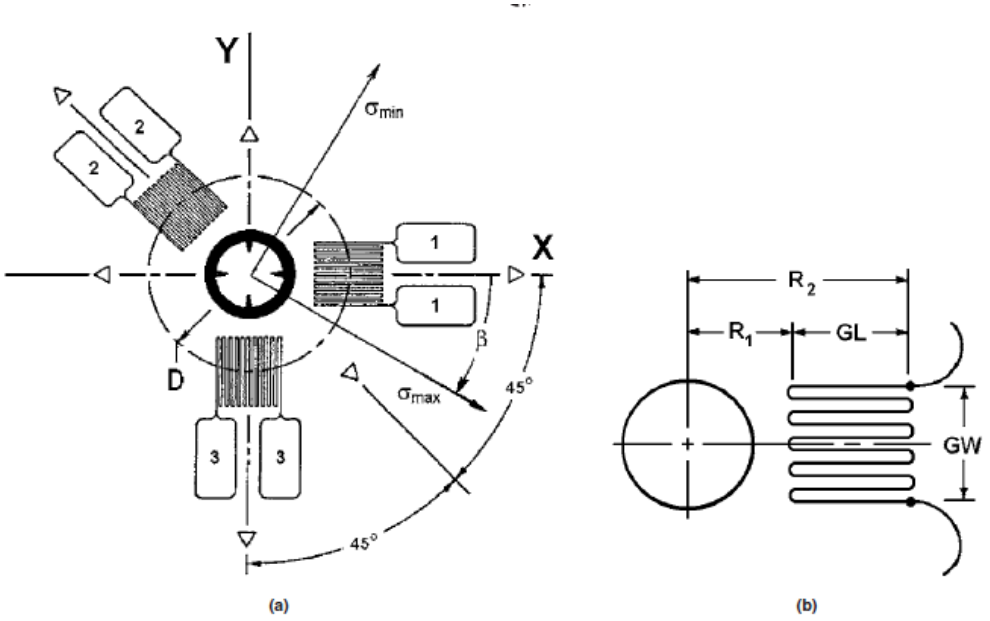

Figure 4.11: Strain gauge geometry (3-gauge rosette) and symbol definitions for a) the rosette layout and b) the strain gauge detail. [88]

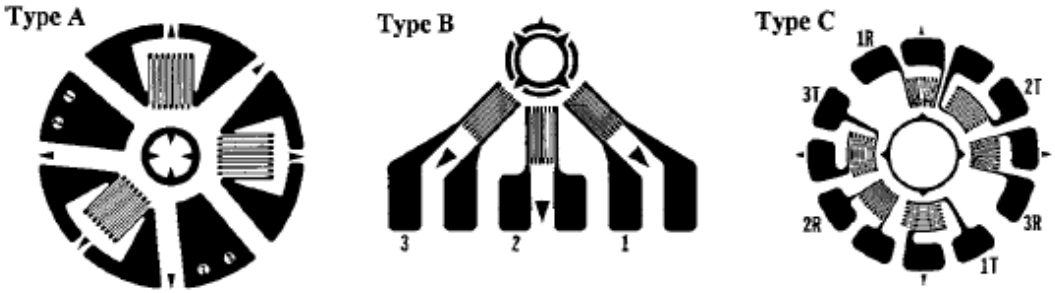

Figure 4.12: Standard strain gauge rosette types used in ASTM E837-08. Type A and Type B rosettes (as used in this study) consist of 3 gauges while the special purpose Type C rosette contains 6 gauges. [88]

The type A rosette was developed by Rendler and Vigness [89] and is used for general purpose applications. The type B rosette is most useful for measurements near an obstacle since the gauges are all positioned on one side of the grid. The type C rosette is a special purpose strain gauge which is used when very high strain sensitivity is required in applications where thermal stability is important.

4.3.4 STRAIN RECORDING INSTRUMENTATION

4.3.4.1 Equipment

The strain recording instrumentation used for the residual stress test is required to have the following capabilities as per ASTM E837-08:

- Instrumentation for recorded strains must have a strain resolution of $\pm 1 \times 10^{-6}$.
- Stability and repeatability of the measurement must be at least $\pm 1 \times 10^{-6}$.
- Lead-wires must be as short as practicable.
- Quarter bridge circuits are used with rosette type A and B.
- External compensating gauge should be used for temperature compensation.

The equipment employed for this purpose consists of the Measurements Group P-3500 strain indicator and the SB-10 Switch & Balance Unit as shown in Figure 4.13. The specifications for these instruments are listed in Table 4.5 below. The P-3500 and SB-10 are connected as shown in the diagram in Figure 4.14. The SB-10 dedicates a channel to each strain gauge on a strain gauge rosette. This system allows quick switching between each gauge when recording the strain data during the analysis.

Table 4.5: Strain instrumentation specifications for the P-3500 Strain Indicator and the SB-10 Switch and Balance Unit.

P-3500 Strain Indicator	
Range	±19,999με at Gauge Factor <6.000. ±6.000 x 19,999με at Gauge Factor >6.000.
Accuracy	±0.5% of reading ±3με for Gauge Factor settings of 1.000 to 9.900. ±0.5% of reading ±20με for Gauge Factor settings of 1.000 to 9.900 when using X10 multiplier.
Resolution	±1με at all Gauge Factor settings.

	±10με when using X10 multiplier.
Gauge Factor	Range 0.500 to 9.900. Accuracy ±0.02% at all settings.
SB-10 Switch & balance unit	
Circuit	10 channels and OPEN position
Quarter and Half bridge balance range	±2,000με with 350Ω half bridge in strain Indicator.
Switching repeatability	Better than 1με.

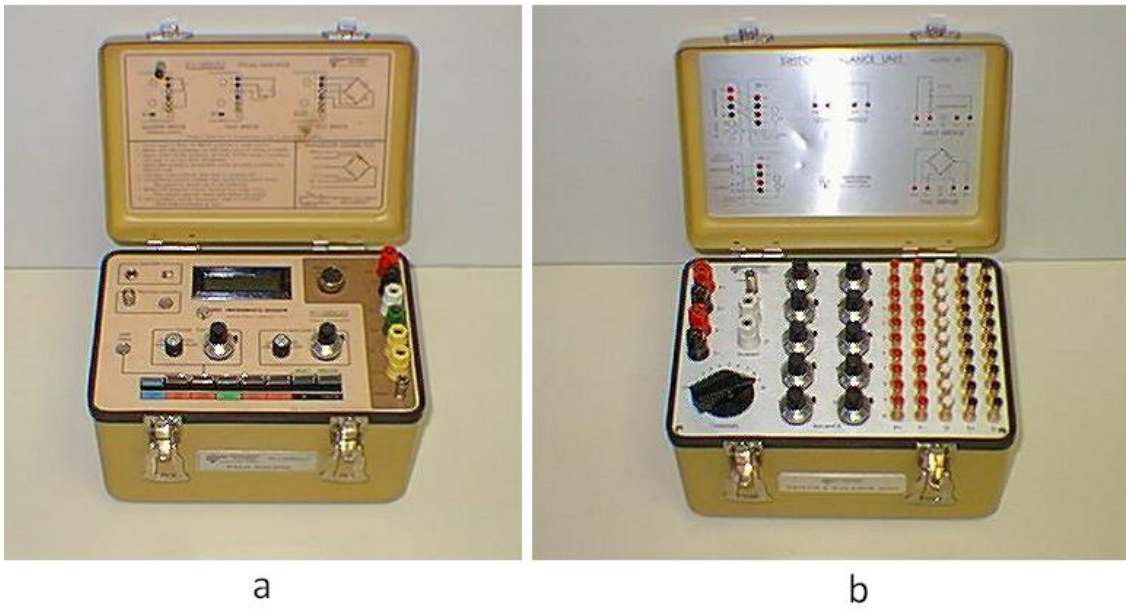

Figure 4.13: The Measurements Group a) P-3500 Strain Indicator and b) SB-10 Switch & Balance unit. [90]

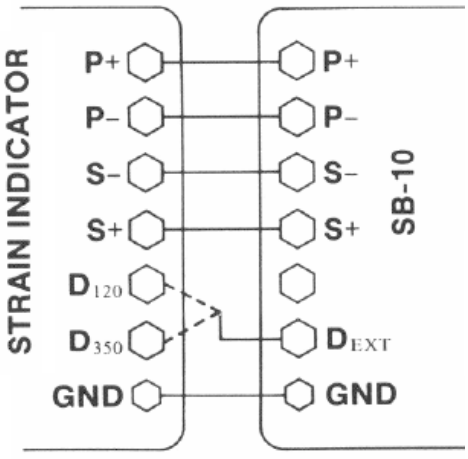

Figure 4.14: Connection diagram for P-3500 Strain Indicator and SB 10 Switch & Balance unit.

4.3.4.2 Strain Gauge Connection

The strain indicator and switch & balance unit use quarter-bridge circuits (see Figure 4.15) with the strain gauges as the active arms of the circuitry. The SB-10 unit dedicates a channel to each active gauge in the strain rosette such that strains can be recorded easily for each depth measurement. The connection diagram in Figure 4.16 illustrates how each strain gauge of the strain rosette is connected to a channel on the SB-10 unit. An external gauge (of the same type as the active gauge) is used instead of the internal 120Ω of the P-3500 since it provides greater accuracy and better temperature compensation.

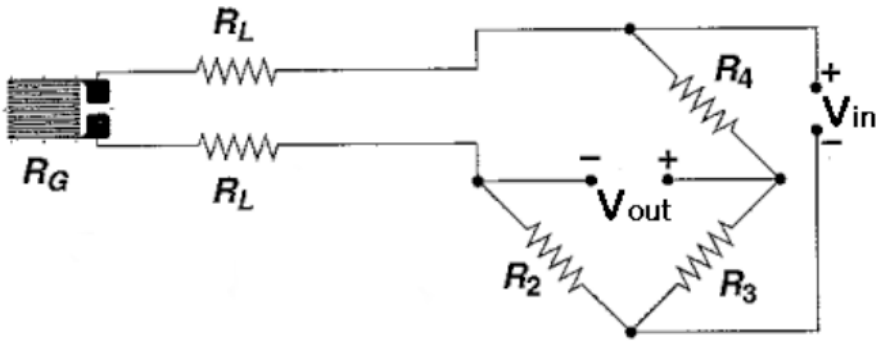

Figure 4.15: Quarter bridge configuration for each strain gauge. [91]

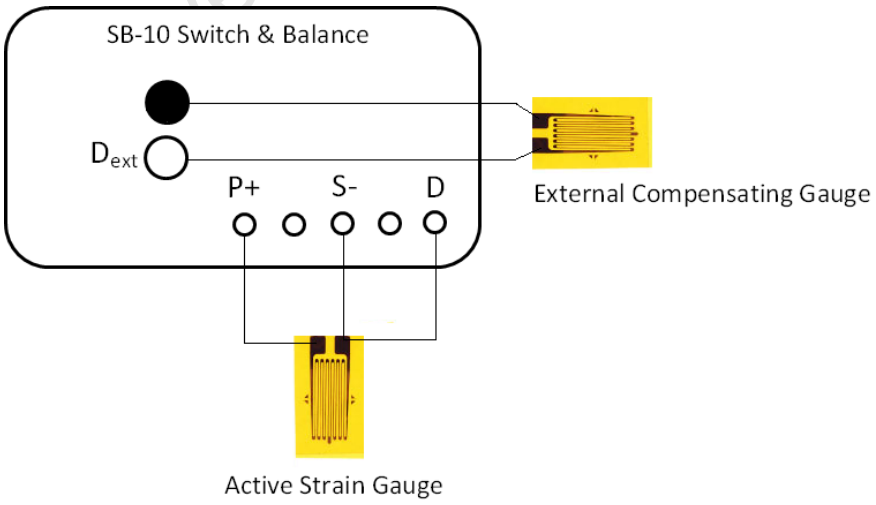

Figure 4.16: Connection diagram for each active strain gauge and the SB-10 unit. Note the use of an external strain gauge of the same type as the active gauge for greater accuracy and temperature compensation.

4.3.4.3 Operating Procedure

The operating procedure for recording the strain registered by the strain gauge rosettes is described below. The schematic in Figure 4.17 shows the controls of the P-3500 strain indicator used in the analysis. The digital readout from this indicator is positive for a compressive strain and negative for a tensile strain.

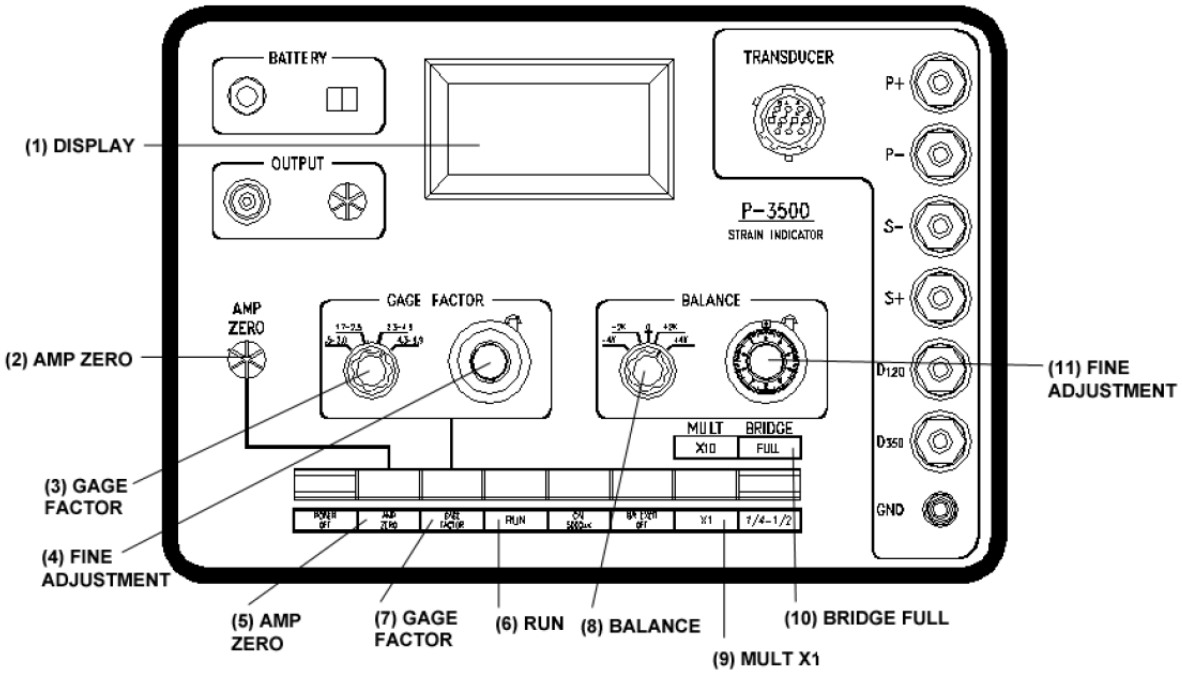

Figure 4.17: P-3500 control panel schematic. [92]

1. Select the AMP ZERO pushbutton and adjust the AMP ZERO adjustment knob until the reading is 0000.
2. Select the GAUGE FACTOR knob and set the gauge factor to that of the strain gauge.
3. Select the RUN pushbutton and select the desired channel on the SB-10 unit.
4. Adjust the BALANCE CONTROL on the SB-10 for each channel such that a reading of 0000 is registered for each gauge.
5. Perform the drilling operation and register the strain for each channel.

4.3.5 HOLE DRILLING SYSTEM

The hole-drilling residual stress technique requires very precise drilling through the geometric centre of the strain gauge. In order to achieve this accuracy, the Micro-Measurements RS-200 optical drilling system with the air turbine drill assembly was used. This section outlines the correct assembly and use of this drilling system. The process begins with the accurate positioning of the rig such that the drill bit will be centred precisely. The microscope assembly is used to accomplish this to an accuracy of within 0.038mm. After the microscope has been positioned satisfactorily, the air drill components are fitted and the hole is drilled. The component assemblies are discussed next.

Microscope Assembly

The RS-200 milling guide is shown below in Figure 4.18 with a) the microscope positioning configuration and, b) the air turbine configuration [9]. In the microscope configuration, the illuminator, microscope and locking collar are fitted to the rig. The rig is positioned using the cross-hair in the microscope. The X-Y adjustment knobs are turned to move the cross-hair in very small increments. It is essential at this stage to level the drilling rig using the vertical height adjustments (with the use of a spirit level). When the cross-hair is accurately positioned on the strain gauge, the drilling configuration is assembled.

Air Turbine Drill Assembly

The microscope assembly is replaced with the drilling assembly when the rig has been positioned. The air turbine drill is used for the favourable results obtained through ultra-high speed drilling. The vernier allows depth drilling with an accuracy of ±0.01mm and a spring assembly ensures no slippage of the drill tube as the drill descends. It is important to note that the disassembly and reassembly of the rig must be accomplished without shifting the milling guide since this will move the drill bit centre from the desired position.

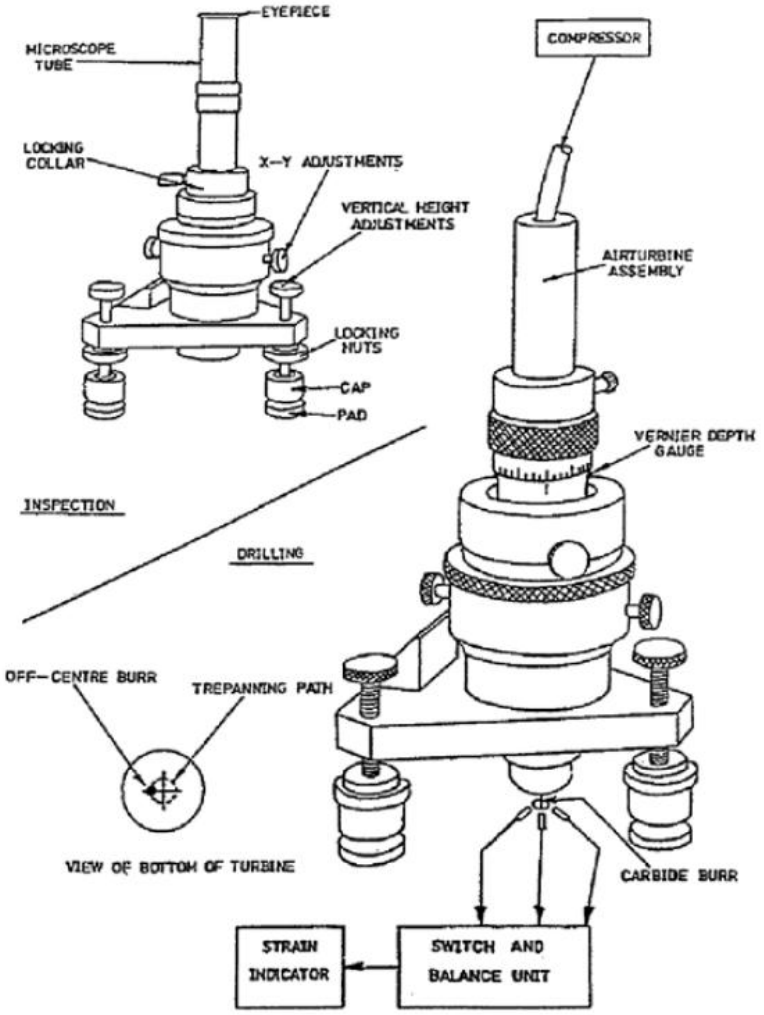

Figure 4.18: Schematic of the hole drilling apparatus used for a) optically centering the device and, b) implementation of the air turbine drill assembly. [93]

4.3.6 DRILL PROCEDURE

The measurement of drilling depth is vital for the accuracy of the recorded strains. When the drill piece has been precisely centred on the strain gauge geometrical centre, the drilling procedure described in this section is used to record the strains. The procedure requires 20 strain recordings at successive depths to complete a residual stress profile for the specimen. These depths are accurately measured via the use of a vernier and the limits for the drilling procedure are shown in Table 4.6 below.

Table 4.6: Recommended workpiece thicknesses, hole diameters and depth steps as per ASTM E837-08.

Rosette Size	D [mm]	Max. thickness of 'thin' workpiece [mm]	Min. thickness of 'thick' workpiece [mm]	Uniform Stresses			Non-Uniform Stresses		
				Min. hole diameter [mm]	Max. hole diameter [mm]	Depth steps [mm]	Min. hole diameter [mm]	Max. hole diameter [mm]	Depth steps [mm]
Type A									
1/16 in. nominal	5.13	2.06	6.17	1.52	2.54	0.25	1.88	2.12	0.05
Type B									
1/16 in. nominal	5.13	2.06	6.17	1.52	2.54	0.25	1.88	2.12	0.05

The procedure listed in this section is for non-uniform residual stress tests with thick workpieces since initial drilling confirmed the non-uniformity of the residual stresses. The procedures for the 'thin' workpiece have been omitted from this report since the specimens received for testing were within the thick workpiece limits.

Thick Workpiece with Non-Uniform Residual Stresses

1. Centre the drill bit using the optical rig and zero-balance the strain indicator readings for each of the strain gauges (see Figure 4.19).
2. Carefully drill through the strain gauge material until the drill bit scratches the specimen surface and note any difference in the strain recordings as the zero/reference point. For simplicity of computation, the strain indicator may be zero-balanced again at this point.
3. Advance the turbine drill 0.05mm as measured from the vernier.
4. Allow the strain readings to settle for 5 seconds if necessary and record the strain for each of the gauges as ε_1, ε_2 and ε_3.
5. Repeat steps 3-4 until the total depth of 1mm is achieved (20 steps).
6. Repeat steps 3-4 with depth increments of 0.2mm until a total depth of 2mm has been attained. Monitor the variance of the readings (as per Prof RB Tait's suggestion).
7. Measure the hole diameter and ensure hole is within sufficient limits as recorded in Table 4.6.

8. Check the hole eccentricity and ensure it does not exceed the tolerance of ±0.038mm.
9. Compute the non-uniform residual stresses from relieved strains.

Figure 4.19: Complete drilling rig setup with the microscope positioning system fitted.

4.3.7 COMPUTATION OF STRESSES

4.3.7.1 ASTM E837-08 Procedure

The strain data collected from the drilling procedure is first analysed to check the 'smoothness' of the data and to observe any outliers or irregular data points. The strains ε_1, ε_2 and ε_3 are plotted against the hole depth. If the data is highly irregular, the hole-drilling test may have to be repeated to ensure the accuracy of the results.

The combination strain vectors are determined from the sets of strain data according to the following equations:

$$p_j = \frac{(\varepsilon_3 + \varepsilon_1)}{2} \quad \textbf{(4-3)}$$

$$q_j = \frac{(\varepsilon_3 - \varepsilon_1)}{2} \quad \textbf{(4-4)}$$

$$t_j = \frac{(\varepsilon_3 + \varepsilon_1 - 2\varepsilon_2)}{2} \quad \textbf{(4-5)}$$

In which the subscript refers to the hole depth step *j*.

The standard deviation vectors are estimated from the combination strains calculated above.

$$p_{std}{}^2 = \sum_{j=1}^{n-3} \frac{\left(p_j - 3p_{j+1} + 3p_{j+2} - p_{j+3}\right)^2}{20(n-3)} \quad \textbf{(4-6)}$$

$$q_{std}{}^2 = \sum_{j=1}^{n-3} \frac{\left(q_j - 3q_{j+1} + 3q_{j+2} - q_{j+3}\right)^2}{20(n-3)} \quad \textbf{(4-7)}$$

$$t_{std}{}^2 = \sum_{j=1}^{n-3} \frac{\left(t_j - 3t_{j+1} + 3t_{j+2} - t_{j+3}\right)^2}{20(n-3)} \quad \textbf{(4-8)}$$

Where *n* is the number of depth increments.

The calibration matrices $\bar{a}_{jk}$ and $\bar{b}_{jk}$which are used in the steps which follow are available in the ASTM E837-08 standard for type A and type B rosettes. These are tabulated according to the drilled hole diameter for the 1/16 in. rosettes.

The Integral Method [94] is used to compute the residual stresses from the sets of strain data as shown in Figure 4.10. This is achieved by solving the matrix equations below.

$$\bar{a}\boldsymbol{P} = \frac{E}{1+v}\boldsymbol{p} \quad \textbf{(4-9)}$$

$$\bar{b}\boldsymbol{Q} = E\boldsymbol{q} \quad \textbf{(4-10)}$$

$$\bar{b}\boldsymbol{T} = E\boldsymbol{t} \quad \textbf{(4-11)}$$

In which the uppercase matrices are defined by:

$$P_k = \frac{(\sigma_y)_k + (\sigma_x)_k}{2} \quad \textbf{(4-12)}$$

$$Q_k = \frac{(\sigma_y)_k - (\sigma_x)_k}{2} \quad \textbf{(4-13)}$$

$$T_k = \frac{(\tau_{xy})_k}{2} \quad \textbf{(4-14)}$$

The equations described above have been found to be ill-conditioned with high numbers of drilling steps which results in the amplification of small strain errors. A regularisation method known as the Tikhonov regularization has been implemented to address this instability. In order to perform this regularisation, a tri-diagonal "second derivative" matrix C is introduced as follows.

$$c = \begin{bmatrix} 0 & 0 & 0 & 0 & 0 \\ -1 & 2 & -1 & 0 & 0 \\ 0 & -1 & 2 & -1 & 0 \\ 0 & 0 & -1 & 2 & -1 \\ 0 & 0 & 0 & 0 & 0 \end{bmatrix} \quad \textbf{(4-15)}$$

In which the number of rows and columns is the number of hole depth steps. The first and last rows are zeros and all other rows have [-1 2 -1] centred along the diagonal. This matrix is then used to augment that of the equations above as follows:

$$(\bar{\boldsymbol{a}}^{\boldsymbol{T}}\bar{\boldsymbol{a}} + \alpha_P \boldsymbol{c}^{\boldsymbol{T}}\boldsymbol{c})\boldsymbol{P} = \frac{E}{1+v}\bar{\boldsymbol{a}}^{\boldsymbol{T}}\boldsymbol{p} \quad \textbf{(4-16)}$$

$$(\bar{\boldsymbol{a}}^{\boldsymbol{T}}\bar{\boldsymbol{a}} + \alpha_Q \boldsymbol{c}^{\boldsymbol{T}}\boldsymbol{c})\boldsymbol{Q} = E\bar{\boldsymbol{b}}^{\boldsymbol{T}}\boldsymbol{q} \quad \textbf{(4-17)}$$

$$(\bar{\boldsymbol{a}}^{\boldsymbol{T}}\bar{\boldsymbol{a}} + \alpha_T \boldsymbol{c}^{\boldsymbol{T}}\boldsymbol{c})\boldsymbol{T} = E\bar{\boldsymbol{b}}^{\boldsymbol{T}}\boldsymbol{t} \quad \textbf{(4-18)}$$

Where the factors α_P, α_Q and α_T control the amount of regularisation used in the process. Initial values for these factors are between 10^{-4} and 10^{-6}. The values of these factors are improved through an iterative process which is described next. The regularisation results in calculated stresses **P**, **Q** and **T** which do not correspond exactly with the measured strains **p**, **q** and **t**. The degree to which the strains differ is measured by misfit vectors determined as shown below.

$$\boldsymbol{p_{misfit}} = \boldsymbol{p} - \frac{1+v}{E}\bar{\boldsymbol{a}}\boldsymbol{P} \quad \textbf{(4-19)}$$

$$\boldsymbol{q_{misfit}} = \boldsymbol{q} - \frac{1}{E}\bar{\boldsymbol{b}}\boldsymbol{Q} \quad \textbf{(4-20)}$$

$$\boldsymbol{t_{misfit}} = \boldsymbol{t} - \frac{1}{E}\bar{\boldsymbol{b}}\boldsymbol{T} \quad \textbf{(4-21)}$$

The mean squares of the misfit vectors are calculated using the following equations.

$$p_{rms}{}^2 = \frac{1}{n}\sum_{j=1}^{n}(p_{misfit})_j^2 \quad \textbf{(4-22)}$$

$$q_{rms}{}^2 = \frac{1}{n}\sum_{j=1}^{n}(q_{misfit})_j^2 \quad \textbf{(4-23)}$$

$$t_{rms}{}^2 = \frac{1}{n}\sum_{j=1}^{n}(t_{misfit})_j^2 \quad \textbf{(4-24)}$$

If the mean squares are within 5% of the standard deviations $p_{std}{}^2$, $q_{std}{}^2$ and $t_{std}{}^2$ as calculated earlier, then the values of the regularisation constants α_P, α_Q and α_T are acceptable and the values of **P**, **Q** and **T** may be used . If however these values differ by more than 5%, an iterative

procedure is used to improve the guessed values of the regularisation constants using equations (4-25), (4-26) and (4-27) below.

$$(\alpha_p)_{new} = \frac{{p_{std}}^2}{{p_{rms}}^2}(\alpha_p)_{old} \quad \textbf{(4-25)}$$

$$(\alpha_Q)_{new} = \frac{{q_{std}}^2}{{q_{rms}}^2}(\alpha_Q)_{old} \quad \textbf{(4-26)}$$

$$(\alpha_T)_{new} = \frac{{t_{std}}^2}{{t_{rms}}^2}(\alpha_T)_{old} \quad \textbf{(4-27)}$$

These values are then substituted into equations (4-16), (4-17) and (4-18) from which new misfit vectors and mean squares are calculated in an iterative fashion. This procedure is repeated until the mean squares are within 5% of the standard deviations. When this condition is met, the final values in **P**, **Q** an **T** have sufficient accuracy and regularisation to be used.

The Cartesian stresses can be calculated when the iterative procedure is completed with the following equations.

$$(\sigma_{max})_k, (\sigma_{min})_k = P_k \pm \sqrt{{Q_k}^2 + {T_k}^2} \quad \textbf{(4-28)}$$

$$\beta_k = \frac{1}{2} arctan\left(\frac{-T_k}{-Q_k}\right) \quad \textbf{(4-29)}$$

The angle β indicates the direction of the maximum principal stress σ_{max}. A positive value for β is measured clockwise from gauge 1 on the strain rosette and vice-versa, a negative value is measured counter-clockwise from gauge 1.

4.3.7.2 Curvature Effects

The cylindrical specimens used in this study have been treated using formulations developed for flat plates. In literature it has been reported that residual stress FEM simulations of 3D cylinders experience errors of between 4-5% in the calibration coefficients $\bar{a}_{jk}$ and $\bar{b}_{jk}$ [95]. This study is considered to be comparative in nature and hence the curvature effect would not significantly affect the outcome of the analysis. Several other hole-drilling studies have also been completed on curved specimens without any reported detrimental effects [96].

4.3.8 CORRECTIVE PROCEDURE FOR HIGH RESIDUAL STRESSES

ASTM E837-08 is limited in its ability to deal with high residual stresses since the plasticity effect becomes significant for residual stresses exceeding 60% of the material yield strength. This effect results in an overestimation of the residual stresses in the specimen and several studies have been conducted into corrective procedures for improved estimations of high residual stresses via the hole drilling technique. Moharami and Sattari-Far [97] have developed a procedure for evaluating very high residual stresses in welded structures using the blind hole drilling technique. This method is particularly relevant for this study due to the similarities between welding and Direct Metal Laser Sintering with regard to thermal gradients. Moharami and Sattari-Far's method may be used for stresses up to and exceeding the yield strength of the material [97]. This technique was employed for the results which exceeded the ASTM E837-08 criterion of 60% of the yield stress. This section introduces Moharami and Sattari-Far's corrective procedure and its usage in this study.

Moharami and Sattari-Far found that the plastic error observed when evaluating residual stresses through the hole drilling technique could be quantified using equation (4-30) below.

$$Plastic\ error\ (\%) = m\left(\frac{\sigma_{maxASTM}}{\sigma_y} - 0.5\right)^2 \qquad \textbf{(4-30)}$$

Where

$$m = p\left(\frac{\sigma_{minASTM}}{\sigma_{maxASTM}}\right)^4 + q \qquad \text{(4-31)}$$

The value of *m* and its coefficients *p* and *q* are heavily dependent on the material properties, most notably the Elastic Tangent Modulus E_p as shown in Figure 4.20. In this study, the value of E_P was taken to be 1.25 GPa and E = 120 GPa for standard Ti-6Al-4V.

Using these parameters, the values of the coefficients *p* and *q* could be obtained as shown below in equations (4-32) and (4-33).

$$p = 24\left(2 - \frac{E_p}{E} - \left(\frac{E_p}{E}\right)^2\right) \qquad \text{(4-32)}$$

$$q = 35\left(1 - \frac{E_p}{E}\right) \qquad \text{(4-33)}$$

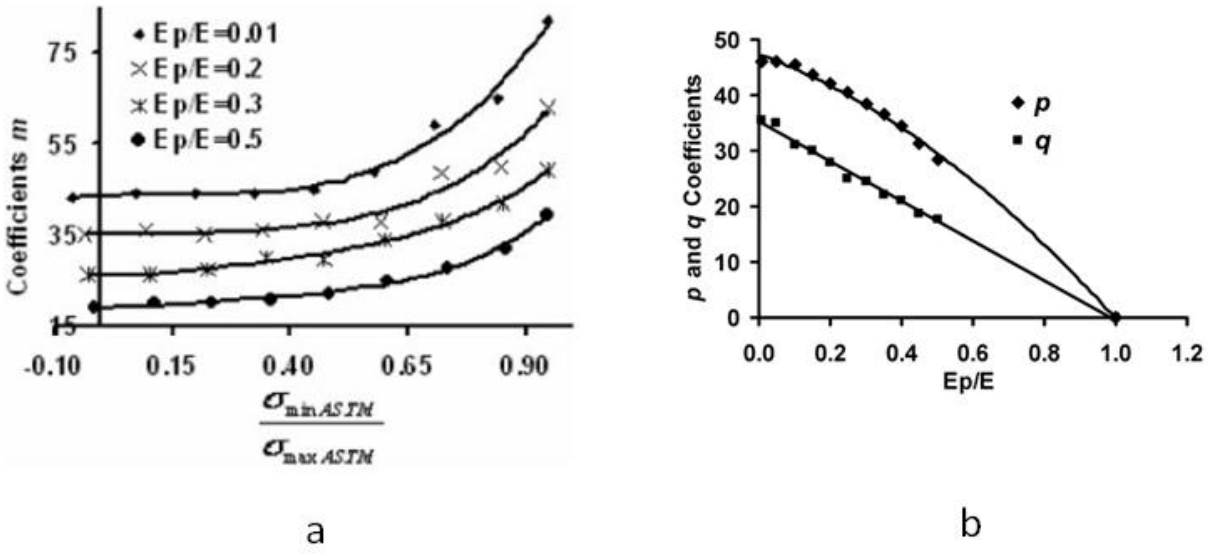

Figure 4.20: Variation in a) the coefficient *m* with differing stress ratios and material properties and, b) coefficients p and q with material properties. [97]

The corrective equation using the coefficients described above is given by equation (4-34).

$$\sigma_{maxCorr} = \frac{100\sigma_{maxASTM}}{m\left(\frac{\sigma_{maxASTM}}{\sigma_{yield}} - 0.5\right)^2 + 100} \quad \textbf{(4-34)}$$

Where σ_{yield} is the yield strength of the material.

The residual stress analysis presented in the preceding sections formed a significant part of this study into the structural integrity of SLM components. The computation of the residual stresses from the strain data described in this section was performed using the MATLAB script given in Appendix C. The next section focusses on the heat treatment specifications and procedures applied to the SLM Ti-6Al-4V specimens.

4.4 HEAT TREATMENT

The previous chapter described in detail the processes and mechanisms for each type of heat treatment. In this section, the temperatures, exposure times and furnace types are specified for each of the four heat treatments. The specimens undergoing heat treatments requiring an air cooling stage (beta and duplex anneals) were coated in ceramic slurry to reduce the oxidation during the process.

4.4.1 STRESS RELIEF TREATMENT

The stress relief treatment was used with the intention of removing 100% of the residual stresses contained within the specimens. This treatment used a vacuum furnace as shown in Figure 4.21. The heat treatment steps are listed below.

1. The cylindrical specimens A1 & D1 were sampled for microstructure prior to heat treatment by removing disk specimens as described in the previous section.
2. Specimens were heated within the vacuum furnace to a temperature of 650°C and maintained at this temperature for 8 hours according to the profile shown below in Figure 4.22.
3. Specimens were furnace cooled (to prevent oxidation) down to room temperature (25°C).

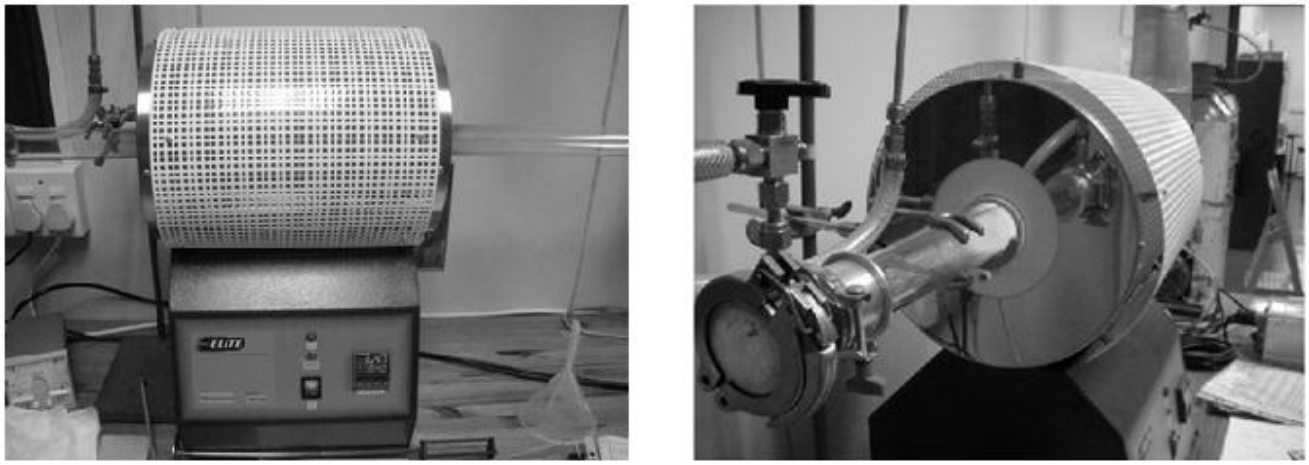

Figure 4.21: Vacuum furnace used for Stress Relief and Recrystallization Annealing treatments.

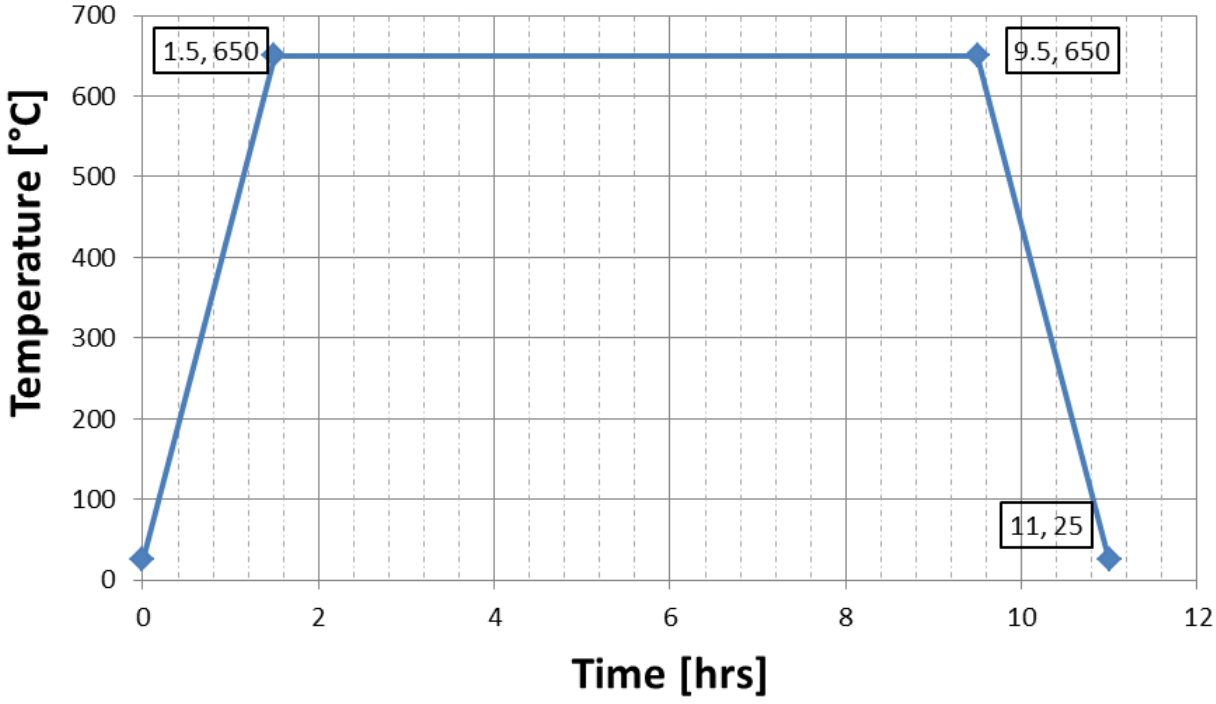

Figure 4.22: Stress Relief heat treatment process schematic

4.4.2 RECRYSTALLIZATION ANNEALING

A recrystallization annealing process was performed on the specimens in a vacuum furnace as with the simple stress relief treatment. The heat treatment steps are listed below.

1. The cylindrical specimens A2 & D2 were sampled for microstructure prior to heat treatment by removing disk specimens as described in the previous section.
2. Specimens were heated within the vacuum furnace to a temperature of 950°C and maintained at this temperature for 1 hour according to the profile shown below in Figure 4.23.
3. Specimens were furnace cooled (to prevent oxidation) down to room temperature (25°C) at 5°C/min.

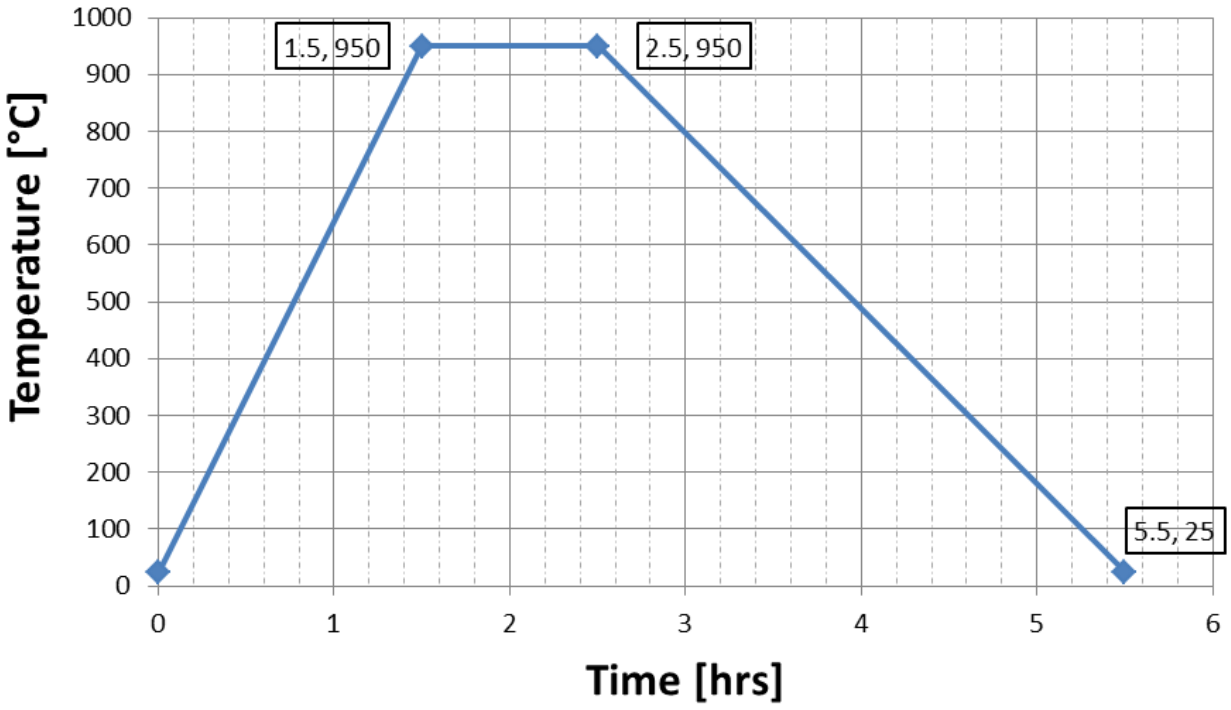

Figure 4.23: Recrystallization annealing process schematic.

4.4.3 DUPLEX ANNEALING

The duplex annealing treatment was performed in a box furnace since the samples needed to be air cooled between the anneal stages. To prevent significant oxidation of the samples, ceramic slurry was used to coat the samples before being placed in the box furnace as shown below in Figure 4.24.

The heat treatment steps are listed below.

1. The cylindrical specimens A3 & D3 were sampled for microstructure prior to heat treatment by removing disk specimens as described in the previous section.
2. Specimens were coated lightly with the ceramic slurry ensuring that no bare metal is exposed. The coating was then cured using a hairdryer.
3. Specimens were placed within the box furnace at a temperature of 950°C for 1 hour and then removed from the furnace to be air cooled back to room temperature.
4. Specimens were placed back into the box furnace and heated to 700°C for 2 hours after which the specimens were removed and air cooled again back to room temperature as shown in the process schematic in Figure 4.25.

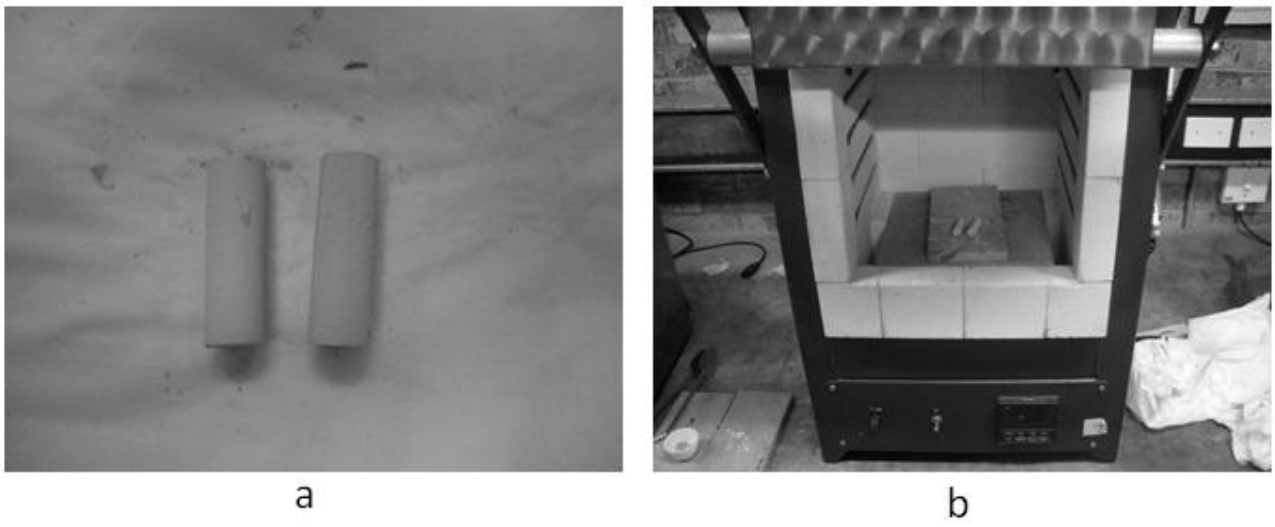

Figure 4.24: a) Ceramic slurry coating to reduce oxidation in the samples and, b) Box furnace with two ceramic coated Ti-6Al-4V samples.

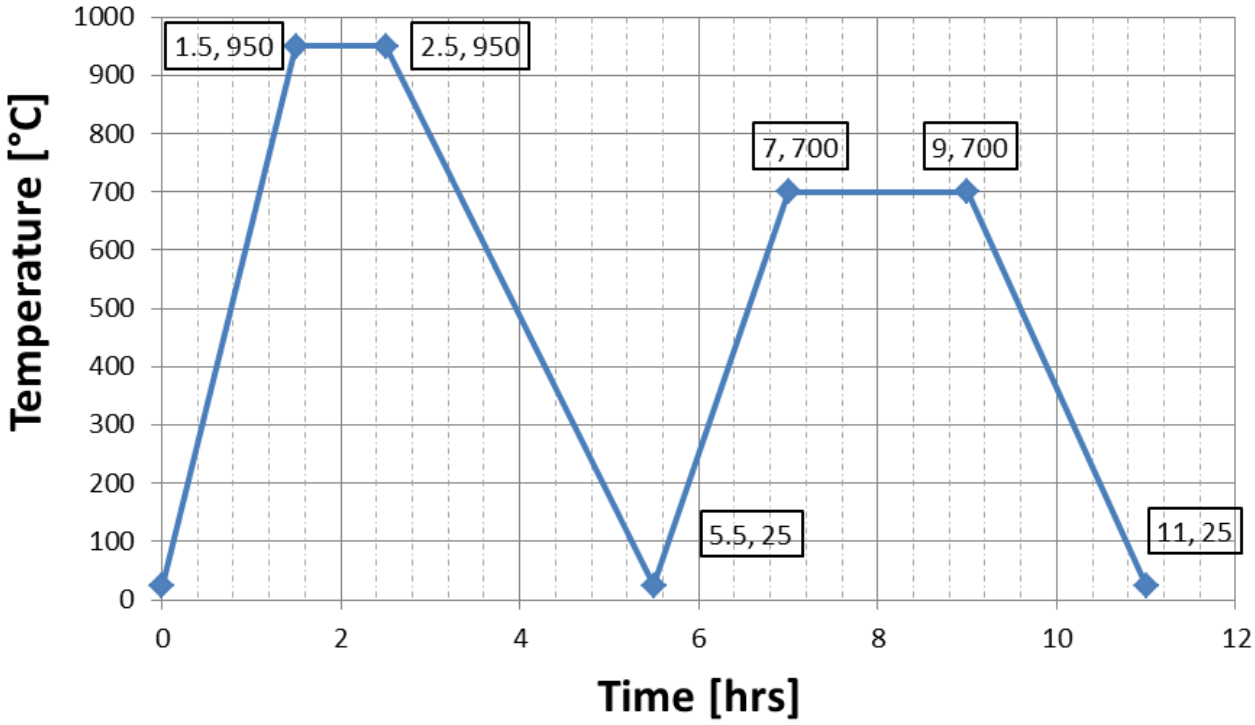

Figure 4.25: Duplex annealing process schematic.

4.4.4 BETA ANNEALING

The beta annealing process was similar to the duplex anneal in that the primary anneal is followed by a stabilisation treatment as shown in Figure 4.26. The beta anneal is performed at a temperature above the β transus and requires air cooling to prevent excessive grain growth. The heat treatment steps are listed below.

1. The cylindrical specimens A4 & D4 were sampled for microstructure prior to heat treatment by removing disk specimens as described in the previous section.
2. Specimens were coated lightly with the ceramic slurry ensuring that no bare metal is exposed. The coating was then dried using a hairdryer.
3. Specimens were placed within the box furnace at a temperature of 1030°C for 1 hour and then removed from the furnace to be air cooled back to room temperature.

4. Specimens were placed back into the box furnace and heated to 650°C for 2 hours after which the specimens were removed and air cooled again back to room temperature as shown in the process schematic in Figure 4.26.

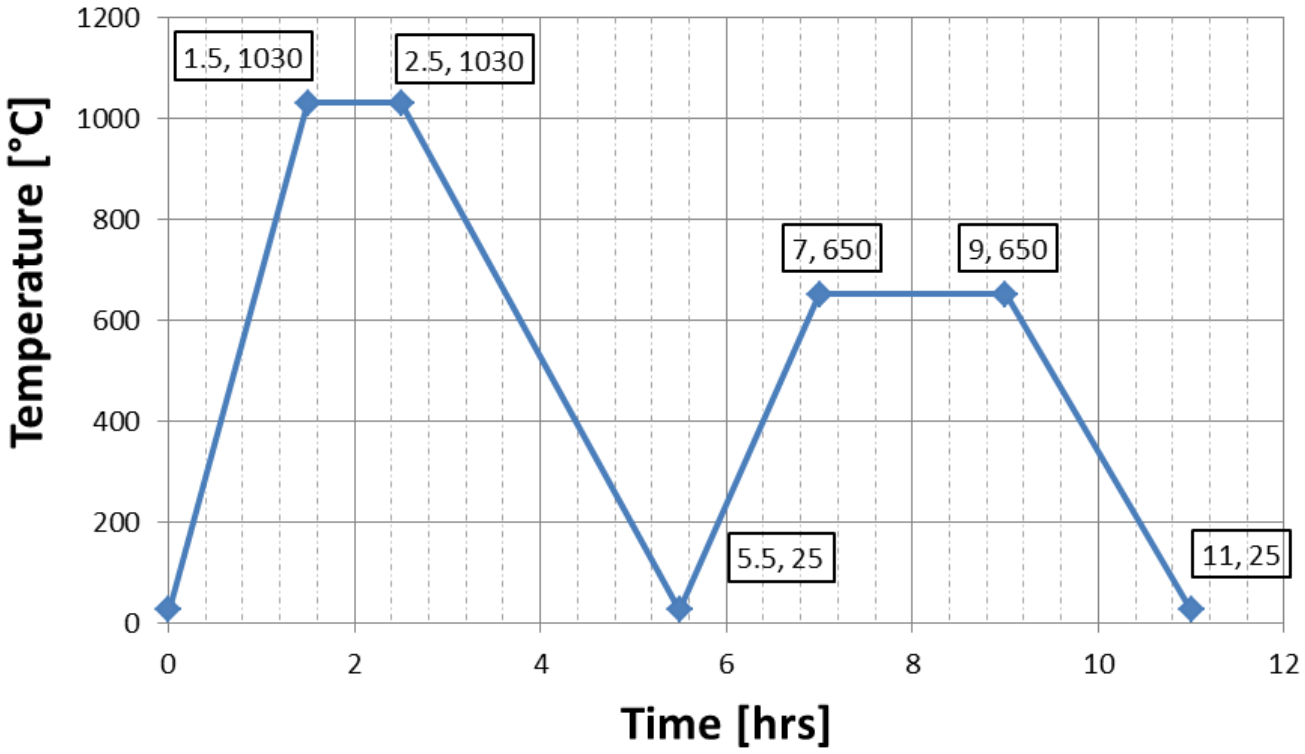

Figure 4.26: Beta annealing process schematic.

The experimental methods reviewed thus far are specific to the requirements of this study. The physical property tests including the density and hardness evaluations are presented next. These experiments are considered to be more universal and are performed in order to further the understanding of this material.

4.5 DENSITY TESTING

4.5.1 WATER DISPLACEMENT TEST

The initial density tests were performed according to ASTM B311-08 [98]. This method determines the density of PM (Powder Metallurgy) materials containing less than 2% porosity and is based on the Archimedes principle of water displacement. This test required an electronic scale with an accuracy of 0.01% of the specimen mass. The procedure is listed briefly below.

1. Weigh test specimen in air, this value is labelled mass A.
2. Fix support stand and test specimen support to a beaker filled with distilled water and place apparatus on the scale as shown in Figure 4.27a. This mass is labelled mass C.
3. Place specimen within test specimen support as shown in Figure 4.27b and record the weight as mass B.
4. Measure the water temperature and record the density as provided in the tables in ASTM B311-08.
5. The specimen density $\rho_{specimen}$ is calculated according to the following expression in equation (4-35).

$$\rho_{specimen} = \frac{A}{\rho_{water}(A - B + C)} \quad \textbf{(4-35)}$$

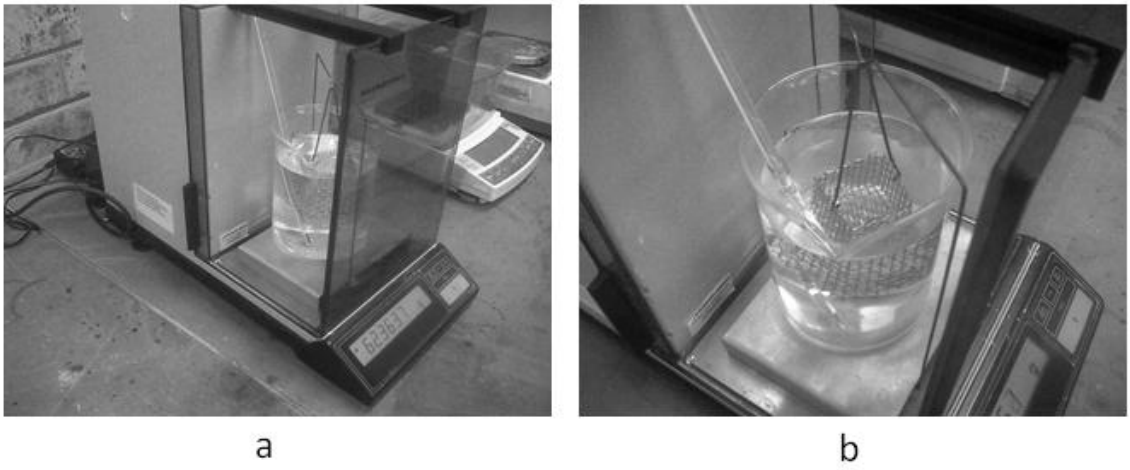

Figure 4.27: a) Density testing rig on scale and, b) specimen support immersed in distilled water.

4.5.2 OPTICAL DENSITY TEST

The ASTM B311 density tests were confirmed using an optical microscopy technique in which digital photographs of polished sections of the specimens were analysed in terms of their pixel spectrum. MATLAB script was used to convert the image to pure grayscale (Figure 4.28a) and analyse the pixel distribution present in a micrograph (Figure 4.28b). The pixel intensity ranges from values between 0 (darkest) and 255 (lightest) from which an intensity threshold could be determined below which all pixels were considered to be void/porous material. The threshold was determined by evaluating a range of threshold values and examining the change in calculated density (Figure 4.28c). Threshold values prior to the first noticeable decline in density were checked according to the intensity scale (Figure 4.28b) and an optimum threshold value was chosen. The MATLAB script used for this process is presented in Appendix C.3.

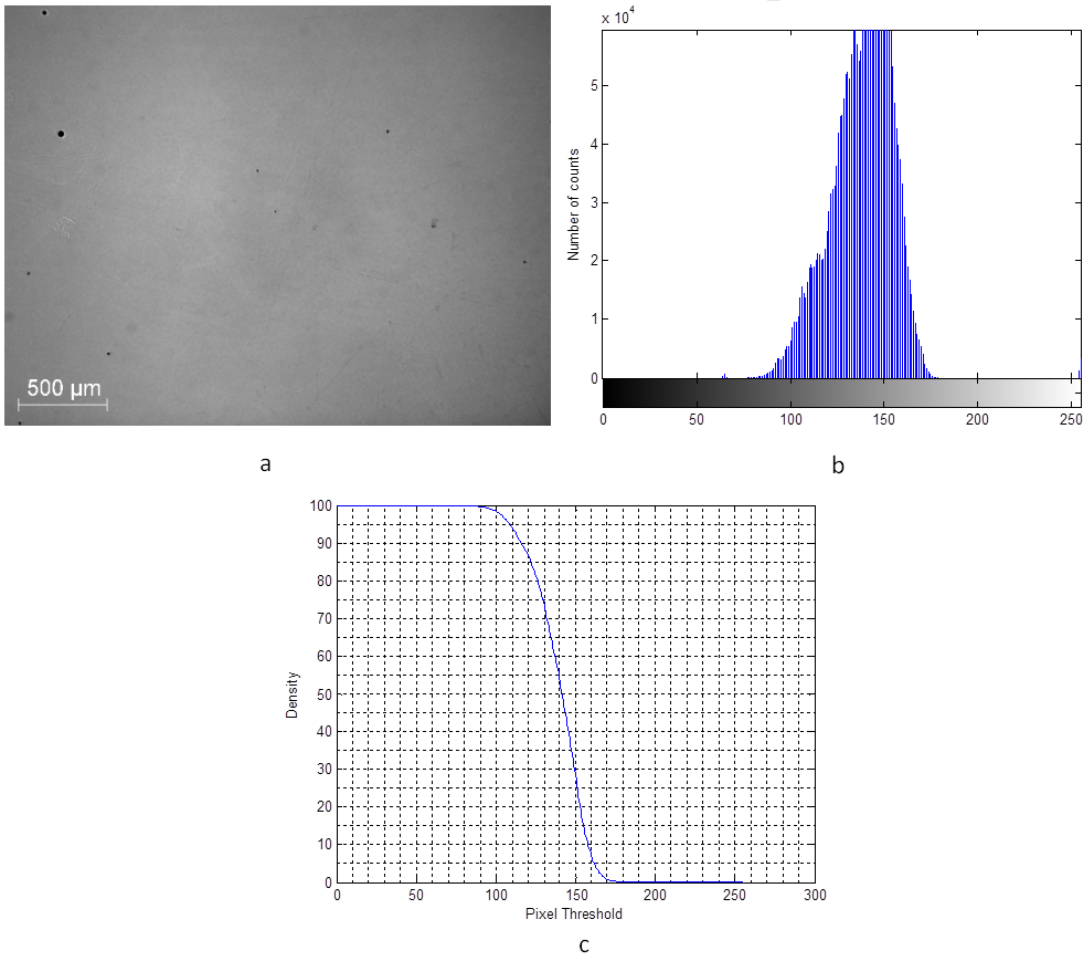

Figure 4.28: Optical micrograph density testing procedure, a) a micrograph of a polished specimen, b) Histogram representing pixel values and number of instances, c) Density variation with pixel threshold.

4.6 HARDNESS TESTING

In addition to the effects on residual stress and the microstructure, heat treatment is also known to affect material hardness. Hardness tests were performed on all heat treated specimens using the Zwick Roell ZHV hardness tester shown in Figure 4.29. The procedure is outlined below:

1. Cut 2mm thick disk samples from the heat treated specimens.
2. Mount the disk specimens using the Struers Hot Mounting system.
3. Surface grind the specimen using SiC 800 grit sandpaper in the automatic polisher to ensure a flat surface prior to the test.
4. Position the diamond indenter using the microscope alignment guide on the Zwick Roell ZHV.
5. Set the force to 30kg for a duration of 10 seconds.
6. Run the test.
7. Align the marker lines to the four corners on the perimeter of the indent and record the hardness.

Figure 4.29: Zwick Roell ZHV hardness tester in the UCT Materials Engineering Laboratory

4.7 SUMMARY

This chapter has described the techniques used in this study to evaluate the residual stress, heat treatment, microstructure and physical properties of SLM Ti-6Al-4V. The residual stress testing method of choice in this investigation is the hole-drilling strain gauge method as standardised in ASTM E837-08. The methods of strain gauge application and drilling need to be carefully followed for precise results. The limitations of ASTM E837-08 with regard to non-uniform residual stress fields have been discussed and the procedure for evaluating high residual stresses by Sattari-Far [97] has been introduced. The methods of microscopy preparation and mounting have been reviewed such that any changes on a microstructural level can be assessed. The heat treatments used in this study have been described fully in terms of their exposure temperature, time and furnace type. The physical property testing in terms of density and hardness have been explained briefly in the final sections of this chapter. These procedures aim to provide insight into the behaviour of SLM Ti-6Al-4V and hopefully provide a method of treatment for removing residual stresses. Chapter 2 established the need to quantify and assess the levels of porosity and micro-flaws within SLM Ti-6Al-4V which is described in the next chapter that follows on the design of a miniaturised tensile rig for micro-flaw exposure.

CHAPTER 5 – MICRO-FLAW EXPOSURE

5.1 INTRODUCTION

The previous chapters have elaborated on the presence of porosity and micro-flaws within material produced by early laser-based manufacturing systems. The levels of porosity have gradually decreased as the powder laying techniques have improved and laser power has increased. The presence of micro-flaws near the surface and within close proximity of each other is a concern in terms of possible flaw interaction. Micro-flaws which are initially small in length can easily grow significantly larger if they interact with nearby flaws. The surface roughness of components built by laser-based systems could also interact with micro-flaws slightly below the surface which could quite easily develop into a large surface crack. These concerns have warranted an investigation into the behaviour of these flaws under a tensile load. This load will be particularly damaging to sharp-edges pores and voids which could develop cracks and intersect with other flaws. The application of a tensile load could also reveal flaws or micro-cracks hidden by plastic deformation during manufacture. This chapter describes the design and operation of a miniaturised tensile rig to introduce high tensile loading to specimens while being observed through an optical microscope. A relatively new method known as Digital Image Correlation (DIC) is introduced which can evaluate the pixel movement within successive micrographs to determine any flaw interaction.

5.2 DIGITAL IMAGE CORRELATION

DIC is a recent technique for analysing and measuring the deformation on the surface of a material. This non-contact technique compares digital photographs of a material at shifting stages of deformation [99]. The photograph is broken down into blocks of pixels which are tracked by the DIC software to give full deformation vector fields as shown in Figure 5.1. DIC can be performed in both 2D and 3D cases with the latter requiring multiple cameras to obtain a topographical mapping. Since DIC is a full-field optical technique, it requires contrast on the

surface of the material to enable the software to identify the movement of individual pixels [100]. Although this contrast is typically present in the natural state of most materials, etching is required for microscopy work to attain the highest accuracy.

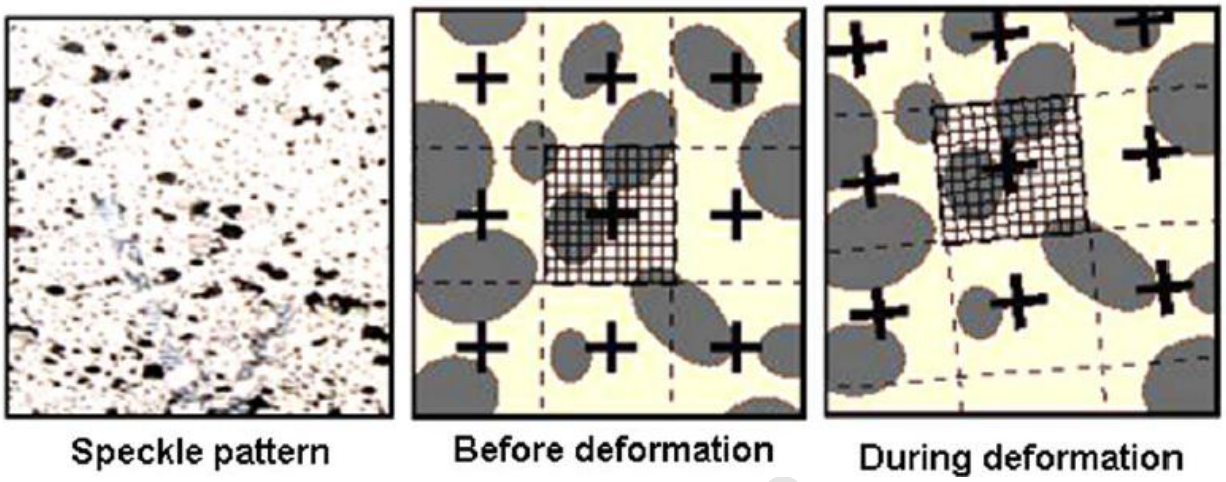

Figure 5.1: Digital Image Correlation tracks the deformation pattern observed in the speckle pattern. The pixel block movement is used in a grid-like fashion to determine the macro-strain. [101]

The deformation observed with the DIC cameras is most often used to measure the strain in a material but can also be used for more complex tasks such as measuring crack tip intensity and crack opening displacement [102]. The effectiveness of crack detection through DIC techniques is clearly visible in Figure 5.2 below. The single crack visible with the naked eye in Figure 5.2a is not the only propagating crack as is evident in Figure 5.2b. Commercial DIC packages are capable of substantial accuracies with sub-pixel resolution from which deformation can be measured to one part per million [99]. These packages are multi-purpose in terms of the types of images which can be correlated. Typical image sources include standard digital cameras, electron microscopes and high speed video. As stated above, DIC is frequently used for strain measurement and crack propagation, but it can also be used in thermal analyses such as electronic component distortion during operation. It has also been used to map dynamic vibrational movement and evaluate the surface strains in bone [101].

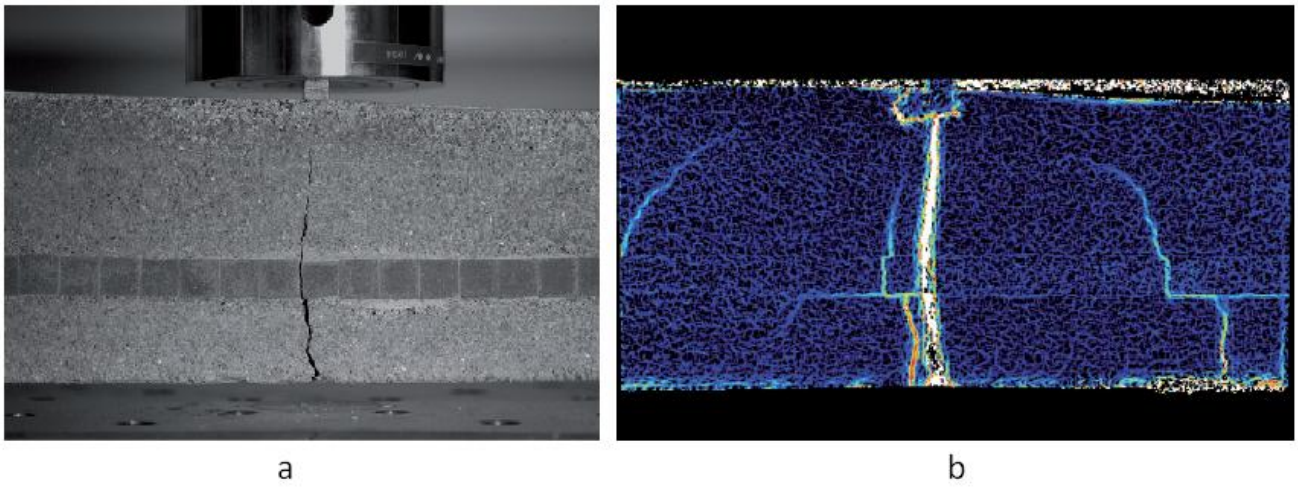

Figure 5.2: a) Crack propagating through concrete, b) Digital Image Correlation used to determine underlying cracks not visible to the naked eye. [99]

This technique was used to analyse the micrographs of SLM Ti-6Al-4V taken by the micro-flaw exposure rig to determine whether any underlying micro-cracking, invisible to the naked eye, could be detected.

5.3 MICRO-FLAW EXPOSURE RIG DESIGN

This section describes the design of the micro-flaw exposure rig for use with the SLM Ti-6Al-4V tensile specimens. The presence of micro-flaws and voids revealed from preliminary microscopy work on the material warranted further investigation into the behaviour of these micro-flaws under a tensile load. This was extended to examine the behaviour of this material up to the ultimate tensile strength.

5.3.1 DESIGN REQUIREMENTS

The objectives and requirements of the rig were specified before the conceptual design phase began. These requirements are listed below and deliberated in the sections which follow.

i. Tensile force delivery
ii. Force measurement

iii. Displacement Measurement
iv. Mounting system
v. Micrograph capture

Tensile force delivery

The apparatus used to apply the tensile force to the specimens is required to transmit a force in increments up to the ultimate tensile strength (1200 MPa) of the material. This force must be applied in a manner such that no bending or shear forces are introduced to the gauge section. Any torsional effects will have a severe impact on the accuracy of the system.

Force measurement

The measurement of the force transmitted through the device must be sufficiently accurate such that the tensile stress within the specimen is recorded to within ± 5 MPa. This measurement system must be capable of registering and storing the force values automatically.

Displacement Measurement

The apparatus should provide a means of measuring the approximate elongation of the specimen such that a qualitative assessment of the strain difference between specimens can be made. This measurement should be captured in a similar fashion to the applied force such that adequate post-processing computation can be applied.

Mounting system

The apparatus is to be fitted to a fixed upright microscope test bed while maintaining the force acting on the specimen. This mounting apparatus should hold the data acquisition system and any other auxiliary componentry without requiring the removal of any wiring between the loading and image capturing stages. Sufficient clearances are required such that the micrographs may be recorded without difficulty and/or damage to the microscope. The system should be sufficiently easy to fit to the test bed without moving the microscope objective lens or the test bed.

Micrograph capture

The specimen is to be positioned in the apparatus such that a micrograph may be taken through the microscope lens. The specimen position must be held constant such that no exterior movement hampers the accuracy of the system. Sufficient clearances are required for the objective lens to focus on the specimen gauge section.

5.3.2 PROOF RING FORCE EVALUATION

The force transmission into the tensile specimens required in this micro-flaw analysis can be achieved very efficiently through the use of a proof ring type apparatus. A proof ring is typically used to measure the force transmitted into a structure and hence functions as a load cell. Load cells of this type are sometimes used in commercial tensile, compressive and fatigue testing machines. These load sensors are highly accurate and use strain gauge combinations to register the force transmission. The foil-type strain gauges are arranged in a full bridge circuit, i.e. strain gauge pairs are placed on either side of the ring such that one gauge is in tension while the other gauge is in compression as shown in Figure 5.3.

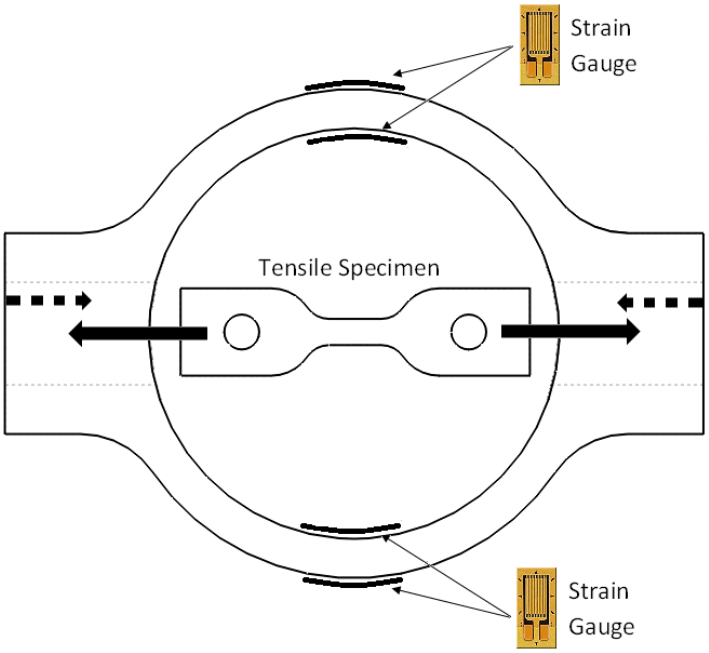

Figure 5.3: Proof ring schematic illustrating the position of the strain gauges, the direction of the force on the ring (dashed arrow) and the force on the tensile specimen (solid arrow).

5.3.3 PROOF RING SENSITIVITY

The sensitivity of the load cell is dependent on the amount of strain registered on the ring surface. If the ring thickness is too great, insufficient strain will occur on the surface and the accuracy of the system will be hampered. On the other hand, if the ring thickness is too thin, the ring itself may yield during the first test and subsequent tests will be rendered imprecise due to the plastic deformation of the ring. The optimal accuracy would be obtained when the force required to break the specimen produces a maximum stress in the ring slightly below the yield strength. This is however not practical in the event that the specimen breaks at a slightly higher stress (which is possible since the behaviour of SLM Ti-6Al-4V has not yet been fully established). It was thus decided to set the sensitivity factor such that the maximum stress attained in the ring was only 80% of the yield strength as shown in Figure 5.4. This criterion would give a satisfactory sensitivity of approximately 1.3 N for every 1 με registered by the strain gauges.

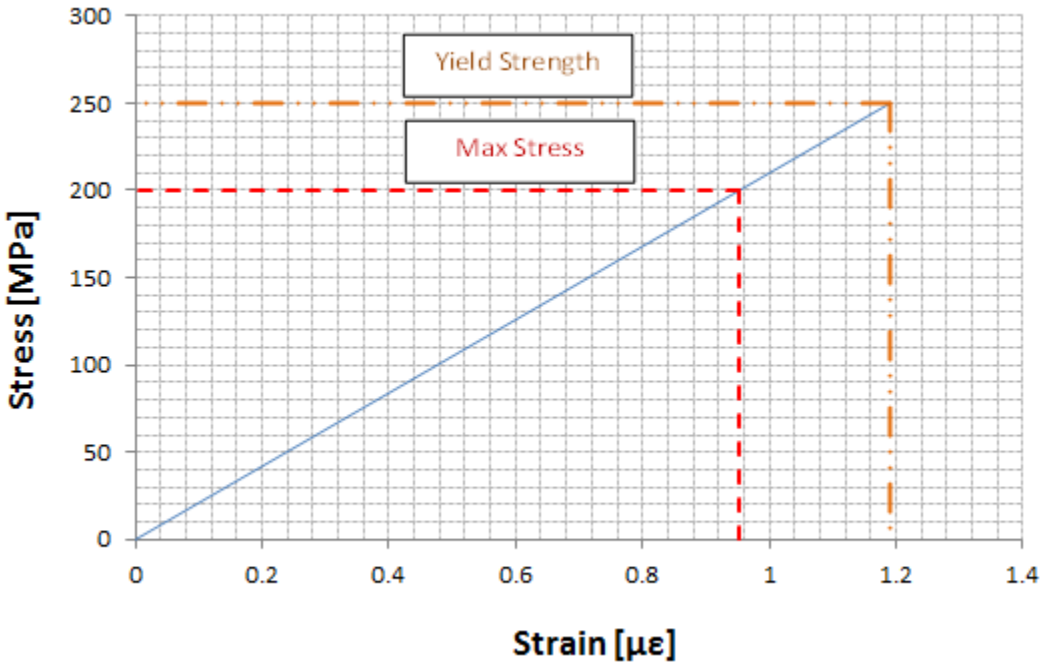

Figure 5.4: Stress-strain diagram (elastic region) for mild steel indicating the maximum stress attained in the ring during operation as stipulated by the strain sensitivity criterion.

The details for the proof ring sensitivity estimates are listed below in Table 5.1.

Table 5.1: Proving ring sensitivity factors

Ultimate tensile strength of SLM Ti-6Al-4V	1200 MPa
Force required to break specimen (UTS)	7200 N
Yield strength of mild steel	250 MPa
Max stress in ring at specimen break	80% Yield
Maximum stress experienced by ring	200 MPa
Proof ring sensitivity	1 με = ±1.5 N

5.3.4 PROOF RING FINITE ELEMENT ANALYSIS VALIDATION

Following the initial design parameters as described in the previous sections, an additional check was performed using Finite Element Analysis (FEA). ABACUS (ver. 6.10) was used to determine the maximum stress in the ring during the specimen loading from which improved ring dimensions could be obtained for optimal system accuracy. The positions of the strain gauges on the ring surface were of particular importance since the instrumentation will determine the force in the specimen according to the strain registered. Any tensile stress approaching or exceeding the yield stress deemed the design dimensions unacceptable. This section outlines the details of the FEA procedure and the results obtained from the post-processing.

5.3.4.1 Pre-Processing

The pre-processing was performed using the ABACUS CAE pre-processor. The CAD model used in this analysis was developed in Solidworks 2011 and imported into the ABACUS software. This model was partitioned as shown in Figure 5.5 for efficient and accurate meshing.

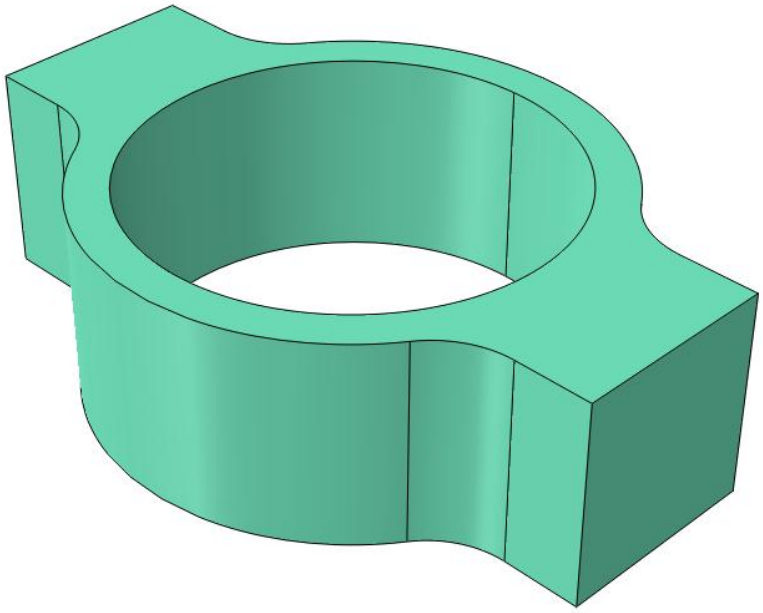

Figure 5.5: Partitions generated using ABACUS finite element analysis software.

The parameters used in the pre-processing of this analysis are listed in Table 5.2. The pre-processing stage ended with the partition meshing (see Figure 5.6) and submission of the job to the ABACUS processor.

Table 5.2: ABACUS pre-processing parameters for the FEA simulation.

Material	Mild Steel
Elastic Modulus	205 GPa
Poisson's Ratio	0.3
Load Type	Uniform Pressure
Magnitude	15.98 MPa
Boundary Condition type	Displacement/Rotation
Boundary Condition restrictions	U1 - 0 U2 - 0 U3 - 0
Element Type	Hex

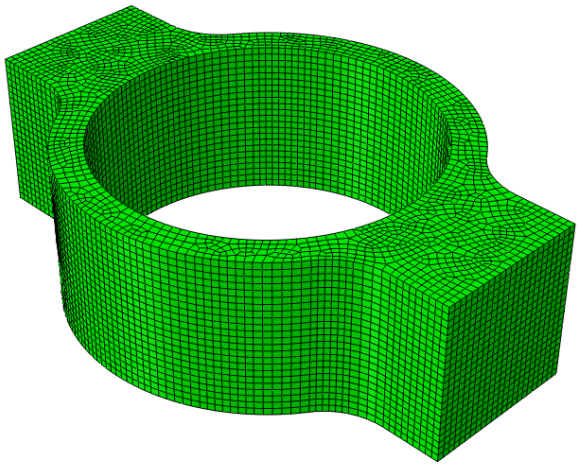

Figure 5.6: Fully meshed proof ring in ABACUS CAE using Hex elements.

5.3.4.2 Post-Processing & Results

The FEA simulation confirmed the stresses designated by the ring sensitivity requirements as outlined in Table 5.1. The Von Mises stress contours are shown below in Figure 5.7 from which the elements at the strain gauge locations were queried for maximum tensile stresses. The results from the FEA simulation with respect to the ring sensitivity requirements are given in Table 5.3.

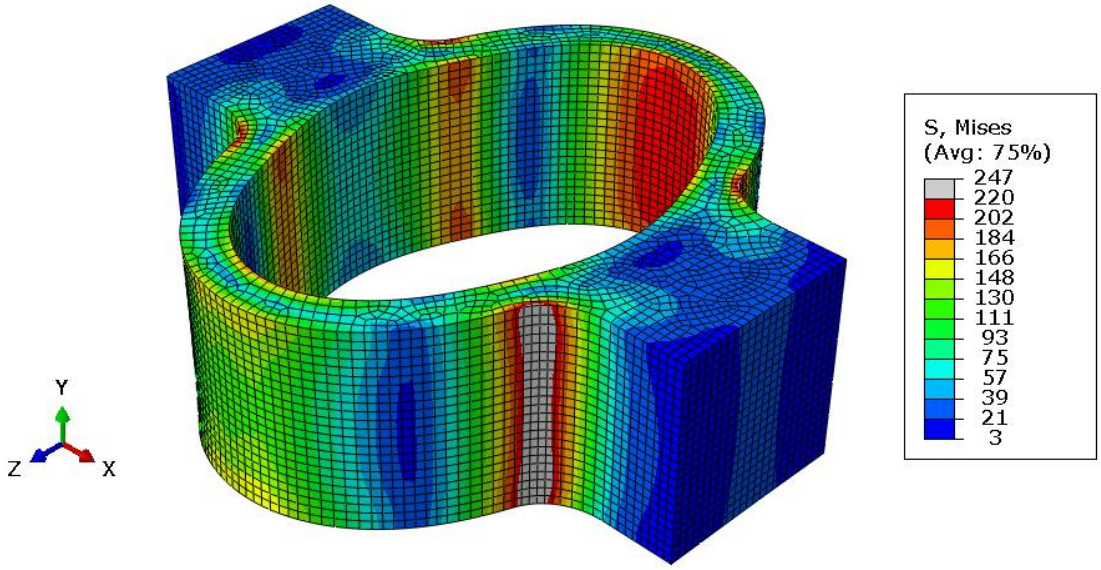

Figure 5.7: FEA contour plot illustrating the deformation and Von Mises stress contours.

Table 5.3: Results obtained from FEA simulation.

Force transmitted into specimen	7200 N
Max tensile stress in ring at specimen break	74% Yield
Maximum stress at strain gauge location	184 MPa
Ring thickness	4.5 mm
Proof ring sensitivity	1 με = 1.3 N

5.3.5 PROPOSED DESIGN OVERVIEW

The proposed design is shown below in the CAD representation in Figure 5.8. This design incorporates a proof ring approach for introducing the load into the specimen. The major components of this design are listed below and discussed more thoroughly in the sections which follow. The detailed drawings of the machined components are given in Appendix D.

i. Load/Proof ring
ii. Mounting system
iii. Force measurement system
iv. Data acquisition & displacement measurement
v. Microscope attachment

5.3.5.1 Load/Proof Ring

The proof ring is shown below in the CAD rendered views in Figure 5.9. Four strain gauges are attached to the ring circuit in tension-compression pairs. As either of the M12 load nuts are fastened, a pure tension load is introduced into the specimen. The torsion experienced during the turning of the nut is prevented from acting on the specimen by two M3 torsion control cap screws which fit into a slot through the load bolt threads. The specifications for the load ring are given in Table 5.4.

Table 5.4: Proof ring specifications

Load/Mounting bolts	M12x1.25 (Metric Fine) High Tensile
Load nuts	M12x1.25 (Metric Fine) High Tensile

Torsion control cap screw	M3 High Tensile
Minimum ring thickness (strain gauge location)	4.5mm
Ring cross-sectional area (strain gauge location)	58.5 mm^2
Strain gauges	4 x Kyowa KFG-4-120-C1

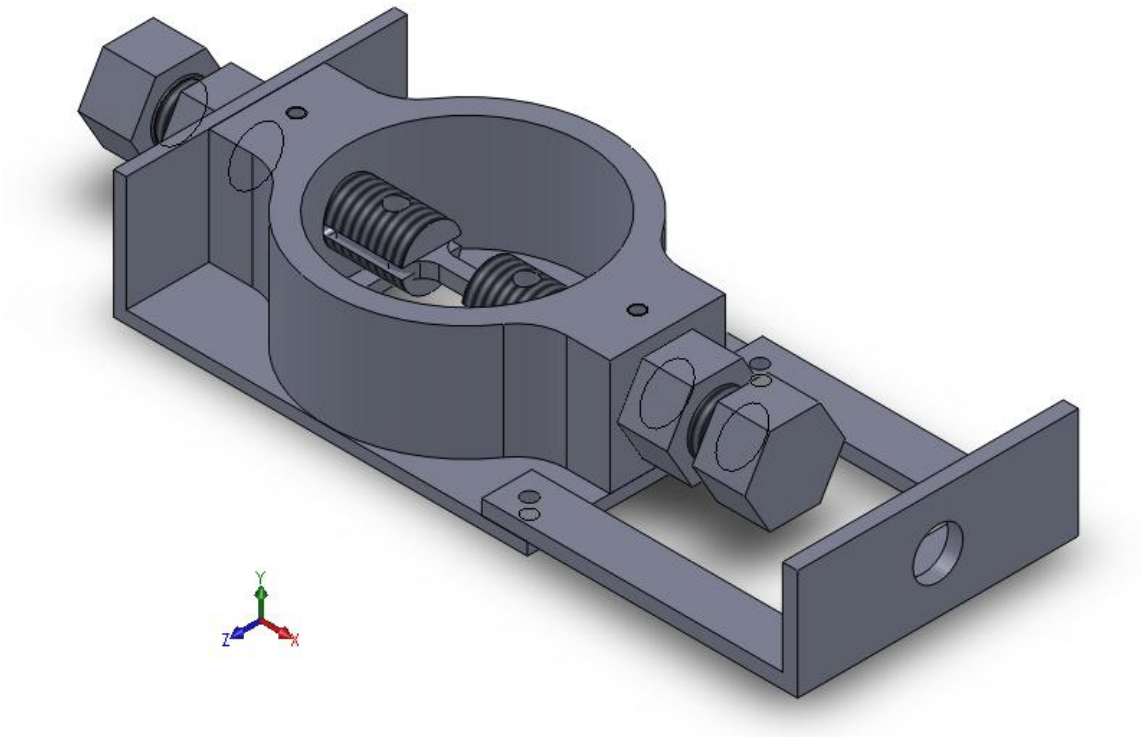

Figure 5.8: Isometric CAD view of the proposed micro-flaw exposure rig (excluding instrumentation and data acquisition systems).

5.3.5.2 Mounting System

The specimen is mounted using the two load/mounting bolts as shown in Figure 5.9 and Figure 5.10. The specimen is fastened into place using two M4 cap screws and nuts. This ensures the specimen is fastened firmly to the load bolts to prevent any distortion under load. The significant loads required to break the Ti-6Al-4V specimens has necessitated that all the bolts and cap screws are High Tensile (Grade 8.8) designation. The load bolts are tensioned as the load nuts are fastened against the ring surface.

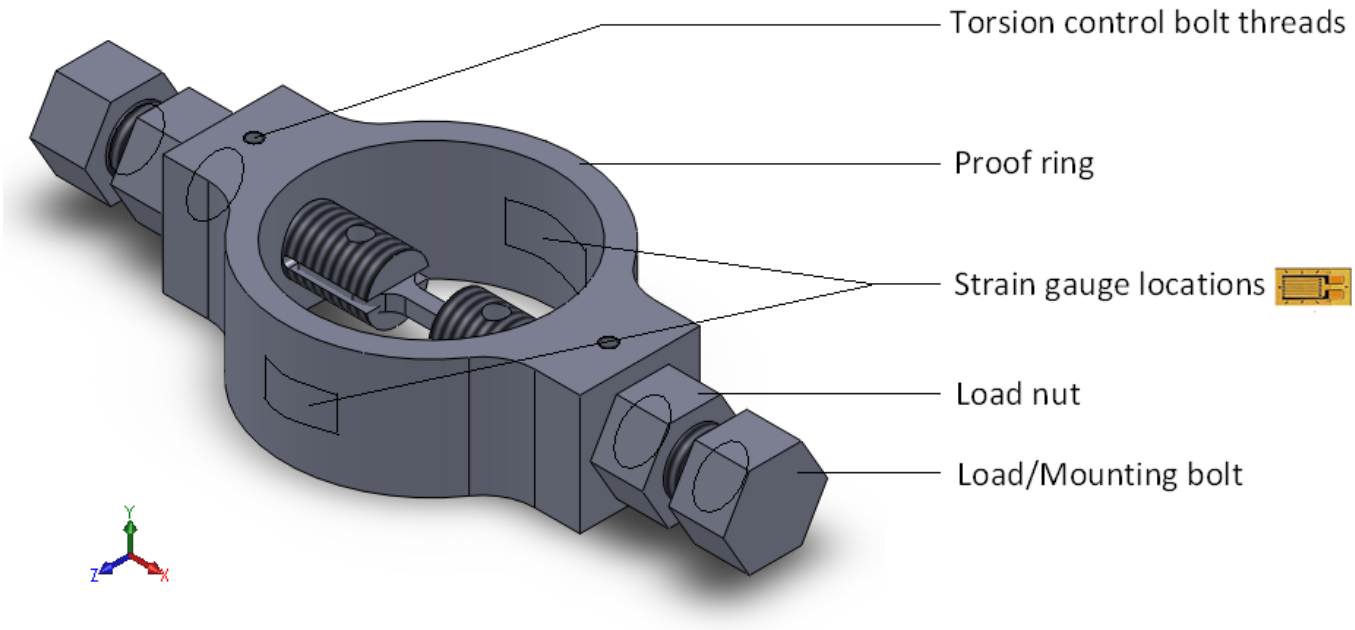

Figure 5.9: Isometric CAD view of the proof ring with the major design features labelled.

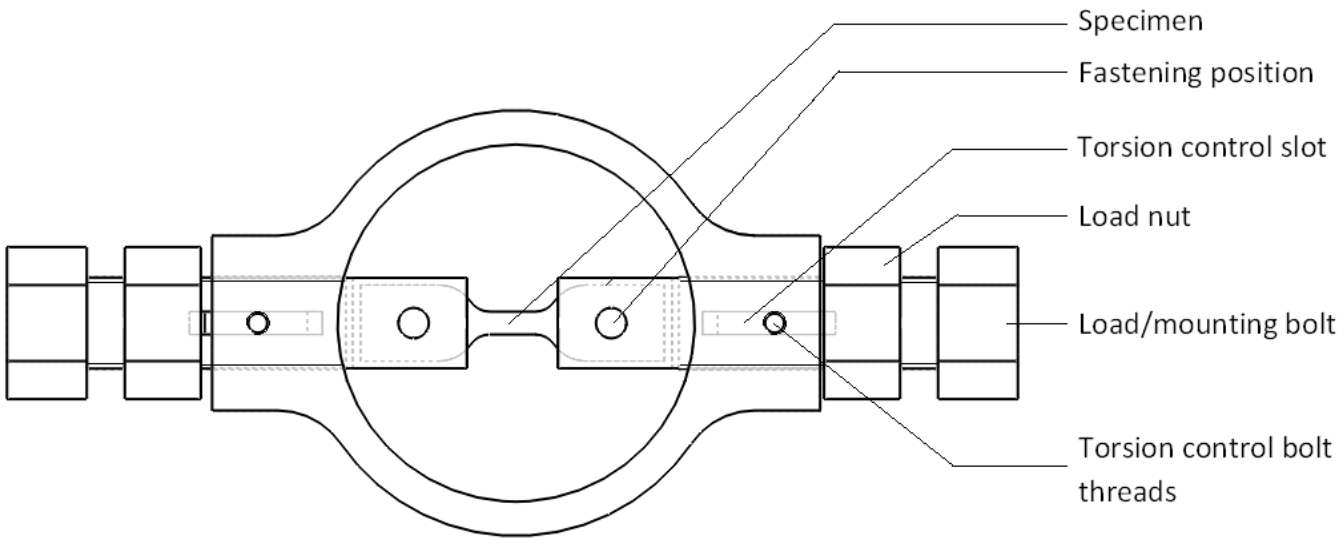

Figure 5.10: Plan view schematic of the specimen mounting system.

5.3.5.3 Force Measurement System

The force measurement is accomplished through the use of four strain gauges on the ring surface. These strain gauges are positioned in tension-compression pairs and connected to a P-3500 strain indicator in a full bridge configuration. The tension-compression pairs are clearly shown in Figure 5.11 below. The strain on the ring is proportional to the force transmitted through the specimen and is calibrated using a tensile testing machine as described later in this chapter. The strain indicator signals are transmitted into the data acquisition system for further processing.

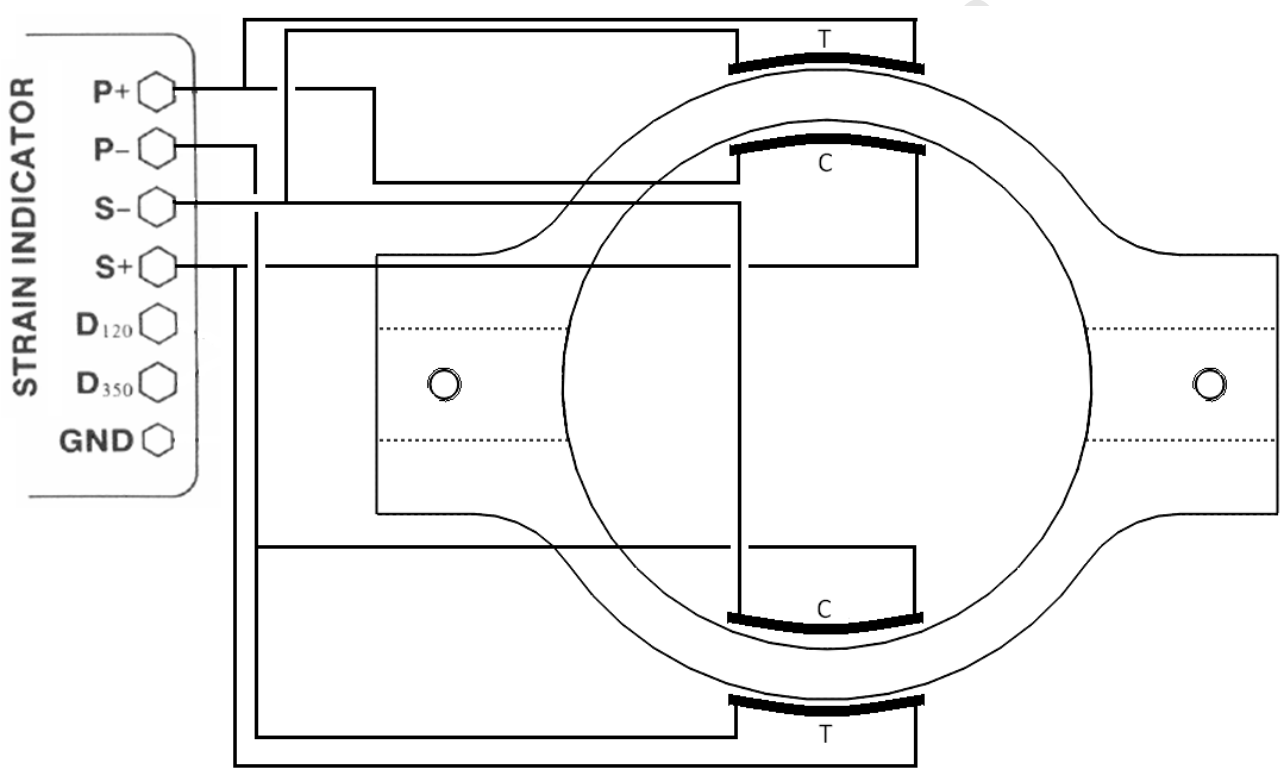

Figure 5.11: Strain indicator connection diagram. The 'T' strain gauges are in tension while the corresponding 'C' strain gauges are in compression.

5.3.5.4 Data Acquisition & Displacement Measurement

Data acquisition is accomplished through the *National Instruments* Ni USB-6009 high speed data acquisition system as shown below in Figure 5.12. This data acquisition device collects the strain gauge readings via the P-3500 strain indicator and the position sensor readings through the

Spectrol 10K Multi-turn potentiometer shown in Figure 5.12. The position sensor detects the angular position of the load nut and calculates the linear movement of the load bolt according to the thread pitch. This system is used to develop an understanding of the relationship between the force applied to the specimen and the system strain. The specifications for this data acquisition system are listed below.

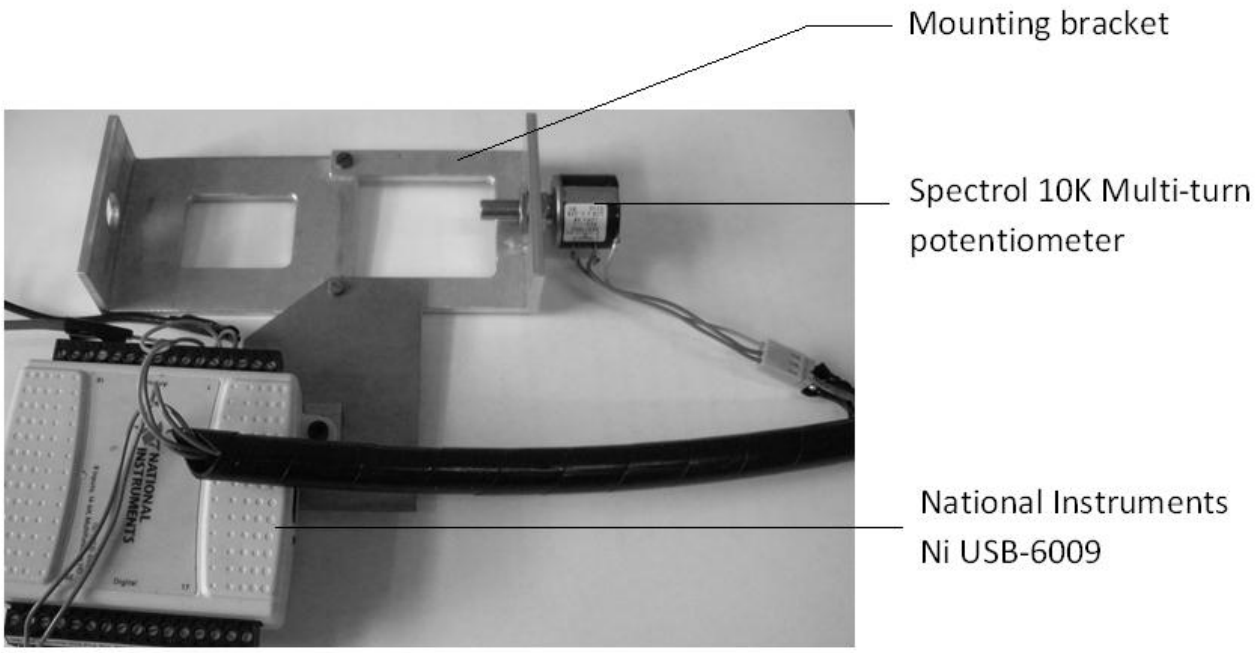

Figure 5.12: Data acquisition devices mounted on the micro-flaw exposure rig bracket.

Table 5.5: Data acquisition system specifications.

Spectrol 10K Multi-turn potentiometer tolerance	Displacement tolerance - ±0.05mm
Strain Indicator	*Measurement Group* P-3500
National Instruments Ni USB-6009	8 analog inputs (14-bit, 48kS/s); 2 analog outputs (12-bit, 150 S/s); 12 digital I/O; 32-bit counter

5.3.5.5 Microscope Attachment

The rig is mounted on the microscope using the mounting bracket and the locating brace attached to the microscope platform as shown in Figure 5.13. This allows for an easy removal of the rig from beneath the microscope lens system for each loading interval. The rig is held in a table-mounted vice as the force is increased in the specimen such that the rig is kept stable as the load nuts are fastened. The rig position for the loading intervals is shown in Figure 5.14.

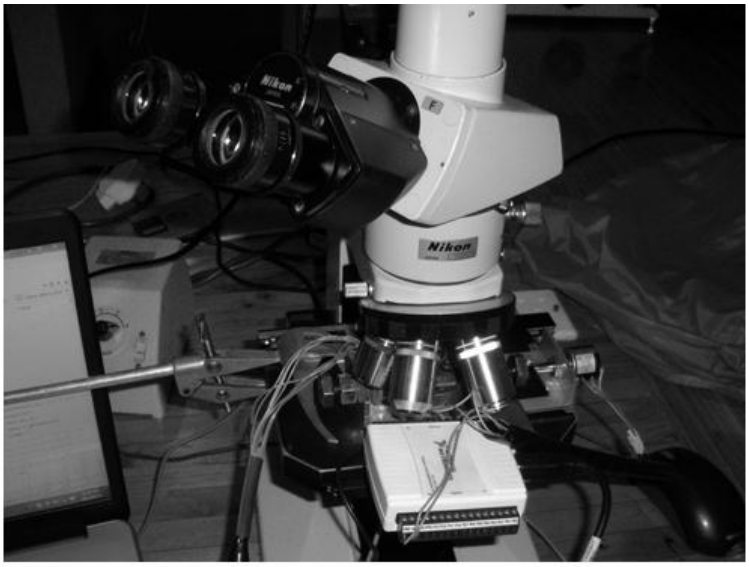

Figure 5.13: Micro-flaw exposure rig in the micrograph acquisition configuration.

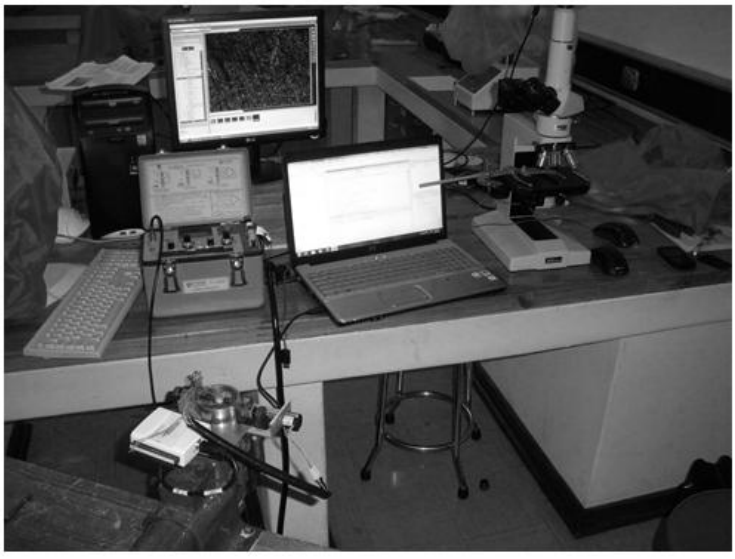

Figure 5.14: Micro-flaw exposure rig in the loading configuration.

5.3.6 MICRO-FLAW EXPOSURE RIG CALIBRATION

The rig was calibrated in the Zwick Universal Testing machine at the Centre for Materials Engineering at UCT. The calibration was performed by loading the proof ring in intervals up to the expected maximum force during operation. The calibration was ten times to ensure the rig consistency. It is important to note here that the strain readings returned to zero after every test indicating that no plastic deformation affected the rig. The calibration details are listed in Table 5.6.

Table 5.6: Micro-flaw exposure rig calibration details

Maximum Force	7200 N
Number of Intervals	10
Force Increments	720 N

The calibration data produced the relationship shown in Figure 5.15. This graph is used to relate the strain experienced by the strain gauges to the force exerted on the ring (from which force transmitted into the specimen may be inferred).

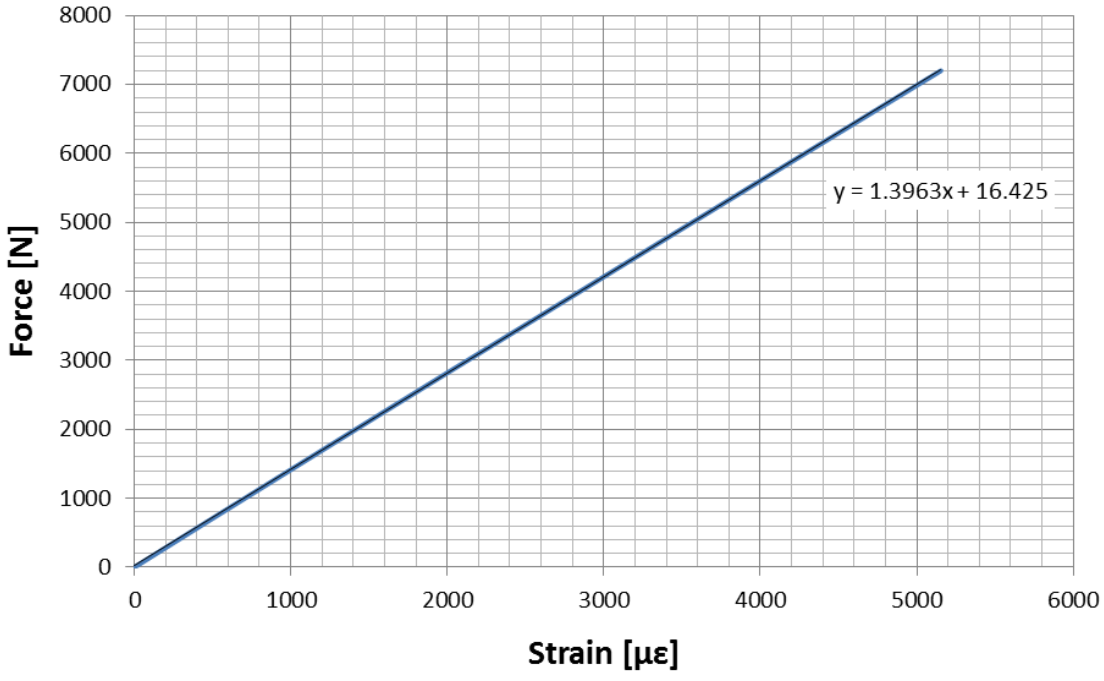

Figure 5.15: Force-Strain calibration graph for the micro-flaw exposure rig.

5.3.7 DEFLECTION CORRECTION PROCEDURE

In order to improve the accuracy of the specimen deflection/elongation measurement, it is necessary to correct the results for the deflection in the rig components. The total deflection of the system is a summation of the respective components as shown in (5-1) below.

$$\delta_{total} = \delta_{specimen} + \delta_{ring} + \delta_{pin} + \delta_{bolts} \quad \textbf{(5-1)}$$

In order to account for the ring deflection, the relationship between the load and ring deflection was obtained during the calibration procedure in the previous section. This relationship is given below in Figure 5.16.

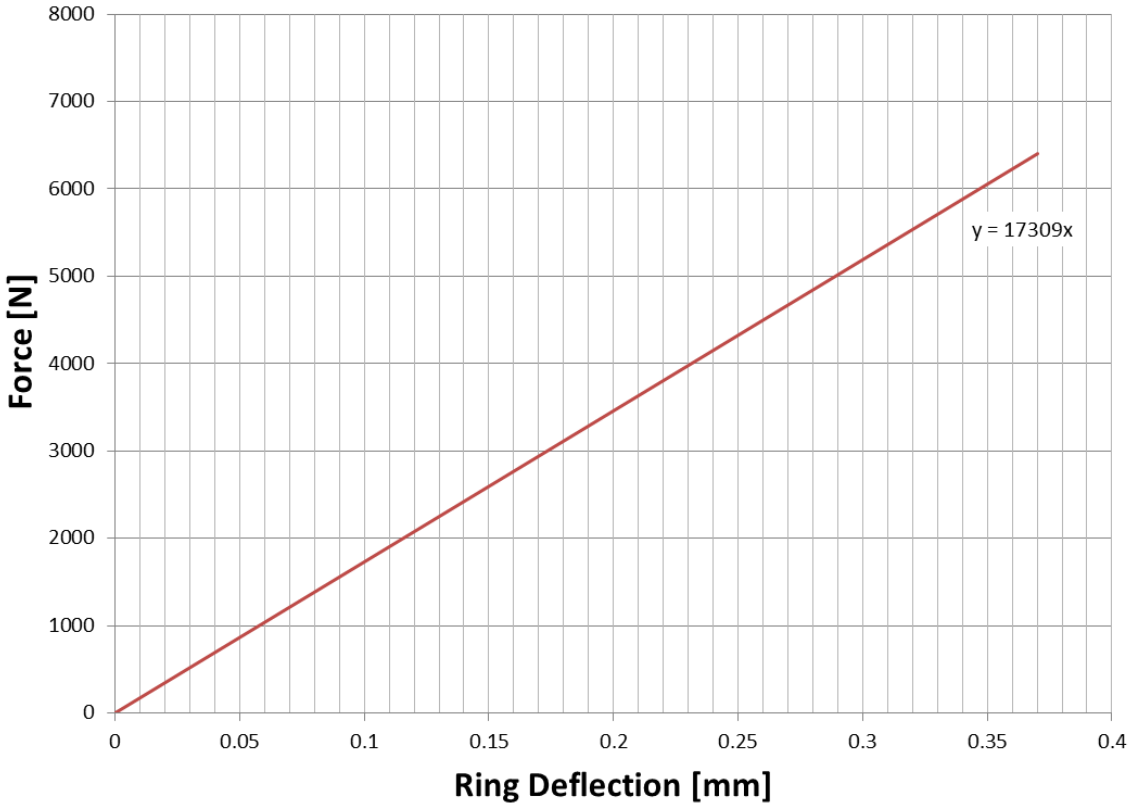

Figure 5.16: Graph of the applied load and the ring deflection as determined by the Zwick Universal Tensile Testing Machine at the University of Cape Town.

The deflection of the pins connecting the specimen to the mounting bolts may be considered zero since the joint is clamped and hence,

$$\delta_{pin} = 0 \quad \textbf{(5-2)}$$

The deflection of the bolts may be determined using a simple mechanics of solids approach which gives the following equation.

$$\delta_{bolt} = \frac{F l_o}{2AE} \quad \textbf{(5-3)}$$

In which F is the applied load [N], l_o is the bolt length, A is the bolt area [mm^2] and E is the Young's modulus [MPa]. Note that the factor of ½ is used since each bolt accounts for half the load applied to the specimen.

Manipulating equation (5-1) and substituting in the results obtained above, the true specimen deflection is determined as follows in equation (5-4).

$$\delta_{specimen} = \delta_{total} - (\delta_{ring} + 2.\delta_{bolt}) \quad \textbf{(5-4)}$$

Further substitution to determine the corrective factor is shown below.

$$\delta_{specimen} = \delta_{total} - \left(\frac{F}{17309} + \frac{F l_o}{AE}\right) \quad \textbf{(5-5)}$$

From which the corrective factor is obtained as shown in (5-6). This factor must be subtracted from the total measured deflection to give the true deflection of the specimen.

$$Corrective\ Factor = -\left(\frac{F}{17309} + \frac{F l_o}{AE}\right) \quad \textbf{(5-6)}$$

This factor is graphed across the load spectrum in Figure 5.17 below. It is noted here that the deflection factor introduced here is an estimate of the errors attained during testing. In order to

determine accurate breaking stress and yield behaviour, specimens would need to be tested in a commercial tensile testing machine such as the Zwick Universal Tester used to calibrate this rig.

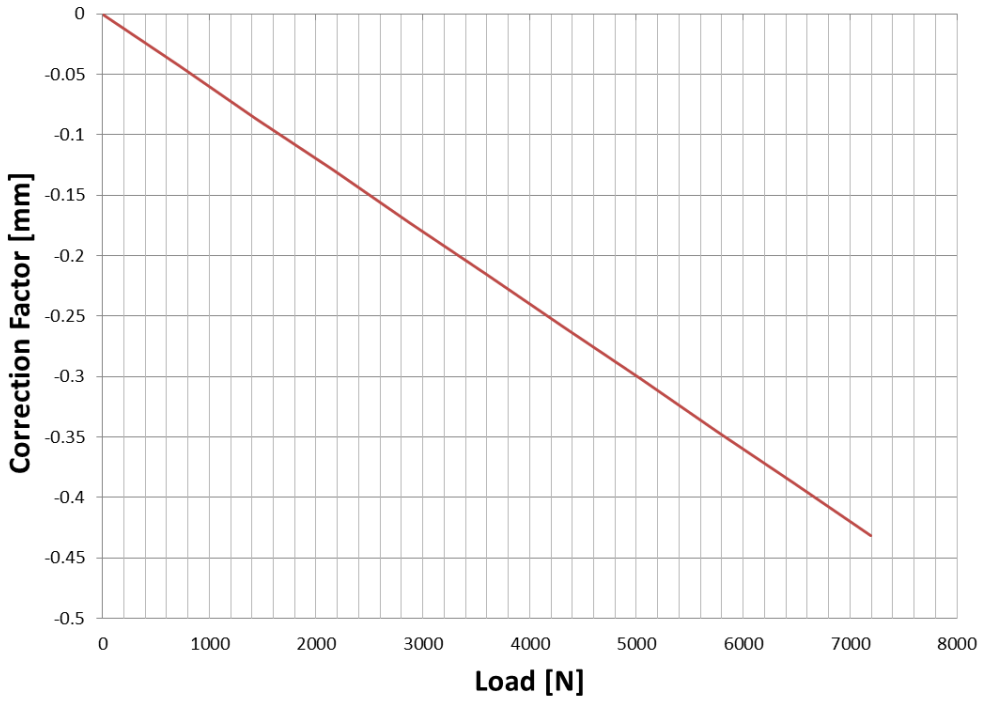

Figure 5.17: Correction factor applied to total deflection to obtain true specimen deflection.

5.4 MINITURE TENSILE RIG OPERATING PROCEDURE

5.4.1 SPECIMEN MOUNTING

1. The specimens are polished in the same manner as those for the microscopy work (see Section 4.2.4). After the polishing procedure, the specimens are removed from the polisher mount.
2. The specimen is positioned in the mounting/load bolts and fastened as shown below in Figure 5.18a and b. Insert the torsion control cap screws to prevent the specimen from turning.
3. The *Spectrol* potentiometer is connected to one of the load nuts using the magnetic arm as shown in Figure 5.18c after which the rig is ready for use (Figure 5.18d).

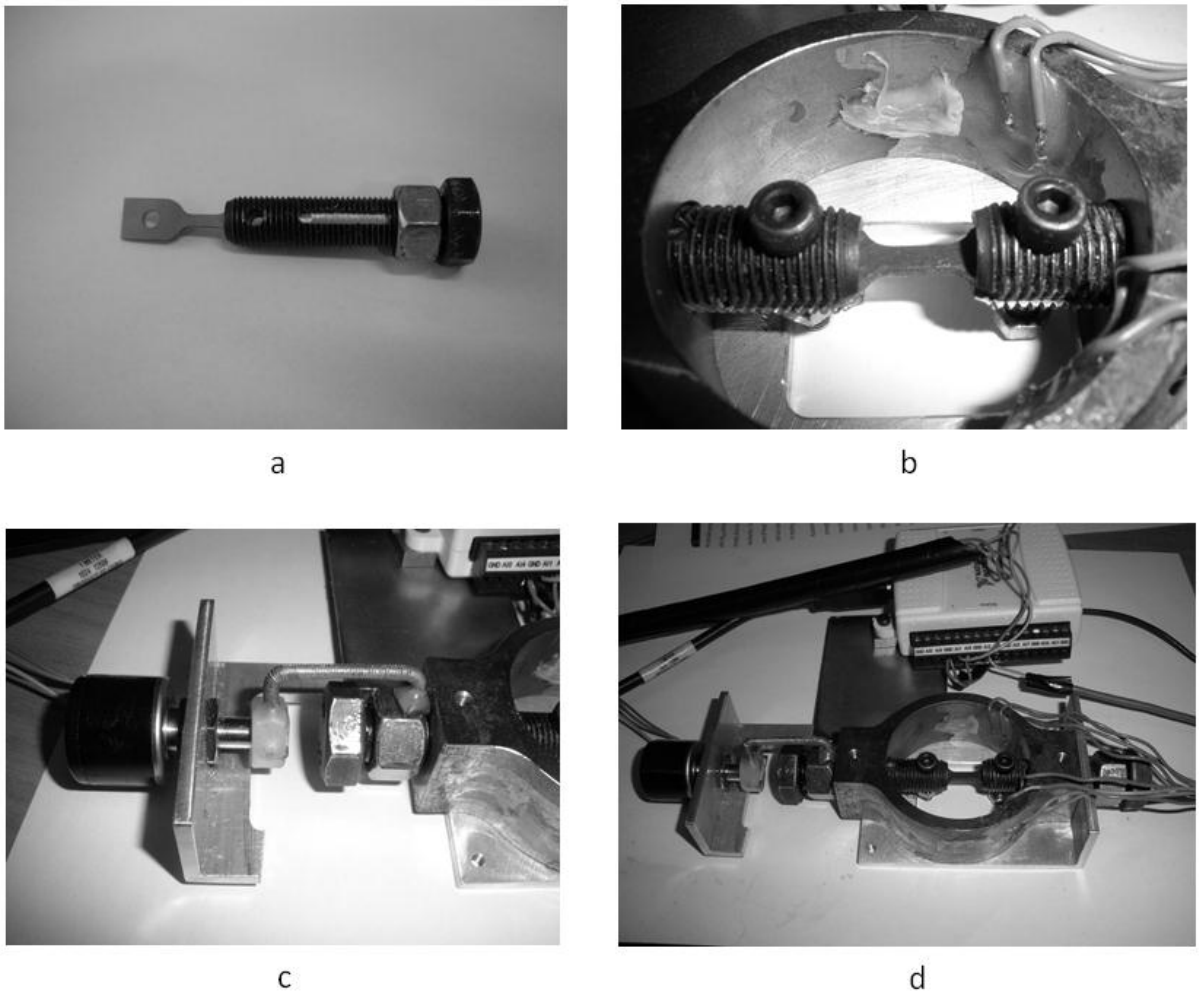

Figure 5.18: a) Specimen positioning within the load/mounting bolt, b) specimen secured within the ring, c) position sensor (potentiometer) attachment and, d) complete rig.

5.4.2 SPECIMEN LOADING

1. The rig is tensioned such that all components are secure and a zero load is noted from the strain gauge readings.
2. The rig is placed within the vice prong to secure the apparatus for the loading procedure.
3. Tighten the load nut against the ring until the force registered by the strain gauges reaches the required level and ensure the data acquisition software has stored the strain and position data successfully.
4. Lift the rig off the vice prong and position the specimen on the microscope platform.

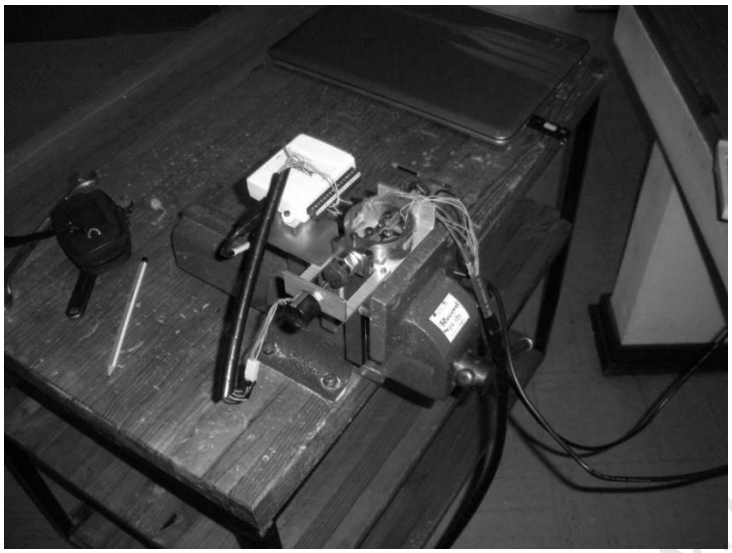

Figure 5.19: Rig positioned in the vice prong in preparation for the loading procedure.

5.4.3 MICROGRAPH CAPTURE

1. The microscope platform stays are fastened into the correct position for specimen viewing. This is done prior to loading by positioning stays such that the rig gauge section is positioned and focused under the microscope X5 lens.
2. Following the loading procedure, the apparatus is positioned on the microscope platform to fit tightly against the platform stays (see Figure 5.20a and b).

Figure 5.20: a) Microscope positioning stays and, b) Rig positioned on the microscope platform.

3. The micrograph is acquired using the LAS Nikon software suite in the TIFF format.
4. This procedure is repeated for each loading interval up to the specimen break. At least 8 micrographs should be captured for the DIC analysis.

5.4.4 IMAGE ANALYSIS & POST-PROCESSING

In addition to the visual analysis, the micrographs captured during the loading intervals are analysed with DIC software written in MATLAB by Chris Eberl et al [103]. This software requires only the images taken by the microscope to perform a complete analysis. This section briefly explains the usage of this software when analysing the micrographs acquired from the previous steps.

1. A filename list needs to be generated to process all the micrographs in the order in which they were acquired. This is accomplished by typing *filelist_generator.m* (function developed by Eberl [103]) into the MATLAB command prompt and completing the steps which follow.
2. Following the completion of the file list generation, the processing grid needs to be created across which all the pixels are evaluated. The grid is used to divide the gauge section into segments which can be tracked using the DIC tracking function (in the next step) as shown in Figure 5.1. The *grid_generator.m* function is used to create and store the desired grid.
3. The *automate_image.m* function is called following a successful grid generation which analyses all the images and tracks the pixel movement.
4. The *displacement.m* function is then called to complete the analysis and process the results.

Detailed descriptions and instructions of the functions in points 1-4 may be obtained from the source code in ref [103].

5.5 SUMMARY

This chapter has described the development and use of a miniature tensile rig intended to reveal micro-flaws under load, and to assess any flaw interaction in the SLM Ti-6Al-4V tensile specimens. This was accomplished through the use of a proof ring concept which was developed and validated using FEA. The completed rig enables the user to load the tensile specimen in intervals and acquire micrographs under known loads. The forces introduced into the specimen and the approximate specimen strain is sampled rapidly using the data acquisition system. The tensile strengths before and after heat treatment can be estimated using the rig and its data acquisition system. The consistency of the specimen breaking strengths and the yielding behaviour of this material can be examined with the intention of better understanding the reliability of components manufactured from SLM. It is also noted here that the tensile breaking strengths and the deflection procedures are used purely for comparative purposes (accurate breaking strengths and deflection would need to be determined using a commercial tensile testing machine). The Digital Image Correlation study of the micrographs was performed using MATLAB script developed by Eberl et al [103]. This analysis was conducted in order to evaluate the stress-strain relationship and to assess the behaviour of any micro-flaws/pores under a tensile load.

In the next chapter, the results from the experiments performed in this study are presented along with observations made during the investigation.

CHAPTER 6 – RESULTS & OBSERVATIONS

This chapter presents the results and observations from all the analyses conducted during the course of the study. The first section details the results from the pilot investigation into the distortion in specimens received from the CFRM[2]. This investigation led to the primary study into the residual stress profiles of SLM Ti-6Al-4V. The results of this primary study with specific interest in the effect of heat treating the specimens are presented in Section 6.2. The density and hardness evaluations (Section 6.3 and Section 6.4 respectively) were completed to further the understanding of this type of material and the impact of heat treatment. The load-deflection results obtained from the micro-flaw exposure rig are presented in Section 6.4. The microstructural analysis which was conducted in parallel with the residual stress evaluation and effect of heat treatment is presented in Section 6.5. The results from the micro-flaw exposure investigation are presented in the final section (Section 6.6) and the limitations of the system in terms of employing DIC to evaluate the micro-flaw interaction.

6.1 PILOT RESIDUAL STRESS ANALYSIS

The preliminary/pilot residual stress examination was performed on the distorted specimens provided by the CFRM. When the specimens were removed from the baseplate of the EOSINT M270 machine, significant distortion was observed as described in Chapter 4. The residual stresses were determined using ASTM E837-08 and corrected using Sattari-Far's correction technique [97] where appropriate. A total of four tests were conducted on the two specimens (two tests per specimen) in two regions, sector A and sector B as indicated in Figure 6.1. Strain rosettes were placed in these positions since they represented the thickest regions of the specimens and would be unaffected circumferentially by the outer cut as shown in the front view

[2] Centre for Rapid Manufacturing at the Central University of Technology (CUT)

in Figure 6.1. In addition, the rosettes were placed on either side of the diameter change to evaluate any potential thickness effects.

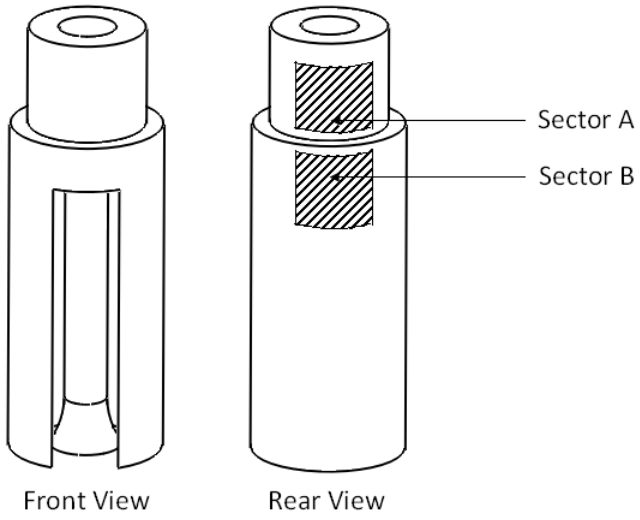

Figure 6.1: Sampling regions for the preliminary residual stress analysis on the distorted specimens

The residual stresses were initially checked for uniformity as per ASTM E837-08 and the results for Specimen 1 and Specimen 2 are plotted in Figure 6.2 and Figure 6.3 respectively. The results, following the processing of the recorded relieved strains, are given below in Table 6.1 for Specimen 1 and Specimen 2. The sector A results for both specimens have been corrected according to Sattari-Far's correction procedure [97] since they exceeded the acceptable limits of ASTM E837-08 (>60% yield strength).

Table 6.1: Residual stress (MPa) results for the distorted specimens.

Specimen	Sector	σmaxASTM [MPa]	σminASTM [MPa]	σy [MPa]	σmaxCorr [MPa]	β [degrees]
1	A	1508	913	1090	1142 ± 285	37 ± 4
	B	618	385	1090	616 ± 60	41 ± 4
2	A	969	832	1090	887 ± 88	38 ± 4
	B	338	135	1090	333 ± 16	37 ± 4

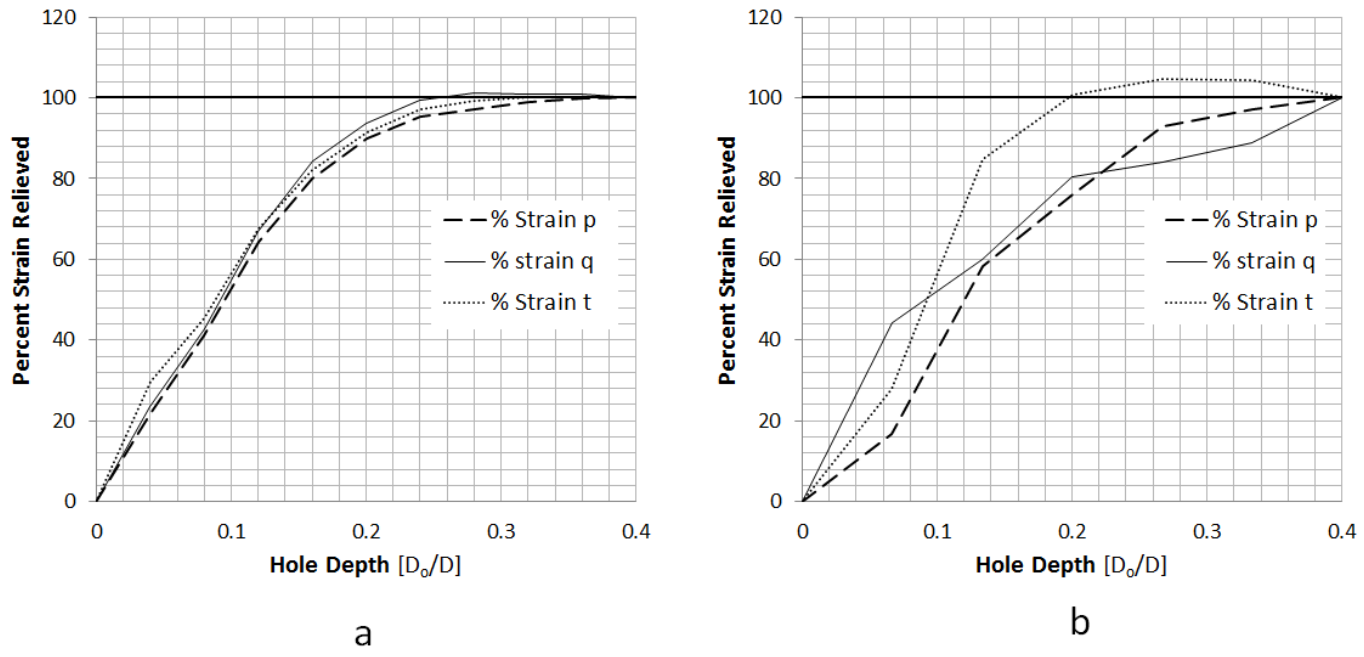

Figure 6.2: Residual stress uniformity test results for specimen 1 regions, a) Sector A and, b) Sector B.

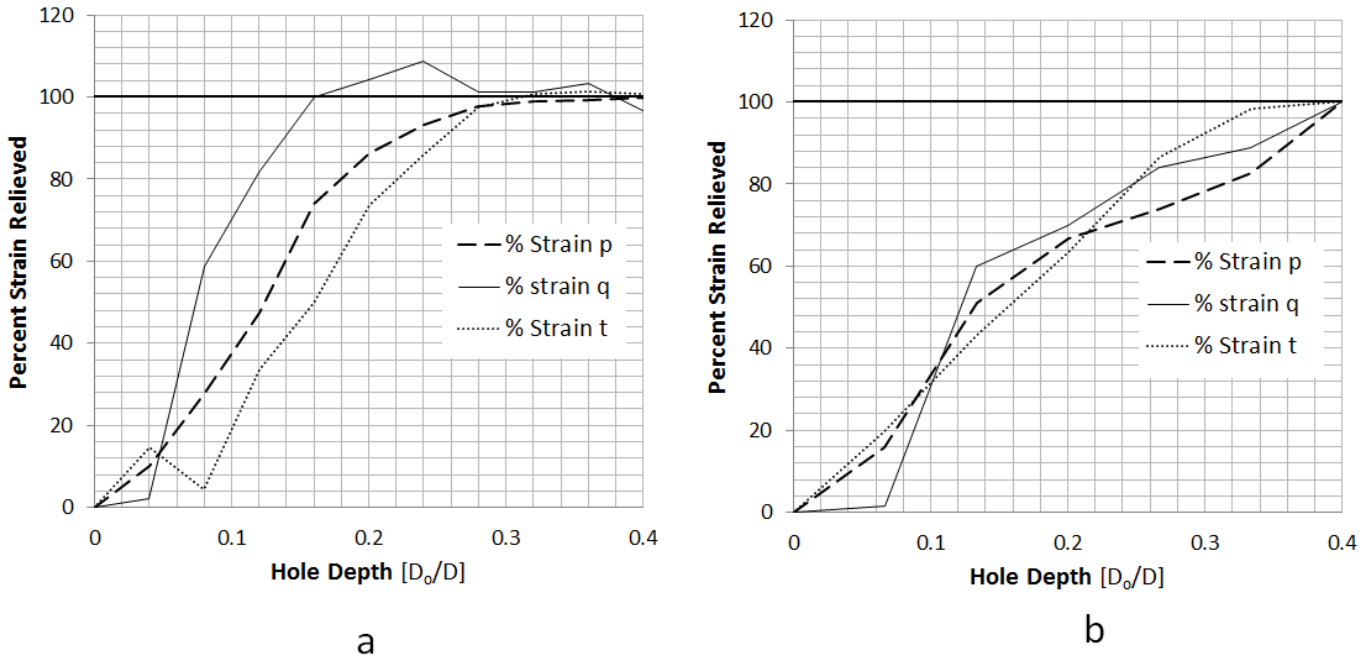

Figure 6.3: Residual stress uniformity test results for specimen 2 regions, a) Sector A and, b) Sector B.

6.2 RESIDUAL STRESS EVALUATION

The results from the pilot study warranted further investigation into the residual stress profiles within SLM produced Ti-6Al-4V. This section presents the results obtained for the primary residual stress analysis including the effects of heat treatment on the residual stress levels. ASTM E837-08 was used in conjunction with the appropriate correction procedures in the event of residual stresses exceeding the limits of the standard. The first section presents the initial residual stress levels present within the specimens in the as-built condition. This is followed by the investigation into the heat treatment effect on these stress levels. The uniformity checks are not presented here since it was established from the previous section that all specimens contained stress profiles which were non-uniform in nature.

The residual stress profiles were generated from two positions on the specimen surface (see Figure 6.4 below) such that an assessment of the stress level consistency could be determined. The specimens were analysed in pairs, i.e. one vertically built cylinder and one horizontally built cylinder were subjected to stress testing before and after heat treatment (four specimen pairs in total). This was done in order to evaluate any differences in the stress levels due to build orientation. The results are designated according to their build orientation and drill position.

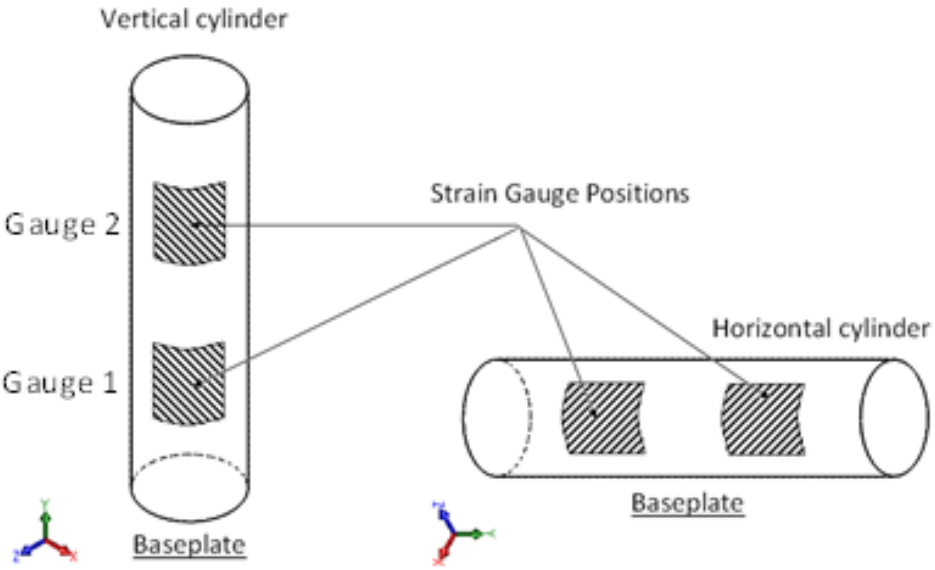

Figure 6.4: Strain rosette positions on the vertical and horizontally grown specimens.

The vertical and horizontal specimen pairs as noted in Figure 6.4 above are listed in Table 6.2 below corresponding to their designations and heat treatments. These designations identify the graphical results in the sections which follow.

Table 6.2: Specimen designation, orientation and heat treatment pairing

Specimen Designation	Build Orientation	Heat Treatment
A1	Vertical	Stress Relief
D1	Horizontal	
A2	Vertical	Recrystallization Anneal
D2	Horizontal	
A3	Vertical	Duplex Anneal
D3	Horizontal	
A4	Vertical	Beta Anneal
D4	Horizontal	

The residual stress profiles determined via ASTM E837-08 are presented in the sections which follow. The stresses were analysed in terms of their minimum and maximum principal directions in order to identify the tensile stress with the greatest magnitude. The strain relief data corresponding to the residual stress results presented in this section is given in Appendix B. The stress profiles for each strain gauge position are shown in an effort to compare the consistency of the residual stress profiles lengthwise across each specimen. This also serves as a check to ensure the specimen stress profile has been determined correctly.

The designation of strain gauge 1 and 2 in Figure 6.4 are particularly important for the vertically built specimens since the variation in stress levels progressively further away from the machine baseplate can be determined. The dual strain gauge usage in the horizontal specimens however serves as a consistency check at the same distance from the machine baseplate.

6.2.1 SPECIMENS A1-D1

The strain gauge rosettes used in specimens A1 and D1 were type B rosettes drilled to a depth of 2mm in total.

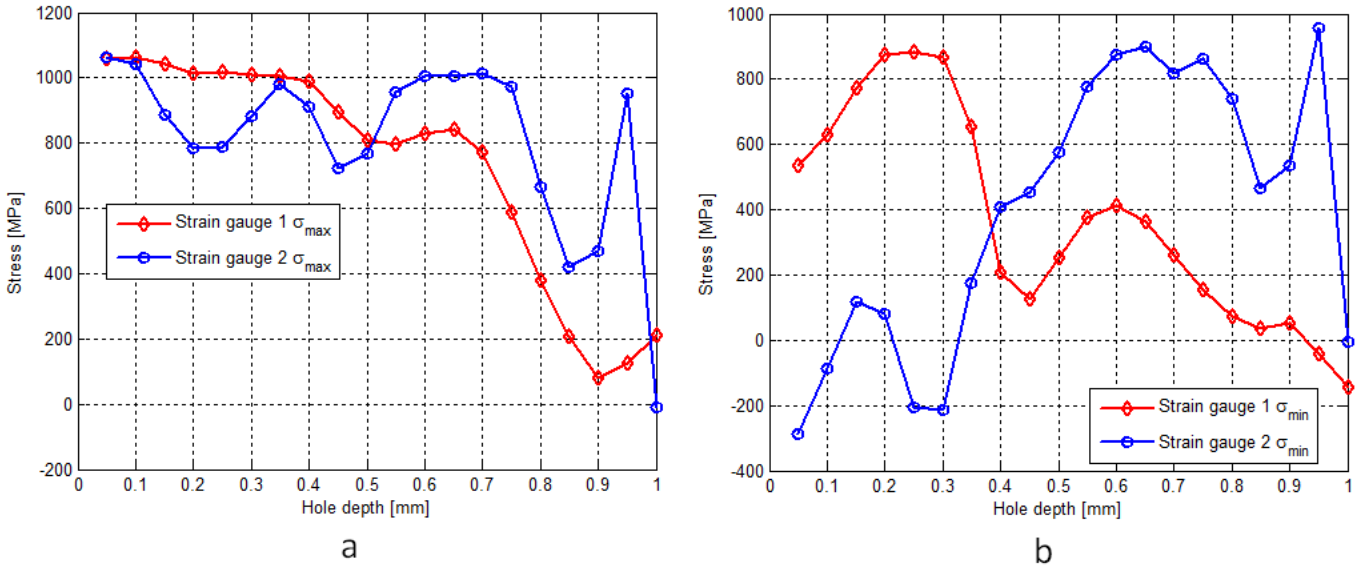

Figure 6.5: Specimen A1 residual stress variation with depth for strain gauge positions 1 and 2 in terms of, a) maximum principal stress and, b) minimum principal stress. [Error bars omitted for image clarity, see Error Analysis]

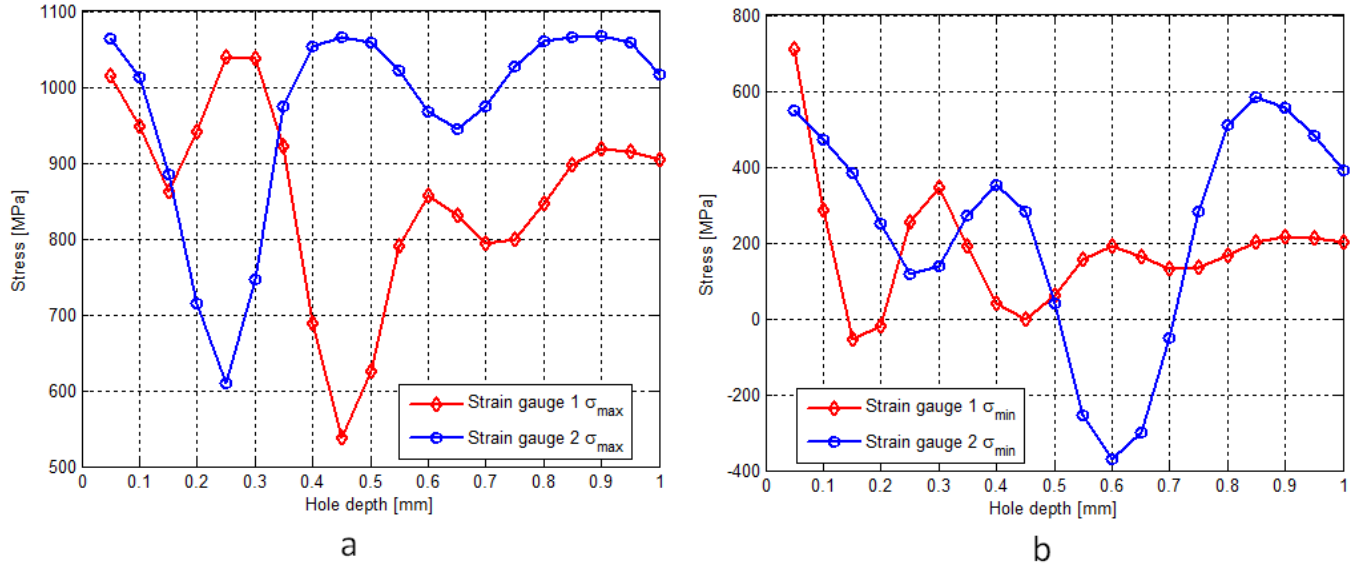

Figure 6.6: Specimen D1 residual stress variation with depth for strain gauge positions 1 and 2 in terms of, a) maximum principal stress and, b) minimum principal stress. [Error bars omitted for image clarity, see Error Analysis]

6.2.2 SPECIMENS A2-D2

The strain gauge rosettes used in specimens A2 and D2 were type A and type B respectively. Both rosettes were drilled to a depth of 2mm in total.

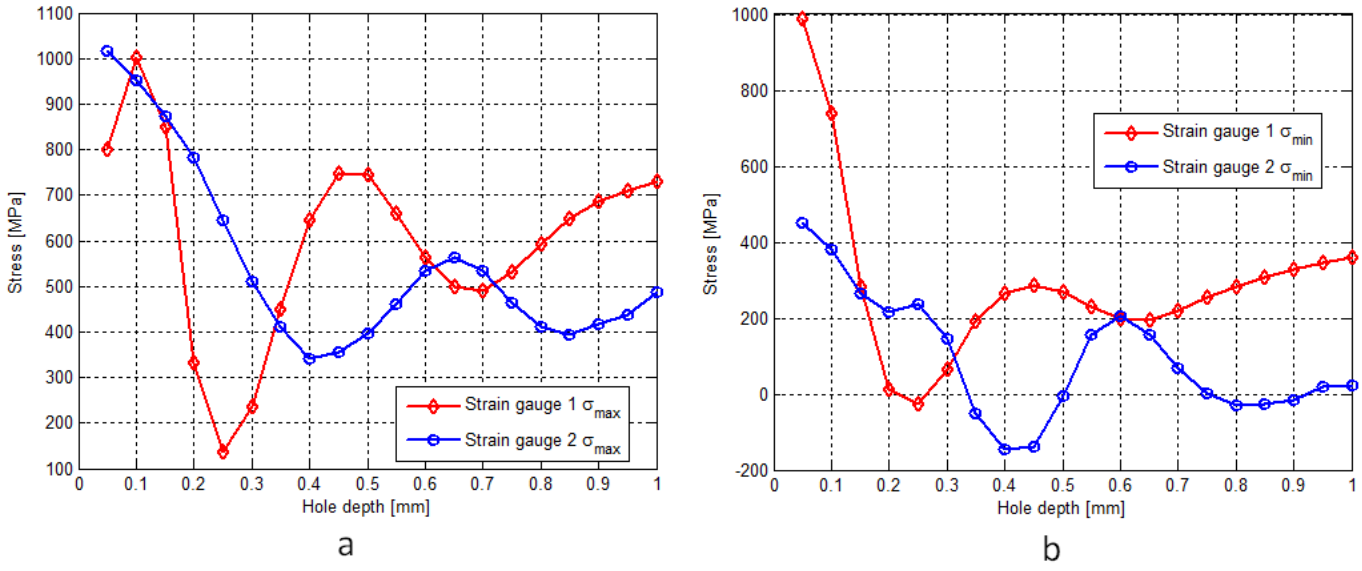

Figure 6.7: Specimen A2 residual stress variation with depth for strain gauge positions 1 and 2 in terms of, a) maximum principal stress and, b) minimum principal stress. [Error bars omitted for image clarity, see Error Analysis]

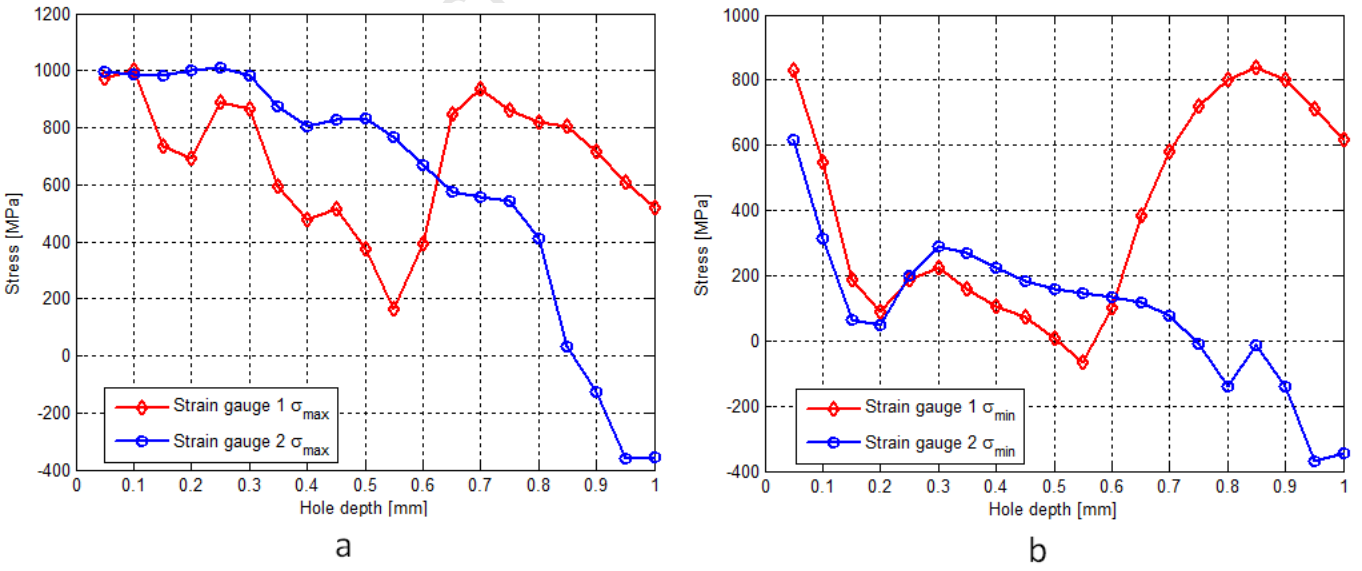

Figure 6.8: Specimen D2 residual stress variation with depth for strain gauge positions 1 and 2 in terms of, a) maximum principal stress and, b) minimum principal stress. [Error bars omitted for image clarity, see Error Analysis]

6.2.3 SPECIMENS A3-D3

The strain gauge rosettes used in specimens A3 and D3 were type B rosettes drilled to a depth of 2mm in total.

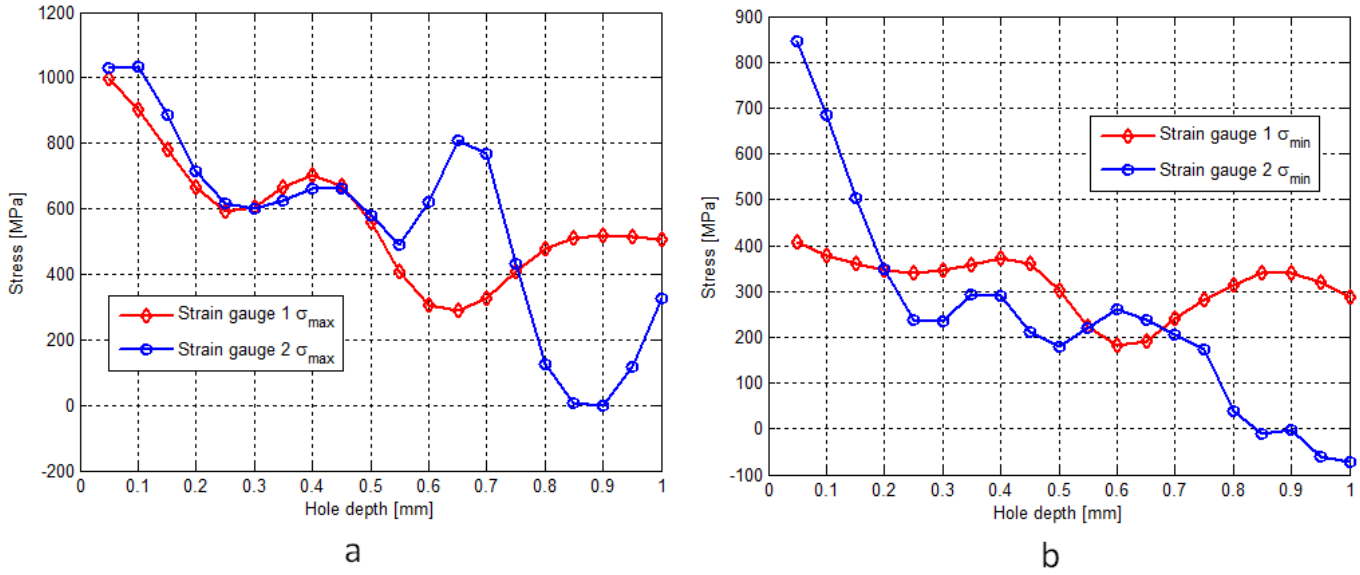

Figure 6.9: Specimen A3 residual stress variation with depth for strain gauge positions 1 and 2 in terms of, a) maximum principal stress and, b) minimum principal stress. [Error bars omitted for image clarity, see Error Analysis]

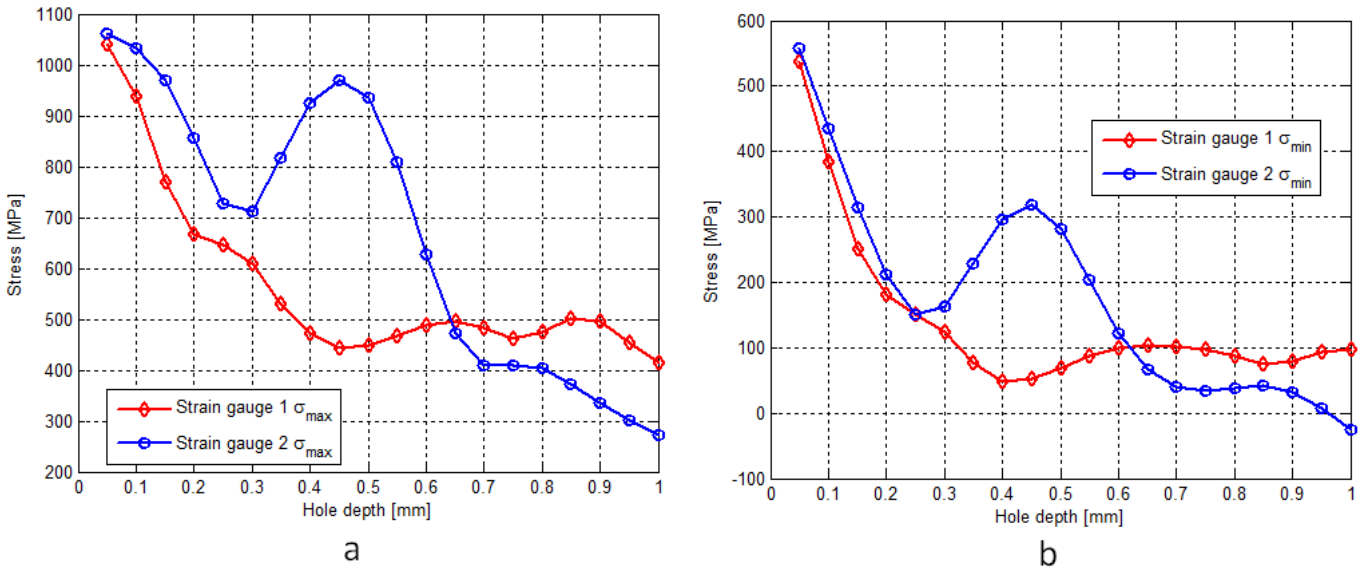

Figure 6.10: Specimen D3 residual stress variation with depth for strain gauge positions 1 and 2 in terms of, a) maximum principal stress and, b) minimum principal stress. [Error bars omitted for image clarity, see Error Analysis]

6.2.4 SPECIMENS A4-D4

The strain gauge rosettes used in specimens A4 and D4 were type B rosettes drilled to a depth of 2mm in total.

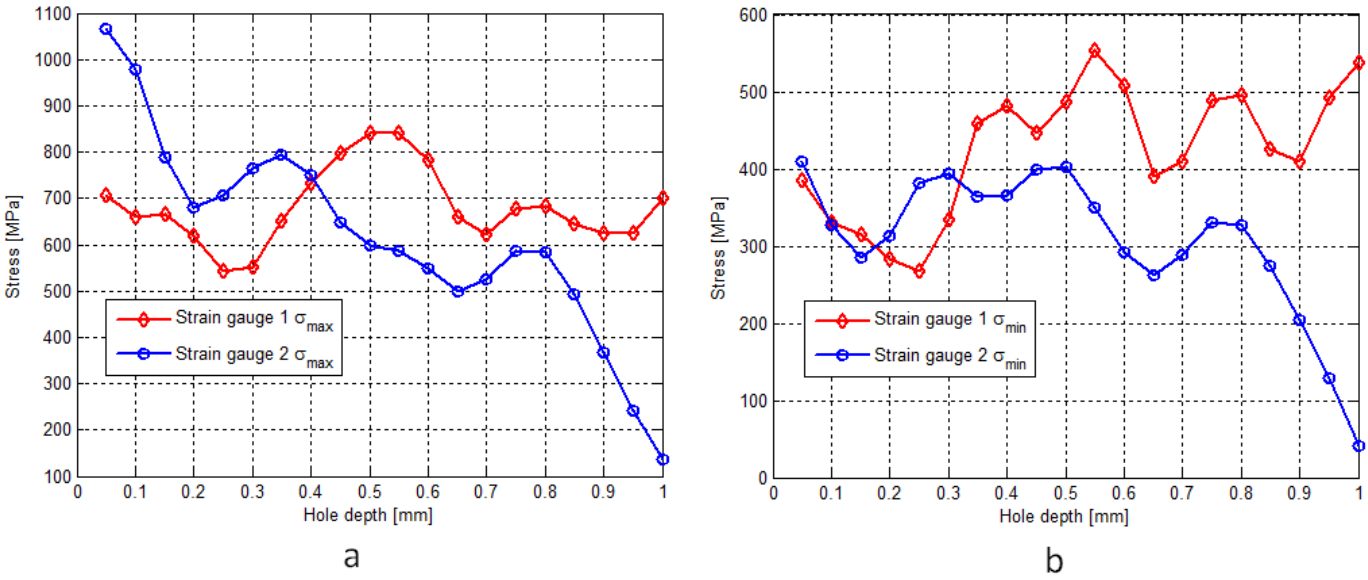

Figure 6.11: Specimen A4 residual stress variation with depth for strain gauge positions 1 and 2 in terms of, a) maximum principal stress and, b) minimum principal stress. [Error bars omitted for image clarity, see Error Analysis]

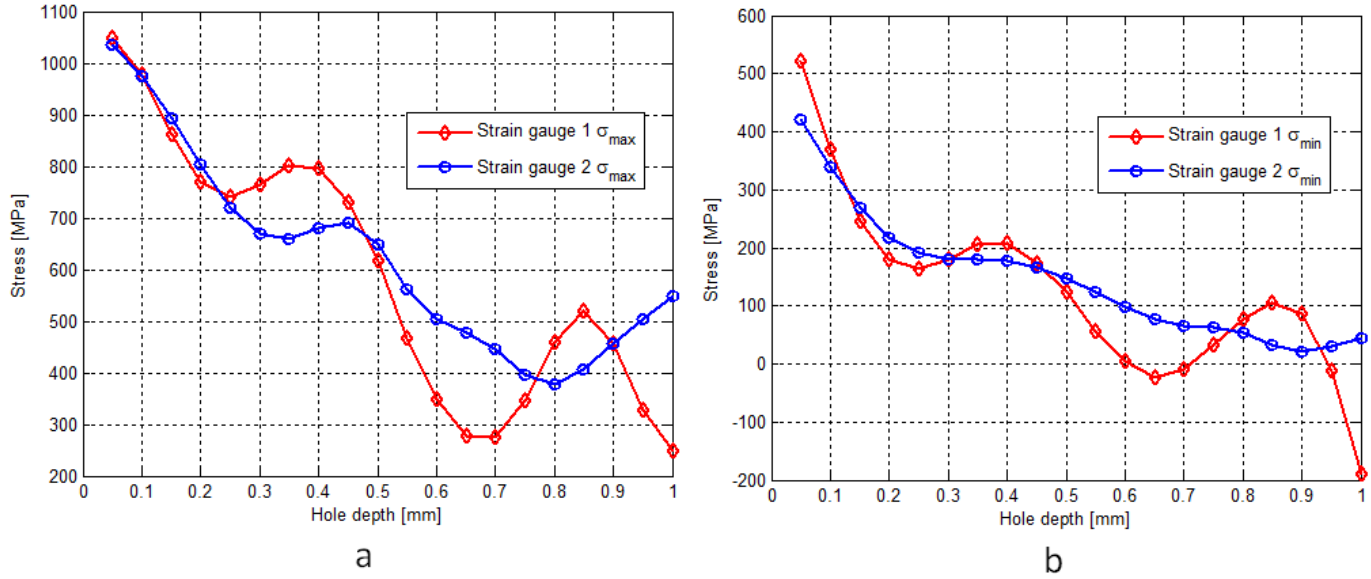

Figure 6.12: Specimen D4 residual stress variation with depth for strain gauge positions 1 and 2 in terms of, a) maximum principal stress and, b) minimum principal stress. [Error bars omitted for image clarity, see Error Analysis]

6.2.5 EFFECT OF HEAT TREATMENT

The post heat treatment evaluation of the specimens designated in Table 6.2 is presented in this section. The residual stress profiles prior to treatment are compared here in terms of their maximum principal stress since this most clearly shows the effects of the heat treatment. The drilling procedures were followed in the same fashion as those prior to the treatment with the exception that the holes were drilled on the opposite side of the specimen to ensure the results were not affected by the previously drilled holes.

The graphical results which follow are partially summarised below in Table 6.3. The average residual stress measurement between both gauge readings on each specimen is presented (values taken from greatest stress level nearest the surface) as well as the corresponding residual stress level present after the heat treatment. The average change in the residual stresses is also given as an indicator to the treatment with the greatest influence.

Table 6.3: Heat treatments and their effect on the maximum principal residual stress levels.

Heat Treatment Type	Specimen	Average Untreated σ_{max} [MPa]	Average Post-treatment σ_{max} [MPa]	Average Stress Level Alleviation
Stress Relief	A1	1030 ± 206	196 ± 18	-81 %
	D1	1015 ± 203	235 ± 22	-76 %
Recrystallization Annealing	A2	995 ± 199	25 ± 2	-97 %
	D2	1006 ± 201	60 ± 5	-94 %
Duplex Annealing	A3	1002 ± 200	82 ± 6	-91 %
	D3	1042 ± 208	50 ± 4	-95 %
Beta Annealing	A4	954 ± 190	78 ± 6	-91 %
	D4	1010 ± 202	93 ± 6	-90 %

6.2.5.1 Stress Relief

Specimens A1 and D1 were subjected to a simple stress relief treatment and their residual stress profiles (maximum principal stress) at both gauge locations are shown in Figure 6.13 and Figure

6.14 respectively. It is evident that the residual stresses have been greatly reduced by this treatment.

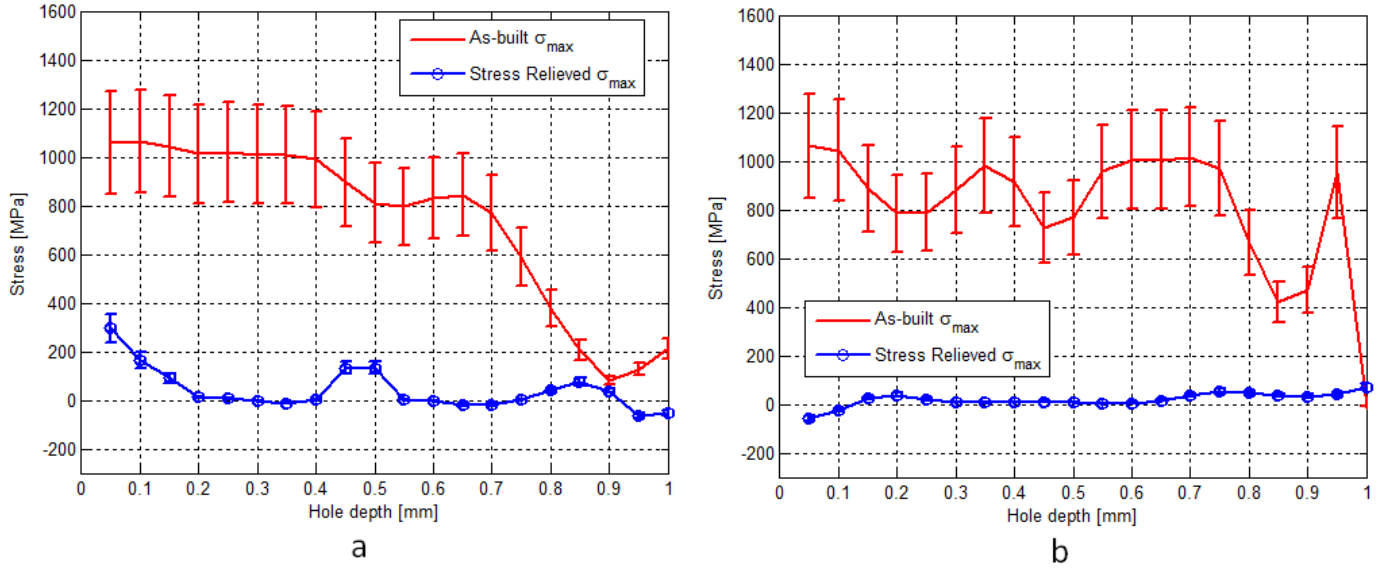

Figure 6.13: Effect of the simple stress relief treatment on the maximum principal stress of specimen A1 at, a) Gauge position 1 and, b) Gauge position 2. (Refer to Figure 6.5 for the principal stress states in the as-built specimen).

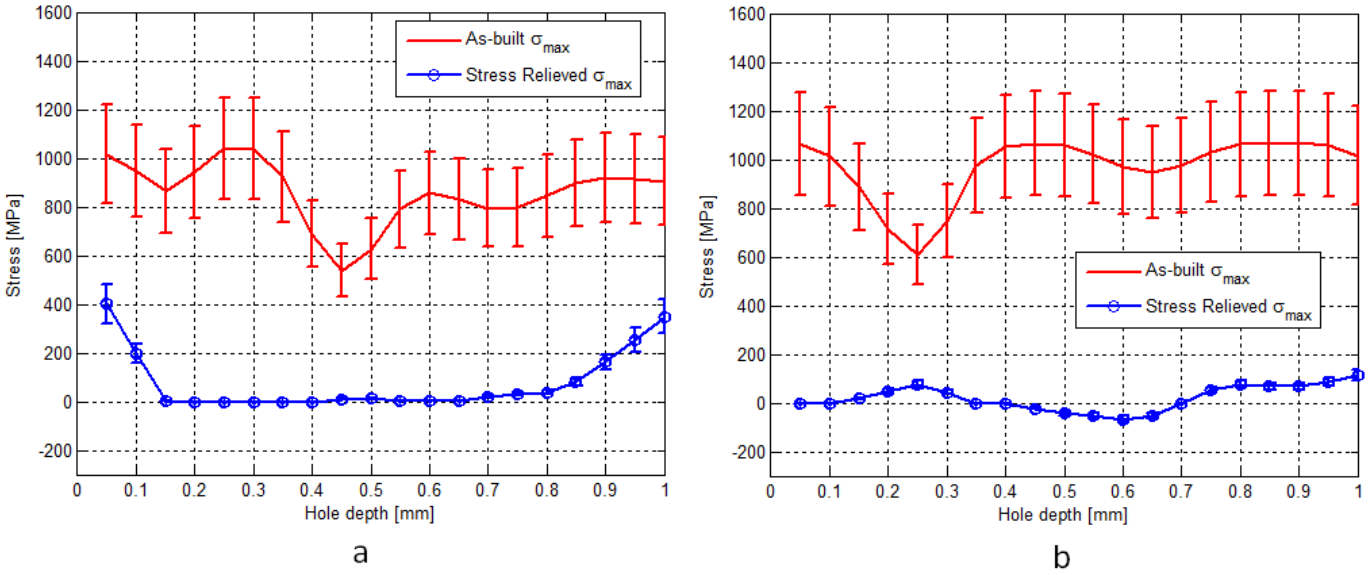

Figure 6.14: Effect of the simple stress relief treatment on the maximum principal stress of specimen D1 at, a) Gauge position 1 and, b) Gauge position 2. (Refer to Figure 6.6 for the principal stress states in the as-built specimen).

6.2.5.2 Recrystallization Annealing

Specimens A2 and D2 were subjected to a recrystallization annealing and their residual stress profiles (maximum principal stress) at both gauge locations are shown in Figure 6.15 and Figure 6.16 respectively. The residual stresses have also been reduced significantly due to this treatment with a large-scale reduction to almost 0 MPa.

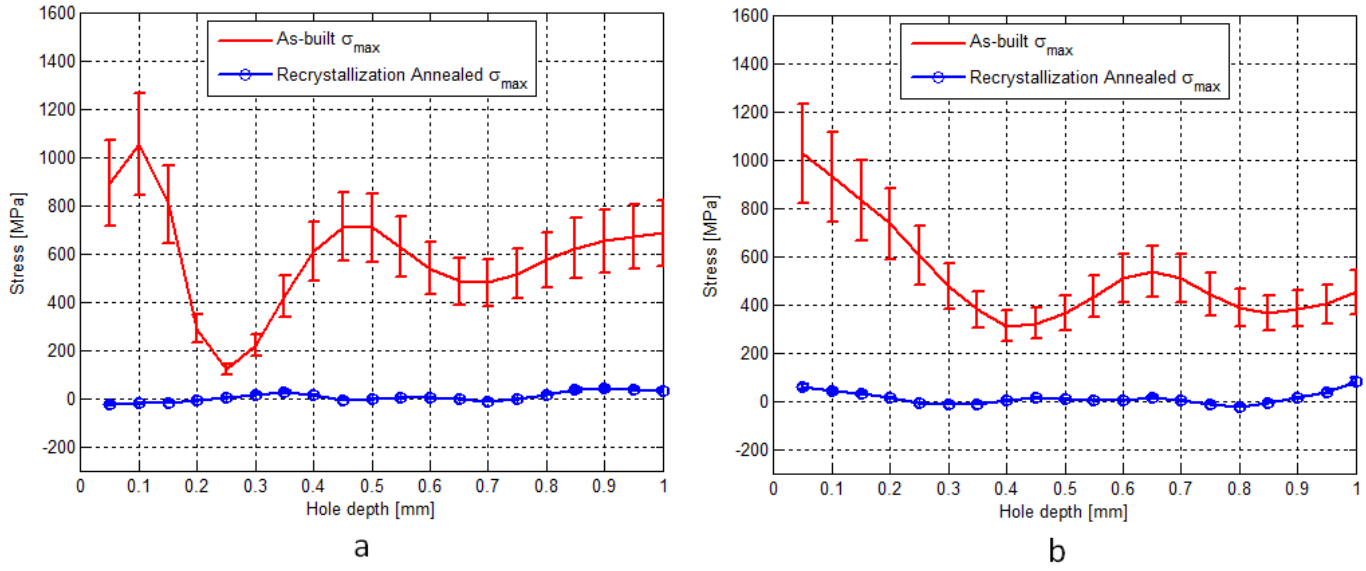

Figure 6.15: Effect of the recrystallization annealing on the maximum principal stress of specimen A2 at, a) Gauge position 1 and, b) Gauge position 2. (Refer to Figure 6.7 for the principal stress states in the as-built specimen).

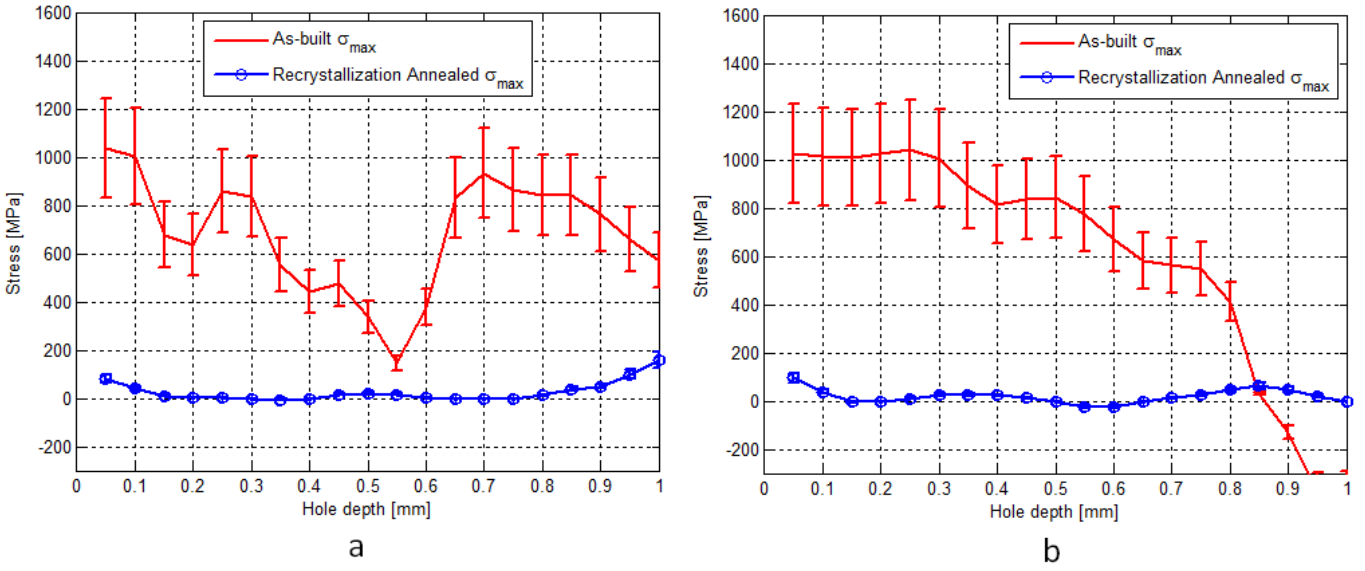

Figure 6.16: Effect of the recrystallization annealing on the maximum principal stress of specimen D2 at, a) Gauge position 1 and, b) Gauge position 2. (Refer to Figure 6.8 for the principal stress states in the as-built specimen).

6.2.5.3 Duplex Annealing

Specimens A3 and D3 were subjected to a duplex annealing and their residual stress profiles (maximum principal stress) at both gauge locations are shown in Figure 6.17 and Figure 6.18 respectively. Again, the residual stresses have been significantly reduced and it can be noted that the residual stress profiles post heat treatment are much more uniform.

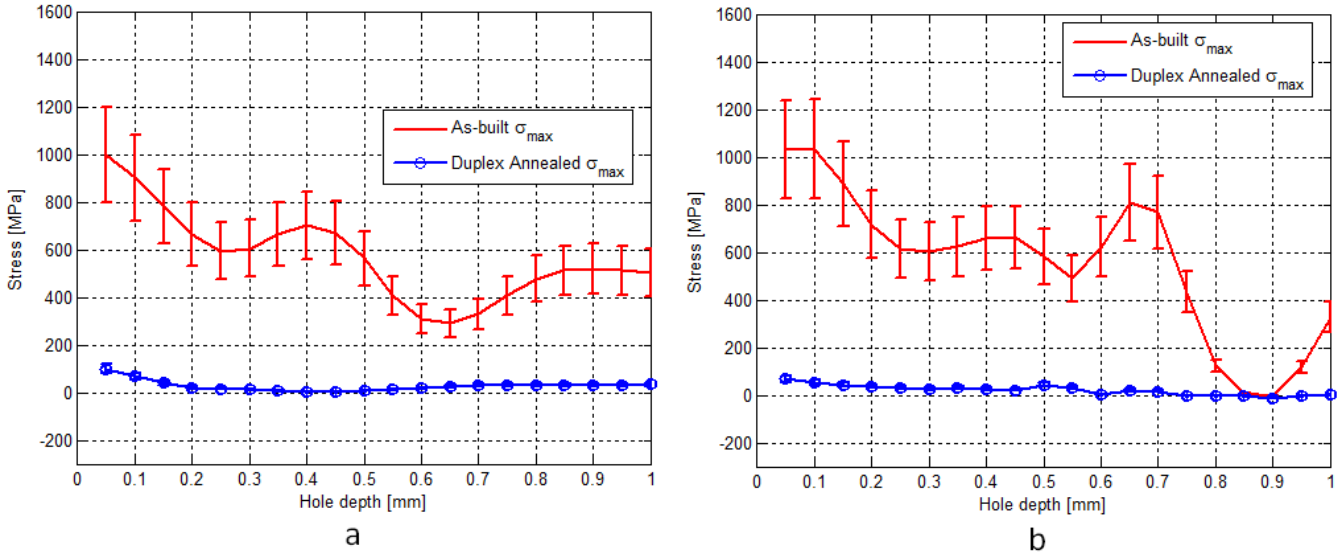

Figure 6.17: Effect of the duplex annealing on the maximum principal stress of specimen A3 at, a) Gauge position 1 and, b) Gauge position 2. (Refer to Figure 6.9 for the principal stress states in the as-built specimen).

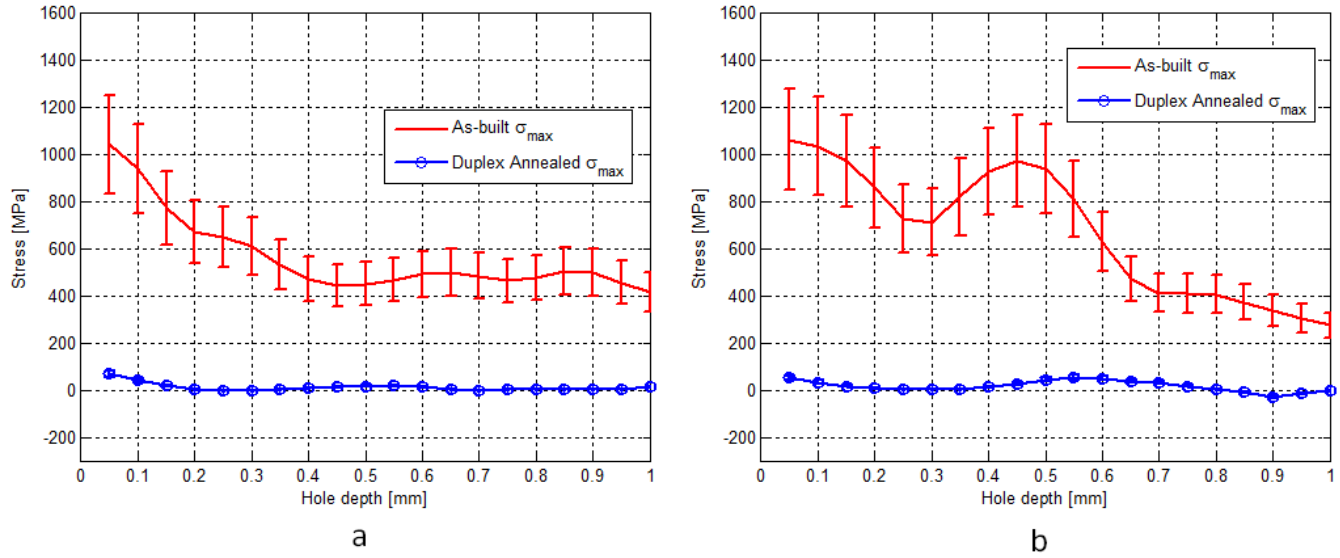

Figure 6.18: Effect of the duplex annealing on the maximum principal stress of specimen D3 at, a) Gauge position 1 and, b) Gauge position 2. (Refer to Figure 6.10 for the principal stress states in the as-built specimen).

6.2.5.4 Beta Annealing

Specimens A4 and D4 were subjected to a beta annealing and their residual stress profiles (maximum principal stress) at both gauge locations are shown in Figure 6.19 and Figure 6.20 respectively. The residual stresses in this final anneal have been greatly reduced as with the other treatments. The rise in stress levels in Figure 6.20b at 1mm in depth is more likely to be measurement error since ASTM E837-08 reduces in accuracy as the depth increases.

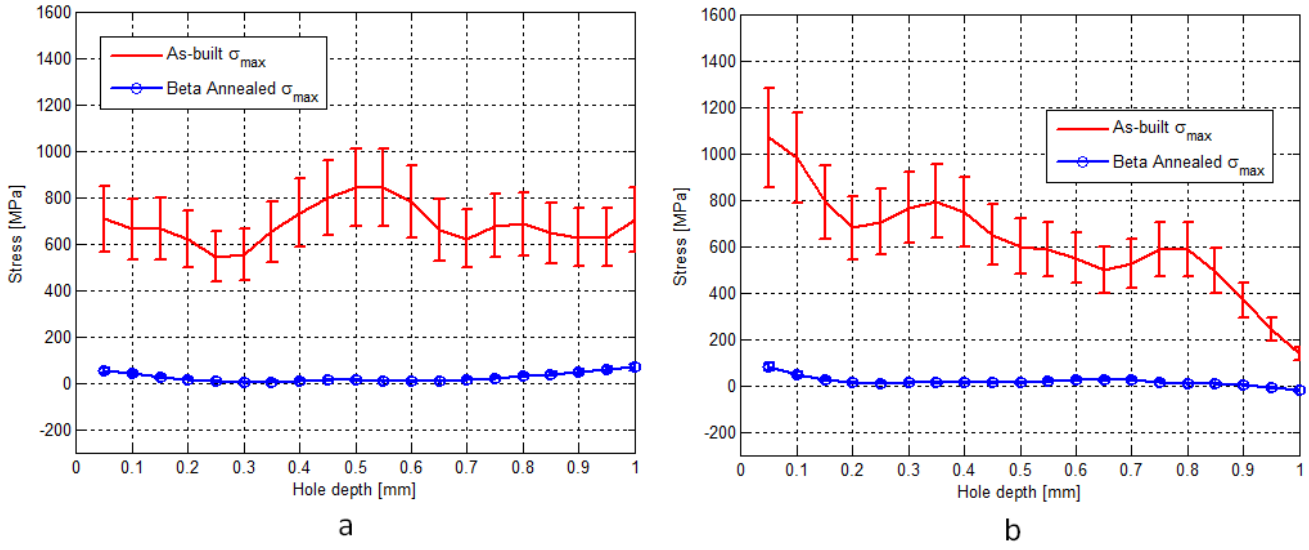

Figure 6.19: Effect of the beta annealing on the maximum principal stress of specimen A4 at, a) Gauge position 1 and, b) Gauge position 2. (Refer to Figure 6.11 for the principal stress states in the as-built specimen).

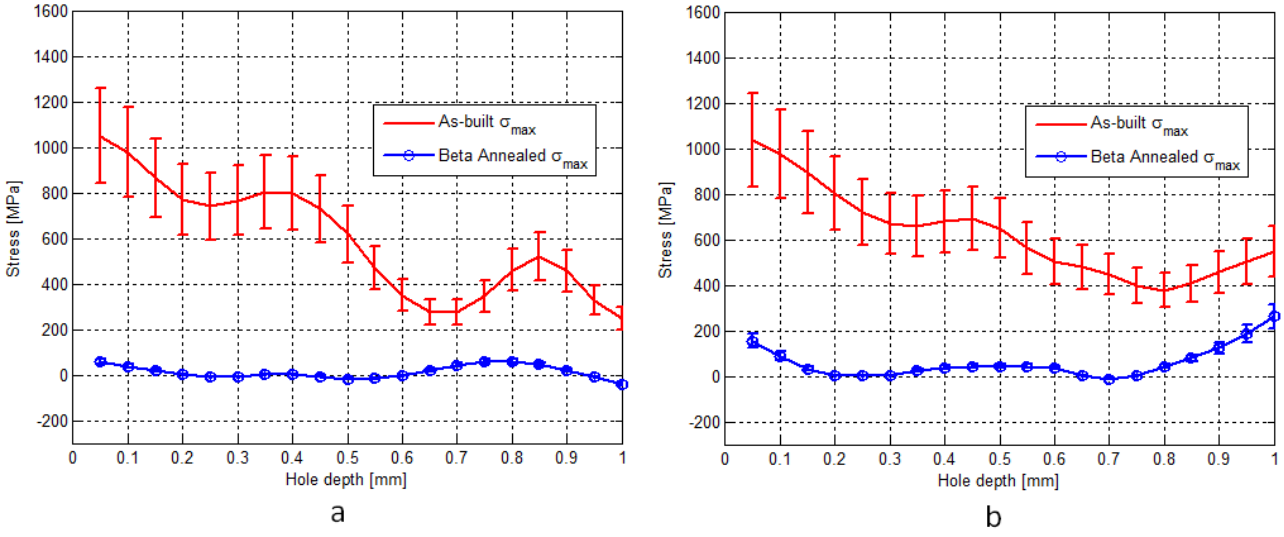

Figure 6.20: Effect of the beta annealing on the maximum principal stress of specimen D4 at, a) Gauge position 1 and, b) Gauge position 2. (Refer to Figure 6.12 for the principal stress states in the as-built specimen).

6.2.5.5 Residual Stress Orientation

The orientation of the residual stresses is determined relative to the strain gauge geometry at the drill position. The angle β is measured clockwise relative to gauge 1 as shown below in Figure 6.21.

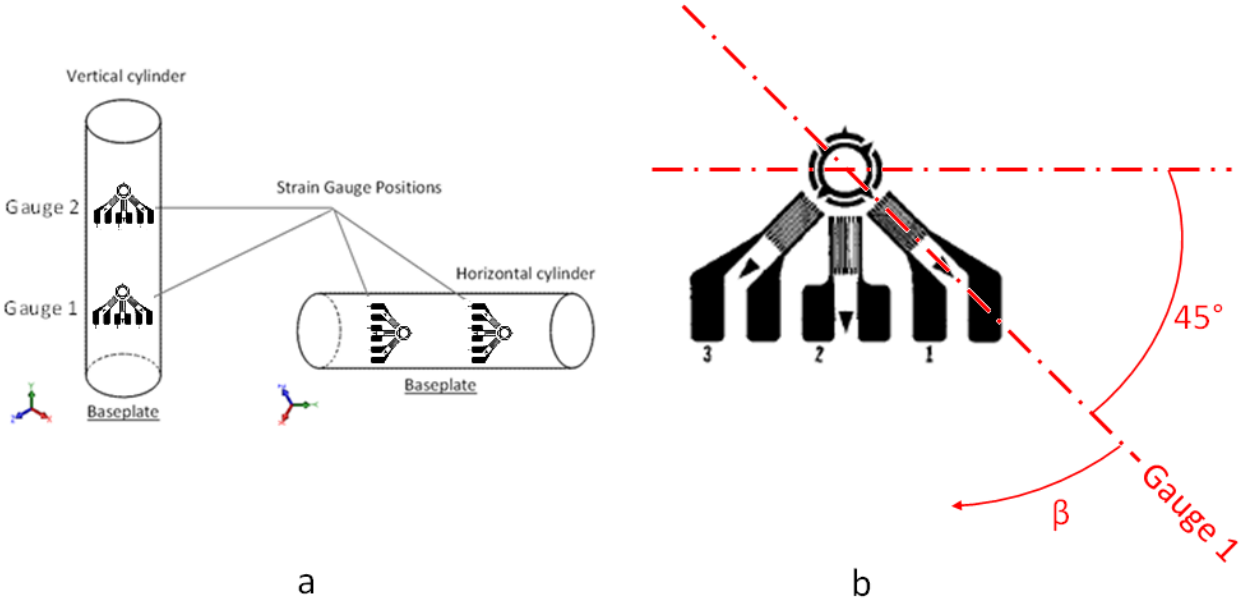

Figure 6.21: a) Position of strain gauges on vertical and horizontal specimens and, b) principal residual stress orientation β as measured from gauge 1 on the strain rosette.

The angle β is determined using the data reduction relationships defined in Chapter 4 in conjunction with the principal stress magnitudes as presented in the previous sections. This section presents the residual stress orientation as determined via ASTM E837-08. A limitation must however be noted here in that the stress correction procedure defined by Sattari-Far [97] does not have the capability of correcting the stress orientation, only the magnitude. Hence the orientation angle β is affected by the inaccuracy due to the high stress magnitudes. The specimens subjected to heat treatment have significantly lower residual stresses and hence the calculation β is not affected by ASTM E837-08's limitation. The results which follow include the orientation β determined prior to heat treatment (purely qualitative) and post heat treatment.

It can be observed from the results in Figure 6.22, Figure 6.23 that the orientation is highly variable which may be consistent with the localised heating strategy of the laser. The scan

pattern for each component may have a significant influence on the orientation changes observed in these results.

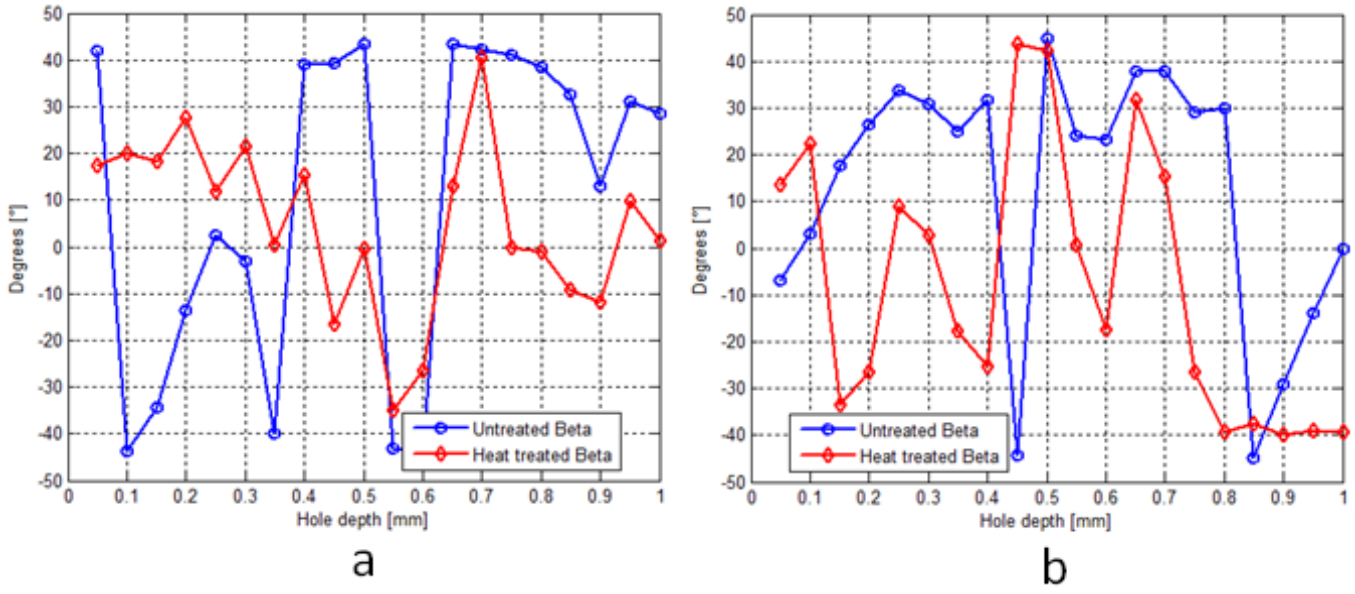

Figure 6.22: Principal stress orientation β clockwise from gauge 1 for a) Specimen A1 and, b) Specimen A2.

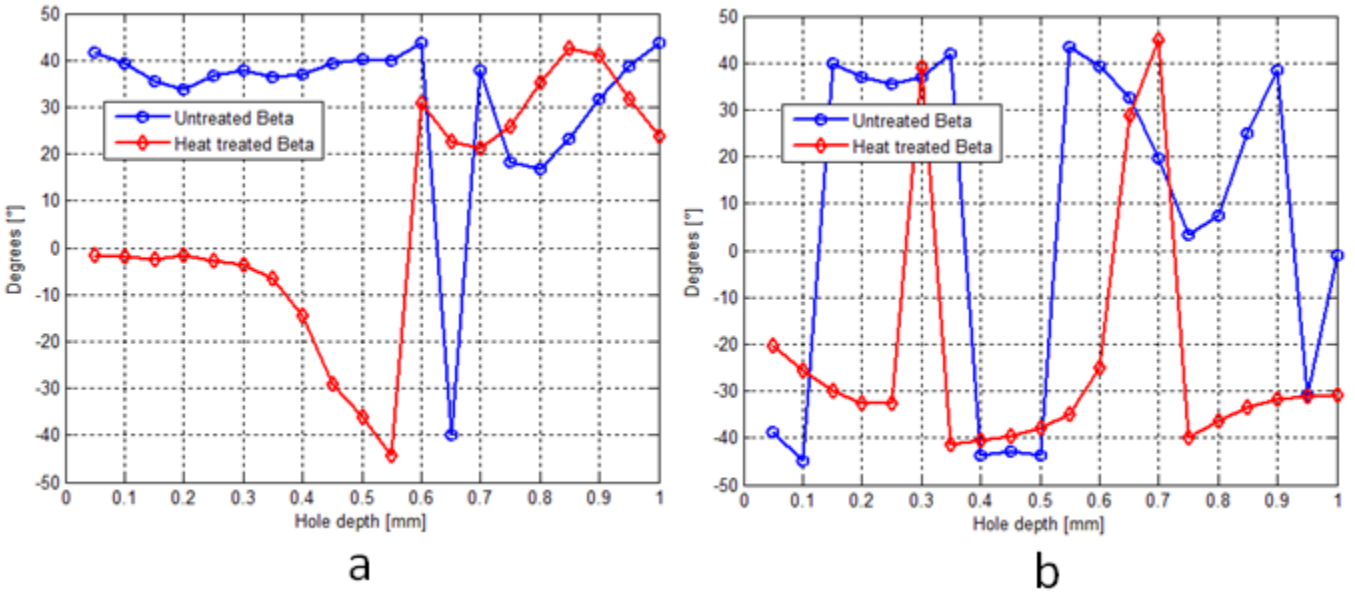

Figure 6.23: Principal stress orientation β clockwise from gauge 1 for a) Specimen A3 and, b) Specimen A4.

The highly variable nature observed in specimens A1-A4 (vertically grown) is similar to that in specimens D1-D4 (horizontally grown). The erratic shifts in orientation in Figure 6.24 and

Figure 6.25 suggest that complex heating gradients are present as the laser traces between the new powder and the previously solidified layer.

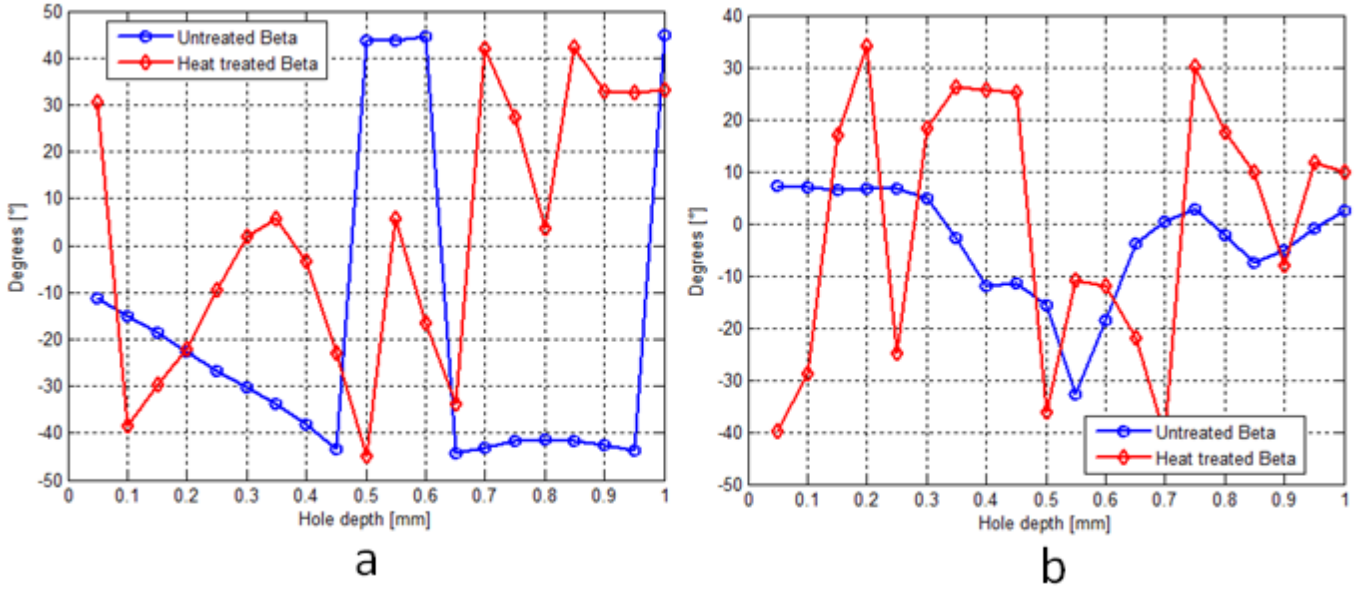

Figure 6.24: Principal stress orientation β clockwise from gauge 1 for a) Specimen D1 and, b) Specimen D2.

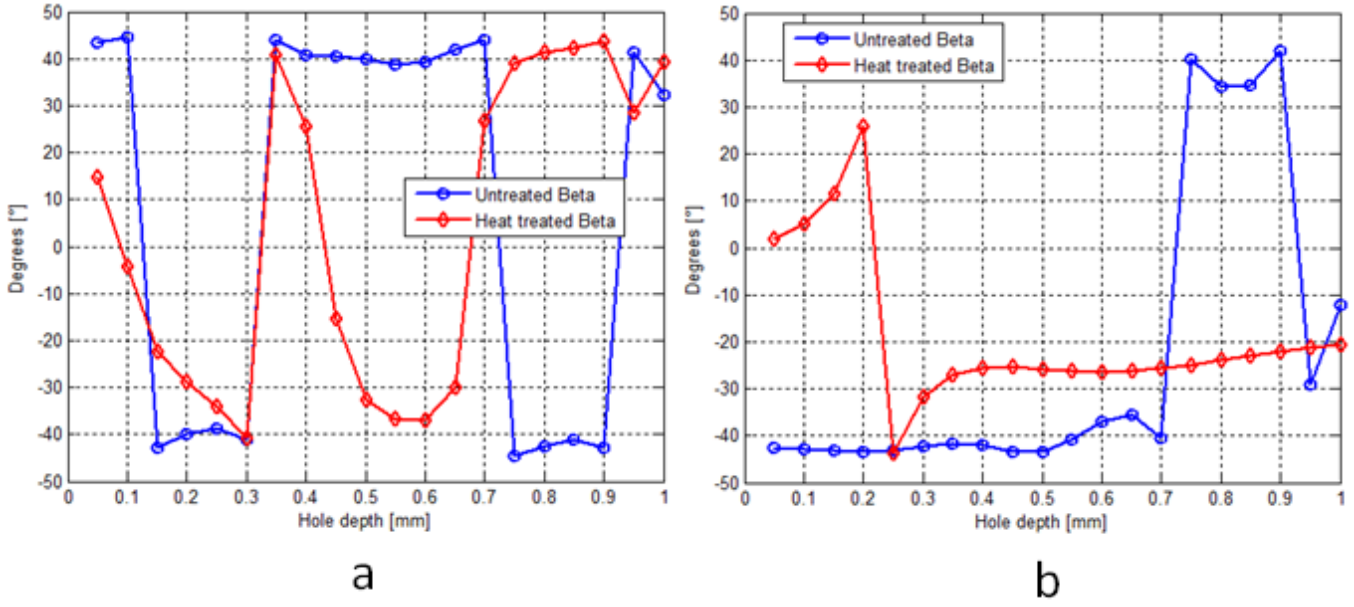

Figure 6.25: Principal stress orientation β clockwise from gauge 1 for a) Specimen D3 and, b) Specimen D4.

6.2.6 ERROR ANALYSIS

The error analysis performed here is under the assumption of uniform residual stresses. This is due to the lack of research into the error estimation for non-uniform residual stresses (no reliable measurement technique in literature has yet been developed). In addition, the correction procedure for high residual stresses developed by Sattari-Far [97] could only provide an uncertainty analysis for uniform residual stresses.

The uncertainty analysis for the residual stress tests was conducted according to the Standards of Measurement and Testing (SM & T) Code of Practise No. 15 [104]. The possible sources of error identified for this study are given below in Table 6.4 below.

Table 6.4: Sources of uncertainty and their effect on the residual stress analysis (adapted from UNCERT Standards of Measurement and Testing (SM & T) Code of Practise No. 15 [104]).

Source of Uncertainty	Range of Uncertainty	Remarks
Test Piece		
Surface	Negligible	Specimen surface was polished
Modulus of Elasticity	±16%	Literature on SLM Ti-6Al-4V still limited
Poisson's ratio	±1%	
Stress distribution o Uniform o Non-uniform	 o ±7% o Unknown	ASTM E837-08 indicates that no study into the uncertainty in non-uniform stress distributions has been undertaken.
Residual stress levels o <50% σ_y o 50 - 70% σ_y o 70 - 100% σ_y	 o Negligible o ±10% o ±17%	Effect of plasticity in specimens with high residual stress is reduced using Sattari-Far's technique. [97]
Distance between measurement points o 5 times drilling diam.	 o ±8%	Measurement distances were always greater than 10 times the

○ 10 times drilling diam.	○ ±2%	drilling diameter
Test System		
Irregularities in hole shape	Negligible	Drill bit replaced after every 3 holes
Drilling depth	Negligible	Vernier accurate to ±0.01mm
Eccentricity	Negligible	
Strain measurement	2 – 5%	From literature
Strain measurement drift	Negligible	From literature
Test Procedure		
Calculation of $\overline{A}$	2 – 7%	Dependant on $\bar{a}$ and $\bar{b}$ for each measurement point
Calculation of $\overline{B}$	2 – 7%	Dependant on $\bar{a}$ and $\bar{b}$ for each measurement point
$\bar{a}$	±2%	See worked example
$\bar{b}$	±2%	See worked example

The error estimation procedure is outlined in Appendix A with a worked example. This analysis was performed on all measurement points to produce the error bars in the graphical results of the previous sections. The average estimated error recorded for the as-built residual stress profiles was approximately 19%. The heat treated specimens produced substantially lower residual stresses which resulted in an average estimated error of 8%. It is also important to note that the principal stress orientation β for the as-built specimens can only be quoted qualitatively here since there is no corrective procedure for the excessive residual stress levels (the work by Sattari-Far [97] applies to the residual stress magnitude only) and thus the error is unknown. The next section describes the physical properties determined in this study.

6.3 PHYSICAL PROPERTIES

6.3.1 DENSITY

The density of the specimens was determined through both the traditional Archimedes water displacement principle (ASTM B311-08) and the optical technique described in the Experimental Methods chapter. The results of these tests are shown below in Table 6.5 for the specimens prior to heat treatment.

Table 6.5: Density test results from ASTM B311-08 and the optical method.

Specimen	ASTM B311-08 [%]	Optical Test [%]
A1	99.75	99.7
A2	99.69	99.5
A3	99.68	99.6
A4	99.74	99.6
D1	99.73	99.8
D2	99.73	99.7
D3	99.57	99.6
D4	99.68	99.5
Average	**99.69**	**99.63**

The density was evaluated such that the similarity between SLM Ti-6Al-4V and other industry forms can be assessed. The manufacturers of SLM machines often quote densities approaching 100% and the results from this study suggest that this is not an exaggeration. The mechanical properties determined through the micro-flaw exposure and hardness testing regimes are presented in the next section.

6.4 MECHANICAL PROPERTIES

6.4.1 HARDNESS

The hardness tests were conducted in order to supplement the information gained on the effect of heat treatment on the specimens. The results from the hardness evaluation are listed in Table 6.6 below. Note the mean hardness value is reported here with the standard deviation.

Table 6.6: Hardness values obtained for the Ti-6Al-4V specimens prior and post heat treatment.

Heat treatment	Specimens	Average Hardness [HV_{10}]	Standard Deviation [HV_{10}]
As-built	All	379	5
Stress-relief	A1, D1	377	9
Recrystallization Anneal	A2, D2	342	4
Duplex Anneal	A3, D3	308	4
Beta Anneal	A4, D4	367	5

The hardness and density properties of SLM Ti-6Al-4V were evaluated in order to further clarify the differences/similarity with other conventionally produced Ti-6Al-4V variants. The next section describes the load-deflection behaviour from the micro-flaw exposure rig.

6.4.2 SPECIMEN LOAD-DEFLECTION RESULTS

The force on the specimens was dependant on the deformation experienced by the ring under load and hence is measured using readings from the strain gauges positioned along the edge of the ring. The force required to break each specimen was established from the data acquisition system upon completion of each test. The elongation was estimated using a position potentiometer which measured the precise number of turns of the tensioning nut. This was translated into specimen elongation using the bolt pitch for the M12 load bolts. The correction procedure described in Chapter 5 was used to account for the deformation of the rig. The figures which follow describe the deflection of the specimens as the load is increased. The graphical results are summarised below in Table 6.7.

Table 6.7: Stress and elongation data from the data acquisition system.

Specimen	Heat treatment	Elongation at break [mm]	Percentage Elongation	Load Applied at Break [N]
B1	None	2.1 ± 0.3	5.2% ± 1.4%	6568 ± 330
C1	None	1.8 ± 0.3	4.5% ± 1.6%	5755 ± 290
B2	None	2.1 ± 0.3	5.2% ± 1.4%	5807 ± 290
C2	None	1.9 ± 0.3	4.7% ± 1.5%	6082 ± 300
B3	Stress Relief	2.8 ± 0.4	7.0% ± 1.4%	8376 ± 420
C3	Stress Relief	2.6 ± 0.4	6.5% ± 1.5%	6184 ± 310
B4	Recrystallization Anneal	4.1 ± 0.5	10.3% ± 1.8%	5444 ± 270
C4	Recrystallization Anneal	3.9 ± 0.5	9.7% ± 1.4%	5347 ± 260
B5	Duplex Anneal	4.0 ± 0.5	10.0% ± 1.8%	6390 ± 320
C5	Duplex Anneal	4.4 ± 0.5	11.0% ± 1.8%	6316 ± 310
B6	Beta Anneal	3.1 ± 0.4	7.7% ± 1.3%	5950 ± 300
C6	Beta Anneal	3.7 ± 0.5	9.2% ± 1.4%	5985 ± 300

The graphical results in Figure 6.26 to Figure 6.30 are grouped according to their processing. The first load-deflection relationships in Figure 6.26 were determined from specimens in their as-built condition. The results for the stress-relieved specimens are given in Figure 6.27. Figure 6.28 illustrates the behaviour of recrystallization annealed specimens. Figure 6.29 and Figure 6.30 show the load-deflection behaviour of specimens which were duplex and beta annealed respectively. The linear region is of particular interest in these results since this is the region of the greatest accuracy. The initial loading intervals up to approximately 1000N are hampered by slippage and misalignment of the tensile rig which produces data points which can be somewhat irregular. At load intervals greater than 1000N however, the rig is tensioned sufficiently to force the correct alignment of the components and the linear region reflective of the material's behaviour under load persists. A trend line has been plotted through the linear regions in Figure 6.26 - Figure 6.30 to demonstrate the loading behaviour. The data points at high loads which

plateau away from the linear region demonstrate the plastic zone of the material. At excessive loads (approx. 6000N), the yield strength of the SLM specimens has been exceeded and plastic deformation occurs which tends to relax the force transmitted through the specimen. This plastic region produced somewhat variable results which is indicative of the unpredictability of material behaviour beyond the yield strength.

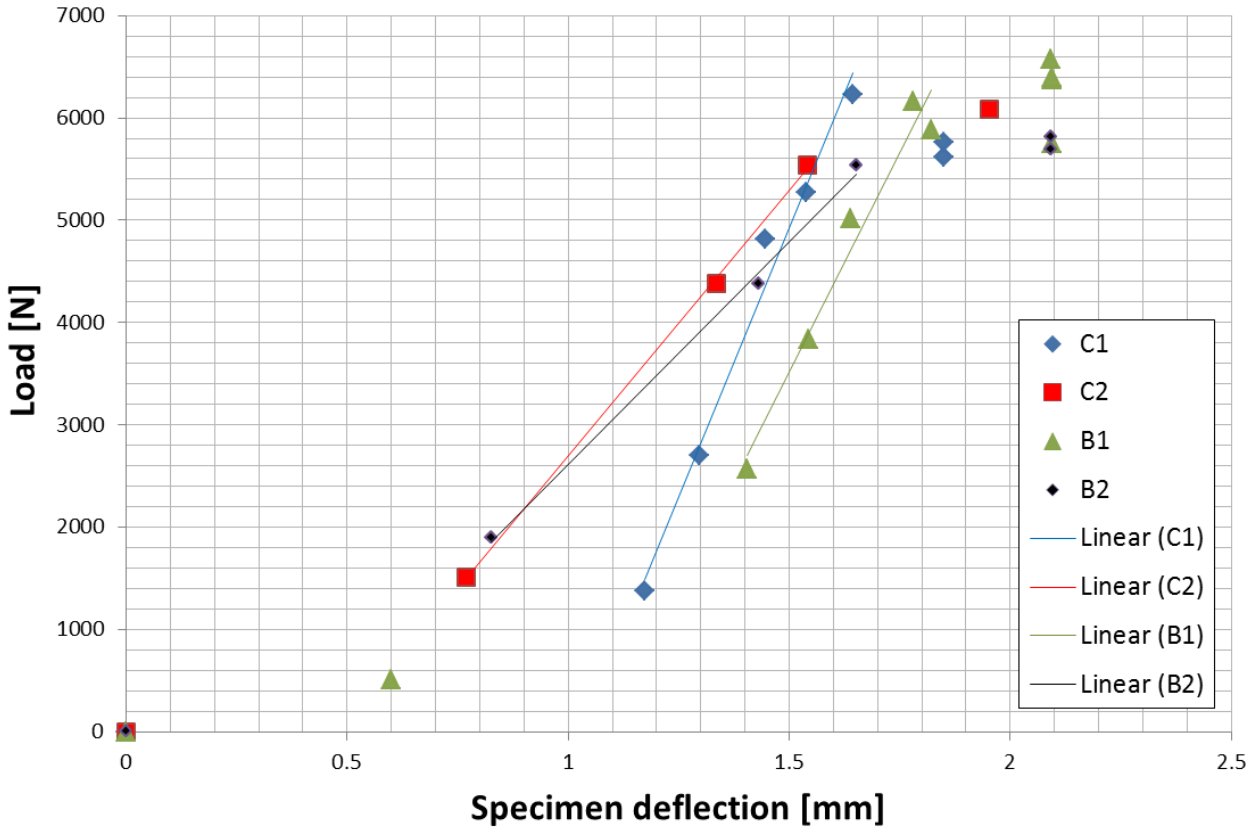

Figure 6.26: Load-deflection graph for the as-built SLM Ti-6Al-4V specimens.

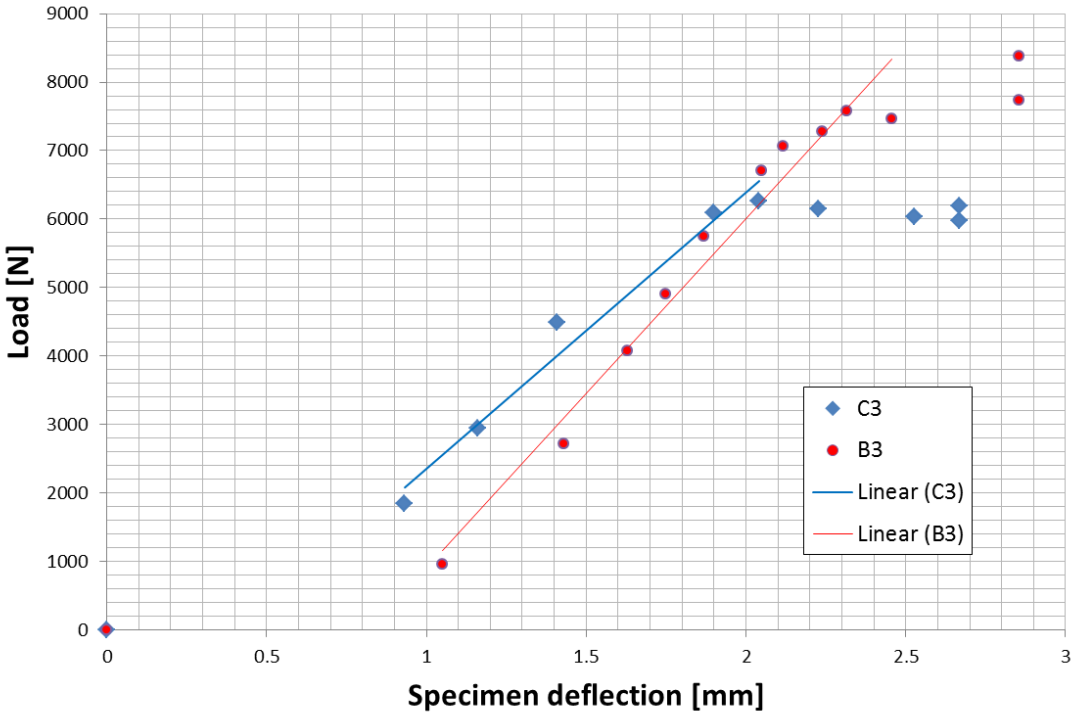

Figure 6.27: Load-deflection graph for the Stress-Relieved SLM Ti-6Al-4V specimens.

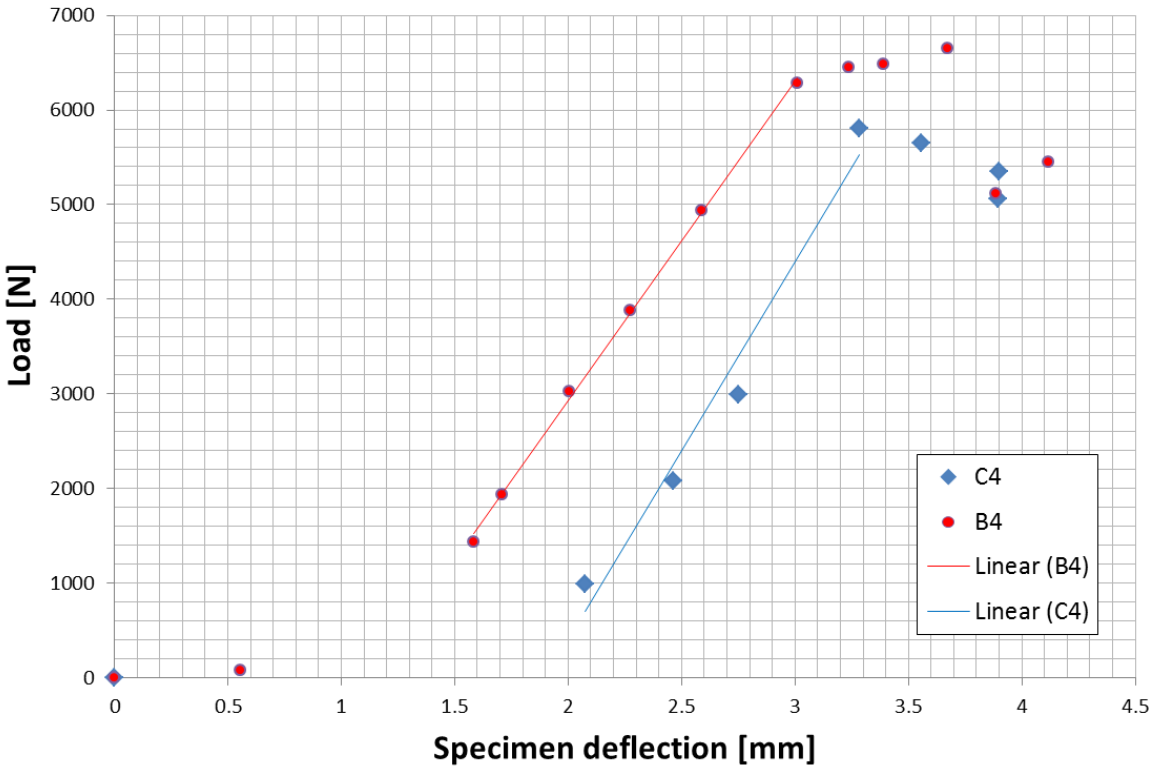

Figure 6.28: Load-deflection graph for the Recrystallization Annealed SLM Ti-6Al-4V specimens.

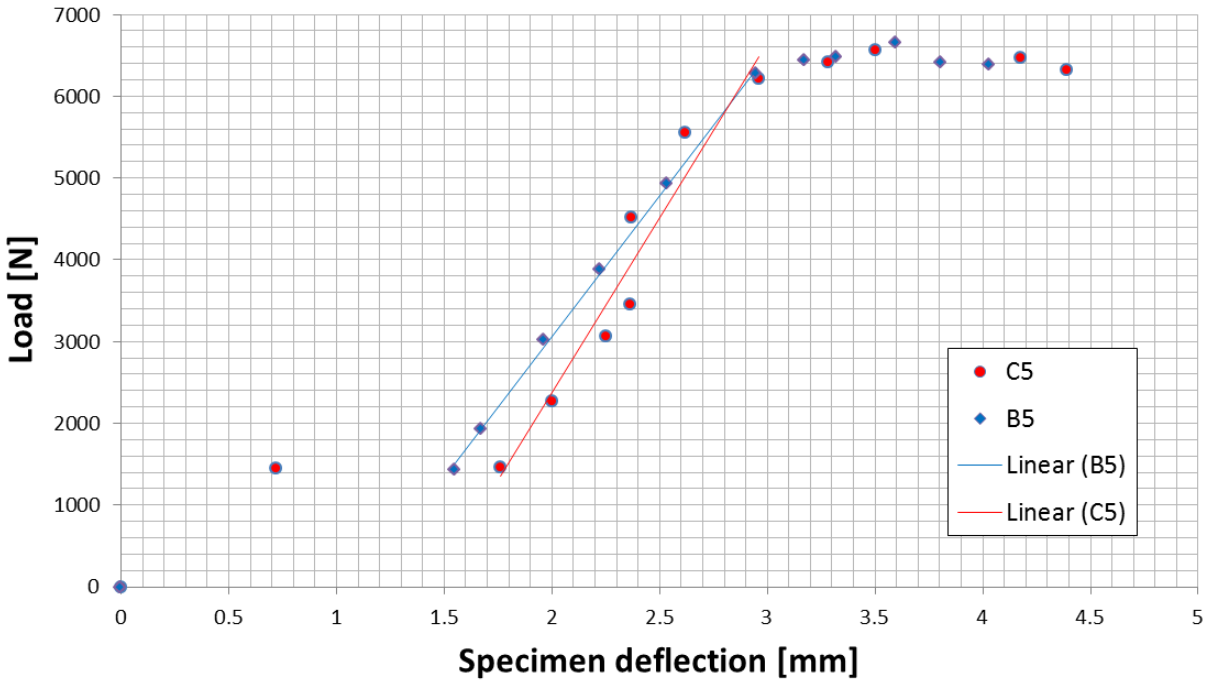

Figure 6.29: Load-deflection graph for the Duplex Annealed SLM Ti-6Al-4V specimens.

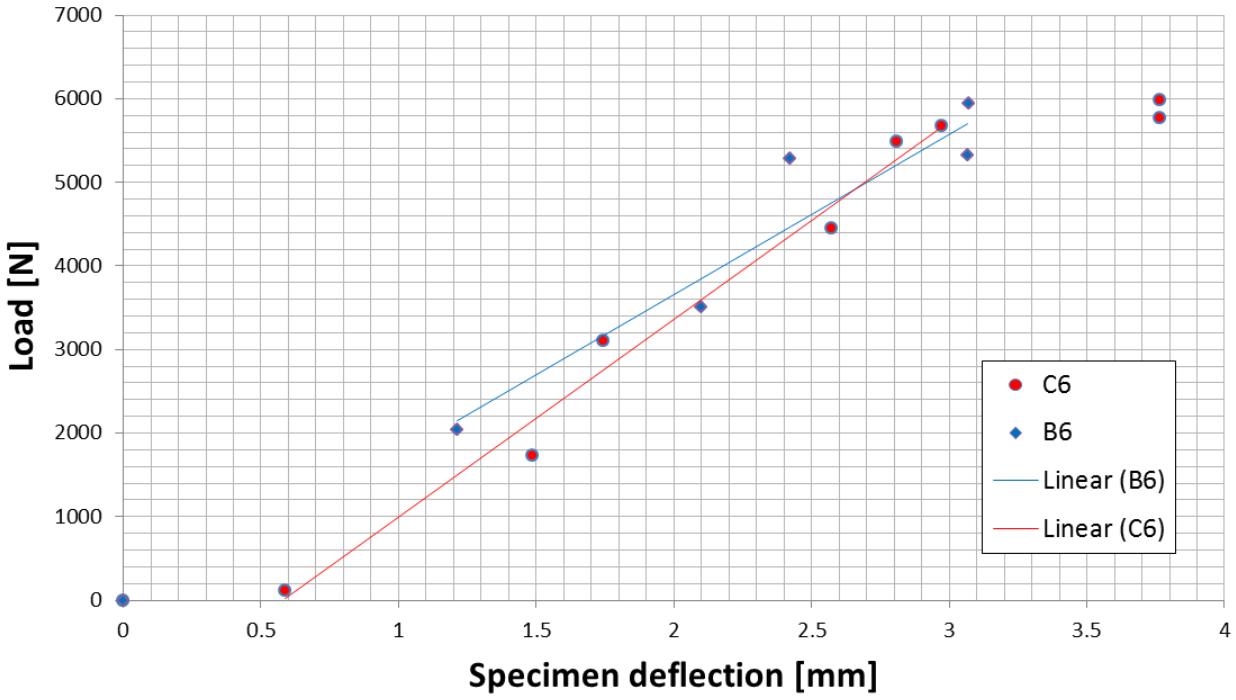

Figure 6.30: Load-deflection graph for the Beta Annealed SLM Ti-6Al-4V specimens.

The next section presents the microscopy work performed before and after heat treatments. This testing was undertaken primarily to infer possible performance changes in the material behaviour due to microstructure transformation based on that reported in literature. Microstructural changes affect the behaviour of a material in terms of its strength, fracture toughness, crack growth rates, creep behaviour etc.

6.5 MICROSTRUCTURE

The microstructure of the SLM Ti-6Al-4V specimens was examined in the as-built condition and after the heat treatments to ascertain any microstructural effects. The microstructure was also examined for porosity and micro-flaws inherent in the specimens from the manufacturing process. The sections which follow present the micrographs of both polished and etched specimens obtained from an optical microscope.

6.5.1 AS-BUILT CONDITION

The microstructure of the SLM produced Ti-6Al-4V is presented in the series of images which follow. The microstructure present in the as-built specimens is shown in Figure 6.31 below. The microstructure in Figure 6.31 is comprised of a martensitic 'needle-like' structure with fine α' plates. This microstructure is very similar to that reported by Hooreweder in Figure 3.12b. This indicates that the SLM process was performed at optimal parameters.

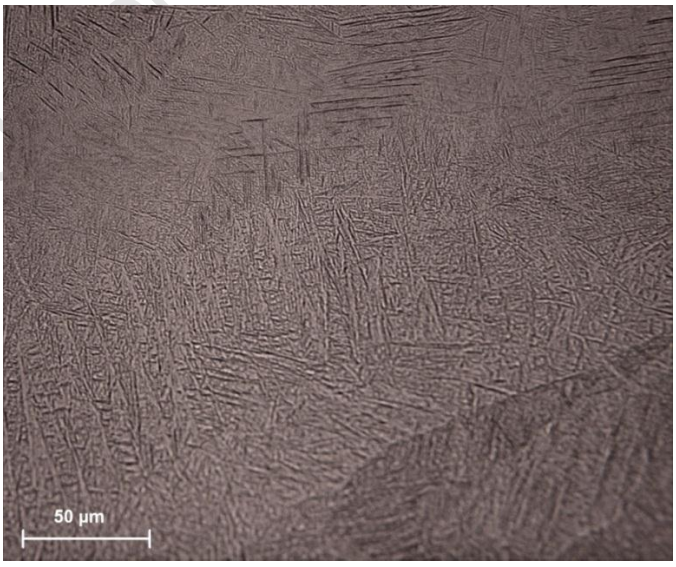

Figure 6.31: As-built microstructure in specimen A1 prior to heat treatment.

6.5.2 STRESS RELIEVED

The stress relieved samples in Figure 6.32 and Figure 6.33 do not show any significant change from the original as-built microstructure in Figure 6.31. As before with the untreated specimens, note the thin α' martensite present in the microstructure.

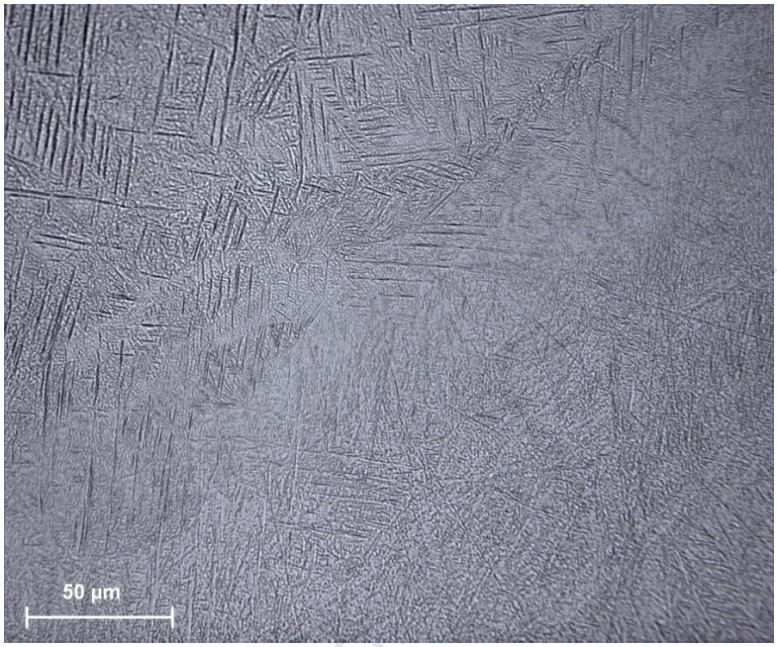

Figure 6.32: Specimen A1 etched (stress relief treatment).

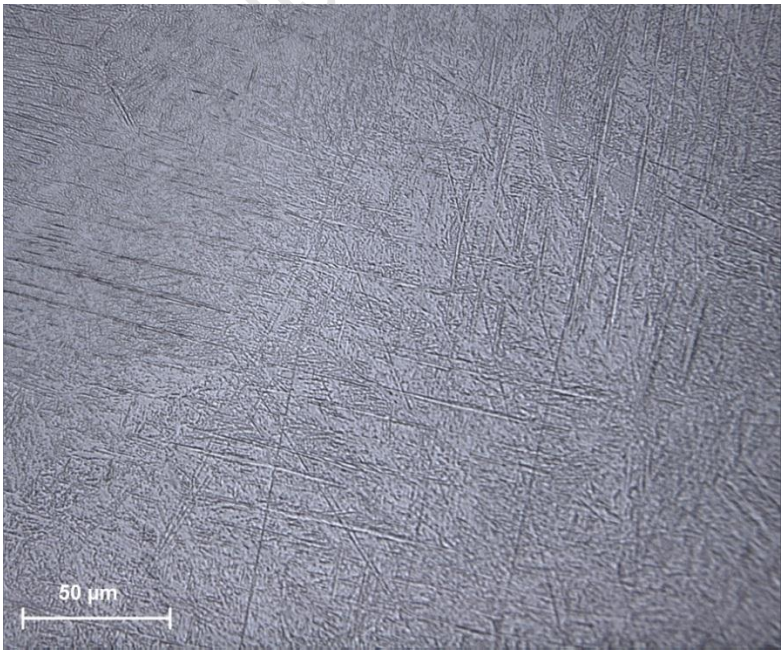

Figure 6.33: Specimen D1 etched (stress relief treatment).

6.5.3 RECRYSTALLIZATION ANNEALED

The recrystallization anneal showed drastic changes on the microstructural level as is clear in Figure 6.34 and Figure 6.35. This microstructure has transformed into a coarse lamellar microstructure which consists of primary α in a matrix of transformed β containing acicular α.

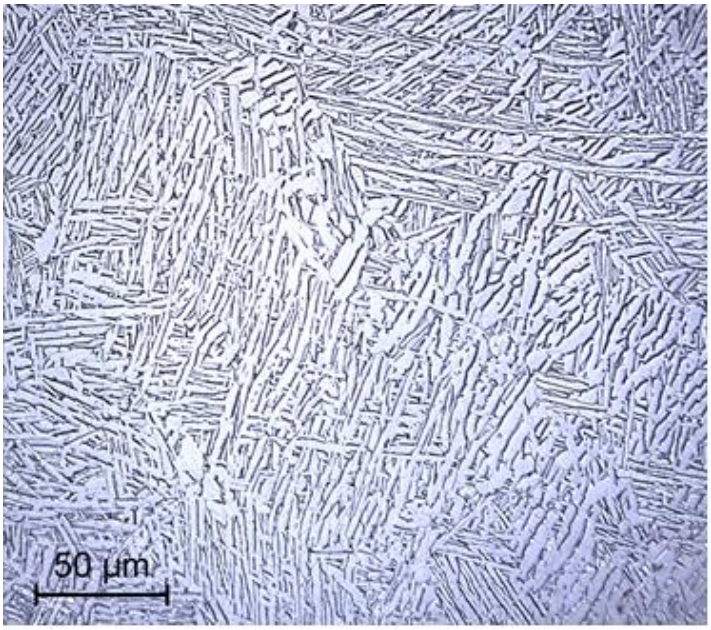

Figure 6.34: Specimen A2 etched (Recrystallization Anneal).

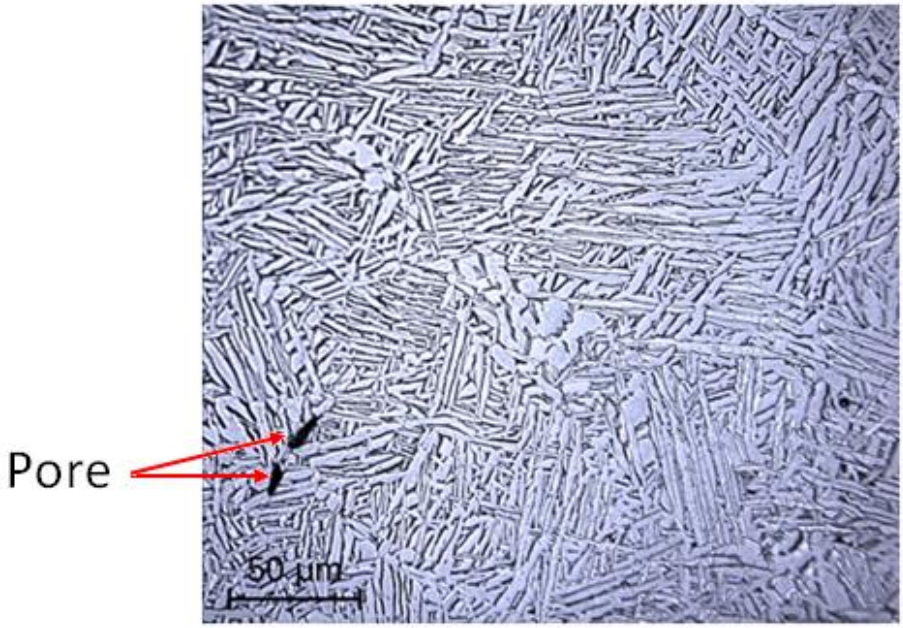

Figure 6.35: Specimen D2 etched (Recrystallization Anneal) showing pores approximately 10µm in length.

6.5.4 DUPLEX ANNEALED

The duplex anneal had an equally drastic change to the microstructure as shown in Figure 6.36 and Figure 6.37. This microstructure has transformed from a martensite into one with small amounts of equiaxed α in a matrix of acicular α (transformed β).

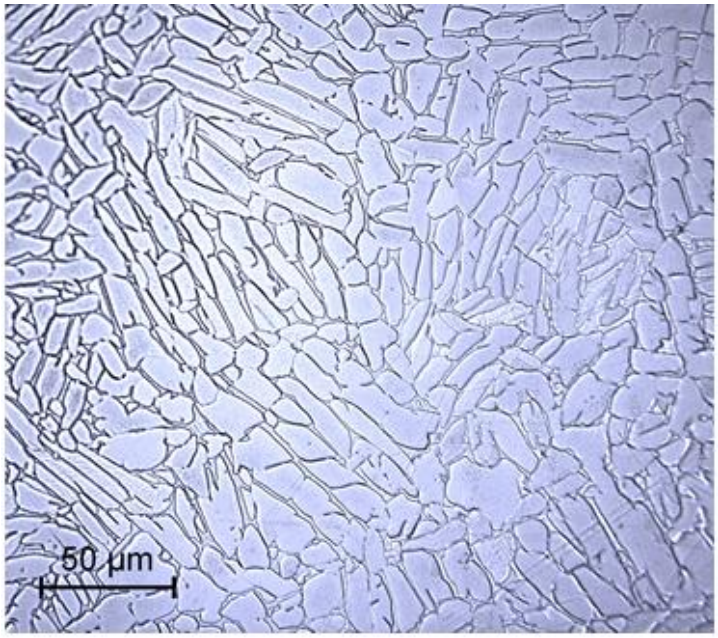

Figure 6.36: Specimen A3 etched (Duplex Anneal).

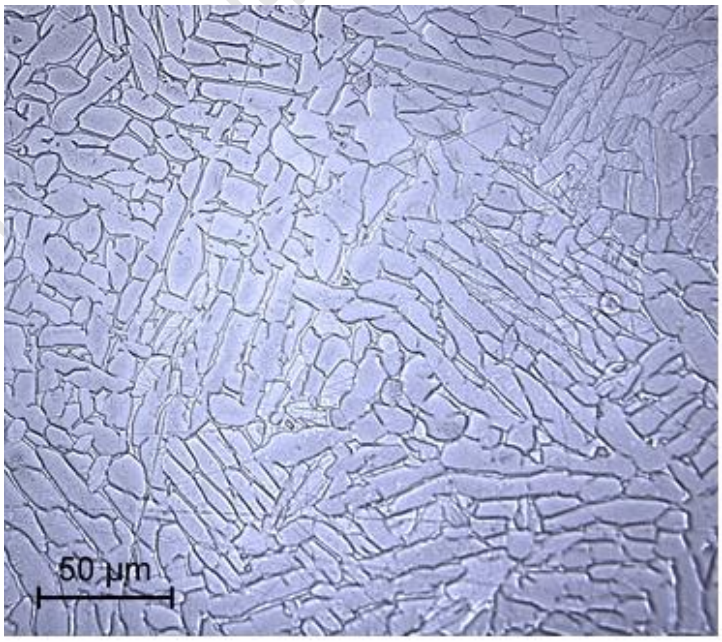

Figure 6.37: Specimen D3 etched (Duplex Anneal).

6.5.5 BETA ANNEALED

The beta anneal also produced changes on the microstructural level as with the other annealing treatments as shown in Figure 6.38 and Figure 6.39. The microstructural change produced a fine microstructure consisting of acicular α (transformed β) with prior β grain boundaries. The 'fineness' of this microstructure is evidence of a moderate cooling rate from above the β-transus.

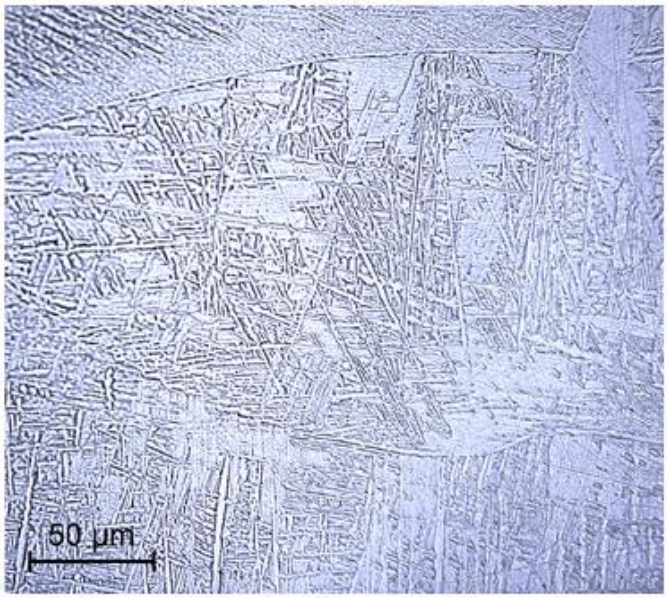

Figure 6.38: Specimen A4 etched (Beta Anneal).

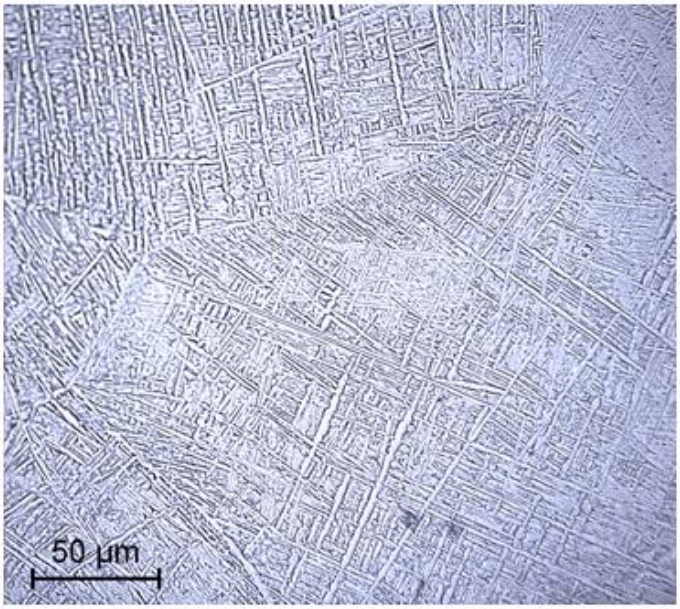

Figure 6.39: Specimen D4 etched (Beta Anneal).

6.5.6 MICRO-FLAWS AND POROSITY

The microscopy work was conducted in order to determine the microstructure of this material and to evaluate any porosity or micro-flaws which are known to afflict laser-based manufacturing systems. The presence of significant porosity is understood to reduce the structural integrity of a component. This section describes the porosity and micro-cracking observed in several of the specimens.

The level of porosity in most of the specimens was very low yet in specimen D3, significant porosity was found at a sampling point in the build plane as shown in Figure 6.40. This porosity was only observed in one sample of this specimen and all other areas examined in D3 indicated a microstructure relatively free of porous material.

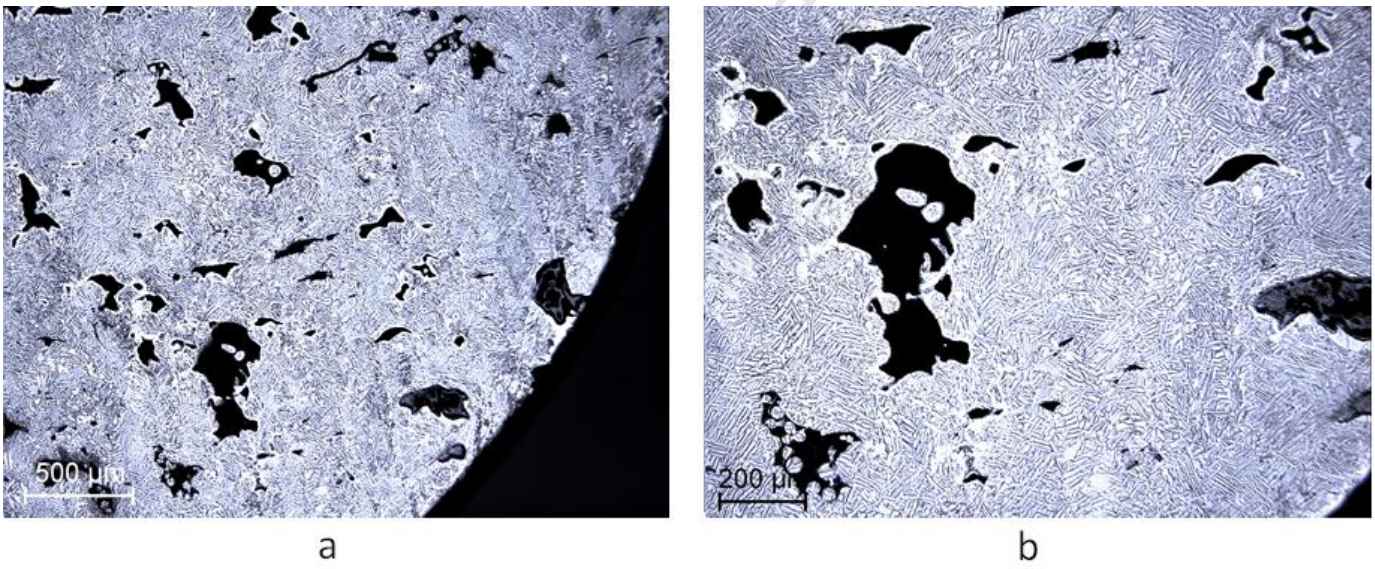

Figure 6.40: Porosity in the build plane observed in specimen D3.

The selection of images in Figure 6.41 and Figure 6.42 confirm the discovery of two circumferential cracks in the plane perpendicular to the building direction in specimen A2 and A3 respectively. The location of the crack on both specimens is approximately 12mm from the baseplate. The porosity observed in the plane of the crack is shown in Figure 6.41b and Figure

6.42b for specimen A2 and A3 respectively. The crack in specimen A3 was only observed after polishing whereas the crack in A2 could be seen in the as-built condition.

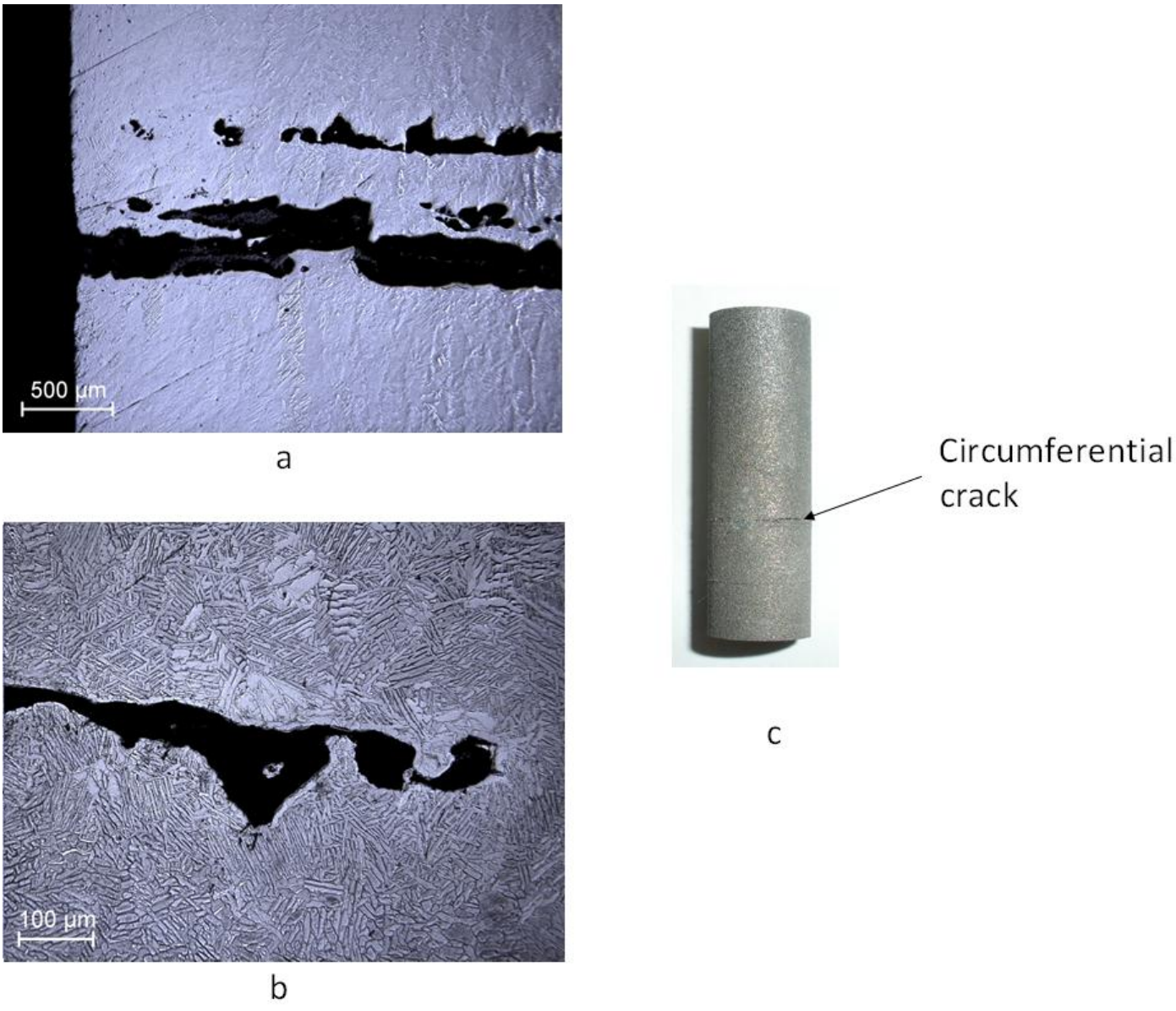

Figure 6.41: Circumferential crack in specimen A2, a) micrograph of crack opening, b) micrograph of layer porosity in the crack plane leading to the crack (etched) and, c) location of the crack on the surface of specimen A2.

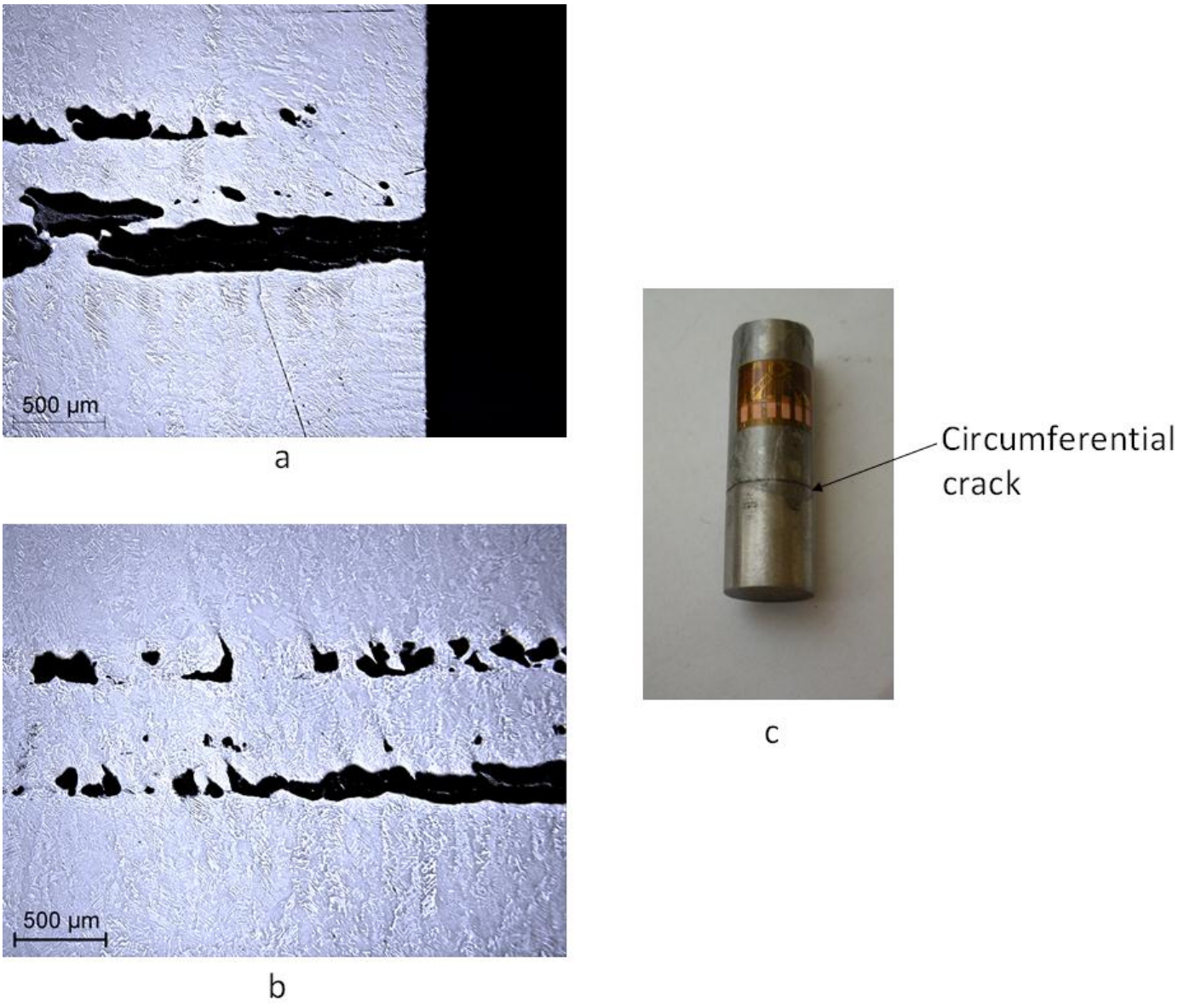

Figure 6.42: Circumferential crack in specimen A3, a) micrograph of crack opening, b) micrograph of layer porosity in the crack plane leading to the crack and, c) location of the crack on the surface of specimen A3.

Having completed the primary analysis into the residual stress fields and the microscopy analysis, the micro-flaw exposure work using the miniaturised tensile rig is presented next.

6.6 MICRO-FLAW EXPOSURE

This section contains the observations made during the loading of the specimens using the miniature tensile rig as explained in the previous chapter. The visual inspection of the micrographs captured during this process revealed some micro-flaw changes and the development of cracks at the sharp edges of pores as in Figure 6.43 below. The images in Figure 6.44 were captured at 11 successive loading increments from which the material reaction to the applied load is visible in surface texture change and distortion. Surface cracking was observed as the stress approached and exceeded the yield strength and a significant change in the surface texture was noticed in Figure 6.44. Micro-cracks developing from several corners of a small pore are shown in Figure 6.45 as the loading increased. The general expansion of surface cracks can also be seen in Figure 6.45.

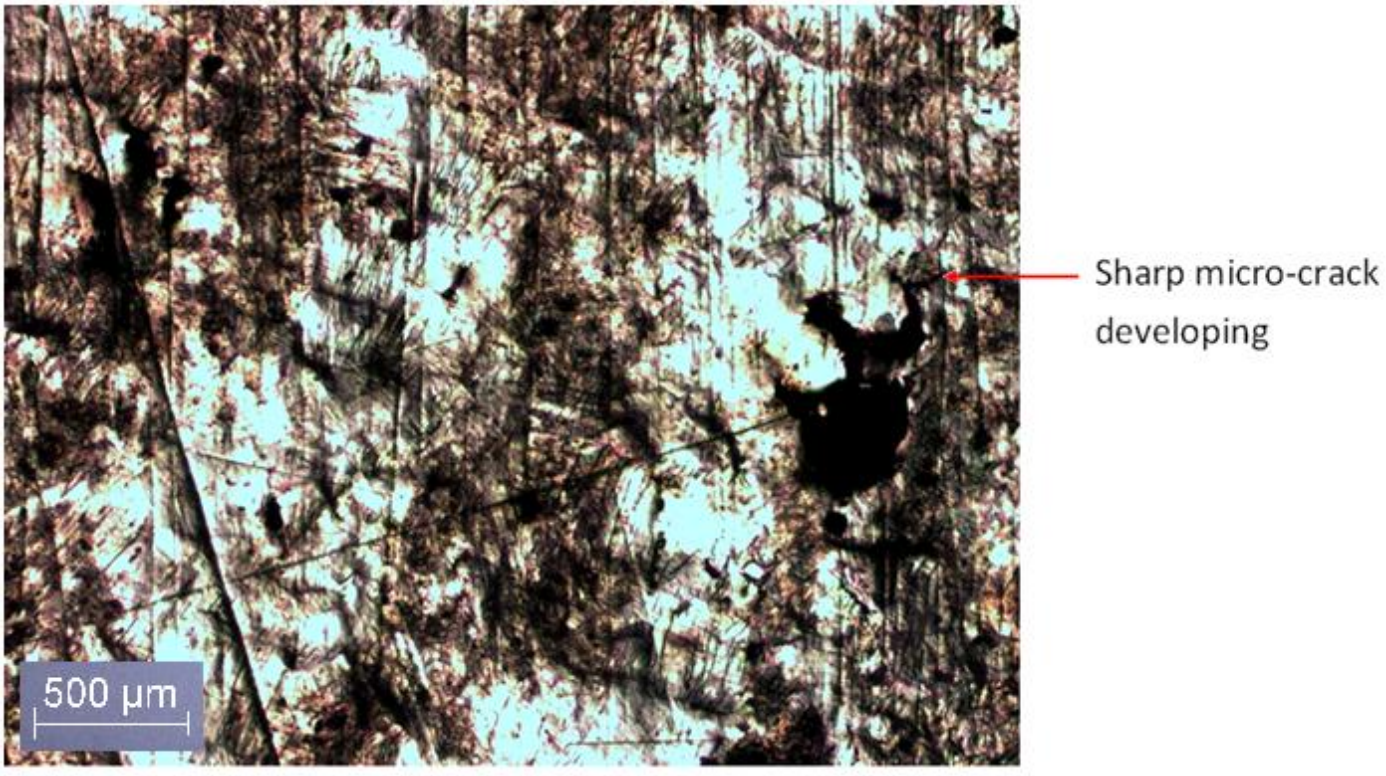

Figure 6.43: Sharp micro-crack developing at the edge of a pore in specimen C6 at a loading interval of 4444N.

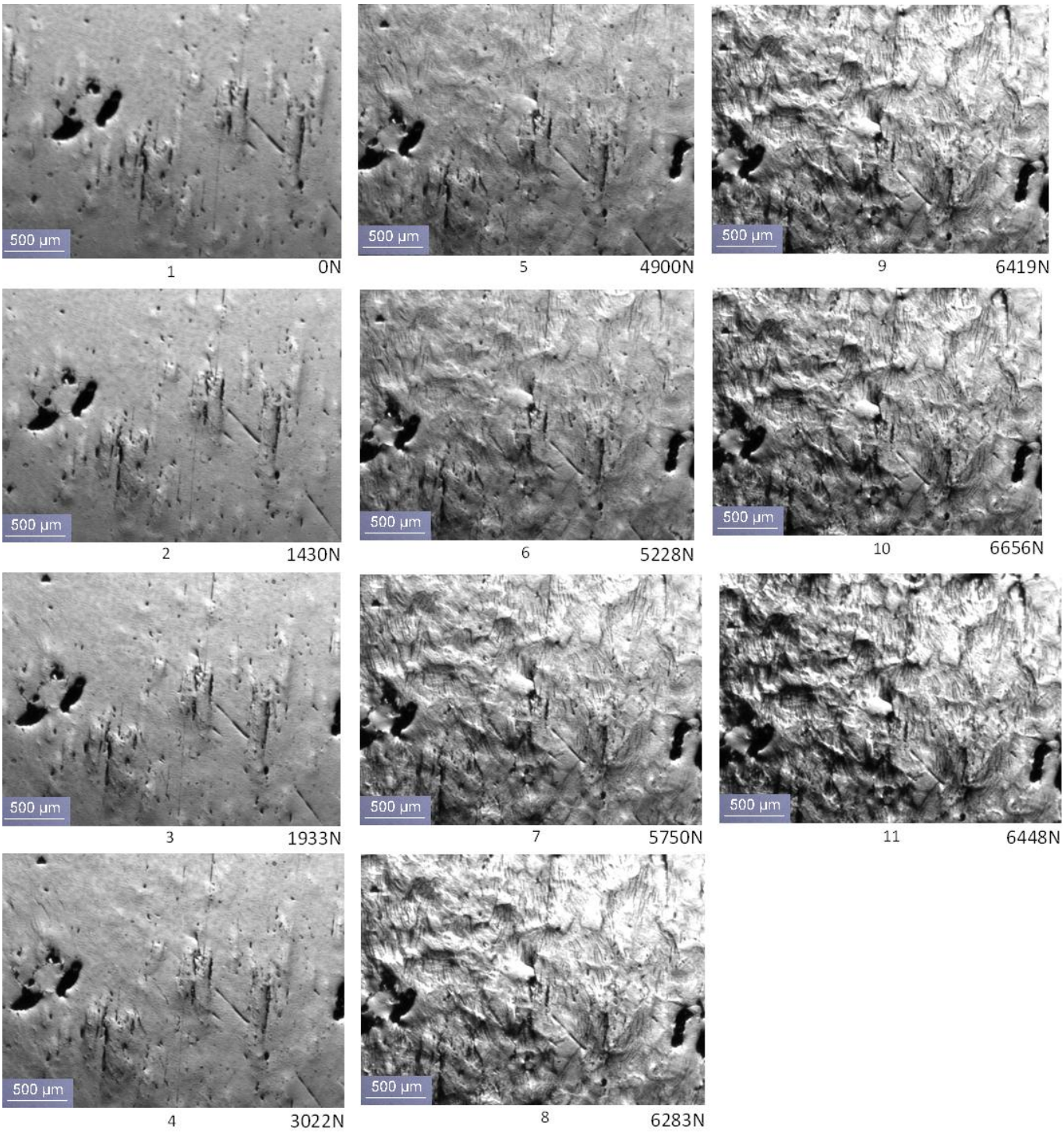

Figure 6.44: Progressive yielding and texture changes observed in specimen C4 with loading intervals numbered 1-11. (NB: The load reported at the bottom of each image is the load registered on the miniature tensile rig at the time the image was captured)

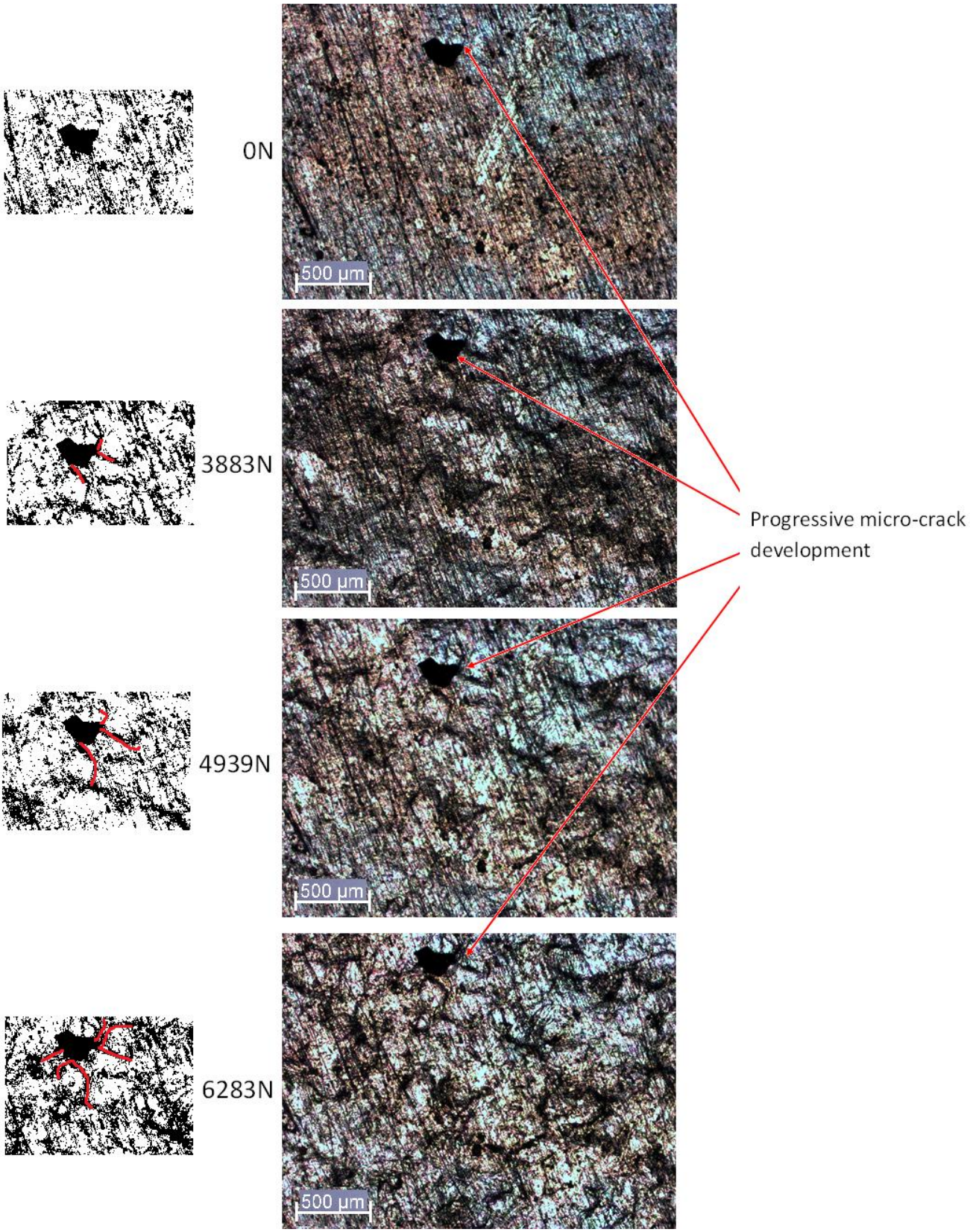

Figure 6.45: Progressive micro-crack development at increasing tensile loading in specimen B4.

6.6.1 DIGITAL IMAGE CORRELATION

The ability of the Digital Image Correlation software to map the strains along the material surface was hampered by poor image quality produced by the camera system. This reduced the number of pixels which could be successfully correlated using the code produced by Eberl et al [103]. The limitations which prevented successful image correlation are listed below and are further discussed in the Chapter 7 with the intention of identifying modifications which could be made to the design to improve the effectiveness of the rig.

- Loading fluctuated as the yield limit of the material was exceeded.
- Deformation of the specimen required re-focussing of the microscope lens.
- Effectiveness of the torsion control screws was reduced as excessive force caused bending of the screw tips.
- Microscope camera produced poor image quality.
- Rigid body motion is problematic when using DIC software to analyse the micrographs.

6.7 SUMMARY

This chapter has presented the results obtained from the various evaluations on the SLM Ti-6Al-4V performed in this study. The residual stress fields in the pilot specimens received from the CFRM were evaluated using the hole-drilling method (ASTM E837-08) which led to the acquisition of more specimens for further study. The primary residual stress analysis revealed excessively high residual stresses in the order of 1000MPa which warranted an investigation into the effect of heat treatments in reducing residual stresses in SLM Ti-6Al-4V. This was successfully undertaken where four different heat treatments indicated that typically 90-95% of the residual stress could be alleviated through the use of an appropriate heat treatment. The microstructural changes and a physical property evaluation were performed to supplement the research on this material. The evaluation of the micro-flaws under a tensile load was attempted using the miniature tensile rig; however successful Digital Image Correlation was not possible due to poor image quality from the microscope. The chapter which follows discusses these results in detail and infers conclusions based on the evidence presented in this chapter. Improvements on the tensile rig are also suggested for future work in developing a successful system for which DIC software can be more readily used.

CHAPTER 7 - DISCUSSION

7.1 INTRODUCTION

This study is comprised of four sections; the pilot study, the residual stress evaluation, the microstructure/microscopy analysis and the micro-flaw exposure investigation. This chapter discusses the results presented in the previous chapter and draws logical conclusions from comparisons with the available literature. The main objective of this thesis is to further the understanding in the new Selective Laser Melting (SLM) manufacturing technique and to identify the areas of concern in components built using this process.

7.2 PILOT/PRELIMINARY RESIDUAL STRESS ANALYSIS

The CFRM provided 2 pilot specimens for this study which were deemed unfit for their intended purpose following deformation when the components were removed from the machine baseplate. The deformation was suspected of being caused by excessive residual stresses produced during the manufacturing process. The initial investigation determined the residual stress levels at two sites on each specimen using the hole-drilling strain gauge technique as standardised in ASTM E837-08. The strain gauge rosettes were placed on regions of the specimen support shell which allowed a blind-hole analysis to be conducted.

The first step in processing the results was to investigate the uniformity of the residual stress levels such that the appropriate post-processing technique could be applied. The stress profiles were found to be irregular and non-uniform in nature which intensified the complexity of determining accurate residual stress levels. The precise effects of non-uniform stress fields are still largely unknown and their effect on the accuracy of the results has not yet been fully assessed in literature [88]. Nonetheless, ASTM 837-08 specifies a procedure for the evaluation of non-uniform stresses which is applicable regardless of the degree of non-uniformity. The residual stress levels were found to be excessively high with the peak result of 1142 ± 285 MPa (tensile) being determined in the sector A of specimen 1. Although this value may be greater

than the stated yield strength of 1090 MPa, the specimen would not yield since the cylindrical section offers no mechanism of yielding. The yield/deformation of the tensile specimen occurred since the act of removing the component with a wire-cutter from the machine baseplate eliminated the reaction forces at the base and hence permitted a yielding mode. During the processing of the results, it was noticed that the smaller diameter area of the specimens were producing greater stress magnitudes (sector A = ± 1090 MPa in specimen 1) compared to the large diameter outer shell (sector B = ± 616 MPa in specimen 1). This is likely due to the large cut-out section on the outer shell which could allow minor plastic deformation when the specimen was removed from the machine. This plastic deformation would have partially relaxed the residual stresses in the nearby drilling position.

This analysis revealed the need for a corrective procedure for plasticity effects since some of the residual stresses exceeded 60% of the yield strength (a limit described by ASTM E837-08). A suitable technique was identified in the work by Sattari-Far in which a corrective procedure is specified for quantifying high residual stresses in welded structures using the hole-drilling strain gauge method [97]. Comparisons may be drawn between SLM and welding since both processes expose the substrate material to localised high temperature gradients and as such this technique is particularly well suited to this residual stress analysis. This procedure was applied to both the pilot study and the subsequent residual stress tests in which the residual stresses exceeded the threshold (>60% yield).

The high residual stresses identified in this initial analysis warranted further investigation into components produced by the machine which would be considered fit for use (i.e. no observable deformation after component removal). The need to quantify these stress levels is predominantly due to the objective of SLM becoming a front-runner in the manufacturing arena for aerospace materials. Studies in literature have identified the fatigue cracking concerns associated with components afflicted by high residual stresses [14], [105], [106]. These initial results also necessitated a study into effective techniques for removing residual stresses from components built by SLM. The literature identified heat treatment as a possible method for residual stress removal which is particularly attractive for SLM since it could be applied regardless of specimen complexity and size.

7.3 RESIDUAL STRESS ANALYSIS

The pilot study prompted further investigation for which another eight specimens were built. These cylindrical specimens were built by the CFRM, with 4 cylinders built in the vertical direction (designated A1 to A4) and 4 built in the horizontal direction (designated D1 to D4). The differing orientations were used to determine any build direction changes on the residual stress profiles and microstructure. The specimens were sampled at 4 positions each, with 2 samples before heat treatment and 2 post-treatment. The distance between measurement points was more than 10x drilling diameter to ensure no detrimental effect on the accuracy of the results (as stipulated by UNCERT [104]). The strain gauges used in this evaluation consisted of both type A and type B rosettes (3-gauge rosettes) with a nominal hole diameter of 2mm as specified by ASTM E837-08. The samples were drilled in incremental depths of 0.05mm to a total depth of 2mm. While ASTM E837-08 only requires a depth of 1mm, Prof RB Tait recommended that the author drill to a 2mm depth to ensure the strain readings reached a steady plateau. All drilled positions attained a plateau at 1mm depth which confirmed the success of the strain gauge readings.

The strain relief data measured using the P-3500 strain indicator (given in Appendix C) confirmed the non-uniformity of the residual stresses in the cylindrical specimens. The residual stress profiles were then generated using the non-uniform methodology presented in ASTM E837-08 and corrected for plasticity effects when necessary by Sattari-Far's method as before [97]. The results in general confirmed those obtained in the initial analysis since the surface residual stresses approached and exceeded the yield strength in some cases. The stress distributions were highly non-uniform and their depth profiles showed relatively little consistency between specimens. The residual stress profiles were generated using their maximum principal stresses such that the greatest tensile stress could be identified (see Figures 6.5 – 6.12). All measurement points produced high magnitude tensile residual stress prior to heat treatment.

The residual stress depth profiles were compared between measuring points on each specimen which served as a check for the accuracy of the measurement technique. It was found that the overall maximum residual stress magnitudes were very consistent between measuring points yet

the depth profile shape differed between sampling points. The build direction had no visible effect on the residual stress depth profile and the magnitudes were similar between all specimens. It was observed from this part of the investigation that the building orientation of the cylinders had no distinguishable influence on the residual stresses within the specimens.

7.3.1 EFFECT OF HEAT TREATMENT

The magnitude of the residual stresses in the as-built condition indicated a need to assess the effectiveness of stress alleviation techniques. Due to the complexity of components built by SLM, it was decided to investigate heat treatment as a method of relieving the residual stresses as opposed to invasive techniques such as shot-peening. Heat treatment could be applied to a component regardless of the intricacy of the design and hence would preserve the major advantage of SLM in terms of the build complexity possible. Fortunately Ti-6Al-4V has an affinity for heat treatment and a great deal of research in literature is available on the types of heat treatments used in industry ([72], [73], [77], [107], [108]). Most heat treatment of α+β alloys is based around the transition temperature (β-transus) which gives a wide variation in mechanical properties depending on the cooling rate. The heat treatments were chosen with the following considerations in mind:

- Quenching or rapid cooling may re-introduce residual stresses [109].
- Slow cooling from above the β-transus may cause undesirable grain growth [110].
- Shorter treatment times will preserve rapid manufacturing philosophy.
- Oxidation occurs above 427°C in Ti-6Al-4V exposed to the air [111].

The treatments chosen for this study were; (1) a simple stress-relief treatment, (2) a recrystallization anneal, (3) a duplex anneal and (4) a beta anneal. The simple stress-relief treatment was prescribed purely for the removal of the residual stress in Ti-6Al-4V while the duplex and recrystallization anneals were used to assess the microstructural transformations and any additional stress relieving benefits from treatment at a higher temperature. The beta anneal was used to evaluate any additional benefit from heating the specimens above the β-transus.

All the heat treatments analysed in this study proved excellent in reducing the residual stress levels in the specimens. The simple stress-relief treatment reduced the residual stresses by 76 and 81% in specimens D1 and A1 respectively. This reduction was not as significant as the other treatments primarily due to the lower temperature and it was deduced that the flow stress in the specimens at 650°C did not allow the higher residual stresses to relax completely during the eight hour treatment. This treatment has the advantage of being a simple single step process at a lower temperature which has potential in terms of modifications which could be made to the EOSINT M270 to reduce the residual stress levels during production. The lower temperature would make this treatment easier to implement in a powder bed heating application. Raising the temperature of the powder bed and surrounding atmosphere to approximately 650°C is likely to have a significant impact on the residual stress levels since the temperature gradient is drastically reduced.

The recrystallization anneal was originally developed by Boeing [112] for use with Ti-6Al-4V components and it demonstrated the greatest effect on the residual stress levels with a reduction of 96% and 97% in specimens D2 and A2 respectively. The strains recorded after this treatment was applied were reduced to within instrument/experiment noise which indicates that the flow stress at 950°C is sufficient to eliminate the highest residual stresses in the specimens. This anneal is also simple in terms of the single-step profile as with the stress-relief treatment. Another significant benefit of the recrystallization anneal is the furnace cooling stage as opposed to an air cool since this eliminates the possibility of any oxidation if performed in a vacuum or inert gas furnace.

The duplex anneal was performed primarily to assess any changes in stress levels by the addition of a second ‘stabilising’ step in the treatment process. This process is similar to a solution treatment and aging (STA) method with the exception of air cooling versus quenching as prescribed by STA. This treatment also had a heavy impact on the residual stress levels yet it was marginally less effective than the recrystallization anneal since stresses in specimen A3 and D3 were reduced by 91 and 95% respectively. The duplex anneal would be more complex to introduce in a powder bed heating scheme since it requires the entire component to be subjected to two annealing steps which increase the exposure time and energy required. The duplex anneal is also problematic due to the air cooling stage between the primary anneal and the stabilisation

treatment since the specimens needed to be covered in a ceramic to prevent oxidation. An interesting observation was made during the duplex anneal in terms of the affinity of Ti-6Al-4V for oxidation. The SLM specimens were found to oxidise slightly despite the ceramic layer and it was ascertained from consultation with Prof Rob Knusten and Dr Sarah George (UCT Centre for Materials Engineering) that the specimens were in fact oxidising through trace amounts of oxygen in the ceramic itself.

The beta anneal was the only heat treatment in this study to be applied above the β-transus for Ti-6Al-4V. This treatment was paired with a stabilisation step as recommended in literature due to the short exposure at high temperature [107]. The primary anneal in this process was followed by an air cool (intermediate cooling rate) since furnace cooling is known to cause rapid grain growth which is detrimental to the material strength. The beta anneal had a slightly reduced effect on the residual stress levels in comparison to the duplex and recrystallization anneals with specimen A4 and D4 recording reductions of 91 and 90% respectively. This marginal difference may have been caused by the more rapid cooling from a higher temperature which re-introduced the residual stress into the specimens. The oxidation observed in the duplex anneal was also apparent in the beta anneal to a slightly higher degree due to the higher temperature and longer overall exposure time.

The principal residual stress orientation β was calculated as per ASTM E837-08 in conjunction with the principal stress magnitudes discussed above. The work by Sattari-Far [97] was unable to prescribe a corrective procedure for the principal stress orientation and as such the orientation of the initial residual stress levels could not be assessed quantitatively. A qualitative assessment however could be made in terms of the general depth profile of β. It was noted from Figures 6.22 to 6.25 that the orientation was highly variable with an oscillatory form as the depth increased. In general the angle β (as measured from the horizontal of gauge 1 on the strain gauge rosette) tended to fluctuate between +40° and -40°. This suggests that the successive movements of the laser shift the residual stress orientation between the layers.

The heat treatment reduced the residual stress levels significantly (to within the 50% yield strength limit prescribed by ASTM E837-08) and hence β could be measured more reliably in the heat treated specimens. The results were plotted as an overlay in Figures 6.22 to 6.25 and it was noted that the principal stress orientation fluctuated with depth as with the measurements prior to

heat treatment. The relaxation of the residual stresses during heat treatment is likely to have affected their orientation yet a complex stress distribution (albeit low stress levels) still remains. Although the exceedingly high stress levels prevented a quantitative assessment of the as-built residual stress orientation, it is interesting to note that some β values at the same depth were mirrored about the 0° orientation before and after heat treatment (particularly in Figure 6.25a). This may be a result of the stress relaxation yet no verification could be obtained.

The microscopy study followed the residual stress analysis and the results from this portion of the investigation are discussed next with specific reference on phase transformations produced by the heat treatments.

7.4 MICROSCOPY WORK

As aforementioned, Ti-6Al-4V is well known in literature as a material in which a great variety of microstructures are possible [72], [73], [107]. The microscopy work performed in this study confirmed this variation in microstructure with three different microstructures forming after heat treatments were completed. The as-built SLM Ti-6Al-4V has a martensitic microstructure with thin acicular (needle-like) α'. The presence of this martensite microstructure suggests that the material is rapidly cooled from above the Martensite Start temperature as described in Section 3.2.2 of Chapter 3. This is to be expected since the SLM laser spot heats the Ti-6Al-4V powder in localised sections to a temperature exceeding the melting point (±1600°C) which then rapidly cools as the laser moves to the next position [5]. Martensite is also responsible for the higher hardness value (379 HV_{10}) attained for the as-built material in comparison to those for the heat treated specimens. From a fatigue perspective, martensitic Ti-6Al-4V is beneficial in terms of small-crack propagation since crack pathways are hampered by the thin acicular α' from which high density grain boundaries are the primary hindrance [105], [113]. The study by Hooreweder found that martensitic Ti-6Al-4V had reduced crack growth rates for cracks below 1mm in length when compared with wrought Ti-6Al-4V [84]. When the crack length exceeds 1mm however, the effect is reversed and martensitic microstructure produced higher crack growth rates as shown in Figure 3.13 [84].

The specimens subjected to the stress-relief treatment were not affected on the microstructural level and retained the martensitic microstructure present in the as-built specimens. This result is particularly important since applications of SLM Ti-6Al-4V in which martensitic microstructure is desirable could use this stress-relief technique to remove much of the residual stress without modifying the microstructure. The drawback however is the extended time-period for which the specimens must be heat treated.

The recrystallization annealed specimens produced drastic changes in the microstructures as is evident from the micrographs in Figure 6.34 and 6.35. The microstructure has transformed from martensite to a coarse lamellar microstructure similar to that in Figure 3.3a. This transformed microstructure consists of primary α in a matrix of transformed β containing acicular α (as confirmed in literature [72]). The effect of this microstructural shift on the hardness is evident with an average hardness of 342 HV_{10}, making it comparable with the wrought variety of Ti-6Al-4V (see Table 3.3) [72]. Literature suggests that the recrystallization anneal will improve the fracture toughness and formability of Ti-6Al-4V with some reduction in strength levels (approximately 15%) when compared to the as-built condition [73].

The duplex anneal also had a significant impact on a microstructural level with the martensitic microstructure transforming into one with small amounts of equiaxed α in a matrix of acicular α (transformed β). The hardness of the duplex annealed specimens was significantly reduced to an average of 308 HV_{10}. In literature, the yield strength of duplex annealed Ti-6Al-4V is reported to be reduced to a value of approximately 903 MPa (a reduction of 20%) with a significantly greater elongation of 18% [72].

The beta anneal produced a lamellar microstructure consisting of acicular α (transformed β) with prior β grain boundaries (as confirmed in literature [72]). This anneal had the least effect on the hardness with a slight reduction down to a hardness of 367 HV_{10}. In literature, the yield strength of beta annealed Ti-6Al-4V is reported to be approximately 913 MPa with an elongation of 12% [73]. This represents a reduction of approximately 17% in strength through the use of a beta anneal.

From the conclusions above, it is evident that the heat treatments (with the exception of the stress-relief treatment) have affected the SLM Ti-6Al-4V significantly on the microstructural,

hardness and subsequent strength levels. In order for these treatments to be applied purely to reduce the residual stress, it is important that the designer understand the implications of the microstructural change on the mechanical properties of the material.

7.4.1 MICRO-FLAWS AND POROSITY

A major part of this investigation was the assessment of porosity in the as-built SLM Ti-6Al-4V. Historically, laser-based Additive Manufacturing (AM) has produced highly porous parts due to the difficulty in laying the powder substrate [26]. Any irregularities in a single powder layer can produce high porosity and micro-flaws within a component which are not visible with the naked eye. This is of course crucial in the aerospace arena in which fatigue cracking is of considerable concern [77]. Micro-flaws and pores are crack initiation sites which have a particular susceptibility to HCF (High Cycle Fatigue) and small-crack propagation [114].

Specimen D3 was sectioned in several positions along the length of the specimen after finding a layer of significant porosity across the entire cross-section as shown in Figure 6.40. The subsequent examinations from the other positions on the specimen length revealed no further porosity or micro-flaws. The layer of highly porous material suggests that a powder layer was not laid successfully and the laser heated the previously produced layer instead of the new powder. This porous layer was not identifiable from the outside of the specimen and hence presents a serious concern in terms of the structural integrity of SLM components. A single layer of highly porous material such as that found in specimen D3 represents a line of weakness which may easily cause the failure of a component despite the remainder of the material being defect-free.

Specimens A2 and A3 were found to contain circumferential cracks at a height of approximately 12mm above the machine baseplate as shown in Figure 6.41 and Figure 6.42 respectively. The crack in Specimen A2 was visible in the as-built form yet the crack within Specimen A3 was only visible after the component was polished. The specimens were sectioned in the plane transverse to the crack and examined in the optical microscope to determine the degree of cracking and any indication as to how the crack formed. The crack opening in both specimens was between 200-250 µm at the surface and extended along the build plane to a depth of approximately 6mm for specimen A2 and 4.2mm for A3. It is probable that this crack formed

from a single porous layer since the porosity is evident in the crack plane aft of the crack (Figure 6.42b). It is also apparent from both crack evaluations that the layers immediately above the crack have been affected by the porosity from the previous layer since they too contain extensive porosity. The layers above and below these affected zones are completely clear of porosity indicating that the process returned to optimal conditions after the faulty layers.

As an indication of the severity of this cracking on the structural integrity of the component, a brief fracture mechanics evaluation can be performed using the LEFM technique outlined in the Literature Review. In this example, the fracture toughness values determined by Hooreweder [84] for SLM Ti-6Al-4V will be used as listed below in Table 7.1. The approximate crack dimensions taken from the microscopy analysis in Specimen A2 and A3 are listed in Table 7.2.

In terms of finding the cyclic stress at which these components would fail immediately with the inherent crack, the stress intensity equation can be re-arranged to form the following relationship in equation (7-1) below.

$$\Delta\sigma_{crit} = \frac{K_{1C}}{Y\sqrt{\pi a}} \qquad \textbf{(7-1)}$$

Table 7.1: Fracture toughness properties and Paris constants for SLM Ti-6Al-4V as determined by Hooreweder et al [84]

Criterion	SLM Ti-6Al-4V
K_{IC} [MPa$\sqrt{m}$]	52.4 ± 3.48
C [m/cycle]	5 x 10^{-12}
m	3.376

Table 7.2: Crack properties as measured in Specimen A2 and A3

	Specimen A2	Specimen A3
Crack length ‘2a’	4.2 mm	6.0 mm
Specimen diameter	10 mm	10 mm

For specimen A2 with a shape constant of Y = 1.2, the cyclic stress $\Delta\sigma_{crit}$ which would cause failure of this component can be determined.

$$\Delta\sigma_{crit\ A2} = \frac{52.4}{1.2\sqrt{\pi \times 0.0021}} \quad (7\text{-}2)$$

$$\Delta\sigma_{crit\ A2} = 537.5MPa \quad (7\text{-}3)$$

Similarly for Specimen A3 with a crack length of 6mm,

$$\Delta\sigma_{crit\ A3} = 449.7MPa \quad (7\text{-}4)$$

Another important LEFM capability is the determination of remaining life (*N*) within a structure in which a defect (of length *a*) is present. This can be achieved by integrating the Paris law as shown below in equation (7-5) between the initial crack length and the critical crack length (at which fracture will occur).

$$\int_0^N dN = \int_a^{a_{crit}} \frac{da}{C\Delta K^m} \quad (7\text{-}5)$$

As an estimate of the effect of a defect of 100µm (which has been observed in specimen A4 in Figure 7.1b below) in a component exposed to a cyclic stress of 500 MPa (i.e. at approximately 50% of yield), the remaining life would be determined by integrating (7-5) above. The critical crack length for a cyclic stress of 500 MPa is first determined using the LEFM equation as shown below.

$$a_{crit} = \frac{{K_{1C}}^2}{Y^2\pi\sigma^2} \quad (7\text{-}6)$$

$$a_{crit} = 0.0024m \quad (7\text{-}7)$$

This result specifies a critical crack length of 2.4mm for this specimen exposed to a cyclic stress of 500 MPa. Using this value as the upper limit in the fatigue life integral, an estimate of the remaining life of this structure can be made.

$$N = \int_{0.0001}^{0.0024} \frac{da}{5 \times 10^{-12}(52.4 - 8.51)^{3.376}} \quad \textbf{(7-8)}$$

$$N = 1312\ cycles \quad \textbf{(7-9)}$$

A compressor blade in a gas turbine engine (which has been constructed of Ti-6Al-4V in several variants of the Rolls Royce Trent engines) will be subjected to much higher stresses and would attain several thousand cycles in a matter of seconds. A component with an inherent defect of 100 µm would thus fail very quickly in this environment. This brief fatigue life estimate highlights the concerns in the aerospace industry with regard to components with defects. In an effort to identify other hidden defects which could further jeopardise the structural integrity of this material, the micro-flaw exposure investigation was performed as described in the next section.

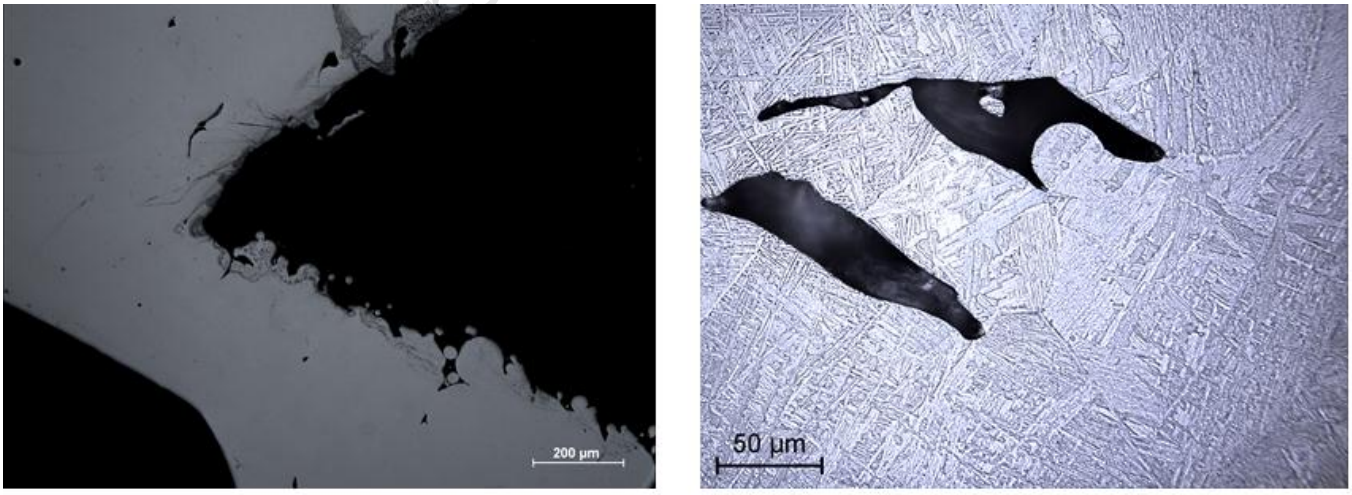

Figure 7.1: Defects observed in SLM Ti-6Al-4V specimens in terms of, a) Surface roughness in the failed tensile specimen 1 and, b) micro-flaws in specimen A4 of approximately 100-200µm in length.

7.5 MICRO-FLAW INTERACTION

Following the discovery of micro-flaws and the exceedingly high residual stresses in the preceding sections, an investigation into the effects of a tensile load on these defects was proposed. The relatively new technique known as Digital Image Correlation (DIC) provided an promising method through which micro-flaws could be evaluated using images taken from an optical microscope. The system was to be designed for an upright Nikon optical microscope using the X5 lens. Several difficulties were identified with this method in terms of the force delivery system since a high pure tensile force was required while keeping the specimens perfectly horizontal such that the microscope could focus on the gauge section at each loading interval.

The concept developed for the miniature tensile rig used a proof/load ring concept in which the specimens were mounted on HT bolts which were fastened against the ring to introduce the force into the specimen. The force transmitted into the specimen was measured using four strain gauges attached to the ring surface in tension-compression pairs. These strain gauge pairs were connected in a full-bridge configuration from which data was sampled and collected through a NiDAQ data acquisition system. The approximate specimen extension was measured using a position potentiometer to measure the precise advancement of the tensioning nut and hence the lateral movement of the load bolt (using the bolt pitch). In order to keep the specimen in a pure tensile load, the load bolts were not permitted to rotate as the tensioning nuts were advanced. This was accomplished using two high tensile cap screws fastened through the ring into slots machined through the load bolt shank. These slots allowed for lateral movement of the load bolt but prevented any rotation of the load bolt as the tension nut was fastened. This system was mounted on a bracket to precisely locate the rig in the microscope test bed.

The sensitivity of the strain gauges on the ring was important when considering the accuracy of the load transmitted into the specimen. The accuracy of the system was dependant on the strain registered by the strain gauges on the ring surface. An important limit was prescribed on this system sensitivity since the proof ring was not permitted to yield as the specimen was loaded. If the force in the proof ring exceeded the yield strength, the plastic deformation would render the results of all subsequent tests invalid. The limit was prescribed to be 80% of the yield strength of

the ring which allowed for a system sensitivity of 1 με = ±1.5 N. This sensitivity was found to produce excellent force measurement results.

The specimen deflection at each loading increment was adjusted using the procedure identified in Section 5.3.7 of Chapter 5. This was used together with the force measurements recorded through the data acquisition device to produce the Load-Deflection diagrams in Figures 6.26-6.30. The region of interest in these diagrams is the linear region which has been identified using the trend line for each specimen. The initial loading (up to approximately 1000N) is affected by rig slippage and misalignment however at greater loads, the specimen force is applied purely to the specimen. The linear region most accurately represents the material response to the applied load. The data points which plateau away from the linear region at greater deflections indicate the yield strength has been exceeded and the specimen behaviour is plastic. This region is difficult to evaluate and high variability is shown between specimens up to the breaking point. The most interesting feature of the Load-Deflection diagrams is the relative position of the linear region in terms of the specimen deflection. For most of the tests, the linear regions were reasonably closely placed which suggests that the build orientation does not play a significant role in component strength. It is also interesting to note that the slope of the linear region varies considerably before and after heat treatment. The slope of the linear region is in general much steeper for the as-built specimens as opposed to the heat treated specimen. This may be attributed to the lower hardness and increased ductility of the heat treated specimens.

7.5.1 DIGITAL IMAGE CORRELATION

The system successfully loaded all the specimens to the breaking stress and stored the behaviour of each sample using the data acquisition system. The Digital Image Correlation component of this investigation however was not effective due primarily to the quality of the images produced by the Nikon camera. Several further limitations of the rig were identified which could be improved upon to increase the potential for complete image correlation.

1. The camera system was not able to maintain the same focus throughout each test and the pixel colouring was not consistent. This resulted in grainy images which could not produce the level of pixel accuracy required.

2. Specimen texture changes reduced the ability focussing ability of the microscope.
3. The HT tension control cap screws yielded slightly in several tests due to the torque experienced on the load bolt during fastening of the load nut.
4. The force measurement system was highly accurate for the force transmitted through the ring yet specimen elongation when the load approached and exceeded the specimen yield strength reduced the accuracy of the system for loads beyond this stress level.
5. Slight inaccuracies in the slot dimensions and the attachment points on the load bolts allowed the specimens to deviate from the horizontal position and subsequently the focussing ability of the microscope was hampered.
6. Movement of the rig between the microscope test bed and the loading vice introduced rigid body motion as the rig could not be re-positioned precisely.

The limitations mentioned above prevented the quantitative assessment of micro-flaw interaction using DIC, however a qualitative assessment could be made based on the micrographs. Micro-cracking was observed in several specimens and is seen in the micrograph of specimen C6 in Figure 6.43. The crack has opened from a sharp edged void which was one of the main concerns behind the porosity investigation of the previous section. It is possible that in the presence of a cyclic load, this crack could develop into a fatigue crack and jeopardise the component's load carrying capability. The progressive yielding observed in all of the specimens is shown most clearly in Figure 6.44 for specimen C4 along with the change in surface texture as the loading is increased.

The miniature tensile rig was successful in identifying micro-flaw interaction in specimen C4 as shown in Figure 7.2 below. This series of images identify three major pores closely grouped together which are monitored as the tensile load is increased. At approximately 4900N, the micrograph reveals the formation of a thin crack developing between two of the pores. As the loading is further increased to 5750N, the thin crack has increased in size and has completely opened between the pores. In the final image at 6419N, the crack has opened completely and effectively joined the pores and created a larger micro-flaw. This flaw interaction is a serious concern in terms of the threshold flaw size in a fatigue situation. The flaw interaction observed in Figure 7.2 has approximately doubled the size of the micro-flaw which greatly increases the risk of a fatigue crack initiating from this site.

In addition to the flaw interaction captured in specimen C4, progressive micro-cracks can be seen developing in Figure 6.45 at the edge of a pore. These examples of flaw interaction and micro-cracking highlight the risks associated with using SLM Ti-6Al-4V in high stress applications. These defects would not be visible to the naked eye yet they have the potential to rapidly grow as shown in the fatigue life prediction in the previous section. Despite the short-comings of the Digital Image Correlation attempt, this study provided a valuable qualitative assessment on the possibility of flaw interaction and micro-cracking. The final section of this discussion amalgamates the results from all the components of this investigation in terms of the structural integrity of Ti-6Al-4V components manufacturing by Selective Laser Melting.

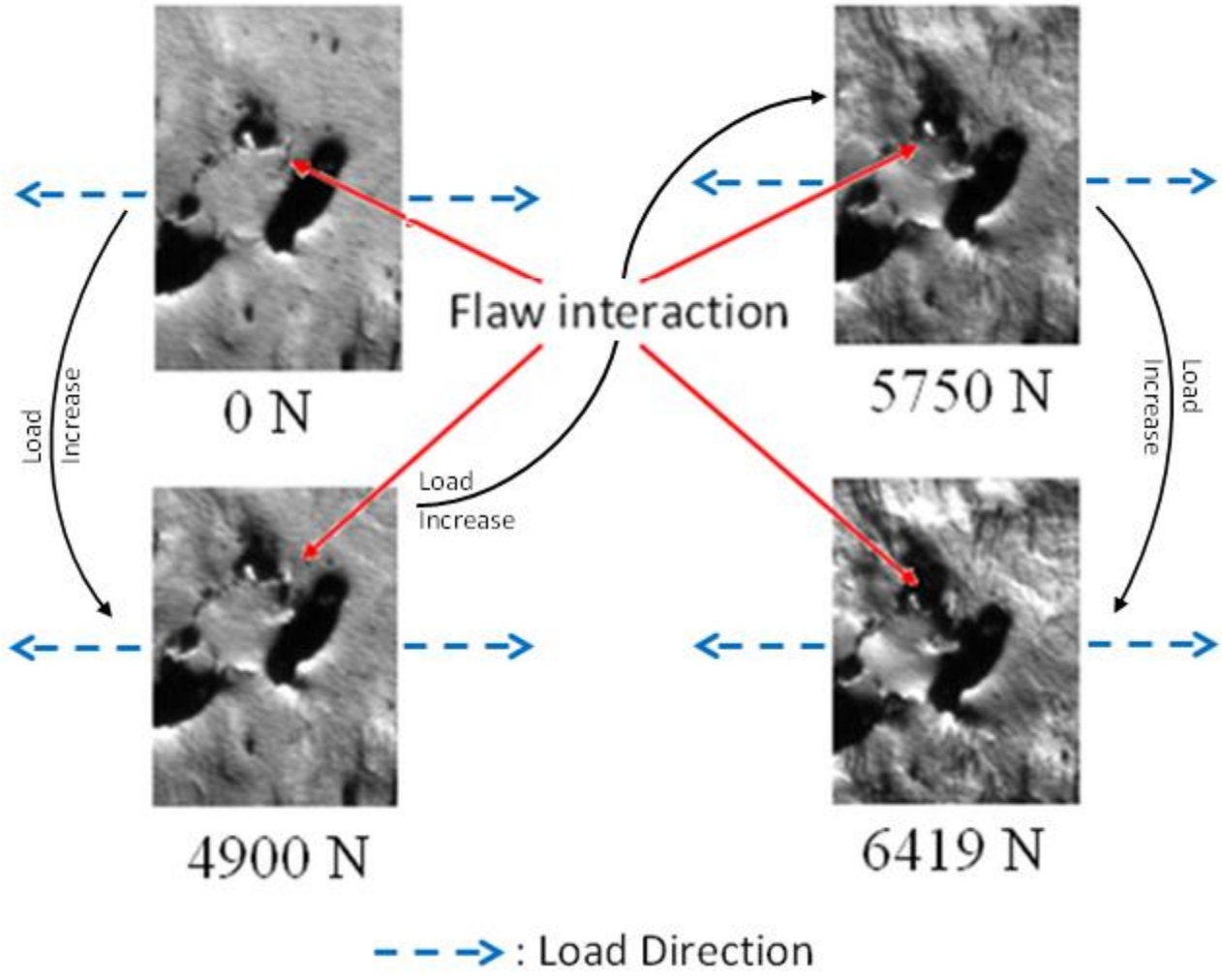

Figure 7.2: Flaw interaction and development in specimen C4.

7.6 STRUCTURAL INTEGRITY IMPLICATIONS

The assessments from each investigation presented in the sections above were accumulated in an effort to make an evaluation on the structural integrity of components produced by the Selective Laser Melting process. The advantages of Additive Manufacturing techniques such as SLM are numerous, particularly in the degree of build complexity possible. This type of manufacturing would drastically reduce the costs in the aerospace industry, particularly in the machining costs of turbine engines. The primary barrier preventing SLM from entering this market is the lack of research into the integrity of components built through this process. The aerospace manufacturing arena is one of the most safety-critical and highly regulated industries in existence and hence a great deal of research is required before new manufacturing systems are implemented. This problem is amplified by the intense performance envelopes in which modern aircraft are required to operate. The industry drive toward fuel efficiency places restrictions on component weight and hence the components are designed nearer to material limits. This places increased pressure on the reliability of materials used in critical components.

The residual stresses caused by the intense temperature gradient during laser exposure are significant as revealed in this investigation. The effects of residual stresses are largely underestimated in terms of their effects on fatigue cracking in cyclically loaded structures. Significant residual stress has the effect of reducing the threshold flaw size, i.e. the size of the flaw which would propagate into a fatigue crack is reduced. The presence of residual stresses then places added pressure on the material to be completely defect-free, i.e. 100% density. The heat treatments tested in this study however did have a significant effect on reducing the residual stress levels which demonstrates great potential in designing a system to reduce or eliminate the stress levels entirely.

The heat treatment of SLM Ti-6Al-4V is effective in significantly reducing the residual stress levels, however microstructural changes need to be taken into account in terms of mechanical property changes. The effect of the microstructural change was noted in the specimen deflection analysis from the miniature tensile rig data acquisition system. The recrystallization annealed specimens in particular demonstrated a reduction in tensile breaking force as observed in Figure 6.28. It is also noted however that the specimen elongation was improved significantly with the recrystallization, duplex and beta annealing as shown in Table 6.7. The duplex and

recrystallization anneals increased the elongation from approximately 4% for the as-built specimens to between 10% and 11%. This indicates an improvement in ductility most likely due to a microstructural shift from martensite to the coarse lamellar structures. This effect is also confirmed in the reduction in hardness levels experienced by the heat treated specimens. Literature confirmed the possible changes in material behaviour post heat treatment and aspects such as the reduction in strength levels need to be accounted for in designs which incorporate the heat treated SLM Ti-6Al-4V.

The prevalence of micro-flaws and surface cracking is a severe problem which needs to be addressed before any critical components can be manufactured from this system. The observations made in this study tend to suggest that the problem is caused by inconsistencies in the powder laying procedure which prevent the correct laser exposure to the new powder layer. Progressive cracking has been observed from the edges of sharp micro-flaws and voids under a pure tensile load. Flaw interaction has also been discovered which could potentially generate the degree of cracking discovered in specimen A2 and A3. Flaw interaction can rapidly increase the size of micro-flaws which could then form crack initiation sites in fatigue conditions. These factors are unfortunately highly detrimental to the structural integrity of SLM Ti-6Al-4V. Ti-6Al-4V is favoured for its high strength in industry and hence would be expected to be implemented into high stress applications. Micro-flaws and surface roughness in the order of 100-200µm however are completely unacceptable for high cyclically loaded applications. The work presented in this study has demonstrated the need to improve the system and its parameters in order to produce components which are defect-free. This may extend to a method in which porosity can be identified during manufacture such that the defective layer may be removed or the component may be discarded before its potentially dangerous implementation.

This study has not examined the effects of a fatigue loading directly and it is suggested that the material be subjected to fatigue tests before and after heat treatment to quantitatively assess the effects of the high residual stresses. In addition, it is suggested that future work be carried out on the design of a system to reduce the residual stress at its conception, i.e. through a powder bed heating system. Any effort to reduce the severe temperature gradient during manufacture will show significant improvements in residual stress levels.

CHAPTER 8 – CONCLUSIONS & FUTURE WORK

8.1 INTRODUCTION

The previous chapter discussed the results from the investigations into the residual stress levels, microstructure, micro-flaw interaction and physical properties of SLM Ti-6Al-4V. This chapter summarises the comments made in Chapter 7 in terms of the objectives stated in Chapter 1. This is also extended to suggestions for future work to continue the research into this new manufacturing methodology. The improvements to the miniature tensile rig are also listed in terms of producing images suitable for successful Digital image Correlation.

8.2 CONCLUSIONS

The conclusions based on the comments from Chapter 7 are listed below.

1. The deformation observed in the pilot study specimens was caused by residual stresses exceeding the yield strength of the material. The removal of the components from the EOSINT M270 baseplate removed the lower constraint on the inner specimen and thus permitted a mechanism of yield through which the plastic deformation could be observed.
2. The hole-drilling strain gauge method (ASTM E837-08) was used to determine the residual stresses within the as-built SLM Ti-6Al-4V cylindrical specimens. These residual stresses were found to be exceedingly high and in some cases approached and exceeded the material yield strength (1090 MPa).
3. The residual stress within as-built SLM Ti-6Al-4V is highly non-uniform and varies significantly with depth.
4. Heat treatment had a significant effect on the residual stress levels in SLM Ti-6Al-4V and a large-scale reduction in stress levels was observed from all heat treatments.

5. The Stress-Relief heat treatment reduced the residual stress levels between 76-81% and retained the martensitic microstructure of the as-built condition. The stress-relief treatment had no noticeable effect on the hardness.
6. The Recrystallization Anneal had the most significant effect on the residual stress levels with a reduction in stress levels of between 94-97%. This treatment transformed the microstructure from a martensite to a microstructure consisting of primary α in a matrix of transformed β containing acicular α. The treatment reduced the hardness to 342 HV_{10}.
7. The Duplex Anneal reduced the residual stress levels by 91-95% and transformed the microstructure from martensite to one with small amounts of equiaxed α in a matrix of acicular α (transformed β). The duplex anneal reduced the specimen hardness to 308 HV_{10}.
8. The Beta Anneal reduced the residual stress levels by 90-91% and transformed the microstructure from martensite to an acicular α (transformed β) with prior β grain boundaries. The hardness was reduced to 367 HV_{10}.
9. Porosity was less significant than the historical systems yet evidence of several pores exceeding 150μm in length were found in both the build plane and the transverse plane.
10. Severe cracking was observed in two specimens with circumferential cracks extending between 4mm and 6mm into the specimen. These cracks were most likely formed from an insufficient powder layer and the nearby layers above the crack plane were also affected with an increase in porosity.
11. Successful Digital Image Correlation was not achieved due to poor image quality from the microscope camera and excessive specimen texture changes.
12. Progressive yielding and surface cracking was observed using the miniature tensile rig and cracks were observed from the edges of a pore.
13. Micro-flaw interaction could be observed using the miniature tensile rig when the force transmitted to the specimen approached 4900N.

8.3 FUTURE WORK

1. A fatigue and fracture analysis needs to be performed for SLM Ti-6Al-4V before and after the heat treatments described in this study to fully quantify the effects of the residual stress on structural integrity.

2. The creep behaviour of SLM Ti-6Al-4V has not yet been determined in literature and would contribute greatly to the analysis of the structural integrity of this material.
3. An assessment should be performed on parameter changes on the EOSINT M270 and the subsequent effects on residual stress levels in the as-built components.
4. The design/assessment of a powder bed heating scheme to reduce the residual stresses during manufacture.
5. The miniature tensile rig can be modified to remove the rigid body motion during loading and in addition an improved camera system is required on the microscope for successful digital image correlation.

REFERENCES

[1] E. Silveira, G. Atxaga, and A. M. Irisarri, "Influence of the level of damage on the high temperature fatigue life of an aircraft turbine disc," *Engineering Failure Analysis*, vol. 16, no. 2, pp. 578–584, Mar. 2009.

[2] R. E. Schafrik and J. C. Williams, "Jet Engine Materials," in *Encyclopedia of Materials: Science and Technology (Second Edition)*, Oxford: Elsevier, 2001, pp. 4331–4338.

[3] T. Godin, S. Harvey, and P. Stouffs, "Theoretical analysis of environmental and energetic performance of very high temperature turbo-jet engines," *International Journal of Thermal Sciences*, vol. 38, no. 5, pp. 442–451, May 1999.

[4] A. S. Gohardani, G. Doulgeris, and R. Singh, "Challenges of future aircraft propulsion: A review of distributed propulsion technology and its potential application for the all electric commercial aircraft," *Progress in Aerospace Sciences*, vol. 47, no. 5, pp. 369–391, 2011.

[5] I. Abd Aziz, "Microstructure and Mechanical Properties of Ti-6Al-4V Produced by Selective Laser Sintering of Pre-alloyed Powders," 2010.

[6] S. J. Hollister and T. L. Bergman, "Biomedical Applications OF Integrated Additive/Subtractive Manufacturing," *Additive/Subtractive Manufacturing Research AND Development IN Europe*, vol. 1001, p. 55.

[7] L. Hao, S. Dadbakhsh, O. Seaman, and M. Felstead, "Selective laser melting of a stainless steel and hydroxyapatite composite for load-bearing implant development," *Journal of Materials Processing Technology*, vol. 209, no. 17, pp. 5793–5801, Aug. 2009.

[8] A. Bandyopadhyay, F. Espana, V. K. Balla, S. Bose, Y. Ohgami, and N. M. Davies, "Influence of porosity on mechanical properties and in vivo response of Ti6Al4V implants," *Acta Biomaterialia*, vol. 6, no. 4, pp. 1640–1648, Apr. 2010.

[9] C. Emmelmann, P. Scheinemann, M. Munsch, and V. Seyda, "Laser Additive Manufacturing of Modified Implant Surfaces with Osseointegrative Characteristics," *Physics Procedia*, vol. 12, Part A, no. 0, pp. 375–384, 2011.

[10] N. McDonald, S. Corrigan, C. Daly, and S. Cromie, "Safety management systems and safety culture in aircraft maintenance organisations," *Safety Science*, vol. 34, no. 1–3, pp. 151–176, 2000.

[11] H. Pohl, A. Simchi, M. Issa, and H. C. Dias, "Thermal stresses in direct metal laser sintering," in *Proc. Of the Solid Freeform Fabrication Symp*, 2001, pp. 366–372.

[12] C. Casavola, S. L. Campanelli, and C. Pappalettere, "Experimental analysis of residual stresses in the selective laser melting process," 2008.

[13] C. Casavola, C. Pappalettere, and F. Tursi, "Non-uniform residual stress fields on sintered materials," in *Youth Symposium on Experimental Solid Mechanics*, 2010.

[14] J. M. Barsom and S. T. Rolfe, *Fracture and fatigue control in structures: applications of fracture mechanics*. ASTM International, 1999.

[15] T. Nicholas, "High cycle fatigue life management in gas turbine engines," *Qualification of Life Extension Schemes for Engine Components*, 1999.

[16] R. O. Ritchie, B. L. Boyce, J. P. Campbell, O. Roder, A. W. Thompson, and W. W. Milligan, "Thresholds for high-cycle fatigue in a turbine engine Ti-6Al-4V alloy," *International Journal of Fatigue*, vol. 21, no. 7, pp. 653–662, Aug. 1999.

[17] V. T. Troshchenko and A. V. Prokopenko, "Fatigue strength of gas turbine compressor blades," *Engineering Failure Analysis*, vol. 7, no. 3, pp. 209–220, Jun. 2000.

[18] C. . Tao, N. . Xi, M. . Xie, P. . Zhong, and Y. Zhang, "Analysis of turbine blade breakages in an engine starting motor," *Engineering Failure Analysis*, vol. 6, no. 4, pp. 245–251, Aug. 1999.
[19] R. M. Arnaldo Valdés and F. Gómez Comendador, "Learning from accidents: Updates of the European regulation on the investigation and prevention of accidents and incidents in civil aviation," *Transport Policy*, vol. 18, no. 6, pp. 786–799, Nov. 2011.
[20] H. T. Kang, Y.-L. Lee, and X. J. Sun, "Effects of residual stress and heat treatment on fatigue strength of weldments," *Materials Science and Engineering: A*, vol. 497, no. 1–2, pp. 37–43, Dec. 2008.
[21] L. Zeng and T. R. Bieler, "Effects of working, heat treatment, and aging on microstructural evolution and crystallographic texture of* a,* a',* a" and* b phases in Ti-6 Al-4 V wire," *Materials Science and Engineering A*, vol. 392, no. 1–2, pp. 403–414, 2005.
[22] D. L. Bourell and J. J. Beaman Jr, "Freeform fabrication-History and current processes," in *Proceedings of Symposium on Rapid Prototyping of Materials*, 2002, pp. 3–17.
[23] J. Beaman, "Solid Freeform Fabrication: An Historical Perspective," *The University of Texas*.
[24] D. L. Bourell and J. J. Beaman, "Methodologies AND Processes," *Additive/Subtractive Manufacturing Research AND Development IN Europe*, vol. 1001, p. 7.
[25] M. Agarwala, D. Bourell, J. Beaman, H. Marcus, and J. Barlow, "Direct selective laser sintering of metals," *Rapid Prototyping Journal*, vol. 1, no. 1, pp. 26–36, 1995.
[26] M. Shellabear and O. Nyrhilä, "DMLS-Development history and state of the art," *Laser Assisted Netshape Engineering*, vol. 4, pp. 21–24, 2004.
[27] J.-P. Kruth, M. C. Leu, and T. Nakagawa, "Progress in Additive Manufacturing and Rapid Prototyping," *CIRP Annals - Manufacturing Technology*, vol. 47, no. 2, pp. 525–540, 1998.
[28] J. P. Kruth, M. Badrossamay, E. Yasa, J. Deckers, L. Thijs, and J. Van Humbeeck, "Part and material properties in selective laser melting of metals," in *Proceedings of the 16th International Symposium on Electromachining*, 2010.
[29] P. . Ciraud, "Process and Device for the Manufacture of any Objects Desired from any Meltable Material," *FRG Disclosure Publication 2263777*, p. 1972.
[30] O. . Munz, "Photo-glyph recording," *US Patent 2,350,796*, 1944.
[31] W. . Swainson, "Method, medium and apparatus for producing a three-dimensional figure product," *US Patent 4,041,476*, 1977.
[32] R. . Housholder, "Molding Process," *US Patent 4,247,508*, 1981.
[33] H. Kodama, "Automatic method for fabricating a three-dimensional plastic model with photo hardening polymer," *Rev Sci Instrum*, pp. 1770–1773, 1981.
[34] A. . Herbert, "Solid object generation," *Journal of Applied Photo Engineering*, vol. 8, no. 4, pp. 185–188, 1982.
[35] C. Hull, "Method for production of three-dimensional objects by stereolithography," *US patent 4,929,402*, 1990.
[36] C. Deckard, "Method and apparatus for producing parts by selective sintering," *US Patent 4,863,538*, 1989.
[37] G. V. Salmoria, C. H. Ahrens, V. E. Beal, A. T. N. Pires, and V. Soldi, "Evaluation of post-curing and laser manufacturing parameters on the properties of SOMOS 7110 photosensitive resin used in stereolithography," *Materials & Design*, vol. 30, no. 3, pp. 758–763, Mar. 2009.

[38] B. Mueller and D. Kochan, "Laminated object manufacturing for rapid tooling and patternmaking in foundry industry," *Computers in Industry*, vol. 39, no. 1, pp. 47–53, Jun. 1999.
[39] "Rapid Prototyping - Laminated Object Modelling and Computer Aided Manufacturing of Laminated Enginee." [Online]. Available: http://www.azom.com/article.aspx?ArticleID=1650. [Accessed: 29-Sep-2011].
[40] N. Mostafa, H. M. Syed, S. Igor, and G. Andrew, "A Study of Melt Flow Analysis of an ABS-Iron Composite in Fused Deposition Modelling Process," *Tsinghua Science & Technology*, vol. 14, Supplement 1, no. 0, pp. 29–37, Jun. 2009.
[41] "Rapid Prototyping Patent Museum." [Online]. Available: http://www.additive3d.com/museum/mp.htm. [Accessed: 29-Sep-2011].
[42] P. Bártolo, *Stereolithography: Materials, Processes and Applications*. Springer, 2011.
[43] L. E. Murr, E. V. Esquivel, S. A. Quinones, S. M. Gaytan, M. I. Lopez, E. Y. Martinez, F. Medina, D. H. Hernandez, E. Martinez, J. L. Martinez, S. W. Stafford, D. K. Brown, T. Hoppe, W. Meyers, U. Lindhe, and R. B. Wicker, "Microstructures and mechanical properties of electron beam-rapid manufactured Ti-6Al-4V biomedical prototypes compared to wrought Ti-6Al-4V," *Materials Characterization*, vol. 60, no. 2, pp. 96–105, Feb. 2009.
[44] L. E. Murr, S. M. Gaytan, A. Ceylan, E. Martinez, J. L. Martinez, D. H. Hernandez, B. I. Machado, D. A. Ramirez, F. Medina, S. Collins, and R. B. Wicker, "Characterization of titanium aluminide alloy components fabricated by additive manufacturing using electron beam melting," *Acta Materialia*, vol. 58, no. 5, pp. 1887–1894, Mar. 2010.
[45] H. Pan, S. H. Ko, and C. P. Grigoropoulos, "The Solid-State Neck Growth Mechanisms in Low Energy Laser Sintering of Gold Nanoparticles: A Molecular Dynamics Simulation Study," *Journal of Heat Transfer*, vol. 130, p. 092404, 2008.
[46] J. P. Kruth, P. Mercelis, J. Van Vaerenbergh, L. Froyen, and M. Rombouts, "Binding mechanisms in selective laser sintering and selective laser melting," *Rapid prototyping journal*, vol. 11, no. 1, pp. 26–36, 2005.
[47] D. Gu and Y. Shen, "Balling phenomena in direct laser sintering of stainless steel powder: Metallurgical mechanisms and control methods," *Materials & Design*, vol. 30, no. 8, pp. 2903–2910, Sep. 2009.
[48] B. Vandenbroucke and J.-P. Kruth, "Selective laser melting of biocompatible metals for rapid manufacturing of medical parts," *Rapid Prototyping Journal*, vol. 13, no. 4, pp. 196–203, 2007.
[49] P. Mercelis and J. P. Kruth, "Residual stresses in selective laser sintering and selective laser melting," *Rapid Prototyping Journal*, vol. 12, no. 5, pp. 254–265, 2006.
[50] E. C. Santos, M. Shiomi, K. Osakada, and T. Laoui, "Rapid Manufacturing of metal components by laser forming," *International Journal of Machine Tools and Manufacture*, vol. 46, no. 12–13, pp. 1459–1468, 2006.
[51] "EOS launch new Aerospace targetted metal powders." [Online]. Available: http://develop3d.com/blog/eos-launch-new-aerospace-targetted-metal-powders. [Accessed: 04-Oct-2011].
[52] "Technical data for the EOS Gmbh M270 Direct Metal Laser Sintering machine." EOS GmbH Electro Optical Systems.

[53] Y. Lu, F. Taheri, M.A. Gharghouri, and H.P. Han, "Experimental and numerical study of the effects of porosity on fatigue crack initiation of HPDC magnesium AM60B alloy," *Journal of Alloys and Compounds*, Mar. 2008.
[54] G. E. Totten, M. A. H. Howes, and T. Inoue, *Handbook of Residual Stress and Deformation of Steel*. ASM International, 2002.
[55] M. James, "Residual Stress Influences in Mechanical Engineering," *Congreso Nacional de Ingeniería Mecánica*, vol. XVIII, 2010.
[56] P. Prevey, "Thermal residual stress relaxation and distortion in surface enhanced gas turbine engine components," DTIC Document, 1998.
[57] K. Hyojin, "Study of the fracture of the last stage blade in an aircraft gas turbine," *Engineering Failure Analysis*, vol. 16, no. 7, pp. 2318–2324, Oct. 2009.
[58] R. Ritchie and Peters, "Foreign-object damage and high-cycle fatigue of Ti-6Al-4V," *Materials Science and Engineering A*, vol. 319–321, pp. 597–601.
[59] T. L. Panontin, *Fatigue and fracture mechanics*. ASTM International, 1999.
[60] R. E. Smallman and R. J. Bishop, *Modern physical metallurgy and materials engineering: science, process, applications*. Butterworth-Heinemann, 1999.
[61] Z. Feng, *Processes and mechanisms of welding residual stress and distortion*. CRC Press, 2005.
[62] M. T. Hutchings, *Introduction to the characterization of residual stress by neutron diffraction*. Taylor & Francis, 2005.
[63] A. Turnbull, A. Maxwell, and S. Pillai, "Residual stress in polymers—evaluation of measurement techniques," *Journal of materials science*, vol. 34, no. 3, pp. 451–459, 1999.
[64] G. S. Schajer, "Hole-Drilling Residual Stress Measurements at 75: Origins, Advances, Opportunities," *Experimental mechanics*, vol. 50, no. 2, pp. 245–253, 2010.
[65] J. Gauthier, T. W. Krause, and D. L. Atherton, "Measurement of residual stress in steel using the magnetic Barkhausen noise technique," *NDT & E International*, vol. 31, no. 1, pp. 23–31, Feb. 1998.
[66] P. Withers and H. Bhadeshia, "Residual stress. Part 1 &# 8211; Measurement techniques," *Materials Science and Technology*, vol. 17, no. 4, pp. 355–365, 2001.
[67] A. T. Zehnder, *Fracture Mechanics*, vol. 77. Springer, 2010.
[68] E. Silveira, G. Atxaga, E. Erauzkin, and A. M. Irisarri, "Study on the root causes for the premature failure of an aircraft turbine blade," *Engineering Failure Analysis*, vol. 16, no. 2, pp. 639–647, Mar. 2009.
[69] N. Benachour,, A. Hadjoui,, M. Benachour,, and M. Benguediab, "Stress Ratio and Notch Effect on Fatigue Crack Initiation and Propagation in 2024 Al-alloy," *World Academy of Science, Engineering and Technology*, vol. 79, 2011.
[70] L. W. Tsay and C. Y. Tsay, "The effect of microstructures on the fatigue crack growth in Ti---6Al---4V laser welds," *International Journal of Fatigue*, vol. 19, no. 10, pp. 713–720, Dec. 1997.
[71] B. Babu, "Physically based model for Plasticity and creep of Ti-6Al-4V," Licentiate Thesis, Luleå University of Technology, Sweden, 2008.
[72] M. J. Donachie, *Titanium: a technical guide*. ASM International, 2000.
[73] E. W. Collings, *Materials properties handbook: titanium alloys*. ASM International, 1994.
[74] C. Leyens and M. Peters, *Titanium and titanium alloys: fundamentals and applications*. Wiley-VCH, 2003.

[75] L. Facchini, E. Magalini, P. Robotti, A. Molinari, S. H\öges, and K. Wissenbach, "Ductility of a Ti-6Al-4V alloy produced by selective laser melting of prealloyed powders," *Rapid Prototyping Journal*, vol. 16, no. 6, pp. 450–459, 2010.
[76] R. Nalla, B. Boyce, J. Campbell, J. Peters, and R. Ritchie, "Influence of microstructure on high-cycle fatigue of Ti-6Al-4V: Bimodal vs. Lamellar Structures," *Metallurgical and Materials Transactions A*, vol. 33, no. 13, pp. 899–918, 2002.
[77] F. C. Campbell, *Manufacturing technology for aerospace structural materials*. Elsevier, 2006.
[78] L. E. Murr, S. A. Quinones, S. M. Gaytan, M. I. Lopez, A. Rodela, E. Y. Martinez, D. H. Hernandez, E. Martinez, F. Medina, and R. B. Wicker, "Microstructure and mechanical behavior of Ti-6Al-4V produced by rapid-layer manufacturing, for biomedical applications," *J Mech Behav Biomed Mater*, vol. 2, no. 1, pp. 20–32, Jan. 2009.
[79] Q. Li, E. Y. Chen, D. R. Bice, and D. C. Dunand, "Transformation Superplasticity of Cast Titanium and Ti-6Al-4V," *Metall and Mat Trans A*, vol. 38, no. 1, pp. 44–53, Jan. 2007.
[80] J. K. Wessel, *The Handbook of Advanced Materials: Enabling New Designs*. John Wiley & Sons, 2004.
[81] S. Denis, E. Gautier, A. Simon, and G. Beck, "Stress–phase-transformation interactions–basic principles, modelling, and calculation of internal stresses," *Materials Science and Technology*, vol. 1, no. 10, pp. 805–814, 1985.
[82] Y. Fan, P. Cheng, Y. L. Yao, Z. Yang, and K. Egland, "Effect of phase transformations on laser forming of Ti–6Al–4V alloy," *Journal of Applied Physics*, vol. 98, no. 1, p. 013518, 2005.
[83] R. Pederson, "Microstructure and phase transformation of Ti-6Al-4V," Licentiate thesis, 2002.
[84] B. V. Hooreweder, D. Moens, R. Boonen, J.-P. Kruth, and P. Sas, "Analysis of Fracture Toughness and Crack Propagation of Ti-6Al-4V produced by Selective Laser Melting," *Advanced Engineering Materials*, vol. 13, 2011.
[85] M. E. Ramosoeu, H. K. Chikwanda, A. S. Bolokang, G. Booysen, and T. N. Ngonda, "Additive manufacturing: Characterization of TI-6AI-4V alloy intended for biomedical application," 2010.
[86] G. F. V. Voort, *Metallography, principles and practice*. ASM International, 1984.
[87] A. Ajovalasit, M. Scafidi, B. Zuccarello, M. Beghini, L. Bertini, C. Santus, E. Valentini, A. Benincasa, and L. Bertelli, "AIAS–TR01: 2010 The hole-drilling strain gauge method for the measurement of uniform or non-uniform residual stresses."
[88] "ASTM Standard E837-08: 'Standard Test Method for Determining Residual Stresses by the Hole-Drilling Strain-Gage Method'," *ASTM International*, 2008.
[89] N. Rendler and I. Vigness, *Hole-drilling Strain-gage Method of Measuring Residual Stresses*. Defense Technical Information Center, 1965.
[90] "Strain Gage Measurement," *Computational design lab*. [Online]. Available: http://computationaldesignlab.org/hnat/ME415Website/Strain.html. [Accessed: 29-Nov-2011].
[91] A. L. Window, *Strain gauge technology*. Springer, 1992.
[92] "Instruction Manual for the Anchor Load Cell (Model ANCLO)." Roctest Limited, 2009.
[93] "Standard Test Method for Determining Residual Stresses by the Hole-Drilling Strain-Gage Method." ASTM International, 2008.

[94] G. S. Schajer, "Measurement of non-uniform residual stresses using the hole-drilling method. Part I - Stress calculation procedures," *J. Eng. Mater. Technol.*, vol. 110, no. 4, Oct. 1988.
[95] J. Luo, G. Montay, and J. Lu, "An Advanced Residual Stress Determination for 3D Cylinder Structure," *Materials Science Forum*, vol. 490–491, pp. 62–66, 2005.
[96] John Press, "An investigation of the residual stress in tube to tube sheet welds of boiler and their alleviation," *University of Cape Town*, Sep. 2000.
[97] R. Moharami and I. Sattari-Far, "Experimental and numerical study of measuring high welding residual stresses by using the blind-hole-drilling technique," *The Journal of Strain Analysis for Engineering Design*, vol. 43, no. 3, pp. 141–148, Mar. 2008.
[98] "ASTM Standard B311 - 08: Standard Test Method for Density of Powder Metallurgy (PM) Materials Containing Less Than Two Percent Porosity," *ASTM International*, 2008.
[99] N. McCormick and J. Lord, "Digital Image Correlation," *Materials Today*, vol. 13, no. 12, pp. 52–54, 2010.
[100] A. Zehnder, "Lecture notes on fracture mechanics," *Sibley School of Mechanical and Aerospace Engineering, Cornell University*, 2009.
[101] P. Sztefek, M. Vanleene, R. Olsson, R. Collinson, A. A. Pitsillides, and S. Shefelbine, "Using digital image correlation to determine bone surface strains during loading and after adaptation of the mouse tibia," *Journal of biomechanics*, vol. 43, no. 4, pp. 599–605, 2010.
[102] G. Catalanotti, P. P. Camanho, J. Xavier, C. G. Dávila, and A. T. Marques, "Measurement of resistance curves in the longitudinal failure of composites using digital image correlation," *Composites Science and Technology*, vol. 70, no. 13, pp. 1986–1993, Nov. 2010.
[103] C. Eberl, R. Thompson, D. Gianola, and S. Bundschuh, "Digital Image Correlation and Tracking with Matlab," Karlsruhe Institute of Technology, Germany, Aug. 2010.
[104] R. Oettel, "The determination of uncertainties in residual stress measurement (using the hole drilling technique)," *UNCERT, Standards Measurement and Testing Project SMT4-CT97-2165, Siempelkamp*, 2000.
[105] M. A. Imam and C. M. Gilmore, "Fatigue and microstructural properties of quenched Ti-6Al-4V," *Metallurgical and Materials Transactions A*, vol. 14, no. 1, pp. 233–240, 1983.
[106] A. C. E.-8 on F. and Fracture and E. S. I. Society, *Fatigue and fracture mechanics: 34th volume*. ASTM International, 2005.
[107] R. R. Boyer, "Titanium and Its Alloys: Metallurgy, Heat Treatment and Alloy Characteristics."
[108] H. M. Flower, *High performance materials in aerospace*. Chapman & Hall, 1995.
[109] J. Cai, F. Li, T. Liu, and B. Chen, "Investigation of mechanical behavior of quenched Ti-6Al-4V alloy by microindentation," *Materials Characterization*, vol. 62, no. 3, pp. 287–293, Mar. 2011.
[110] M. J. R. Barboza, C. Moura Neto, and C. R. M. Silva, "Creep mechanisms and physical modeling for Ti-6Al-4V," *Materials Science and Engineering A*, vol. 369, no. 1–2, pp. 201–209, 2004.
[111] R. Filip, K. Kubiak, W. Ziaja, and J. Sieniawski, "The effect of microstructure on the mechanical properties of two-phase titanium alloys," *Journal of Materials Processing Technology*, vol. 133, no. 1–2, pp. 84–89, Feb. 2003.
[112] "Heat Treating of Titanium and Titanium Alloys," *Key to Metals*, 31-Nov-2011. [Online]. Available: http://www.keytometals.com/Article97.htm. [Accessed: 31-Oct-2011].

[113] R. M. Pelloux, G. R. Romanoski, and others, “The fatigue behavior of small cracks in aircraft turbine disk alloys,” Massachusetts Institute of Technology, 1990.

APPENDIX A

A.1 RESIDUAL STRESS UNCERTAINTY MEASUREMENT

The assumptions used in the error analysis presented in this section are listed below.

- Plane stress condition
- Uniform residual stress
- Distance between neighbouring measurement holes > 10 x D_o
- No measurements taken near significant geometry changes

The constants used in the calculations which follow are given below in Table A.1.

Table A.1: Material and test constants

E	120 ± 20 GPa
μ	0.32 ± 0.01
D	5.14 mm
D_o	1.8 mm

The worked example is taken from strain gauge 1 of specimen A4 prior to heat treatment. The measurements in Table A.2 are used for a depth of 2mm from the surface.

Table A.2: Strain relieved after 2mm depth attained on specimen A4 (strain gauge 1) prior to heat treatment.

ε_1	-868×10^{-3}
ε_2	-1203×10^{-3}
ε_3	-778×10^{-3}

Step 1:

The uncertainty of $\bar{a}$ and $\bar{b}$ are first determined in the calculations which follow.

The uncertainties are calculated using the extreme values of the drilling constants, i.e.

$$\frac{D_O}{D} = \frac{1.81}{5.13} = 0.3502 \quad \textbf{(A-1)}$$

$$\frac{D_O}{D} = \frac{1.79}{5.15} = 0.3476 \quad \textbf{(A-2)}$$

The corresponding values obtained from ASTM E837-08 for the drilling depths are,

$$\frac{D_O}{D} = 0.3502 \quad : \quad \bar{a} = 0.1481, \qquad \bar{b} = 0.3717 \quad \textbf{(A-3)}$$

$$\frac{D_O}{D} = 0.3528 \quad : \quad \bar{a} = 0.1577, \qquad \bar{b} = 0.3895 \quad \textbf{(A-4)}$$

From which the tolerances are calculated to be:

$$\bar{a} = 0.150 \pm 0.0021 \ (\pm 1.5\ \%) \quad \textbf{(A-5)}$$

$$\bar{b} = 0.376 \pm 0.0044 \ (\pm 1.2\ \%) \quad \textbf{(A-6)}$$

Step 2:

These uncertainties are carried forward into $\bar{A}$ and $\bar{B}$ as shown below along with the uncertainties of the material constants given in Table A.1.

$$\bar{A} = -\frac{(1+\mu)}{2E}.\bar{a} \quad \textbf{(A-7)}$$

$$\bar{B} = -\frac{1}{2E}.\bar{b} \quad \textbf{(A-8)}$$

From which the maximum and minimum values for $\bar{A}$ and $\bar{B}$ represent the uncertainty.

Step 3:

The residual stress uncertainty is then obtained from all combinations of the uncertainties according to the equations from ASTM E837-08, i.e. the maximum and minimum values of σ_{max}, σ_{min} and β.

$$\sigma_{min}, \sigma_{max} = \frac{\varepsilon_3 + \varepsilon_1}{4\bar{A}} \pm \frac{\sqrt{(\varepsilon_3 - \varepsilon_1)^2 + (\varepsilon_3 + \varepsilon_1 - 2\varepsilon_2)^2}}{4\bar{B}} \quad \textbf{(A-9)}$$

$$\beta = \frac{1}{2} arctan\left(\frac{\varepsilon_3 + \varepsilon_1 - 2\varepsilon_2}{\varepsilon_3 - \varepsilon_1}\right) \quad \textbf{(A-10)}$$

Step 5:

The usage of Sattari-far's correction procedure for high residual stresses produced uncertainties between 15-18 % in the tests conducted by the authors [97]. Since no further information is available for the error estimation of non-uniform residual stresses (as per ASTM E837-08) or for residual stress greater than 70% yield, the maximum error stated by Sattari-Far will be adopted in addition to those uncertainties calculated in the previous steps, i.e.

$$Correction\ procedure\ uncertainty = \pm 18\% \quad \textbf{(A-11)}$$

APPENDIX B

B.1 STRAIN RELIEF DATA

B.1.1 OVERVIEW

This section gives the raw strain relief data as measured using the P-3500 strain indicator. The strains are measured according to the gauge number, i.e. ε1, ε2 and ε3 in specimens A1-4 and D1-4. This strain data was used to calculate the residual stress as per ASTM E837-08. They are presented here to demonstrate the differences in strain relieved before and after heat treatments and to re-affirm the results from the calculations.

The strain relief data for specimens A1 and D1 which were subjected to the Stress-Relief treatment is given below in Figure B.1 and Figure B.2 respectively.

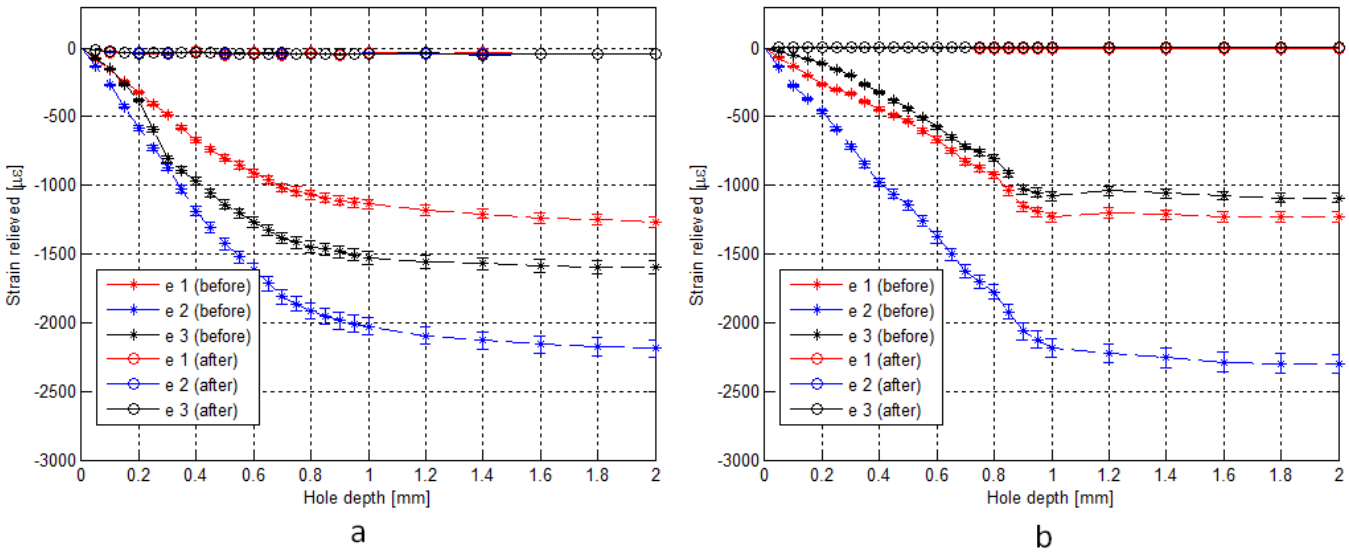

Figure B.1: Raw strain relief data for specimen A1 prior and post heat treatment at, a) gauge 1 and, b) gauge 2.

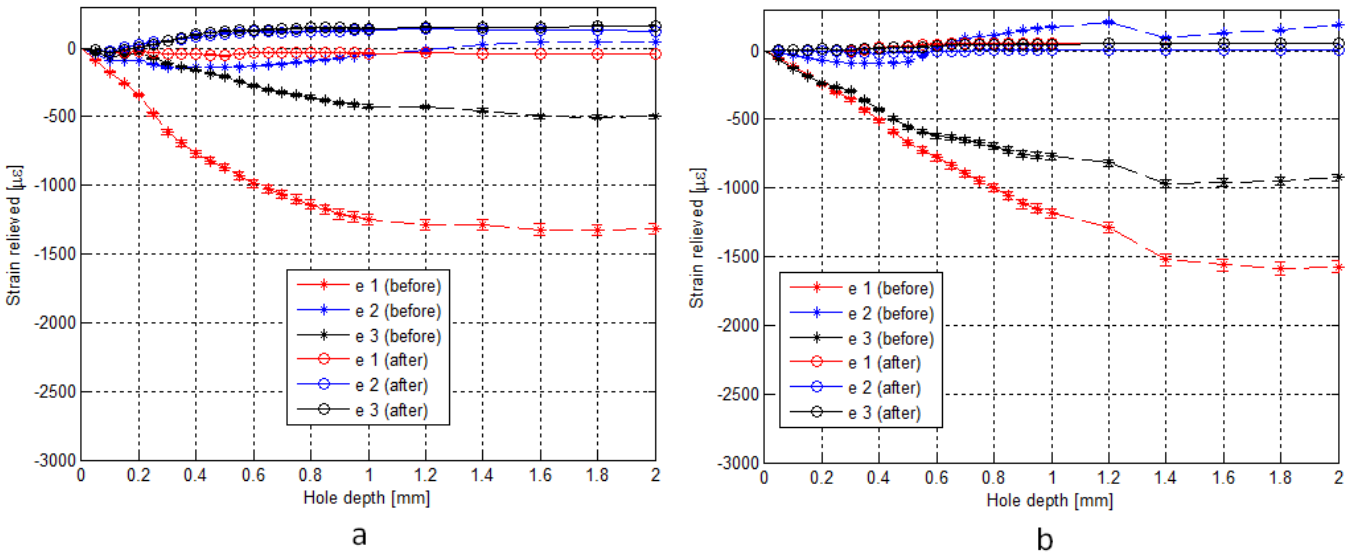

Figure B.2: Raw strain relief data for specimen D1 prior and post heat treatment at, a) gauge 1 and, b) gauge 2.

The strain relief data for specimens A2 and D2 which were subjected to Recrystallization Anneal is given below in Figure B.3 and Figure B.4 respectively.

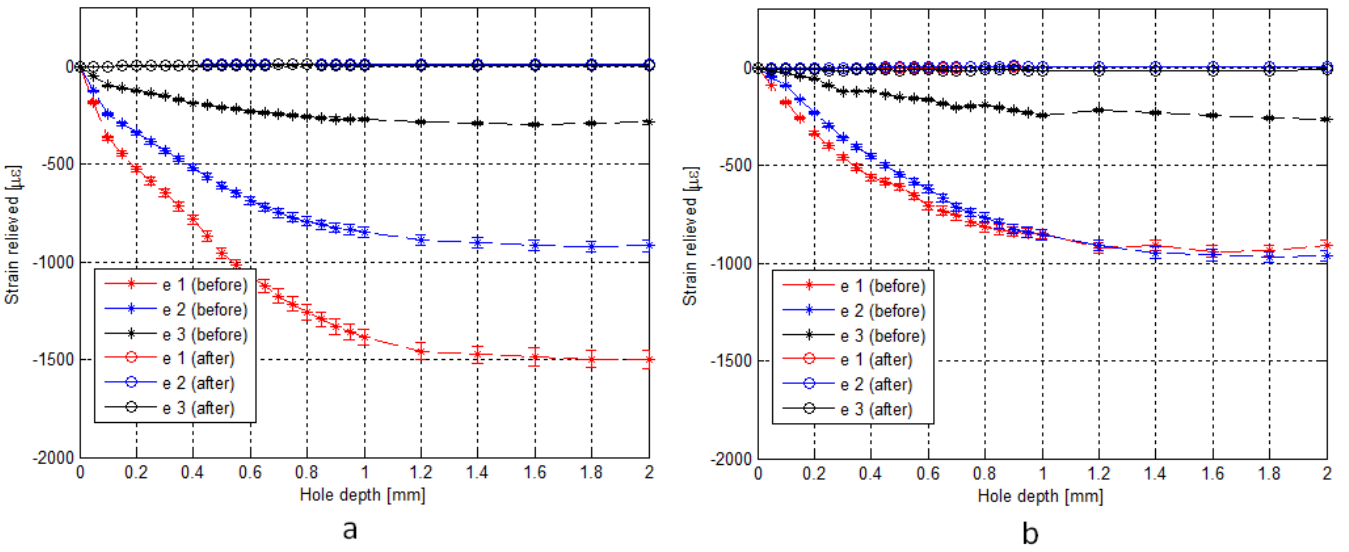

Figure B.3: Raw strain relief data for specimen A2 prior and post heat treatment at, a) gauge 1 and, b) gauge 2.

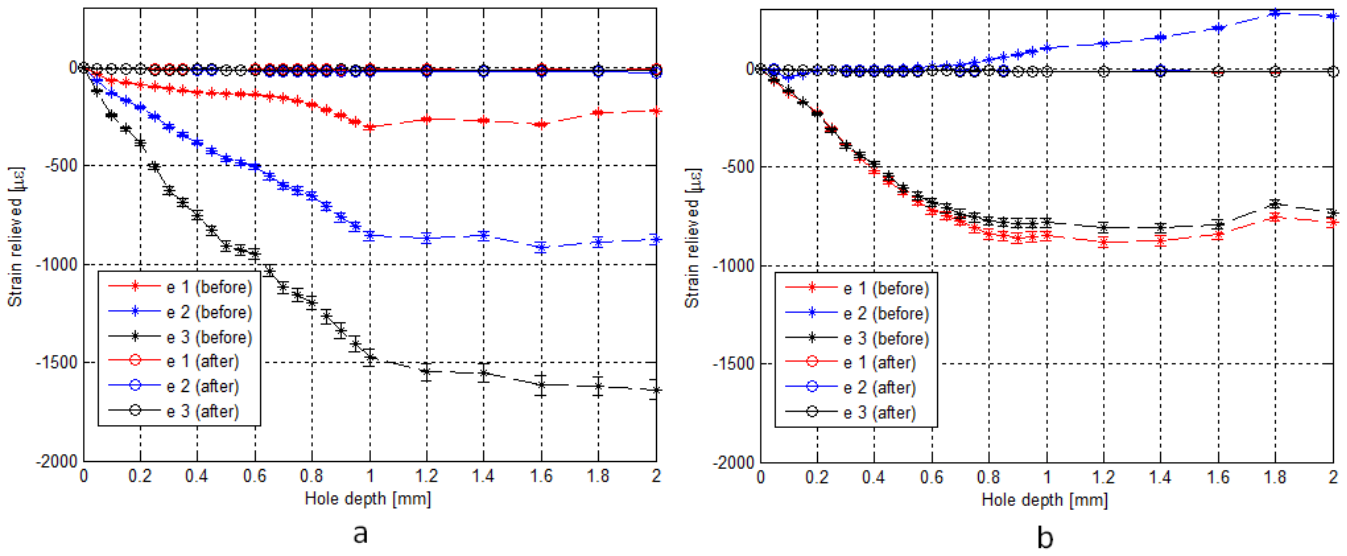

Figure B.4: Raw strain relief data for specimen D2 prior and post heat treatment at, a) gauge 1 and, b) gauge 2.

The strain relief data for specimens A3 and D3 which were subjected to the Duplex Anneal is given below in Figure B.5 and Figure B.6 respectively.

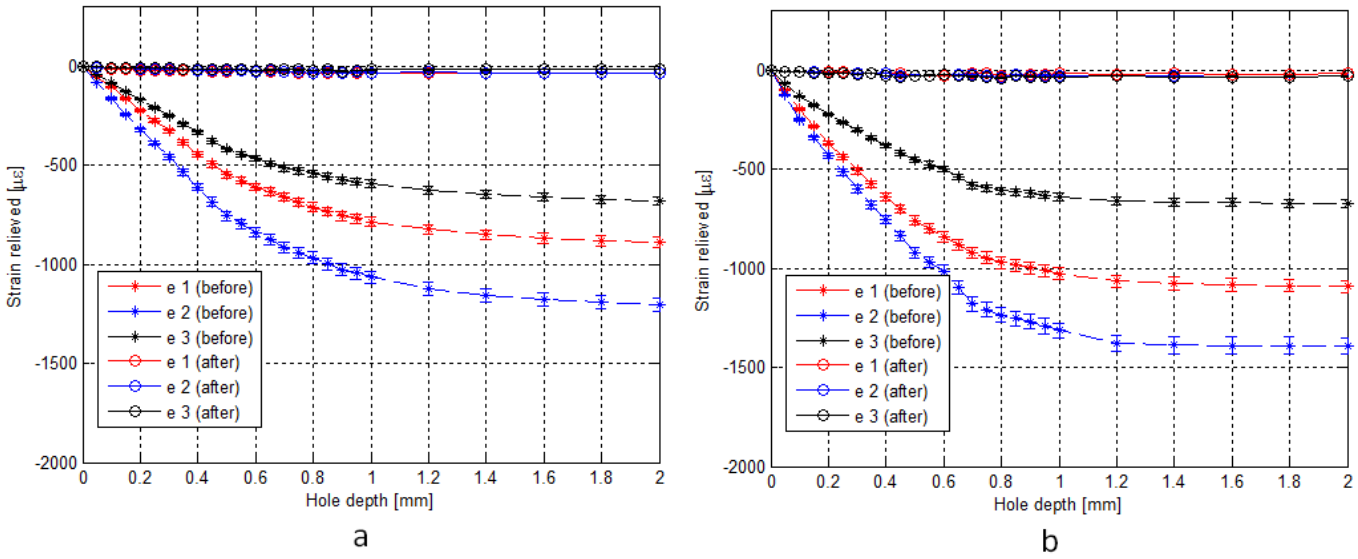

Figure B.5: Raw strain relief data for specimen A3 prior and post heat treatment at, a) gauge 1 and, b) gauge 2.

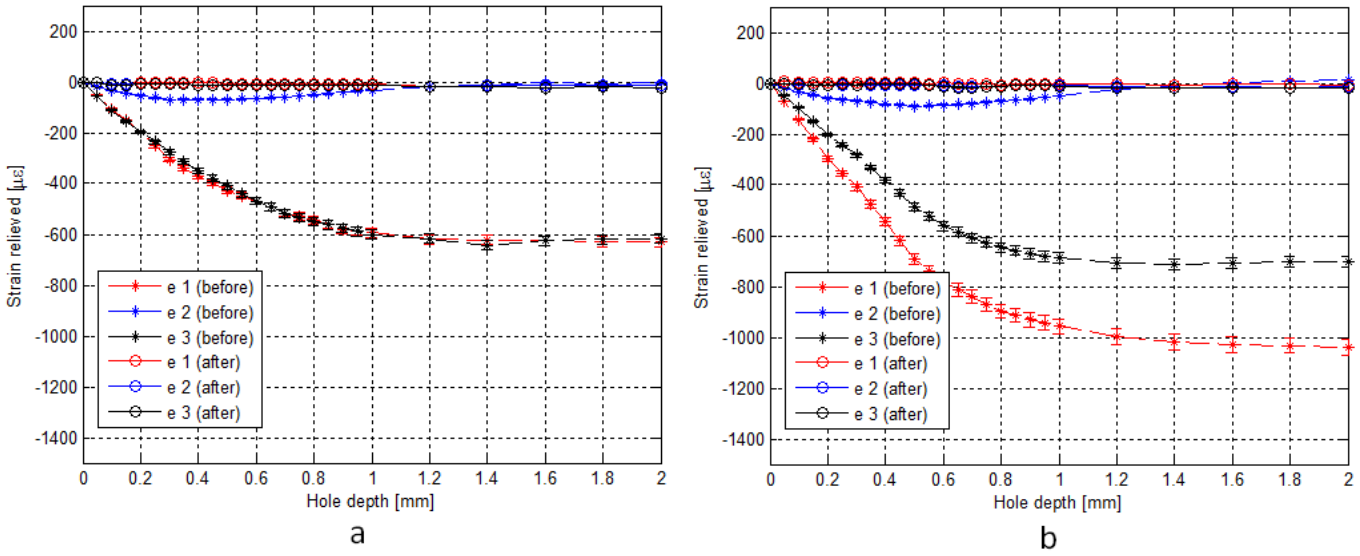

Figure B.6: Raw strain relief data for specimen D3 prior and post heat treatment at, a) gauge 1 and, b) gauge 2.

The strain relief data for specimens A4 and D4 which were subjected to the Beta Anneal is given below in Figure B.7 and Figure B.8 respectively.

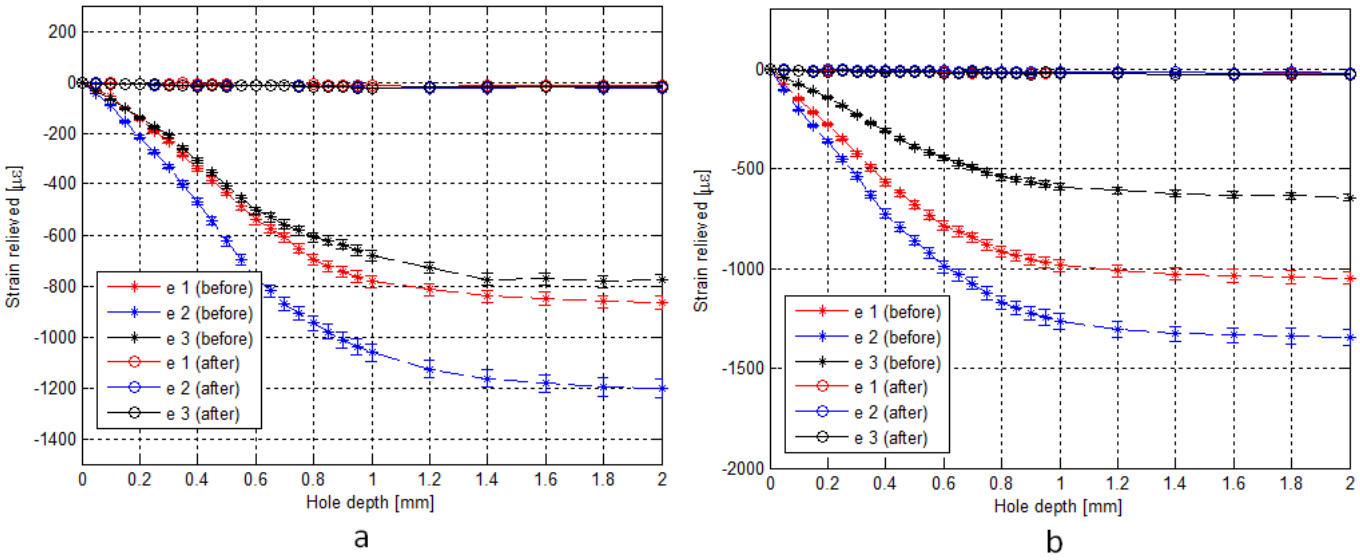

Figure B.7: Raw strain relief data for specimen A4 prior and post heat treatment at, a) gauge 1 and, b) gauge 2.

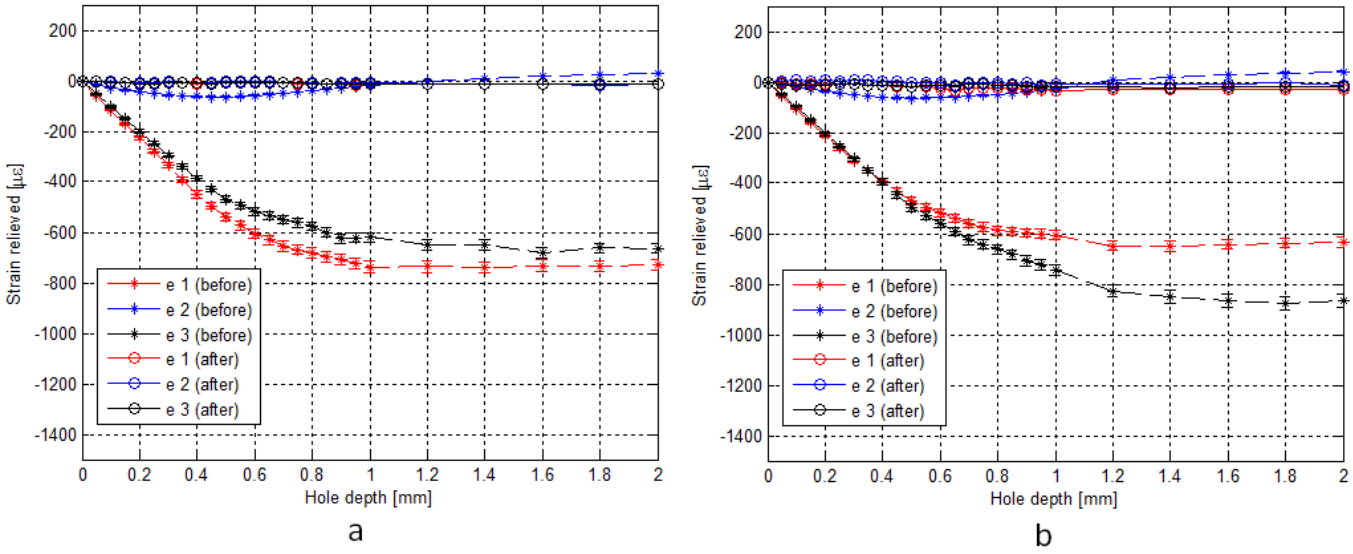

Figure B.8: Raw strain relief data for specimen D4 prior and post heat treatment at, a) gauge 1 and, b) gauge 2.

APPENDIX C

C.1 RESIDUAL STRESS ANALYSIS MATLAB CODE

C.1.1 NON-UNIFORM STRESS ANALYSIS CODE

```
function non_uniform_stress_A_rosette

% ------------------------------------------------------------------------
% Material Constants
E = 120;
E_t = 1.25;
yield = 1090;
v = 0.321;
% Number of strain increments
n = 20;

% ------------------------------------------------------------------------
% Imported strain results
strain = [--14.5    -11 -17
-29 -22 -34
-28.5   3   -15.5
-28 28  3
-33.5   42  26.5
-39 56  50
-39.5   68  75
-40 80  100
-48.5   93  112.5
-57 106 125
-45 113.5   126.5
-33 121 128
-34 118.5   133
-35 116 138
-35 119.5   142.5
-35 123 147
-35.5   123 147
-36 123 147
-37 126.5   144.5
-38 130 142];

% Isolating strain vectors e_1, e_2 and e_3
e_1 = strain(:,1);
e_2 = strain(:,2);
e_3 = strain(:,3);

% ------------------------------------------------------------------------
% Determining strain combination vectors p, q and t
p = (e_3 + e_1)/2000;
q = (e_3 - e_1)/2000;
```

```
t = (e_3 + e_1 - 2*e_2)/2000;

% ------------------------------------------------------------------------
% Initialising standard deviation vectors
p_std = 0;
q_std = 0;
t_std = 0;

% Analysing standard deviation from each set of strain data
for j = 1:n-3
    p_std = p_std + (p(j) - 3*p(j+1) + 3*p(j+2) - p(j+3))^2/(20*n-60);
    q_std = q_std + (q(j) - 3*q(j+1) + 3*q(j+2) - q(j+3))^2/(20*n-60);
    t_std = t_std + (t(j) - 3*t(j+1) + 3*t(j+2) - t(j+3))^2/(20*n-60);
end

% ------------------------------------------------------------------------
% Calibration matrix a for strain gauge type A
a = (1.6/2)^2*[-0.00679 0   0   0   0   0   0   0   0   0   0   0   0   0   0
0   0   0   0   0
-0.00815    -0.00714    0   0   0   0   0   0   0   0   0   0   0   0   0   0
0   0   0   0
-0.00937    -0.00844    -0.00734    0   0   0   0   0   0   0   0   0   0   0
0   0   0   0   0   0
-0.01046    -0.0096 -0.00858    -0.00739    0   0   0   0   0   0   0   0   0
0   0   0   0   0   0   0
-0.01141    -0.01063    -0.00968    -0.00856    -0.00728    0   0   0   0   0
0   0   0   0   0   0   0   0   0   0
-0.01223    -0.01152    -0.01064    -0.0096 -0.00839    -0.00701    0   0   0
0   0   0   0   0   0   0   0   0   0   0
-0.01291    -0.01227    -0.01147    -0.0105 -0.00936    -0.00806    -0.00659
0   0   0   0   0   0   0   0   0   0   0   0
-0.0136 -0.01287    -0.01207    -0.01132    -0.01015    -0.00893    -0.00759
-0.00615    0   0   0   0   0   0   0   0   0   0   0   0
-0.01416    -0.01344    -0.01264    -0.01184    -0.01082    -0.0097 -0.00846
-0.00712    -0.00567    0   0   0   0   0   0   0   0   0   0   0
-0.01463    -0.01392    -0.01312    -0.01223    -0.01134    -0.01031    -
0.00917    -0.00793    -0.00657    -0.00511    0   0   0   0   0   0   0   0
0   0
-0.01508    -0.01434    -0.01354    -0.0127 -0.01173    -0.01072    -0.00977
-0.00854    -0.0073 -0.006  -0.00464    0   0   0   0   0   0   0   0   0
-0.01545    -0.01471    -0.01391    -0.01306    -0.01211    -0.01113    -
0.01013    -0.00906    -0.00791    -0.0067 -0.00543    -0.00411    0   0   0
0   0   0   0   0
-0.01578    -0.01503    -0.01422    -0.0134 -0.01243    -0.01146    -0.01049
-0.00938    -0.00842    -0.00722    -0.00604    -0.00485    -0.00364    0   0
0   0   0   0   0
-0.01606    -0.01531    -0.0145 -0.01366    -0.01271    -0.01175    -0.01078
-0.0097 -0.00869    -0.00765    -0.00655    -0.00544    -0.00431    -0.00316
0   0   0   0   0   0
-0.01629    -0.01554    -0.01473    -0.0139 -0.01294    -0.01199    -0.01102
-0.00996    -0.00892    -0.00795    -0.00693    -0.00589    -0.00484    -
0.00378    -0.0027 0   0   0   0   0
-0.01649    -0.01574    -0.01493    -0.0141 -0.01313    -0.01217    -0.01123
-0.01018    -0.00919    -0.00815    -0.00716    -0.00624    -0.00524    -
0.00425    -0.00328    -0.00231    0   0   0   0
```

```
-0.01665    -0.0159 -0.0151 -0.01426    -0.0133 -0.01234    -0.01138    -
0.01036    -0.00938    -0.00836    -0.00738    -0.00644    -0.00555    -
0.00464    -0.00373    -0.00283    -0.00195    0   0   0
-0.01679    -0.01604    -0.01523    -0.01441    -0.01344    -0.01248    -
0.01151    -0.01049    -0.00955    -0.00852    -0.00755    -0.00665    -
0.00574    -0.00492    -0.00406    -0.00323    -0.00241    -0.00162    0   0
-0.01692    -0.01617    -0.01536    -0.01452    -0.01357    -0.01261    -
0.01164    -0.01063    -0.00967    -0.00866    -0.0077 -0.00679    -0.00592
-0.00508    -0.00432    -0.00353    -0.00277    -0.00203    -0.00131    0
-0.01704    -0.01628    -0.01548    -0.01465    -0.01368    -0.01272    -
0.01176    -0.01074    -0.00978    -0.00877    -0.00781    -0.0069 -0.00605
-0.00521    -0.00448    -0.00374    -0.00303    -0.00234    -0.00167    -
0.00103];

% -------------------------------------------------------------------------
% Calibration matrix b for strain gauge type A
b = (1.6/2)^2*[-0.01264 0   0   0   0   0   0   0   0   0   0   0   0   0   0
0   0   0   0   0
-0.0147 -0.01352    0   0   0   0   0   0   0   0   0   0   0   0   0   0   0
0   0   0
-0.01656    -0.01554    -0.01414    0   0   0   0   0   0   0   0   0   0   0
0   0   0   0   0   0
-0.01821    -0.01735    -0.01611    -0.01449    0   0   0   0   0   0   0   0
0   0   0   0   0   0   0   0
-0.01967    -0.01897    -0.01789    -0.01642    -0.01458    0   0   0   0   0
0   0   0   0   0   0   0   0   0   0
-0.02092    -0.02038    -0.01946    -0.01815    -0.01647    -0.01439    0   0
0   0   0   0   0   0   0   0   0   0   0   0
-0.02197    -0.02159    -0.02083    -0.01968    -0.01815    -0.01624    -
0.01395    0   0   0   0   0   0   0   0   0   0   0   0   0   0
-0.02308    -0.02256    -0.02182    -0.02112    -0.01952    -0.01778    -
0.01576    -0.01348    0   0   0   0   0   0   0   0   0   0   0   0
-0.024  -0.02351    -0.0228 -0.02202    -0.02072    -0.01917    -0.01735    -
0.01525    -0.01289    0   0   0   0   0   0   0   0   0   0   0
-0.02481    -0.02434    -0.02366    -0.02273    -0.02167    -0.02031    -
0.01868    -0.01678    -0.0146 -0.01216    0   0   0   0   0   0   0   0   0
0
-0.02554    -0.02507    -0.0244 -0.02362    -0.02235    -0.02103    -0.01981
-0.01793    -0.01599    -0.01386    -0.01156    0   0   0   0   0   0   0   0
0
-0.02616    -0.02571    -0.02505    -0.02428    -0.02305    -0.02177    -
0.02045    -0.0189 -0.01715    -0.01522    -0.0131 -0.01081    0   0   0   0
0   0   0   0
-0.02668    -0.02625    -0.02561    -0.02487    -0.02364    -0.02239    -
0.02109    -0.01949    -0.01813    -0.01623    -0.0143 -0.01226    -0.01013
0   0   0   0   0   0   0
-0.02715    -0.02673    -0.02611    -0.02536    -0.02417    -0.02294    -
0.02164    -0.02012    -0.01866    -0.01708    -0.01531    -0.01345    -
0.01149    -0.00944    0   0   0   0   0   0
-0.02753    -0.02713    -0.02653    -0.02582    -0.02463    -0.02341    -
0.02213    -0.02064    -0.01911    -0.01767    -0.01608    -0.01439    -
0.0126 -0.01073    -0.00875    0   0   0   0   0
-0.02789    -0.02749    -0.0269 -0.0262 -0.02502    -0.02382    -0.02256    -
0.02108    -0.01968    -0.01807    -0.01652    -0.01511    -0.01344    -
0.01172    -0.00995    -0.00812    0   0   0   0
```

```
-0.02821    -0.02781    -0.02722    -0.02652    -0.02536    -0.02417    -
0.02292    -0.02146    -0.02007    -0.0185 -0.01698    -0.01549    -0.01408
-0.01251    -0.01089    -0.00921    -0.00747    0   0   0
-0.02848    -0.02809    -0.0275 -0.02682    -0.02565    -0.02447    -0.02324
-0.02176    -0.02041    -0.01885    -0.01736    -0.0159 -0.01441    -0.01312
-0.011591   -0.01004    -0.00847    -0.00688    0   0
-0.02871    -0.02832    -0.02774    -0.02706    -0.02591    -0.02473    -
0.0235 -0.02204    -0.02067    -0.01916    -0.01769    -0.01624    -0.0148 -
0.0134 -0.01213    -0.01072    -0.00928    -0.00781    -0.00632    0
-0.02889    -0.02851    -0.02794    -0.02727    -0.02612    -0.02495    -
0.02373    -0.02227    -0.02089    -0.0194 -0.01796    -0.01655    -0.01511
-0.01367    -0.01249    -0.01121    -0.00989    -0.00856    -0.00719    -
0.00581];

% ------------------------------------------------------------------------
% Forming regularisation matrix c for Tikhonov regularisation
for i = 2:n-1
    c(i,i) = 2;
    c(i,i-1) = -1;
    c(i,i+1) = -1;
end
c(n,n) = 0;

% Initial values for regularisation constants
alpha_p = 10^-4;
alpha_q = 10^-4;
alpha_t = 10^-4;
indicator = 1;

% Un-regularised calculation for comparison purposes
P_mat = E/(1+v)*(a)^-1*p;
Q_mat = E*(b)^-1*q;
T_mat = E*(b)^-1*t;
for u=1:n
Sigma_max_unreg(u) = P_mat(u) + ((Q_mat(u))^2 + (T_mat(u))^2)^0.5;
Sigma_min_unreg(u) = P_mat(u) - ((Q_mat(u))^2 + (T_mat(u))^2)^0.5;
Beta_unreg(u) = 180/pi*(0.5*atan(-T_mat(u)/-Q_mat(u)));
end

% ------------------------------------------------------------------------
% Regularisation loop
while indicator == 1;

% Determining stress matrices P, Q and T
P_matrix = (a'*a + alpha_p*(c)'*c)^-1*E/(1+v)*(a)'*p;
Q_matrix = (b'*b + alpha_q*(c)'*c)^-1*E*(b)'*q;
T_matrix = (b'*b + alpha_t*(c)'*c)^-1*E*(b)'*t;

% Determining misfit vectors
p_misfit = p - (1+v)/E*a*P_matrix;
q_misfit = q - 1/E*b*Q_matrix;
t_misfit = t - 1/E*b*T_matrix;

% Initialising RMS error functions
p_rms = 0;
```

```
q_rms = 0;
t_rms = 0;

% Determining RMS error from the misfit vectors
for i = 1:n
    p_rms = p_rms + 1/n*(p_misfit(i))^2;
    q_rms = q_rms + 1/n*(q_misfit(i))^2;
    t_rms = t_rms + 1/n*(t_misfit(i))^2;
end

% Improved regularisation constants
alpha_p = p_std/p_rms*alpha_p;
alpha_q = q_std/q_rms*alpha_q;
alpha_t = t_std/t_rms*alpha_t;

% Nested if statements checking sufficient regularisation is achieved
    if abs((p_rms - p_std)/p_std) > 0.05
        indicator = 1;
    else if abs((q_rms - q_std)/q_std) > 0.05
        indicator = 1;
        else if abs((t_rms - t_std)/t_std) > 0.05
                indicator = 1;
            else
                % If RMS and standard deviation values differ by less than
                % 5% then the results are sufficiently accurate
                indicator = 0;
            end
        end
    end
end

% ------------------------------------------------------------------------
% Determining the cartesian and principal stresses and their orientation
for i=1:n
Cartesian_x(i) = P_matrix(i) - Q_matrix(i);
Cartesian_y(i) = P_matrix(i) + Q_matrix(i);
Cartesian_xy(i) = T_matrix(i);
Sigma_max(i) = P_matrix(i) + sqrt((Q_matrix(i))^2 + (T_matrix(i))^2);
Sigma_min(i) = P_matrix(i) - sqrt((Q_matrix(i))^2 + (T_matrix(i))^2);
Beta(i) = 180/pi*(0.5*atan(-T_matrix(i)/-Q_matrix(i)));
end

% ------------------------------------------------------------------------
% Corrective procedure for high residual stresses
p = 24*(2-E_t/E-(E_t/E)^2);
q = 35*(1-E_t/E);

for i = 1:n
    m_val(i) = p*(Sigma_min(i)/Sigma_max(i))^4+q;
    plastic_error(i) = m_val(i)*(Sigma_max(i)/yield-0.5)^2;
    Sigma_max_corr(i) = 100*Sigma_max(i)/(m_val(i)*(Sigma_max(i)/yield-
0.5^2)^2+100);
end

% ------------------------------------------------------------------------
```

```
% Print results to screen
% Relieved strain
figure
plot((0.05:0.05:1),e_1,'--.red')
hold on
plot((0.05:0.05:1),e_2,'-..blue')
plot((0.05:0.05:1),e_3,':.green')
grid on
legend('e 1','e 2','e 3','Location','Best')
xlabel('Hole depth [mm]')
ylabel('Strain relieved [\mu\epsilon]')

% Maximum principal stresses
figure
plot((0.05:0.05:1),Sigma_max, 'b-..','LineWidth',2);
hold on
plot((0.05:0.05:1),Sigma_max_unreg, 'r:.','LineWidth',2);
hold on
plot((0.05:0.05:1),Sigma_max_corr, 'g:.','LineWidth',2);
grid on
legend('Regularised \sigma_m_a_x','Un-regularised \sigma_m_a_x','Corrected
\sigma_m_a_x','Location','Best');
xlabel('Hole depth [mm]')
ylabel('Stress [MPa]')

% Maximum principal stresses
figure
plot((0.05:0.05:1),Sigma_max, 'b-..','LineWidth',2);
hold on
plot((0.05:0.05:1),Sigma_max_unreg, 'r:.','LineWidth',2);
hold on
plot((0.05:0.05:1),Sigma_max_corr, 'black- diamond','LineWidth',1.3);
grid on
legend('Regularised \sigma_m_a_x','Un-regularised \sigma_m_a_x','Corrected
\sigma_m_a_x','Location','Best');
xlabel('Hole depth [mm]')
ylabel('Stress [MPa]')

% Plastic Error
figure
plot((0.05:0.05:1),plastic_error, 'b-..','LineWidth',2);
grid on
legend('Plastic error','Location','Best');
xlabel('Hole depth [mm]')
ylabel('Plastic error [%]')

% Orientation
figure
plot((0.05:0.05:1),Beta, 'b-..','LineWidth',2);
hold on
plot((0.05:0.05:1),Beta_unreg, 'r:.','LineWidth',2);
grid on
legend('Regularised Beta','Unregularised Beta','Location','Best');
xlabel('Hole depth [mm]')
ylabel(['Degrees [' char(176) ']'])
end
```

C.2 DATA ACQUISITION MATLAB CODE

C.2.1 POSITION CAPTURE CODE

```
function Position_capture

% Clear variables and assign analog input device
clear all
ai = analoginput('nidaq','Dev1');

%% Apply settings to the data acquisition device
set(ai,'InputType','Differential');
% Speed of sample acquisition
ai.SampleRate = 10000;
% Number of samples measured per trigger
ai.SamplesPerTrigger = 100;
% Analog channel from nidaq device
addchannel(ai, 1); % Position sensor
addchannel(ai, 2); % Strain indicator
ai.Channel(2).InputRange=[-2 2];

%% Initialising plot variables
time=0;
pos=0;
str=0;
% Handle for displacement plots
figure
displacement = plot(time,pos,'r*--');
hold on;
plot(0,0,'k+');
axis([0 100 0 5]);
grid on;
xlabel('Time');
ylabel('Position');
hold off;
% Handle for strain plots
figure
strain = plot(time,str,'k*--');
hold on;
plot(0,0,'k+');
axis([0 100 0 7500]);
grid on;
xlabel('Time');
ylabel('Strain');
hold off;

%% Data storage variable
store_data=[];

%% Kill switch
global KEY_IS_NOT_PRESSED
KEY_IS_NOT_PRESSED = 0;
```

```
gcf;
set(gcf, 'KeyPressFcn', @myKeyPressFcn);

%% Live data acquisition
change_to_force = 508/0.0219;
tic;
while ~KEY_IS_NOT_PRESSED
start(ai);
wait(ai,8);
data = getdata(ai);
pos=mean(data(:,1));
str=mean(data(:,2));
time=toc;
set(displacement,'XData',time);
set(displacement,'YData',pos);
set(strain,'XData',time);
set(strain,'YData',(str+1.3976)*change_to_force);
drawnow
store_data=[store_data;[time,pos,str]];
end
disp('loop ended')

%% Clean up and data saving
nextset = [100000, 100000];
dlmwrite('data.csv',nextset,'-append');
dlmwrite('data.csv',store_data,'-append');
stop(ai);
delete(ai);
```

C.2.2 KILL-SWITCH CODE

```
% Code developed by Matthew Molteno 08/11/2011
function myKeyPressFcn(hObject, event)
global KEY_IS_NOT_PRESSED
KEY_IS_NOT_PRESSED = 1;
disp('key is pressed')
```

C.3 OPTICAL DENSITY TESTING CODE

```
function Determine_Density

close all
clear all
clc

%% Import Image

% Load Image and convert to grayscale
specimen_col = imread('Test2.jpg');
specimen = rgb2gray(specimen_col);
% Display the image
figure, imshow(specimen)
% Plot histogram of pixel intensities
figure, imhist(specimen)
xlabel('Pixel Intensity');
ylabel('Number of counts');

%% Extract image pixel data

[counts,Pixel_Intensity] = imhist(specimen);
% Pixel_Intensity is a column vector from 0 (darkest) to 255 (lightest)
% counts is the number occurences of each pixel_intensity
Total_Pixels = sum(counts);
voids = 0;

%% Determine Density

% Setting void threshold
pix_threshold = 40;
for i=1:pix_threshold
    voids = voids + counts(i);
end
Density = 100 - voids/Total_Pixels*100

%% Threshold variation check

for threshold = 1:256
    for j = 1:threshold
        voids = voids + counts(j);
    end
    Threshold_check(threshold) = 100 - voids/Total_Pixels*100;
    voids = 0;
end
figure
plot(1:256,Threshold_check)
xlabel('Pixel Threshold');
ylabel('Density');
grid minor;
```

APPENDIX D

D.1 PILOT STUDY SPECIMENS

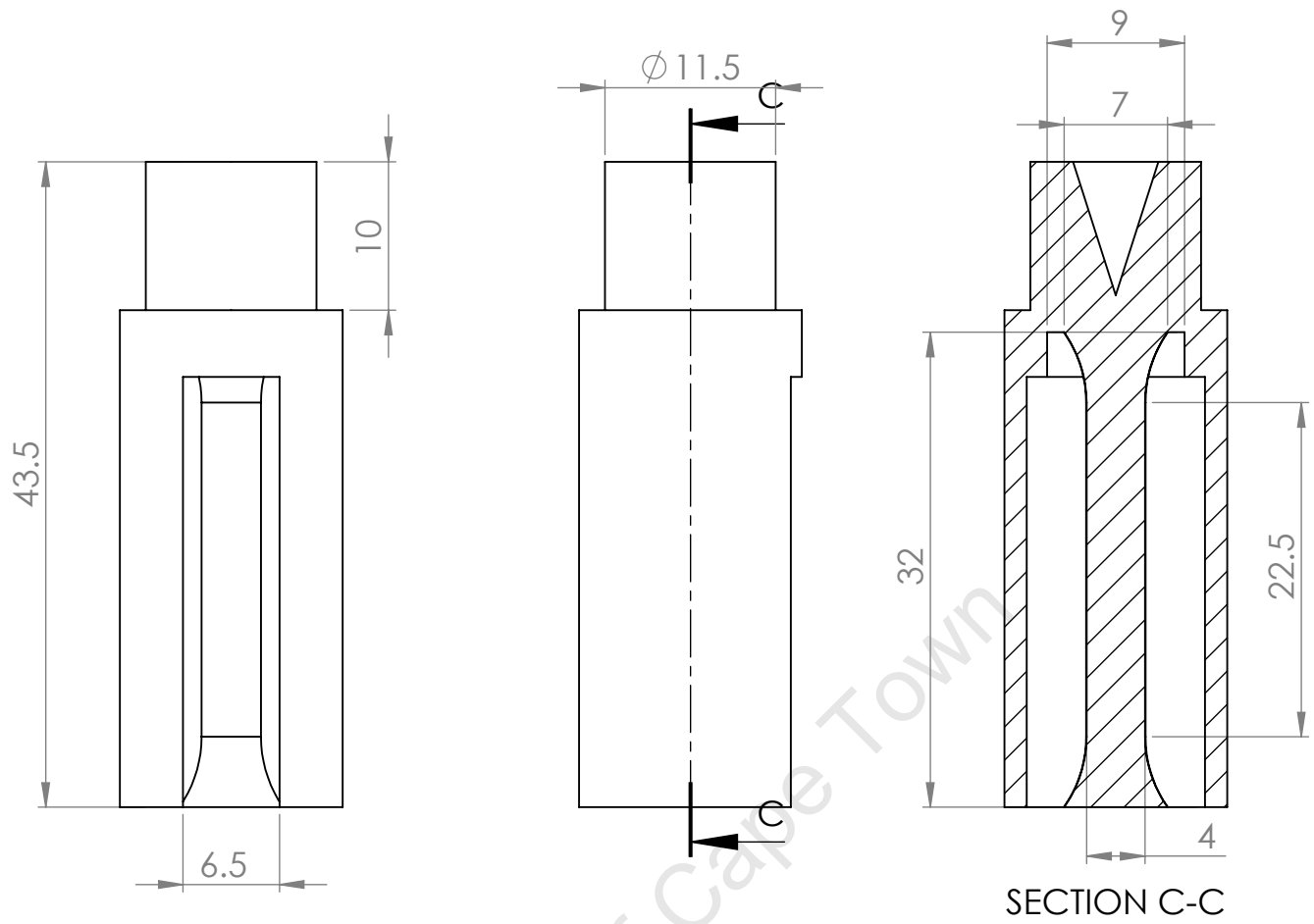

UNLESS OTHERWISE SPECIFIED: DIMENSIONS ARE IN MILLIMETERS SURFACE FINISH: TOLERANCES: LINEAR: ANGULAR:	FINISH:	DEBUR AND BREAK SHARP EDGES	DO NOT SCALE DRAWING / REVISION

	NAME	SIGNATURE	DATE
DRAWN			
CHK'D			
APPV'D			
MFG			
Q.A			

TITLE: Failed Specimen

MATERIAL: SLM Ti-6Al-4V

DWG NO. DWG 1

A4

WEIGHT:

SCALE:2:1

SHEET 1 OF 1

D.2 MINIATURE TENSILE RIG DRAWINGS

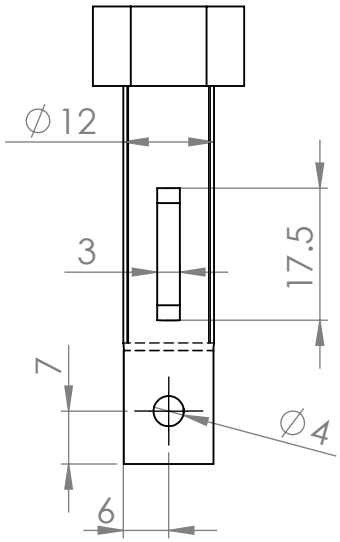

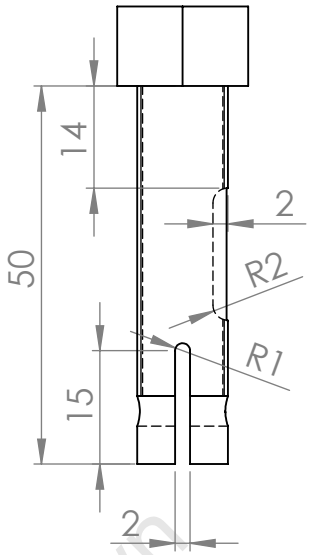

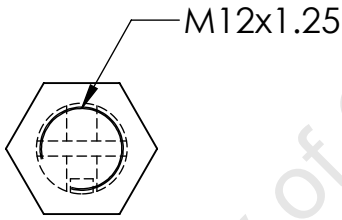

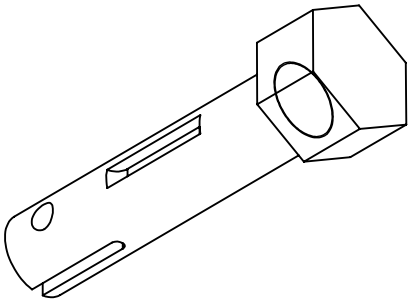

UNLESS OTHERWISE SPECIFIED: DIMENSIONS ARE IN MILLIMETERS SURFACE FINISH: TOLERANCES: +-0.01mm LINEAR: ANGULAR:	FINISH:		DEBUR AND BREAK SHARP EDGES		DO NOT SCALE DRAWING	REVISION
	NAME	SIGNATURE	DATE		TITLE:	
DRAWN					Load ring bolt	
CHK'D						
APPV'D						
MFG						
Q.A				MATERIAL:	DWG NO.	A4
				High tensile bolt Gr 8.8	Craig Knowles & Prof R B Tait	
				WEIGHT:	SCALE:2:1	SHEET 1 OF 1

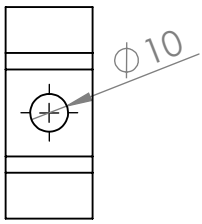

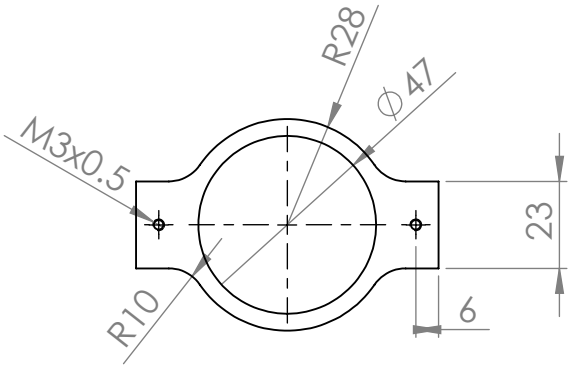

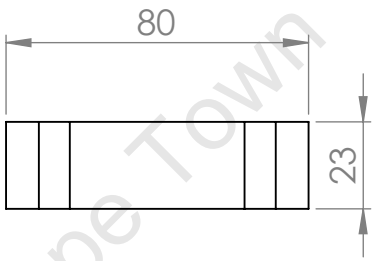

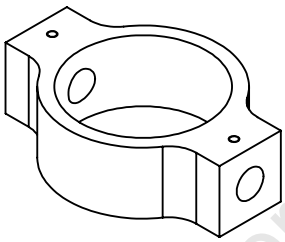

Approved RB Tait

UNLESS OTHERWISE SPECIFIED: DIMENSIONS ARE IN MILLIMETERS SURFACE FINISH: TOLERANCES: LINEAR: ANGULAR:	FINISH:		DEBUR AND BREAK SHARP EDGES	DO NOT SCALE DRAWING	REVISION	
	NAME	SIGNATURE	DATE	TITLE:		
DRAWN				Load Ring		
CHK'D						
APPV'D						
MFG						
Q.A				MATERIAL: Mild Steel	DWG NO. Craig Knowles & Prof RB Tait	A4
				WEIGHT:	SCALE:1:2	SHEET 1 OF 1

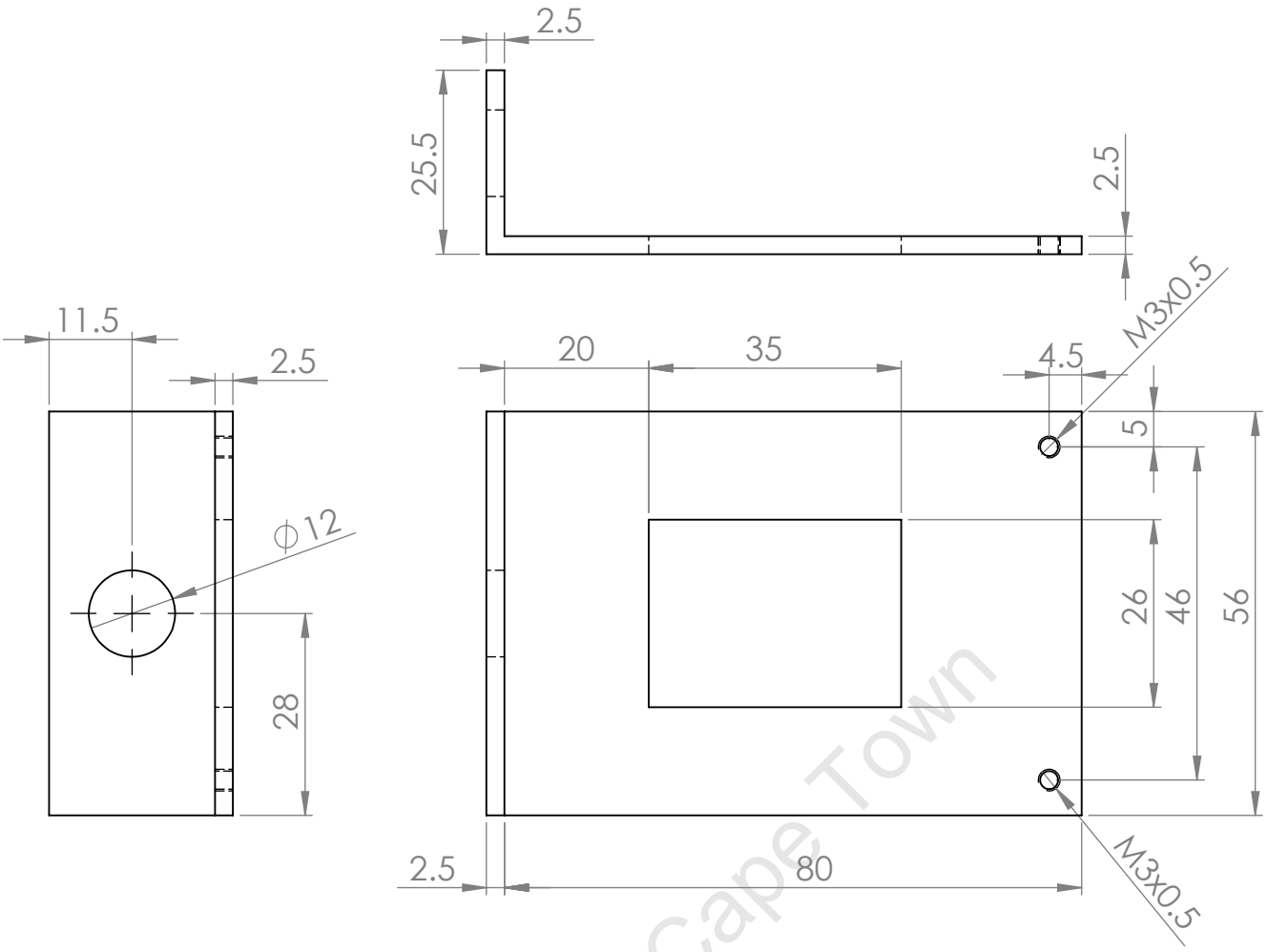

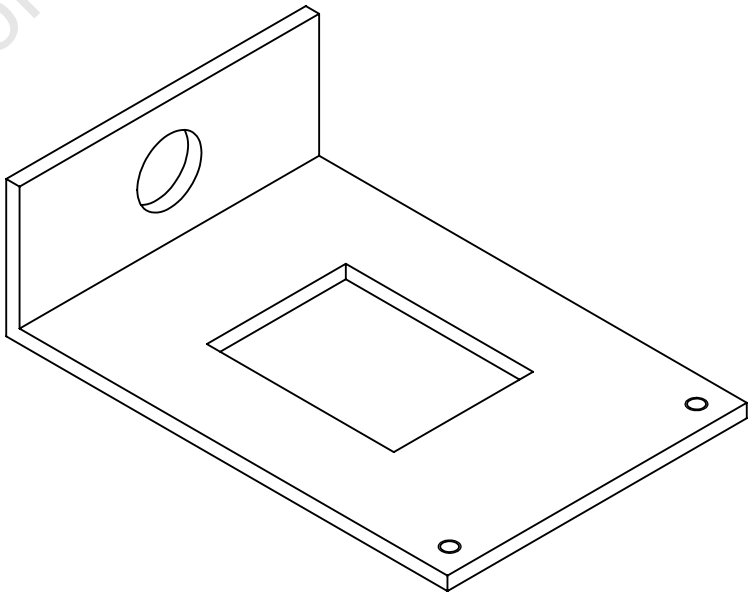

UNLESS OTHERWISE SPECIFIED: DIMENSIONS ARE IN MILLIMETERS SURFACE FINISH: TOLERANCES: LINEAR: 0.1mm ANGULAR:		FINISH:		DEBUR AND BREAK SHARP EDGES		
				DO NOT SCALE DRAWING		REVISION
	NAME	SIGNATURE	DATE			
DRAWN				TITLE:		
CHK'D				Locating plate		
APPV'D						
MFG						
Q.A				MATERIAL:	DWG NO.	A4
				Aluminium	Craig Knowles & Prof RB Tait	
				WEIGHT:	SCALE:1:2	SHEET 1 OF 1

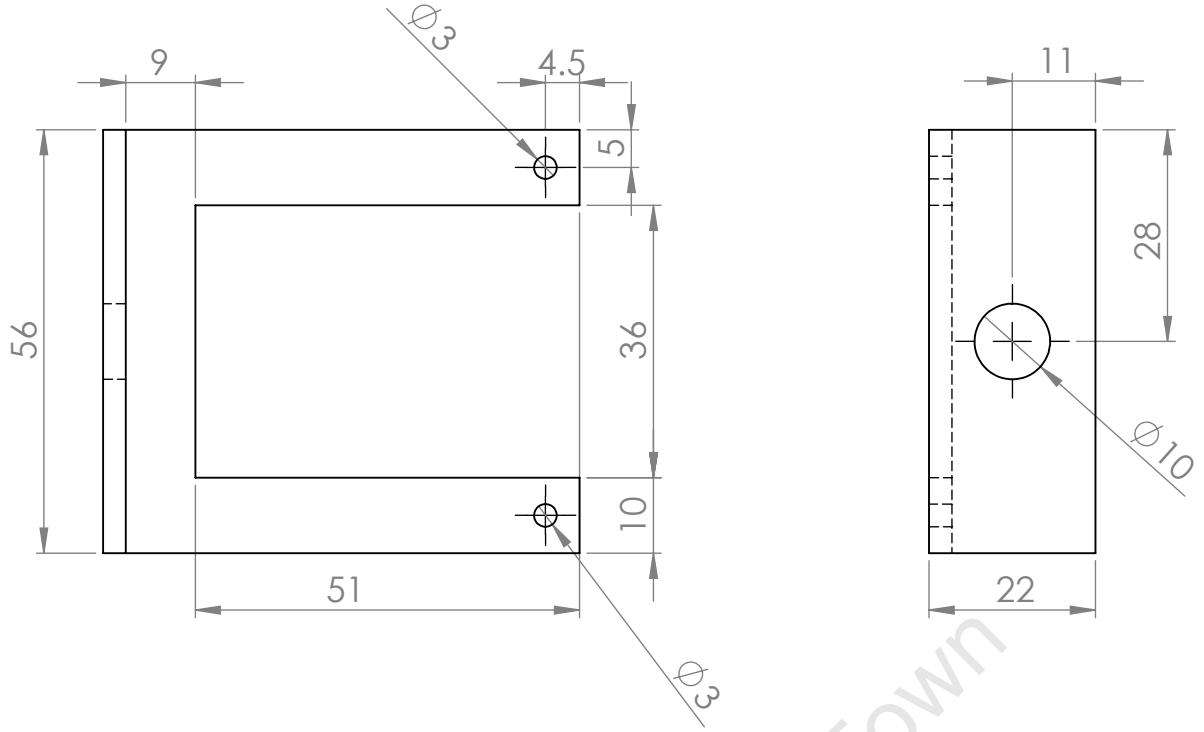

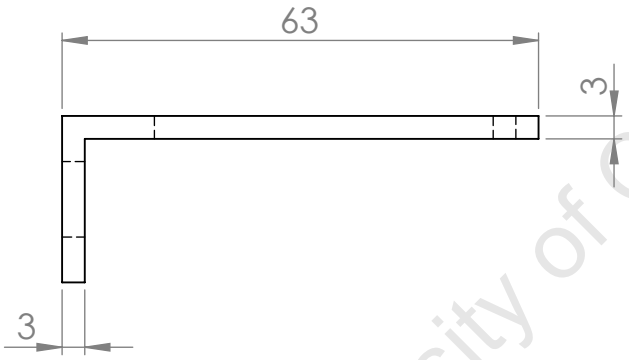

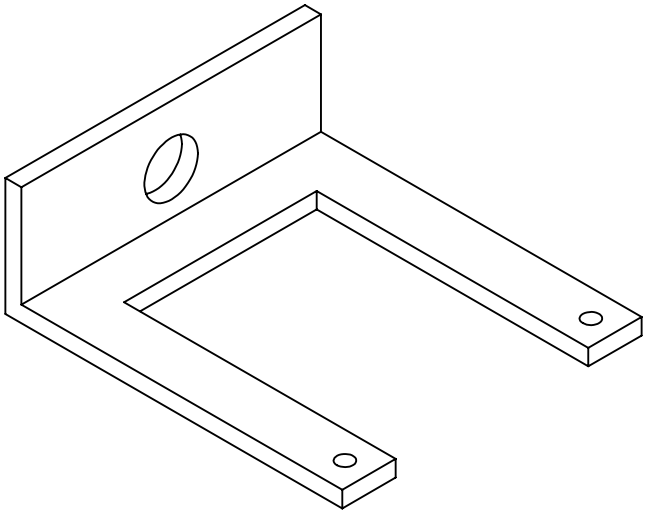

UNLESS OTHERWISE SPECIFIED: DIMENSIONS ARE IN MILLIMETERS SURFACE FINISH: TOLERANCES: LINEAR: ANGULAR:	FINISH:		DEBUR AND BREAK SHARP EDGES	DO NOT SCALE DRAWING	REVISION	
				Prof RB Tait & Craig Knowles		
	NAME	SIGNATURE	DATE	TITLE:		
DRAWN				Position sensor plate		
CHK'D						
APPV'D						
MFG						
Q.A				MATERIAL: Aluminium	DWG NO.	A4
				WEIGHT:	SCALE:1:2	SHEET 1 OF 1

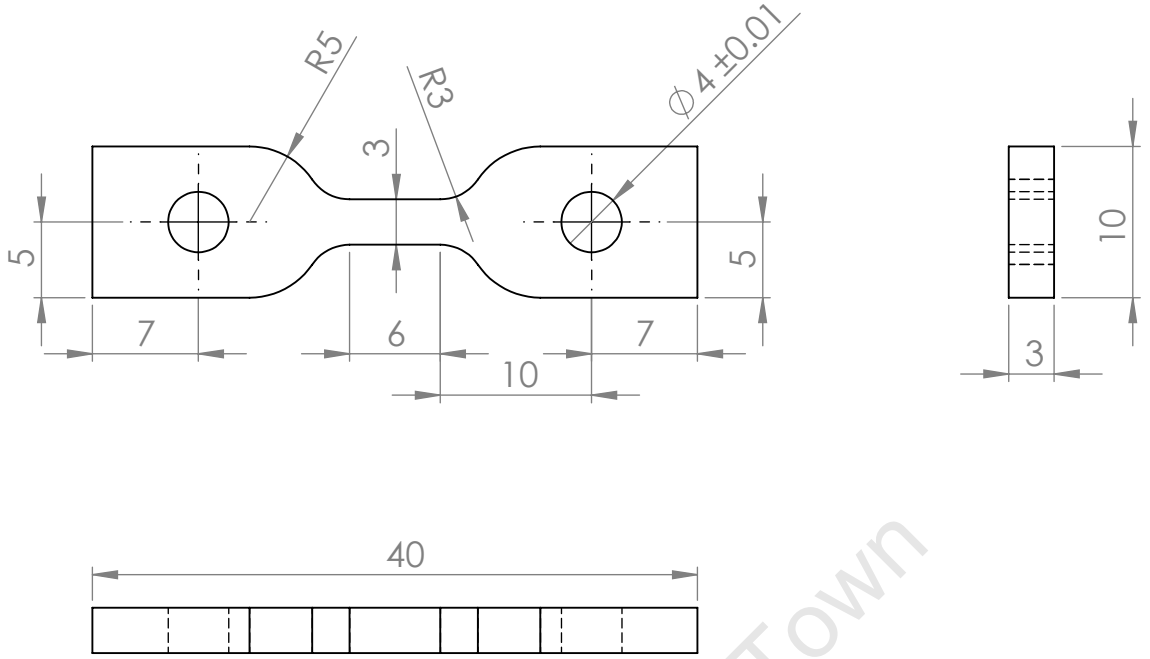

UNLESS OTHERWISE SPECIFIED: DIMENSIONS ARE IN MILLIMETERS SURFACE FINISH: TOLERANCES: LINEAR: ±0.01mm ANGULAR:	FINISH:	DEBUR AND BREAK SHARP EDGES	DO NOT SCALE DRAWING / REVISION

	NAME	SIGNATURE	DATE
DRAWN			
CHK'D			
APPV'D			
MFG			
Q.A			

TITLE: Ti-6Al-4V tensile specimen

MATERIAL: Ti-6Al-4V

DWG NO.

A4

WEIGHT:

SCALE:2:1

SHEET 1 OF 1